Surface Modification of Copper-Based Alloys in Antibacterial Application

Dissertation

zur Erlangung des Grades
des Doktors der Ingenieurwissenschaften
der Naturwissenschaftlich-Technischen Fakultät
der Universität des Saarlandes

UNIVERSITÄT
DES
SAARLANDES

vorgelegt von
Aisha Saddiqa AHMED

Saarbrücken
2025

Tag des Kolloquiums:	19.02.2026
Dekan	Prof. Dr. Dirk Bähre
Berichterstatter:	Prof. Dr. Frank Mücklich
	Prof. Dr. Jean-François Pierson
	Priv.-Doz. Dr. Ruth Hemmersbach
	Prof. Dr. Philippe Steyer
Vorsitz:	Prof. Dr. Volker Presser
Akad. Mitarbeiter:	Dr. Stéphanie Bruyere
Mitglieder des Prüfungsausschusses:	Dr. Marthe Rousseau

Thèse

Pour l'obtention du titre de:

DOCTEUR de L'UNIVERSITÉ DE LORRAINE

Spécialité : Sciences des Matériaux

présentée par:

Aisha Saddiqa AHMED

Modification de Surface des Alliages à Base de Cuivre pour des Applications Antibactériennes

Soutenue publiquement le 2026 à Sarrebruck devant le jury composé de :

Directeur de These	Frank Mücklich	Professor, Functional Materials, Saarland University
Co-directeur de These	Jean-François Pierson	Professor, Institut Jean Lamour, University of Lorraine
Président de jury	Volker Presser	Professor, Energy Materials, Saarland University
Rapporteur	Ruth Hemmersbach	Professor, Institut für Luft- und Raumfahrtmedizin, German Aerospace Center (DLR)
Rapporteur	Philippe Steyer	Professor, Institut National des Sciences Appliquées de Lyon
Examinateur	Stéphanie Bruyere	Researcher, Institut Jean Lamour, University of Lorraine
Examinateur	Marthe Rousseau	Researcher, SAINBIOSE, University of Saint-Etienne

Institut Jean Lamour, UMR 7198, ARTEM – CS 50840-54011 Nancy Cedex
Université de Lorraine – Ecole doctorale Chimie – Mécanique – Matériaux – Physique (C2MP)

"Everything depends on wisdom, and wisdom depends on good manners."

- Imam Ali (a.s.)

TABLE OF CONTENTS

ACKNOWLEDGEMENTS

I would like to express my deepest gratitude to my supervisor, Prof. Dr.-Ing. Frank Mücklich, at the *Lehrstuhl für Funktionswerkstoffe (FuWe)*, *Universität des Saarlandes (UdS)*, for giving me the opportunity to be part of this remarkable project. His insightful guidance, valuable discussions, and unwavering support have been instrumental throughout my PhD journey. He has broadened my understanding beyond theoretical and experimental aspects, helping me to appreciate the practical relevance of my research and my development as a researcher. I am equally grateful to my supervisor at the *Institut Jean Lamour (IJL)*, *Université de Lorraine*, Prof. Dr. Jean-François Pierson, whose optimism and encouragement inspired me to strive for excellence in my work. Their combined expertise and mentorship were pivotal in successfully completing this thesis.

My heartfelt thanks go to Dr.-Ing. Daniel Wyn Müller, my colleague and project leader, who not only made my integration into the institute seamless but also served as an informal mentor. His constant support, constructive feedback, and readiness to help have been of immense value, both scientifically and personally. I am also thankful to my students Diego Sancio and Sebastian Wältermann for their enthusiasm and valuable contributions to our research. A special word of thanks goes to M.Sc. Maria Martins for her meticulous proofreading of this thesis; her attention to detail and thoughtful feedback greatly improved the clarity and coherence of the final document.

This doctoral research forms part of a broader framework of international collaborations, including the projects *BIOFILMS*, *Touching Surfaces*, and *ConTACTS Concordia*. I would like to thank the group of Prof. Ralf Müller at the *Deutsches Zentrum für Luft- und Raumfahrt (DLR)* for this excellent collaboration.

Furthermore, this work was carried out under a cotutelle agreement between *Universität des Saarlandes* and *Université de Lorraine*. My sincere appreciation goes to Dr.-Ing. Flavio Soldera and Dr. Claudia Heß for their guidance in managing the

cotutelle process, their coordination of the cooperation between the universities, and their efforts in securing financial support from the *Deutsch-Französische Hochschule (DFH)* during my doctoral stay in France.

I am also deeply thankful to all co-authors, especially the research groups led by Prof. Dr. Ralf Kautenburger (*UdS*), Prof. Dr. Karin Jacobs (*UdS*), and Prof. Dr. Jean Audinot (*Luxembourg Institute of Science and Technology, LIST*), for their valuable input and fruitful collaboration, which contributed to our joint publications.

To my colleagues at *FuWe* and *IJL*, especially Daniel Müller, Jiaqi Luo, Tobias Fox, Jenifer Barrirero, Stéphanie Bruyere, Christoph Pauly, Sebastian Suarez, Pranav Nayak, Bruno Alderete, Idriss El Azhari, and Maria Martins, thank you for your generosity, knowledge-sharing, and continuous support.

Finally, I extend my warmest thanks to my friends and colleagues, particularly Maria, for making this PhD journey not only intellectually stimulating but also truly enjoyable. Your friendship, encouragement, and sense of humour brightened even the most demanding moments.

Most importantly, I owe my deepest gratitude to my family. To my parents, Bashir and Naz, without whom none of this would have been possible, thank you for investing in me in every possible way so that I could reach this point in my life. Words cannot fully express how grateful I am for your unconditional love and support. To my siblings, Rida, Iqra, and Ayaan, thank you for being there through every high and low, and for always motivating me to persevere. To my husband, Imran, thank you for your constant encouragement, faith in me, and for always pushing me to reach my fullest potential while never letting me give up on my dreams. And to my son, Imaad, you have taught me to slow down, to cherish what truly matters, and to find balance amidst the chaos. You are the anchor in my busy and sometimes turbulent life.

To everyone who has contributed in one way or another to this work, your support, patience, and kindness are deeply appreciated. Thank you.

ABSTRACT

The rise of multidrug-resistant pathogens highlights the need for antimicrobial materials beyond conventional antibiotics. Copper has intrinsic antibacterial activity, but its practical use is limited by durability and corrosion issues. This doctoral research utilizes ultrashort pulsed direct laser interference pattering (USP-DLIP) to create microscale structures on copper-based alloys to enhance the antibacterial efficiency. Brass, bronze, and copper-nickels alloys were structured, and systematically characterized using microscopy, diffraction, and spectroscopy, and finally assessed against *Escherichia coli*. The findings demonstrate that three factors - alloy composition, oxidation and topography - play a joint role in modulating the antibacterial activity on these laser structured surfaces. In this case, the microscale structures with dimensions (3 μm) matching that of the bacterial cells showed an enhanced contact-killing effect. While, removing oxides via citric acid etching restored the copper-rich surface leading to a further increase in antibacterial activity. Overall, the line-like structures due to a better dimension compatibility outperformed other complex honeycomb patterns. These findings establish a strong framework for designing durable and scalable antimicrobial copper-based alloys with relevance in healthcare, public infrastructures, and international initiatives such as *Biofilms*, *Touching Surface*, and *ConTACTS Concordia*.

KURZFASSUNG

Der Anstieg multiresistenter Pathogene verdeutlicht den Bedarf an antimikrobiellen Materialien über konventionelle Antibiotika hinaus. Kupfer besitzt intrinsische antibakterielle Eigenschaften, jedoch ist seine praktische Anwendung durch begrenzte Haltbarkeit und Korrosionsanfälligkeit eingeschränkt. Dieser Arbeit nutzt die ultrakurzgepulste „Direct Laser Interference Patterning"-Methode (USP-DLIP), um Mikrotopographie auf Kupferlegierungen zu erzeugen und die antibakterielle Wirksamkeit zu verbessern. Messing, Bronze und Kupfer-Nickel-Legierungen wurden strukturiert, mittels Mikroskopie, Beugung und Spektroskopie charakterisiert und gegen *Escherichia coli* getestet. Die Ergebnisse zeigen, dass Legierungszusammensetzung, Oxidation und Oberflächentopographie gemeinsam die antibakterielle Wirksamkeit bestimmen. Strukturen auf der Mikroskala von etwa 3 μm, vergleichbar mit der Größe bakterieller Zellen, zeigten einen verstärkten Contact-Killing-Effekt. Das Entfernen von Oxiden durch Zitronensäureätzung stellte eine kupferreiche Oberfläche wieder her und erhöhte die antibakterielle Aktivität weiter. Linienförmige Strukturen übertrafen komplexe Wabenmuster aufgrund besserer dimensionsbezogener Kompatibilität. Diese Erkenntnisse schaffen einen Rahmen für die Entwicklung langlebiger, skalierbarer antimikrobieller Kupferlegierungen, was für das Gesundheitswesen, die Infrastruktur und internationale Initiativen wie *BIOFILMS*, *Touching Surfaces* und *ConTACTS Concordia* von Bedeutung ist.

RÉSUMÉ

L'augmentation des pathogènes multirésistants souligne la nécessité de développer des matériaux antimicrobiens au-delà des antibiotiques conventionnels. Si le cuivre possède une activité antibactérienne intrinsèque, son utilisation pratique est limitée par sa durabilité et sa sensibilité à la corrosion. Ce travail de thèse applique la technique USP-DLIP (Direct Laser Interference Patterning) á impulsions ultracourtes pour texturer la surface d´ alliages à base de cuivre et améliorer leur efficacité antibactérienne. Des alliages de laiton, de bronze et de cuivre-nickel ont été structurés, caractérisés par microscopie électronique, diffraction des rayons X et spectroscopie, puis testés contre *Escherichia coli*. Les résultats montrent que la composition de l'alliage, l'oxydation et la topographie de la surface influencent conjointement l'activité antibactérienne. Des microstructures d'environ 3 μm, comparables à la taille des bactéries, ont renforcé l'effet de destruction par contact. L'élimination des oxydes par gravure à l'acide citrique a permis de restaurer une surface riche en cuivre et d'augmenter encore l'activité antibactérienne. Les structures linéaires ont surpassé les motifs alvéolaires complexes en raison d'une meilleure compatibilité dimensionnelle. Ces résultats fournissent un cadre pour la conception d'alliages de cuivre antimicrobiens durables et évolutifs, pertinents pour les soins de santé, les infrastructures et les initiatives internationales.

ERWEITERTE ZUSAMMENFASSUNG

Die wachsende Bedrohung durch multiresistente (MDR) Mikroorganismen stellt eine dringende Herausforderung für die moderne Gesellschaft dar, die sich vor allem aus dem übermäßigen Einsatz von Antibiotika und das daraus resultierende Auftreten von unbehandelbaren Infektionen zurückzuführen ist. Diese Erreger verbreiten sich in Gesundheitseinrichtungen leicht über Kontakt und Biofilmbildung und machen Oberflächen zu einem wichtigen Übertragungsweg. Sterilisations- und Desinfektionsmethoden sind zwar nach wie vor unerlässlich, jedoch arbeitsintensiv und nur vorübergehend wirksam. Ein nachhaltigerer Ansatz liegt in der Entwicklung antimikrobieller Materialien, die das Überleben von Bakterien bei Kontakt hemmen und so sowohl das Infektionsrisiko als auch den Wartungsaufwand reduzieren.

Kupfer gehört zu den wirksamsten bekannten Materialien zur Abtötung von Keimen, was in erster Linie auf die Freisetzung von Cu^{+}- und Cu^{2+}-Ionen zurückzuführen ist, die die Membranen und intrazellulären Bestandteile von Bakterien schädigen. Allerdings weist reines Kupfer eine begrenzte mechanische Festigkeit und Korrosionsbeständigkeit auf, was seinen Anwendungsbereich einschränkt. Durch Legieren von Kupfer mit Elementen wie Zink, Zinn oder Nickel lassen sich die Eigenschaften für die jeweilige Anwendung optimieren. Darüber hinaus sind die Mechanismen, die die Legierungszusammensetzung, die laserinduzierte Oberflächenstrukturierung, die Oxidation und das antibakterielle Verhalten miteinander verbinden, noch nicht ausreichend verstanden. Um diese Wissenslücke zu schließen, untersucht die vorliegende Doktorarbeit systematisch, wie Zusammensetzung, Oberflächentopographie und Chemie die antibakteriellen Eigenschaften von Kupferlegierungen beeinflussen, die durch ultrakurzgepulste direkte Laserinterferenzstrukturierung (USP-DLIP) modifiziert wurden.

Die Arbeit umfasst fünf begutachtete Studien, die zusammen eine umfassende Untersuchung von Messing (mit 15 und 37 Gew.-% Zn), Bronze (mit 6 Gew.-% Sn) und

Kupfer-Nickel-Legierungen (mit 10 und 30 Gew.-% Ni) bilden. Diese binären Systeme wurden ausgewählt, um den Einfluss von Zink, Zinn und Nickel auf die Wechselwirkung zwischen Laser und Material, die Oxidbildung und die Reaktion der Bakterien zu untersuchen. Ziel der Studie ist es, die antibakterielle Wirksamkeit durch Vergrößerung der effektiven Kontaktfläche mittels Strukturierung auf der Mikroskala zu verbessern.

Im ersten Teil der Arbeit wurden Messinglegierungen mittels Laser strukturiert, um periodische linienförmige Muster mit einer Größe von 3 µm zu erzeugen, die mit *E. coli*-Zellen vergleichbar sind. Fortgeschrittene Oberflächenanalysen (GI-XRD, STEM-EDS, APT, Raman und XPS) zeigten nanoskalige Veränderungen in einer Tiefe von einigen hundert Nanometern, darunter eine Anreicherung mit Zink und die Bildung von ZnO-, Cu_2O- und CuO-reichen Oxidschichten. Diese Veränderungen hatten einen erheblichen Einfluss sowohl auf das Korrosionsverhalten als auch auf die antibakterielle Wirkung. Die laserstrukturierten Messingoberflächen wiesen im Vergleich zu polierten Oberflächen eine geringere Abtötungsrate auf, was in erster Linie auf eine geringere Kupferkonzentration an der Oberfläche und die Bildung chemisch stabiler Zinkoxide zurückzuführen war, da diese die Freisetzung von Cu-Ionen begrenzten. Durch Zitronensäure-Ätzung wurden jedoch ZnO und CuO selektiv entfernt und gleichzeitig die Cu-reichen Bereiche wiederhergestellt, was insbesondere bei Messing mit geringerem Zinkgehalt zu einer verbesserten antibakteriellen Wirkung führte. Die Ergebnisse zeigen, dass der Zinkgehalt die Oxidstabilität und damit die antibakterielle Wirkung stark beeinflusst. Messinglegierungen mit einem Zinkgehalt von weniger als 30 Gew.-% bieten ein günstiges Gleichgewicht zwischen Korrosionsbeständigkeit und Kupferverfügbarkeit.

Aufbauend auf diesen Ergebnissen wurde das zweite System, Bronze (Cu mit 6 Gew.-% Sn), untersucht, um die Rolle von Zinn bei der Laserstrukturierung und dem antibakteriellen Verhalten zu bewerten. Unter Verwendung derselben USP-DLIP-Technik wurden periodische Linienstrukturen mit einer Breite von 3 µm hergestellt, und durch anschließendes Ätzen wurden die während der Bearbeitung entstandenen

Oxidschichten effizient entfernt. Die resultierenden Oberflächen wiesen eine erhöhte Hydrophobie und eine um bis zu 2,5-fach größere effektive Oberfläche als polierte Bronze. Antibakterielle Tests gegen *E. coli* zeigten Abtötungsraten, die mit denen von reinem Kupfer vergleichbar waren, was bestätigt, dass die strukturelle Kompatibilität zwischen Bakteriengröße und Strukturperiodizität ein entscheidender Faktor für die Kontaktabtötung ist. Diese Studie hat gezeigt, dass einfache Linien-Geometrien, wenn sie dimensional optimiert sind, ausreichen, um eine signifikante antibakterielle Verbesserung zu erzielen, und dass USP-DLIP solche Mikrotopographien reproduzierbar und mit hoher Präzision erzeugen kann.

In der nächsten Forschungsphase wurden die Oxidationseffekte in gemeinsam gesputterten Cu-Ni-Dünnschichten untersucht, um zu verstehen, wie die Oberflächenchemie allein die antibakterielle Wirksamkeit modulieren kann. Thermische Oxidationsexperimente zeigten, dass das Oxidationsverhalten stark vom Kupfergehalt abhängt. Cu-reiche Schichten (92 at. %) bildeten bei 200 °C Cu_2O-Schichten, während Ni-reiche Schichten (55 at. %) für eine vergleichbare Oxidation 250 °C benötigten. Diese chemische Entwicklung ging mit erheblichen Veränderungen der antibakteriellen Leistung einher: Die Oxidation beeinträchtigte die Aktivität in Cu-reichen Schichten, verstärkte sie jedoch in Ni-reichen Schichten, was bestätigt, dass eine kontrollierte Oxidation je nach Zusammensetzung die antibakterielle Funktion entweder unterdrücken oder fördern kann. Diese Erkenntnisse führten dazu, dass die Oxidation als einstellbares Designinstrument zur Verbesserung weniger aktiver Kupferlegierungen durch Modifikation der Oberflächenchemie eingeführt wurde.

Schließlich wurde die Laserstrukturierungsstrategie auf Cu-Ni-Legierungen (CuNi10 und CuNi30) angewendet, um die Kontrolle der Zusammensetzung und der Topografie zu kombinieren. Zwei periodische Designs – linienförmig und wabenförmig – wurden von USP-DLIP hergestellt. Chemische Analysen ergaben, dass die Laserbearbeitung die Bildung von kupfer- und nickelreichen Oxiden induzierte, wobei die CuNi10-Oberflächen von Cu_2O und die CuNi30-Oberflächen von NiO dominiert wurden. Nach dem Ätzen waren die CuNi10-Oberflächen überwiegend

Kupferreich, während NiO aufgrund seiner hohen Stabilität teilweise auf CuNi30 erhalten blieb. Antibakterielle Tests zeigten, dass geätzte CuNi10-Linienstrukturen die schnellste Abtötung von Bakterien erzielten, während CuNi30 eine wesentlich geringere Aktivität aufwies, was auf den Kupfergehalt zurückzuführen war, der unter den wirksamen antibakteriellen Schwellenwert (~60 Gew.-%) fiel. Darüber hinaus übertrafen Linienstrukturen durchweg Wabenstrukturen, was zeigt, dass die Effizienz der Kontaktabtötung sowohl von der Verfügbarkeit von Kupfer als auch von der dimensionalen Kompatibilität zwischen Bakteriengröße und Oberflächenmerkmalen abhängt. Diese Ergebnisse definierten einen kritischen Zusammensetzungsbereich (70–90 Gew.-% Cu) für die Aufrechterhaltung des antibakteriellen Verhaltens in laserstrukturierten Cu-Ni-Legierungen und unterstrichen das Potenzial der Kombination von Legierungsdesign mit geometrischer Optimierung.

In allen untersuchten Systemen zeigt diese Arbeit einen klaren Zusammenhang zwischen Legierungszusammensetzung, Oxidchemie und antibakterieller Wirksamkeit. Legierungselemente beeinflussen die Wechselwirkung zwischen Laser und Material sowie das Oxidationsverhalten stark: Zink und Nickel neigen dazu, stabile Oxide zu bilden, die die Freisetzung von Kupferionen begrenzen, während Zinn ein kontrolliertes Oxidwachstum fördert. Oberflächenbehandlungen wie Ätzen oder kontrollierte Oxidation können diesen Effekten entgegenwirken, indem sie kupferreiche Bereiche wieder freilegen.

Die Oberflächentopografie bietet eine weitere Kontrollmöglichkeit: Mikroskopisch kleine Linienstrukturen mit einer Periodizität von ~3 μm bieten durch Maximierung des Bakterienkontakts bei gleichzeitiger Erhaltung einer ausreichenden Kupferexposition die höchste antibakterielle Wirksamkeit.

Mechanistische Analysen bestätigten diese Trends: ICP-MS zeigte, dass die Freisetzung von Kupferionen mit der antibakteriellen Wirksamkeit korreliert, während HR-SIMS und SEM Nanoagglomerate auf Bakterienmembranen nachwiesen, was eine direkte Wechselwirkung zwischen Kupfer und Bakterien belegt. Somit ist die

durch ionenvermittelte und mechanische Schäden verursachte Kontaktabtötung der dominierende antibakterielle Mechanismus, wobei Benetzungseffekte nur eine untergeordnete Rolle spielen.

Insgesamt schafft diese Arbeit einen umfassenden Rahmen, der Zusammensetzung, Struktur und Oberflächenchemie mit antibakterieller Funktion verbindet. Die effektive Leistung ergibt sich aus der gemeinsamen Optimierung dieser Faktoren: Die Laserstrukturierung erhöht den Kontakt mit Bakterien, das Ätzen stellt aktives Kupfer wieder her und die kontrollierte Oxidation stabilisiert funktionelle Oxide. Diese Erkenntnisse bilden die Grundlage für die rationale Entwicklung antibakterieller Materialien auf Kupferbasis und unterstützen nachhaltige, selbstdesinfizierende Anwendungen im Gesundheitswesen, im öffentlichen Raum und unter Weltraumbedingungen.

RÉSUMÉ DÉTAILLÉ

La menace croissante que représentent les micro-organismes multirésistants (MDR) constitue un défi urgent pour la société moderne. Elle est principalement due à l'utilisation excessive d'antibiotiques et à l'apparition d'infections incurables qui en résulte. Ces agents pathogènes se propagent facilement dans les établissements de santé par contact et par la formation de biofilms, faisant des surfaces un vecteur de transmission important. Les méthodes de stérilisation et de désinfection restent indispensables, mais elles sont laborieuses et n'ont qu'une efficacité temporaire. Une approche plus durable consiste à développer des matériaux antimicrobiens qui inhibent la survie des bactéries au contact, réduisant ainsi à la fois le risque d'infection et les besoins d'entretien.

Le cuivre est l'un des matériaux les plus efficaces connus pour tuer les germes, principalement grâce à la libération d'ions Cu^{+} et Cu^{2+} qui endommagent les membranes et les composants intracellulaires des bactéries. Cependant, le cuivre pur présente une résistance mécanique et une résistance à la corrosion limitées, ce qui restreint son champ d'application. L'alliage du cuivre avec des éléments tels que le zinc, l'étain ou le nickel permet d'optimiser ses propriétés pour l'application concernée. De plus, les mécanismes qui relient la composition de l'alliage, la structuration de surface induite par laser, l'oxydation et le comportement antibactérien ne sont pas encore suffisamment compris. Afin de combler cette lacune, cette thèse examine de manière systématique comment la composition, la topographie de surface et la chimie influencent les propriétés antibactériennes des alliages de cuivre modifiés par structuration directe par interférence laser à impulsions ultrabrèves (USP-DLIP).

Le travail comprend cinq études évaluées qui, constituent ensemble une analyse complète des alliages de laiton (avec 15 et 37 % massique de Zn), de bronze (avec 6 % massique de Sn) et de cuivre-nickel (avec 10 et 30 % massique de Ni). Ces systèmes binaires ont été sélectionnés afin d'étudier l'influence du zinc, de l'étain et du nickel

sur l'interaction entre le laser et le matériau, la formation d'oxyde et la réaction des bactéries. L'objectif de l'étude est d'améliorer l'efficacité antibactérienne en augmentant la surface de contact effective grâce à une structuration à micro-échelle.

Dans la première partie du travail, des alliages de laiton ont été structurés au laser afin de créer des motifs linéaires périodiques de 3 µm, comparables à la taille des cellules *E. coli*. Des analyses de surface avancées (GI-XRD, STEM-EDS, APT, Raman et XPS) ont révélé des modifications à l'échelle nanométrique à une profondeur de quelques centaines de nanomètres, notamment une accumulation de zinc et la formation de couches d'oxyde riches en ZnO, Cu_2O et CuO. Ces modifications ont un impact significatif tant sur le comportement à la corrosion que sur l'effet antibactérien. Les surfaces en laiton structurées au laser présentent un taux de destruction plus faible que les surfaces polies, principalement en raison d'une concentration plus faible en cuivre à la surface et de la formation d'oxydes de zinc chimiquement stables qui limitent la libération d'ions Cu. Cependant, la gravure à l'acide citrique a permis d'éliminer sélectivement le ZnO et le CuO tout en restaurant les zones riches en Cu, ce qui a amélioré l'effet antibactérien, en particulier pour le laiton à faible teneur en zinc. Les résultats montrent que la teneur en zinc a une forte influence sur la stabilité de l'oxyde et donc sur l'effet antibactérien. Les alliages de laiton dont la teneur en zinc est inférieure à 30 % massique offrent un équilibre favorable entre la résistance à la corrosion et la disponibilité du cuivre.

Sur la base de ces résultats, le deuxième système, le bronze (Cu avec 6 % massique de Sn), a été étudié afin d'évaluer le rôle de l'étain dans la structuration laser et le comportement antibactérien. En utilisant la même technique USP-DLIP, des structures linéaires périodiques d'une largeur de 3 µm ont été produites, puis les couches d'oxyde formées pendant le traitement ont été efficacement éliminées par attaque chimique. Les surfaces obtenues montrent une hydrophobicité accrue et une surface effective jusqu'à 2,5 fois plus grande que celle du bronze poli. Les tests antibactériens contre *E. coli* ont montré des taux de destruction comparables à ceux du cuivre pur, ce qui confirme que la compatibilité structurelle entre la taille des bactéries et la périodicité

de la structure est un facteur déterminant pour la destruction par contact. Cette étude a montré que des géométries linéaires simples, lorsqu'elles sont optimisées sur le plan dimensionnel, suffisent pour obtenir une amélioration antibactérienne significative, et que l'USP-DLIP est capable de produire de telles microstructures de manière reproductible et avec une grande précision.

Au cours de la phase suivante de la recherche, les effets de l'oxydation ont été étudiés dans des couches minces de Cu-Ni laborées par co-pulvérisation afin de comprendre comment la chimie de surface peut à elle seule moduler l'efficacité antibactérienne. Des expériences d'oxydation thermique ont montré que le comportement à l'oxydation dépend fortement de la teneur en cuivre. Les couches riches en cuivre (92 % at.) ont formé des couches de Cu_2O à 200 °C, tandis que les couches riches en nickel (55 % at.) ont nécessité une température de 250 °C pour une oxydation comparable. Cette évolution chimique s'est accompagnée de changements significatifs dans les performances antibactériennes : l'oxydation a réduit l'activité des couches riches en cuivre, mais l'a renforcée dans les couches riches en nickel, ce qui confirme qu'une oxydation contrôlée peut soit supprimer, soit favoriser la fonction antibactérienne en fonction de la composition. Ces résultats ont conduit à l'introduction de l'oxydation comme outil de conception ajustable pour améliorer les alliages de cuivre moins actifs en modifiant la chimie de surface.

Enfin, la stratégie de structuration laser a été appliquée à des alliages Cu-Ni (CuNi10 et CuNi30) afin de combiner le contrôle de la composition et de la topographie. Deux motifs périodiques – linéaire et en nid d'abeille – ont été produits par l'USP-DLIP. Les analyses chimiques ont révélé que le traitement au laser induisait la formation d'oxydes riches en cuivre et en nickel, les surfaces CuNi10 étant dominées par le Cu_2O et les surfaces CuNi30 par le NiO. Après gravure, les surfaces CuNi10 étaient principalement riches en cuivre, tandis que le NiO était partiellement conservé sur le CuNi30 en raison de sa grande stabilité. Les tests antibactériens ont montré que les structures linéaires CuNi10 gravées ont permis d'obtenir la destruction la plus rapide des bactéries, tandis que le CuNi30 a montré une activité nettement moindre, liée à sa

teneur en cuivre inférieure au seuil antibactérien efficace (~60 % en poids). De plus, les structures linéaires ont systématiquement surpassé les structures en nid d'abeille, ce qui montre que l'efficacité de la destruction par contact dépend à la fois de la disponibilité du cuivre et de la compatibilité dimensionnelle entre la taille des bactéries et les caractéristiques de la surface. Ces résultats ont défini une plage de composition critique (70-90 % en poids de Cu) pour le maintien du comportement antibactérien dans les alliages Cu-Ni structurés au laser et ont souligné le potentiel de la combinaison de la conception des alliages et de l'optimisation géométrique.

Dans tous les systèmes étudiés, ce travail montre un lien clair entre la composition de l'alliage, la chimie de l'oxyde et l'efficacité antibactérienne. Les éléments d'alliage influencent fortement l'interaction entre le laser et le matériau ainsi que le comportement à l'oxydation : le zinc et le nickel ont tendance à former des oxydes stables qui limitent la libération d'ions cuivre, tandis que l'étain favorise une croissance contrôlée de l'oxyde. Les traitements de surface tels que la gravure ou l'oxydation contrôlée peuvent contrer ces effets en exposant à nouveau les zones riches en cuivre.

La topographie de la surface offre une autre possibilité de contrôle : des structures linéaires microscopiques avec une périodicité d'environ 3 μm offrent la plus grande efficacité antibactérienne en maximisant le contact avec les bactéries tout en maintenant une exposition suffisante au cuivre.

Des analyses mécanistiques ont confirmé ces tendances : l'ICP-MS a montré que la libération d'ions cuivre est corrélée à l'efficacité antibactérienne, tandis que la HR-SIMS et le MEB ont détecté des nano-agglomérats sur les membranes bactériennes, ce qui prouve une interaction directe entre le cuivre et les bactéries. Ainsi, la destruction par contact causée par les dommages ioniques et mécaniques est le mécanisme antibactérien dominant, les effets de mouillage ne jouant qu'un rôle secondaire.

Dans l'ensemble, ce travail crée un cadre complet qui relie la composition, la structure et la chimie de surface à la fonction antibactérienne. La performance effective résulte de l'optimisation conjointe de ces facteurs : la structuration au laser augmente le

contact avec les bactéries, la gravure restaure le cuivre actif et l'oxydation contrôlée stabilise les oxydes fonctionnels. Ces résultats constituent la base du développement rationnel de matériaux antibactériens à base de cuivre et soutiennent des applications durables et auto-désinfectantes dans le secteur de la santé, dans les espaces publics et dans les conditions spatiales.

ABBREVIATIONS & SYMBOLS

A_{spot}	mm²	Area for DLIP spot
APT	-	Atom Probe Tomography
at-%	-	Atomic Percentage
BS		Bacterial Solution
CA	-	Contact Angle
CFU	-	Colony Forming Units
CLSM	-	Confocal Laser Scanning Microscopy
Cu		Pure Copper
CuNi10	-	Copper-Nickel alloy with 10% Nickel and 90 % Copper
CuNi30	-	Copper-Nickel alloy with 30% Nickel and 70 % Copper
CuSn6	-	Bronze with 6% Tin and 94 % Copper
CuZn15	-	Brass with 15% Zinc and 85 % Copper
CuZn37	-	Brass with 37% Zinc and 63 % Copper
Δx	-	Pulse Overlap in the x-Direction
Δy	-	Step Size or Hatch Distance along the y-Axis
DLIP	-	Direct Laser Interference Patterning
DNA	-	Deoxyribonucleic Acid
DOE	-	Diffractive Optical Element
E_{pulse}	J	Pulse Energy
E. coli	-	*Escherichia coli*
ETD	-	Everhart-Thornley Detector
f	Hz	Frequency
F_{acc} or Φ	J/cm²	Accumulated Fluence (Energy per Area)
F_{pulse}	J/cm²	Pulse Fluence
FEI	-	Field Electron and Ion Company (Microscopy)
FEM	-	Forschungsinstitut Edelmetalle + Metallchemie
FIB	-	Focused Ion Beam
fs	-	Femtosecond (10^{-15} seconds)

GI-XRD	-	Grazing Incidence X-Ray Diffraction
HAZ	-	Heat Affected Zone
HIM	-	Helium Ion Microscope
ISS	-	International Space Station
λ	nm	Wavelength
LB	-	Lysogeny Broth
MDR	-	Multidrug Resistant
n_{acc} or N	-	Accumulated Number of Pulses
p	μm	Periodicity of the Structures
θ	°	Angle of incidence / Contact Angle
τ_p	s	Pulse Duration
PBS	-	Phosphate-Buffered Saline
PVD	-	Physical Vapor Deposition
ROI	-	Regions of Interest
ROS	-	Reactive Oxygen Species
SAED	-	Selected Area Electron Diffraction
SE	-	Secondary Electron
SEM	-	Scanning Electron Microscopy
SIMS	-	Secondary Ion Mass Spectrometry
SS		Stainless Steel 304
STEM-EDS	-	Scanning Transmission Electron Microscopy with Energy Dispersive Spectroscopy
STM/STS	-	Scanning Tunneling Microscopy and Spectroscopy
TEM	-	Transmission Electron Microscopy
TLD	-	Through Lens Detector
USP-DLIP	-	Ultrashort Pulsed Direct Laser Interference Patterning
UV	-	Ultraviolet
wt-%	-	Weight Percentage
WT	-	Wild Type
XPS	-	X-ray Photoelectron Spectroscopy

1. Introduction

The significant increase in infectious diseases and antibiotic resistance has raised concern for public health, which is mainly driven by the over- und misuse of antibiotics, leading to rise in the multidrug-resistant (MDR) pathogens[1]. These pathogens are responsible for an increasing number of untreatable infections, especially in the hospitals. Moreover, direct as well as indirect contact in such scenarios can lead to transmission of infections and biofilm formation, further facilitating the spread of such harmful microorganisms[2–5].

The transmission of pathogen can take place through various means such as contaminations systems (e.g., pipelines), materials (air or liquid), surfaces, or food and living organisms[6–10]. While strategies such as immunization and sanitation might help mitigate the spread of harmful microorganisms, MDR pathogens remain a critical concern[11,12]. Moreover, the more conventional strategies, including sterilization and isolation of patients, are effective but resource intensive. Therefore, a more sustainable approach would be development of antimicrobial surfaces that can inhibit the colonization of MDR pathogens and reduce maintenance requirements[13].

Nature offers a blueprint for such functionality[14–16]. For instance, the nano pillars on cicada wings show a natural antibacterial effect[17]. On the other hand, lotus leaves exhibit hydrophobic nature with self-cleaning properties, which is due to its micro- to nanoscale surface structures and its surface chemistry[18]. Beyond these properties, such structures are also responsible for a wide range of effects e.g., the vibrant coloration of butterfly wings and peacock feathers results from structural coloration rather than pigments[15], the anti-reflective properties of moth eyes are a result of the nanoscale surface structures[19], and the skin of shark reduces drag and microbial adhesion through microscopic riblets[20]. These natural systems have been a motivation for researchers, which has led to replication and fabrication of such nature-

inspired surface structures to achieve multifunctional properties for application in optics, fluid as well as antimicrobial technologies.

One of the most promising technologies for fabricating structures at micro- and nanoscale is direct laser interference patterning (DLIP)[21,22]. This technique enables fabrication of periodic surface structures at micro- and nanoscale by interfering two or more coherent laser beams[23–25]. When combined with ultrashort pulsed (USP) lasers, this method offers a minimal thermal damage to the bulk material leading to a precise surface modification[26,27]. The ultrashort pulse duration ensures that the energy is confined to the superficial layer, avoiding heat diffusion into the bulk material allowing for a clean ablation and precise structuring[28,29]. Hence, making USP-DLIP ideal for engineering nature-inspired functionals surface[30,31].

For the antimicrobial applications, one of the most effective strategies is the use materials that kill pathogens and inhibit its growth via direct contact[32,33]. Among such materials, copper is the most widely acknowledged for its inherent contact-based killing properties. This is, primarily, due to its rapid release of copper ions upon contact with any microorganism, which damage the cell membrane and hinder intracellular processes[34–36]. Prior studies have shown that modifying copper surfaces at microscale with USP-DLIP can further enhance this inherent property[30,37].

Despite its inherent antibacterial properties, the use of copper comes with limitation due to its relatively low mechanical strength and corrosion susceptibility, which can restrict its long-term performance in the real-world applications[38]. These limitations can be addressed through alloying, which enables optimization of the mechanical, chemical, and functional properties according to a desired application. Several alloying elements such as zinc, tin, and nickel can be used for copper to acquire an improved durability and corrosion resistance while preserving its inherent antibacterial properties[38–40]. This doctoral thesis focuses on modification of copper-based surfaces using USP-DLIP and the aim is to understand the effect of alloying on

the laser-material interaction as well as on the bacteria-substrate interaction. Therefore, this research focuses only on binary copper-based alloys - brass (CuZn15, CuZn37), bronze (CuSn6), and copper-nickel-alloys (CuNi10, CuNi30) - to evaluate the influence of each alloy element and its concentration on the aforementioned interactions. The alloying element concentration was limited to below 40 wt-%, since international standards recognize copper-based alloys with at least 60 wt-% copper as antimicrobial[32,41].

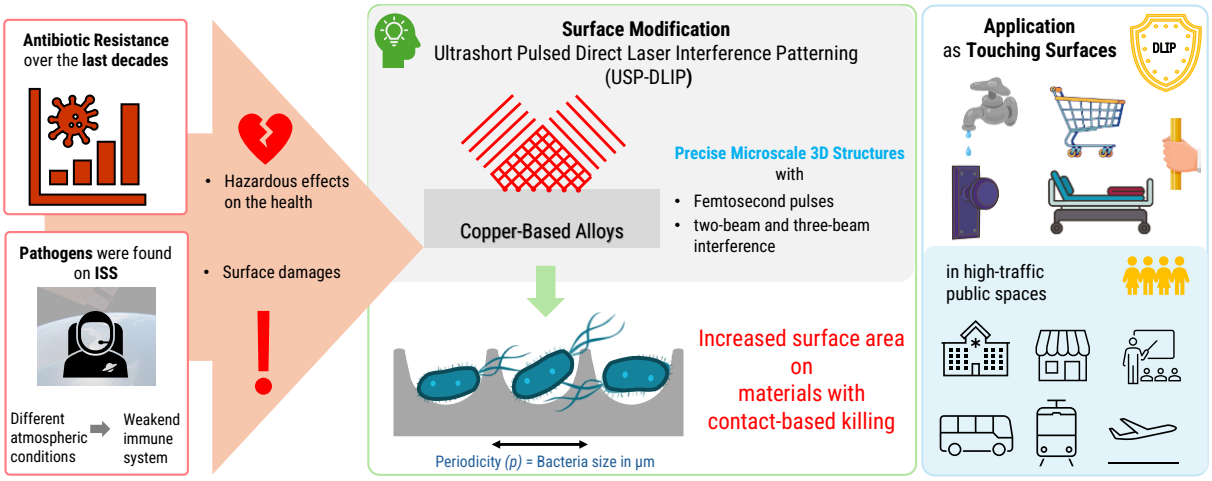

Figure 1: Motivation for this doctoral research — using USP-DLIP to modify copper-based alloys as a solution for antimicrobial surfaces, with potential applications in high-touch public environments.

The central aim of this research is to increase the contact area of copper alloys' surfaces via USP-DLIP, thereby enhancing their antibacterial properties. Therefore, it investigates the influence of alloying elements – zinc, tin, and nickel - on surface topography, surface chemistry and antibacterial activity. By pursuing this, the goal is to achieve surface designs that are durable and low maintenance with effective antibacterial properties. With this a real-world application in healthcare, public infrastructure, and related fields can be realised. Moreover, it aligns with the collaborative research work conducted with the German Aerospace Center (DLR) on antimicrobial surfaces on earth and under spaceflight conditions[42–44]. This work is embedded in a broader framework of international projects such as *Biofilms*[42], *Touching Surface*[44], and *ConTACTS Concordia*, which collectively investigate the

antimicrobial performance of steel, copper, and copper alloys in polished, micro- as well as nanostructured states, under diverse environmental conditions.

The *BIOFILMS* project examines these surfaces both on Earth and under spaceflight conditions, including microgravity, against a wide range of pathogenic microorganisms[42]. On the other hand, *Touching Surface* is centred around "Touch Arrays" that are placed in high-contact environments, which include the International Space Station (ISS) and various public institutions. The goal hereby to observe how microorganisms survive on these materials after human interaction. Ultimately, through this approach, the project sheds light on how surface materials behave in everyday environments as well as under the unusual conditions of spaceflight[44].

Similarly, the *ConTACTS Concordia* project, which is carried out at the Concordia Station in Antarctica, focuses on antimicrobial surfaces in an isolated and extreme setting. This project presents valuable insight into how microorganisms interact with materials in such closed habitats, where environmental factors such as humidity play a key role, not just in the survival of these microbes but also in the long-term performance of antimicrobial surfaces. This doctoral research is placed within these international collaborations highlights its broader relevance that extending from terrestrial applications to those in space and other extreme environments.

This research work is organized as follows: **Chapter 2** focuses on the theoretical as well as research background of antibacterial activity, relevant material properties, and fundamentals of laser processing. Furthermore, it explores the current state of art on surface modification of copper and copper alloys, while outlining the objectives of this research. **Chapter 3** presents the experimental section from materials and their preparation to the methods and techniques used for modification, antibacterial testing and characterization of alloy surfaces. **Chapter 4** provides an overview of this research, while **Chapter 5** presents the core findings in form of **Publications I-V**, which are the main part of this cumulative. The thesis concludes with the summary of the results and an outlook in **Chapters 6-7**, respectively.

2. Scientific Background and Research Objectives

2.1 Biological Fundamentals Relevant to the Study

2.1.1 Antibacterial Efficiency

The ability to reduce or inhibit the growth of bacteria, especially the harmful ones, can be defined as antibacterial efficiency. Several methods have been used to achieve this affect. One of the most widely used methods is to develop drugs that can combat these pathogens. Over the decades, several methods have been developed to screen the antibacterial activity of these drugs such as disk-diffusion, agar or broth dilution, cross-streak method, and time-kill test[45–48]. However, the over- und misuse of these drugs has led to increase in MDR pathogens. This has led to new methods, which include research on materials with focus on enhancing the antibacterial properties. In this case, the antibacterial activity can be achieved through either higher contact in the case of materials that generally show a toxic behavior towards the microorganisms[49,50], or less contact for all material to avoid adhesion of the bacteria to the surface[42]. In such cases, viability can be tested through wet plating method, live/dead staining with fluorescent, contact killing in combination with the wet plating method, adhesion tests, etc.[51–53]. In this study, contact killing method followed by wet plating method is used to quantify the surviving colony-forming units. This approach highlights the interaction between substrate and bacteria to assess the antibacterial activity of the tested surfaces.

2.1.2 Characteristics of *Escherichia coli*

Escherichia coli (*E. coli*) is a species of bacteria belonging to the Enterobacteriaceae family. It comprises a number of strains, some of which are pathogenic[54], but most of which are harmless and constitute a large proportion of the adaptable bacteria found in the digestive tract of vertebrates. These non-pathogenic strains play an important role in digestion and maintaining intestinal health[55]. *E. coli* is characterized by its

Gram-negative, rod-shaped, and non-spore-forming structure (see Figure 2). The bacteria measure approximately 3 μm in length and 1 μm in diameter.

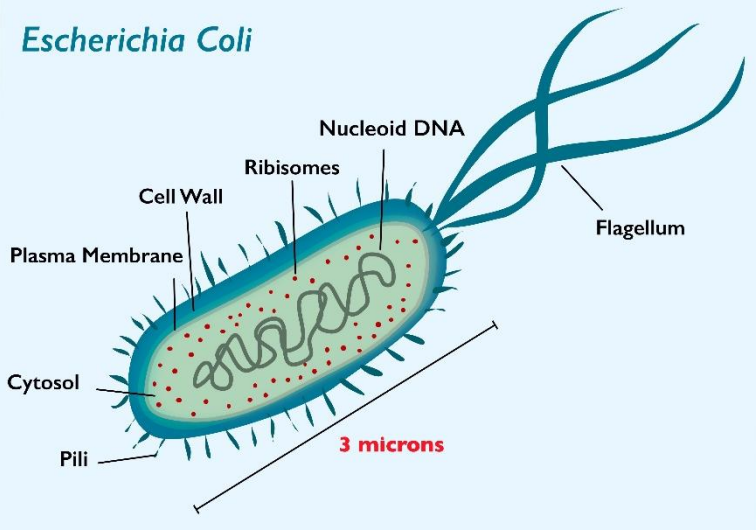

Figure 2: Cell structure of *E. coli* according to previous studies[56,57]

In this study, the wild-type strain K-12 (BW25113) of *E. coli*, a non-pathogenic bacterium, is used for all experiments. BW25113 is the parent strain of the Keio collection, an extensive library of single-gene knockout mutants of *E. coli* that facilitates the study of the effects of individual gene deletions on cell function[58]. This strain is widely used in genetic and microbiological studies and well-documented, therefore, ideal for ongoing research.

2.2 Materials with a Focus on Antibacterial Activity

2.2.1 Overview of Antibacterial Materials

Certain metals such as silver and copper have been used since ancient times for their antimicrobial properties[59]. Silver is traditionally valued for water purification and wound care[60], while copper is better known for its antibacterial effect on surfaces[35]. Both metals are known to kill bacteria, possibly by disrupting both extracellular and intracellular processes, although the exact mechanisms are still unclear[61–63]. To better understand their antibacterial properties, these metals, as well as cadmium, have recently been studied in their pure form, as alloys, and as nanoparticles synthesized using advanced nanotechnologies to enhance their

antimicrobial efficacy[34,64,65]. In addition, other materials such as graphene oxide, zinc oxide nanoparticles and titanium dioxide are also being actively researched in this category[66–69]. Unlike conventional materials, some of these materials require specific conditions to achieve maximum effectiveness. For example, titanium dioxide and zinc oxide exhibit antibacterial activity only under UV irradiation. Although zinc itself is cytotoxic to bacterial cells, it is less effective than copper in its pure form[70].

2.2.2 Pure Copper

Copper is an essential trace element in human biology and plays an important role in various physiological processes. It is an important component of many enzymes, supports the function of mitochondria in energy production, contributes to bone formation, maintains tissue and skin health, strengthens the immune system, and protects the nervous system from oxidative stress[71–73]. Also, observing from the materials science perspective, copper has outstanding electrical and thermal conductivity, which can be attributed to its densely packed atomic structure with high density of free electrons and a high melting point[74]. Therefore, its applications include cable and coils for motors and transformers, plates and tubes for heat exchangers and heat sinks for computers[75–78]. In addition, it holds a unique position in modern engineering due to its high durability and significant antibacterial properties. Copper and copper alloys have been the center of extensive research over the past century due to these distinctive characteristics[79]. Copper is valued for its antibacterial effects and relatively low cytotoxicity compared to other materials[80]. Thereby, making it ideal for applications in healthcare, consumer products, and public infrastructure due to its safety for human health.

2.2.3 Toxicity and Interactions with Bacteria

Copper surfaces are known to release ions upon contact with microorganisms, leading to an accumulation of copper ions. Consequently, this results in microbial death, a phenomenon known as" Contact-Killing"[35]. However, the exact interactions between the ions and microorganism cells are not fully understood, although various theories have emerged through extensive research. Research by Tsvetkov et al.

(2022)[62] explores the role of copper within living organisms. Though copper is an essential trace element for all forms of life, an excess of intracellular copper can be toxic to cells. This toxicity may come from copper's binding properties, which can cause damage to the proteins within cells.

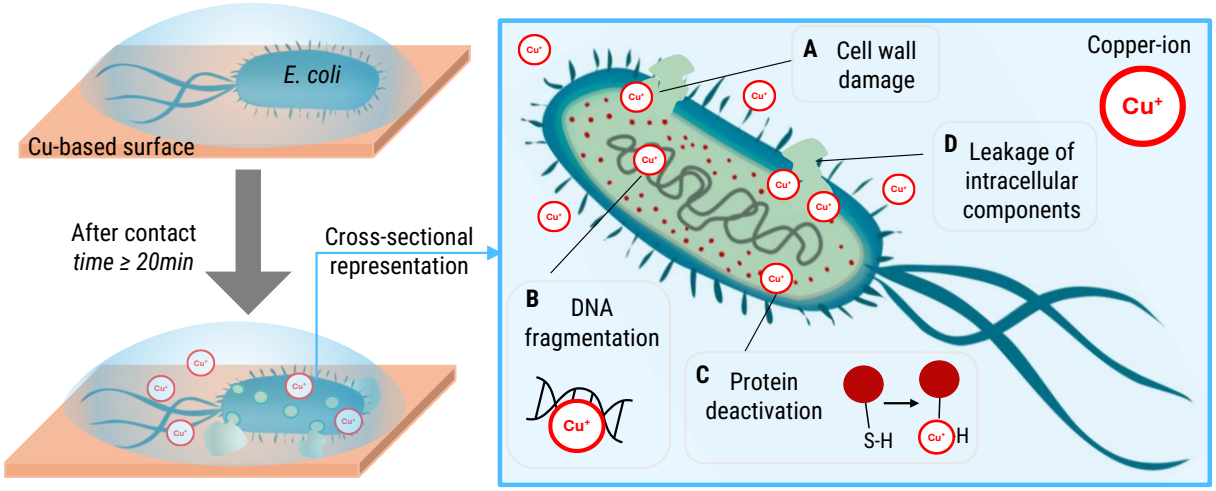

Figure 3: Schematic representation of possible microbiological toxicity mechanisms of copper ions on a bacterial cell according to previous studies[49,51,81]: A) cell wall damage, B) DNA fragmentation, C) protein deactivation, D) Leakage of intracellular components.

A previous study[51] on *E. coli* suggests that copper ions initially act at an extracellular level by targeting the lipopolysaccharide membrane and causing structural damage. When the cell membrane is damaged, intracellular components leak out, ultimately leading to cell death. Alternatively, another study[81] proposes that copper ions may initially accumulate on the cell membrane due to electrostatic attractions, altering the Zeta-potential of the outer cell wall and increasing membrane permeability. This change assists the absorption of copper ions into the cell, where they are likely to interact with cellular components and DNA, then to form copper complexes. These complexes can disrupt the cell's natural repair systems, eventually leading to its breakdown[81]. The broad redox potential of copper, resulting from its two oxidation states, Cu(II) and Cu(I)[35], may help explain the wide range of reactions that occur inside bacterial cells. As shown in Figure 3, copper ions can exert their toxic effects through several possible mechanisms acting on the bacterial cell.

One of the main reasons this phenomenon remains only partially understood may be the numerous factors that influence copper ion release during antibacterial testing. For instance, recent studies[82,83] using the droplet method for contact killing experiments demonstrate that experimental conditions, such as buffer type and bacterial presence, significantly impact copper surface corrosion, thereby affecting copper ion release. Samples using phosphate-buffered saline (PBS) with *E. coli* showed increased copper ion release, leading to higher bacterial mortality and highlighting the importance of surface-bacteria contact in this process.

Furthermore, Bezza et al. (2020)[84] investigated copper oxide nanoparticles' toxicity in gram-negative and gram-positive bacteria, showing that environmental factors, such as temperature, pH of the bacterial solution, and sample dimensions, significantly influence antibacterial effectiveness. Other variables, such as surface state and composition, which also affect the antibacterial activity of copper surfaces, are discussed in following sections as well as in the results of this study.

2.2.4 Copper-Based Alloys

In this study, two main criteria were used for selecting materials. The first and most important was maintaining copper's antibacterial functionality, which required that each alloy contain more than 60 wt-% copper, consistent with international standards[41,85,86] . The second criterion was simplicity in composition: each material was limited to a single alloying element. Since the focus of this work was on surface modifications, minimizing the number of variables in each alloy was essential for drawing clear comparisons with pure copper. This design makes it possible to precisely assess how each alloying element influences surface behavior and antibacterial performance. Zinc, tin, and nickel were selected as alloying elements for this study because all of these elements have practical mechanical and physical properties[74]. In addition, all three represent different types of binary phase systems when comparing phase systems.

Brass alloys are generally classified according to their zinc content as alpha brass (<35% Zn by weight) and alpha-beta brass (35–45% Zn by weight). Alpha brass with a higher copper content (80–90 wt-% Cu) is often used in architectural applications, while alloys with 60–63 wt-% Cu are better suited for extensive cold forming processes[87,88]. In this study, brass is represented in a binary eutectoid system (see Figure 4 a), in which a single solid phase simultaneously transforms into two different solid phases at a specific temperature and composition[89].

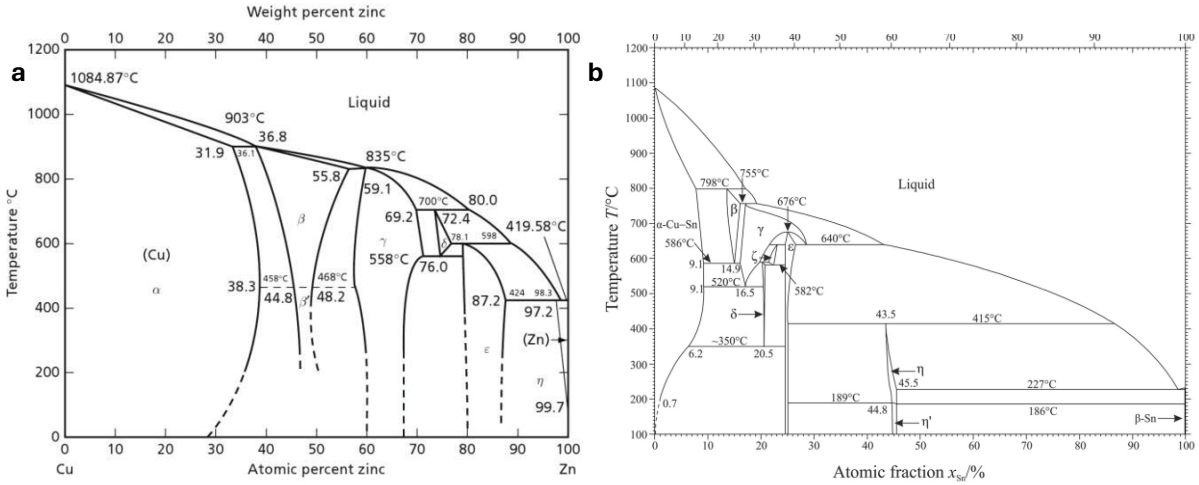

Figure 4: The Phase diagram of binary systems: a) Cu-Zn phase diagram, Original from Kejzlar et al. (2017)[89], and b) Cu-Sn original from Leineweber et al. (2023)[90].

Bronze, like brass, is another popular copper alloy, mainly alloyed with tin. Tin gives bronze a high yield strength and excellent corrosion resistance. Commercial binary bronzes typically contain 4–8 wt-% tin, although many industrial bronzes contain additional elements such as aluminum, nickel, and phosphorus, which further improve strength, wear resistance, and machinability[91–93]. The Cu–Sn binary phase diagram shown in Figure 4 b represents an eutectoid system, in which phase transformations take place at specific compositions and temperatures, similar to those observed in brass[94].

In contrast, copper–nickel alloys exhibit an isomorphous system characterized by the complete mutual solubility of both elements, leading to a single crystal structure throughout all compositions[95]. The addition of nickel increases hardness and

corrosion resistance while reducing susceptibility to biofouling. These properties make copper–nickel alloys particularly well suited for underwater applications, including seawater piping and hydraulic systems[96–99].

2.2.5 Antibacterial Applications

Copper has been extensively studied for its antibacterial properties in a variety of forms, including its pure metallic state, oxides, complexes, and alloys. Research in this area spans multiple scales, from bulk material sheets and thin films to nanoparticles, nanowires, and surface coatings. In recent decades, a range of metal(II) complexes, particularly those involving copper, have been investigated for potential antibiotic applications. Chai et al. (2018)[100] reported that copper(II) complexes display stronger antibacterial activity than many other metal(II) complexes, with effectiveness approaching that of conventional antibiotics, though remaining slightly lower. This enhanced activity is generally attributed to copper's ability to exist in multiple oxidation states, which provides it with a wide redox potential and enables participation in various biological reactions and complex formations[35,101].

However, excessive concentrations of copper can be toxic to the human body [102]. This toxicity arises from copper's capacity to generate reactive oxygen species (ROS), which can damage cell membranes, proteins, DNA, and other intracellular components[103]. Conversely, this same ROS-generating ability can be beneficial in certain therapeutic contexts, particularly for treating some chronic diseases [71]. In recent years, increasing attention has been directed toward copper nanoparticles and their capacity to induce ROS for biomedical purposes [104]. Owing to their high surface-area-to-volume ratio, these nanoparticles exhibit remarkable efficiency in combating pathogens at the nanoscale. They hold promise not only as standalone antimicrobial agents or drug delivery vehicles but also as surface coatings for titanium-based dental and orthopaedic implants [105,106].

A less invasive strategy for mitigating pathogen transmission involves the use of copper and copper-based materials as contact-active surfaces[107–109]. These

materials can be incorporated into infrastructure to inhibit microbial growth on frequently touched areas. Such applications are particularly valuable for reducing hospital-acquired infections and could also be extended to high-traffic public spaces, including schools, buses, and other communal environments. Recent studies[107–109] have highlighted the use of copper and copper alloys in commonly touched fixtures—such as door handles, bedrails, handrails, and grab bars—as well as in copper-impregnated textiles like wound dressings and face masks, as a promising strategy to reduce the spread of infections.

In recent years, various methods have been utilized to further enhance the antibacterial effectiveness of these contact-based copper surfaces. These methods are typically for modifications at the surface level and include the use of copper nanoparticles, coatings, laser structuring, and other surface engineering methods, as discussed in section 2.5.1.

2.3 DLIP Fundamentals and Ultrafast Laser–Surface Interaction Dynamics

The term "LASER" stands for *Light Amplification by Stimulated Emission of Radiation*[110]. A laser beam has very significant characteristics. It is highly directional, operates within a narrow frequency range, and exhibits both temporal as well as spatial coherence. These characteristics make laser beams exceptionally well suited for precision applications across a wide range of disciplines[110].

Lasers can cover a broad portion of the electromagnetic spectrum, from infrared to X-rays and, in the case of pulsed beams, it can achieve extremely high-power densities. Since their invention in the 1960s, lasers have been the focus of extensive research and have found applications in various areas such as medicine, communications, and industrial manufacturing[21,110].

One particularly advanced technique enabled by the laser technology is direct laser interference patterning (DLIP)[21]. This method makes it possible to fabricate periodic surface structures at the micro- and submicron scales[21]. DLIP operates by

overlapping two or more coherent, high-power pulsed laser beams in such a way that their interference creates periodic energy distributions on the target surface[111,112]. The spatial period p of these patterns can be precisely controlled by the laser wavelength λ and the angle θ between interfering beams[22], following the relationship:

$$p = \frac{\lambda}{(2 * tan\theta).} \qquad \text{Eq. 1}$$

Depending on the number of beams and their geometric configuration, various pattern types can be produced, ranging from dot-like to line-like to grid-like structures[21], as shown in Figure 5. DLIP provides remarkable precision, with sub micrometer features as small as 700 nm successfully achieved on metallic surfaces[23].

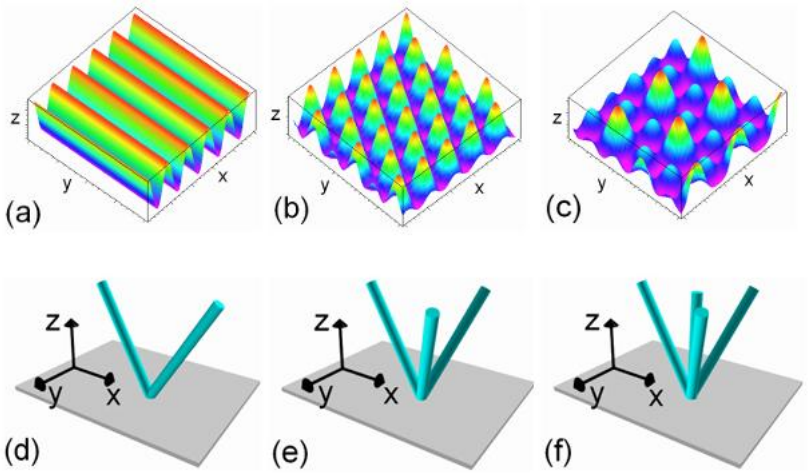

Figure 5: Schematic representation of interference in the DLIP process for (a, d) two beams, (b, e) three beams, and (c, f) four beams. Top: simulated intensity profiles resulting from the superposition of the respective beam configurations. Bottom: arrangement of the individual beams. Adapted from Lasagni et al. (2006)[112].

This technique has been applied across a broad range of materials, including metals (e.g., copper, stainless steel, titanium), polymers, ceramics, and various thin films[23,25,113,114]. Thereby, making DLIP a highly versatile tool for applications in materials science, surface engineering, and optics.

2.3.1 DLIP Pattern Formation and Laser Parameters

The formation of interference patterns via DLIP is highly dependent on both laser and material parameters[115]. In this case, key factors such as wavelength, fluence, and polarization influence the precision and outcome of patterning. Overall, laser parameters like fluence, intensity distribution, and pulse energy can be controlled to achieve uniform and reproducible patterning[22,26,116,117]. Additionally, material properties such as optical absorption, surface morphology, and thermal conductivity are decisive factors in determining the form and evolution of patterns during laser exposure[23,118].

The first periodic pattern chosen for this study, i.e., line-like structure, can be fabricated using two-beam DLIP setup (as described in Chapter 3). Achieving a consistent topographic effect over the entire sample is essential for this study and it depends on scanning parameters, which must be tailored to achieve uniform coverage across the patterned area[115,119]. These scanning parameters are influenced by several initial laser settings. A primary factor is the laser pulse fluence (F_{pulse}), which is calculated from single pulse energy (E_{pulse}) or laser power. Defined as the energy per unit area (A_{spot}) for each pulse, F_{pulse} is calculated as shown in Eq. 2 following the approach by Fox et al.[119].

$$F_{pulse} = \frac{E_{pulse}}{A_{spot}} \quad \text{Eq. 2}$$

For a broader processed area, the fluence is defined by Eq. 3 and is known as the accumulated fluence (F_{cc})[119].

$$F_{cc} = \frac{E_{pulse}}{\Delta x * \Delta y} \quad \text{Eq. 3}$$

where Δx represents the pulse overlap in the x-direction (scan direction) and Δy is the step size or hatch distance along the y-axis[119]. From these, the number of accumulated pulses (n_{cc}) over a specified surface area can be derived with Eq. 4[119].

$$n_{cc} = \frac{F_{cc}}{F_{pulse}} \quad \text{Eq. 4}$$

This same framework can also be extended to multi-beam setups (e.g., three-beam DLIP) to achieve more complex periodic structures with tailored symmetry.

2.3.2 Ultrafast Laser–Material Interaction

The fundamental mechanism behind laser-based surface processing is the interaction between the laser beam and the material's surface during irradiation. This interaction depends on the material's optical and thermal properties, as well as on laser parameters like wavelength, polarization, fluence, and pulse duration[120,121].

When a sample surface is irradiated with a laser beam, the energy is absorbed and reflected based on the absorption coefficient of material and surface characteristics[122]. In case of conductive materials like metals, absorption is significantly influenced by free electron behavior, which can be modeled using the Drude model[122,123]. The nature and efficiency of absorption determine the extent of energy transfer and ultimately, the resulting material response[124,125].

Upon initial absorption, the laser energy is rapidly taken up by the electrons in the surface layer of the material[126]. The electrons, in this case, heat up almost instantaneously, while the atomic lattice remains relatively cool[127]. Over a short time scale, the energy is transferred from the electrons to the lattice, creating a localized thermal equilibrium[125]. This Two-Temperature model describes how electrons and the lattice reach thermal balance through electron–phonon coupling[128,129]. The rapid rise in temperature can induce a variety of material responses, including melting, recrystallization, thermal expansion, phase transitions, and defect formation[111,121,130].

As the laser fluence exceeds the atomic binding energy, laser ablation occurs, which results in material removal from the surface[131]. This material removal process depends on the fluence regime. At moderate fluences, melting and spallation dominate[27,132]. Melting occurs through competing processes, where the liquid-

crystal interface progresses inward from the surface while homogenous nucleation and liquid phase growth arise within the crystalline matrix[133]. Conversely, spallation results from anisotropic expansion and internal pressures induced by laser irradiation. Consequently, fractures are generated parallel to the surface, and this results in layer ejection[121,134]. At elevated laser fluences, phase explosion prevails, with temperatures far surpassing the boiling point and inducing rapid, extensive homogeneous nucleation within the material[133,135].

These fundamental mechanisms occur across all laser types, but they manifest differently depending on the pulse duration[27]. In particular, ultrashort laser pulses, such as femtosecond (fs) pulses, introduce unique interaction dynamics highly relevant to direct laser interference patterning (DLIP)[120].

In ultrafast laser processing, the pulse duration is shorter than the timescale of thermal diffusion or lattice relaxation. As a result, energy is deposited faster than it can be dissipated, leading to cold ablation—a process with minimal heat-affected zones and highly precise removal[131,136–138]. Because energy is confined both spatially and temporally, ultrafast lasers significantly reduce the ablation threshold, enabling finer control of surface features[124,139]. For example, nanosecond lasers may require fluence levels around 10^8 W/cm^2, while femtosecond systems may require up to 10^{13} W/cm^2, depending on the material[27].

Overall, DLIP in combination with ultrashort pulse durations is of great significance, given its effectiveness at generating highly controlled interference patterns with minimal thermal side effects[140]. Their ability to produce sharp, periodic structures at submicron resolution makes them ideal for advanced surface engineering applications[21]. Hence, it is very favorable to employ the central principles of laser–material interaction alongside the advantages of ultrashort pulse durations for DLIP systems to achieve exceptional precision and versatility in surface patterning.

2.4 Critical Surface Characteristics Relevant to the Study

Surface aging is a critical factor, as it can significantly impact a material's lifespan by altering long-term performance and functionality. Additionally, other factors that are related to environmental exposure, such as oxidation, corrosion, or contamination, can lead to further changes in essential surface characteristics, including wettability, chemical composition, and ion release behavior. These modifications are especially relevant to antibacterial activity, as noted in the literature reviewed in this section, where shifts in surface properties directly affect antibacterial efficacy.

2.4.1 Oxidation and Corrosion

In this study, the laser process utilized in the modification of the surfaces can lead to the possible formation of oxides. Copper has two naturally occurring, stable isotopes that distribute differently across environmental and biological processes. This variability also influences its oxidation states and oxide formation. In dry conditions and at subsurface levels, cuprous oxide (Cu_2O) tends to form, while cupric oxide (CuO) forms more readily in humid environments and on surface layers[141].

Understanding the interplay between corrosion and antibacterial activity is essential, particularly as copper ion release is a key mechanism for bacterial elimination. Luo et al. (2019)[82] examined the correlation between corrosion and antibacterial activity of copper and cuprous oxide coatings in two buffer solutions, Phosphate-buffered saline (PBS) and Na-4-(2-hydroxyethyl)-1-piperazineethanesulfonic acid (Na-HEPES), commonly used in *E. coli* antibacterial tests. Their findings indicate that cuprous oxide exhibited superior antibacterial efficacy overall. Comparing the buffer solutions, copper ion release was lower in PBS. However, in the presence of *E. coli*, corrosion was accelerated, leading to an increased release of copper ions in PBS. In another study, Luo et al. (2020)[142] demonstrated that when sodium chloride, which is commonly found in buffer solutions, was compared to pure water, this led to increased presence of chloride ions, which likely further contributed to increased corrosion. This effect is attributed to chloride ions promoting the growth of cuprous oxide on copper surfaces.

Several studies[30,141,143] have investigated the impact of copper oxidation on antibacterial behavior. The findings revealed that cuprous oxide (Cu_2O) had a higher antibacterial effect in comparison to cupric oxide (CuO). This suggests that the specific oxidation state of copper significantly influences its antibacterial properties.

The copper alloys chosen for this research contain additional elements such as zinc, tin, or nickel, all of which possess higher affinities for oxidation than copper. Due to their lower activation energies for oxide formation, these elements preferentially oxidize under ambient conditions, leading to surface layers of zinc oxide, tin oxides, or nickel oxides as described in the literature[144].

Among these, zinc is particularly notable for both its corrosion-related and antibacterial properties. In mild environments, the formation of zinc oxide (ZnO) on brass surfaces adds to the passive, protective barrier that enhances corrosion resistance[145]. However, in more aggressive environments—such as acidic or chloride-rich conditions—zinc becomes susceptible to dezincification and a consequent loss of structural and mechanical integrity[146].

Similarly, tin and nickel form their respective oxide layers, which contribute to passivation and improved corrosion resistance[98,147,148]. The effectiveness of this passivation is highly dependent on its concentration in the alloy; higher tin or nickel content generally results in greater corrosion resistance in humid or aqueous conditions. Notably, in copper-nickel alloys with low nickel content, cuprous oxide is still the dominant copper oxide phase formed[148]. Moreover, since the alloy surface typically includes copper, the resulting oxide layer is often a heterogeneous mixture of copper and alloying element oxides.

In contrast to zinc, there is currently no substantial evidence supporting independent antibacterial properties of elements tin or nickel.

Zinc, however, has been studied for its antimicrobial potential[66,149]. However, its antimicrobial efficacy is significantly lower than that of copper and is highly dependent on both its particle size, morphology, and chemical form[66]. A

commonality between zinc and copper lies in their ion release behavior; zinc ions (Zn^{2+})[70], much like copper ions (Cu^{+}/Cu^{2+}), play a critical role in antimicrobial activity, as discussed for copper in section 2.2.3.

Research[66,150] indicates that zinc oxide (ZnO) nanoparticles can enhance antibacterial effectiveness due to their increased surface-to-volume ratio. Nevertheless, this enhancement is often contingent upon UV irradiation, which facilitates the release of zinc ions from the nanoparticulate structure. Zinc oxide (ZnO) nanoparticles are primarily investigated for incorporation into pharmaceutical formulations. However, when applied as surface coatings, they may offer potential antimicrobial benefits. Despite this, their efficacy under ambient, non-UV-irradiated conditions is generally limited. Consequently, in comparison to bulk copper alloys, the practical applicability of ZnO nanoparticles for high-touch surface applications remains significantly constrained.

2.4.2 Wettability

Wetting behavior is another key surface characteristic that influences antibacterial activity. In this study, antibacterial tests are conducted using the wet plating method (see section 3.2.3), making wettability a particularly relevant parameter to characterize and understand.

Wetting behavior describes how a liquid interacts with and spreads across a solid surface and is normally characterized by the contact angle (CA) of a three-phase system involving the liquid, solid surface, and air[151]. A CA less than 90° indicates a hydrophilic surface, which readily attracts water, while a CA greater than 90° signifies a hydrophobic surface that repels water. Surfaces with a contact angle exceeding 150° are classified as superhydrophobic, demonstrating extreme water repellency[152,153].

The measurement is usually performed using the sessile drop (droplet) method, in which a droplet of a volume of 2–5 μL is placed on the surface, and the static contact angle is measured[151]. This can then be analyzed using Young's model for smooth surfaces and Wenzel or Cassie-Baxter model for rough surfaces[154,155].

Inspired by natural systems such as lotus leaves and insect wings, several studies have sought to mimic nature-inspired surface architectures to tailor wetting properties[156–159]. Research[30,139,160,161] shows that surface chemistry and texture down to the micro- and nanoscale can influence the wetting behavior and hence the antibacterial activity. A consistent finding across these studies is that surfaces exhibiting moderate hydrophobicity tend to show enhanced antibacterial effects, likely due to reduced bacterial adhesion and increased disruption of microbial membranes in the case of non-copper surfaces[139,160], and—in the case of copper surfaces—a favorable balance between these effects and direct bacterial contact with the copper itself [30].

In this context, direct laser interference patterning (DLIP) has emerged as a precise and versatile technique for engineering both surface topography and surface chemistry, enabling fine-tuning of wetting behavior on a variety of materials[111,113,162].

A recent study[163] investigating the wettability of laser-structured copper surfaces in relation to surface chemistry revealed distinct differences between polished and laser-treated specimens. For polished copper, wettability is predominantly influenced by surface chemistry, particularly the adsorption of airborne hydrocarbons. In contrast, laser-structured surfaces exhibit inherently hydrophobic behavior due to the micro- and nano-roughness introduced by laser patterning. This study, along with recent work on stainless steel[164], highlights that line-like laser structures result in anisotropic wettability, whereby the wetting behavior varies depending on the direction of the surface features. These findings underscore the importance of surface topology in governing liquid–surface interactions.

2.5 Current State of Research

Extensive research has been conducted on pure copper in relation to its surface modification and antibacterial performance. Multiple studies [33,64,83,141] confirm that direct contact between bacteria and the copper surface is very crucial for antibacterial activity, and this is primarily due to localized ion release and membrane disruption. Building upon this foundational knowledge, recent work has turned toward enhancing copper's antibacterial efficacy through advanced surface engineering techniques.

2.5.1 Role of Surface Modifications in Antibacterial Performance

Various approaches have been taken for the surface modification to enhance antibacterial activity and then to investigate such contact-active materials, particularly copper and its alloys. These strategies include the use of antibacterial coatings, nanoparticles, and laser-based surface texturing[165–168].

Antibacterial coatings typically operate by either releasing ions to kill bacteria or by preventing microbial adhesion and colonization. For coatings, materials such as copper and silver are widely used and deposited as thin films or embedded in porous matrices[167,168]. These coatings are fabricated using techniques like physical vapor deposition (PVD), sputtering, and chemical surface treatment[169–171].

However, coatings that rely on ion release, especially the ones incorporated with silver or copper, often face challenges related to long-term efficacy, as the active ions may gradually become depleted[165]. Furthermore, factors like durability, mechanical robustness, and cost-effectiveness might still be a hindrance to applications on a larger scale[165]. Therefore, future development must focus not only on enhancing antimicrobial activity but also on ensuring stability and scalability under real-world conditions.

One way to address these challenges is the implementation of scalable surface structuring techniques, such as laser-based texturing, which have emerged as promising alternatives[172,173]. These methods enable the fabrication of precisely

controlled micro- and nanostructures, which can simultaneously promote contact-based bacterial killing and inhibit bacterial adhesion, and this without relying on consumable chemical agents[173]. Such dual-function surfaces represent a promising direction for the next generation of durable, effective antibacterial materials.

2.5.2 Surface Modification of Copper-Based Alloys using DLIP

Surface modification of copper alloys using ultrashort pulsed laser systems has only recently become the focus of a limited number of studies. Margetic et al. (2000)[136] examined the differences in ablation processes and morphology in brass when using nanosecond versus femtosecond pulse durations. Their findings highlighted those various brass compositions influence ablation rates, whereas these appeared most probably to be independent of pulse duration. This effect is likely due to differences in optical properties, a key material parameter in laser processing.

In a subsequent study, Caneve et al. (2006)[174] investigated laser ablation of ternary and quaternary bronze alloys using laser-induced breakdown spectroscopy, employing both single and double pulses. The analysis was carried out on the depth and shape of the resulting craters. They observed that ablation depth increased with the number of laser shots, and the double pulses, in this case, consistently produced deeper craters. Another significant finding was the effect of zinc on ablation composition. Still, due to concurrent variation in tin and lead, the precise role of individual elements remains unresolved, highlighting a critical gap in isolating compositional effects during laser processing.

Hans et al. (2012)[111] offered an initial insight into fabricating microscale periodic line-like structures on a bronze (CuSn8) and brass (CuZn23Al3Co) surfaces with a nanosecond pulsed laser, focusing on wetting behavior. These findings suggest anisotropic wetting behavior with hydrophobicity, similar to the ones mentioned in section 2.4.2. It is an insight relevant to this study, given the established link between surface wettability and antibacterial performance.

Similarly, Müller et al. (2020)[25] adopted a comparable approach to achieve topographical modifications, producing micro- and sub microscale periodic structures on brass. This study also examined the effects of single and double laser pulses on the thermal response of brass along with copper, and stainless-steel surfaces. While this study advances our understanding of morphological evolution, it does not fully address how specific alloying elements influence laser-induced transformations under USP conditions.

Collectively, these studies offer valuable foundational insights into laser–alloy interaction mechanisms for copper-based materials. However, they also reveal a critical knowledge gap: the complex interplay between chemical composition and laser–material interaction dynamics in the context of ultrashort pulsed lasers remains insufficiently understood. Specifically, the role of individual alloying elements, such as zinc, tin, and nickel, in governing ablation behavior, oxide formation, and the development of functional surface properties has not been systematically investigated. Addressing this knowledge gap is critical for advancing composition-tailored laser processing strategies, particularly in applications where contact-mediated antibacterial activity is required.

2.5.3 USP-DLIP Processing on Pure Copper

In the context of contact-based bacterial inactivation, prior studies[33,175] have shown that direct contact with copper surfaces is critical to facilitating copper ion release, which drives antibacterial efficacy. To optimize this mechanism, surface structuring at the bacterial scale has been proposed as a means of improving bacteria–surface interaction[30,37]. Direct laser interference patterning (DLIP) enables the fabrication of highly controlled, periodic surface features at micro- to sub micrometer scales, making it a promising technique for tailoring antibacterial copper surfaces.

Recent studies[25,31] have applied USP-DLIP to pure copper to create line-like structures on a micro- and sub-micrometer scale, focusing on how laser settings can be optimized to shape surface topography and affect chemical changes. These studies

show that laser fluence plays a crucial role in defining pattern geometry during USP-DLIP processing. At lower fluences, copper surfaces develop sharp, well-defined edges. However, as fluence increases past the phase explosion threshold, the resulting lattice heating causes melt expulsion, which makes patterns less precise. Additionally, laser-induced roughness and oxidation enhance copper's absorptivity, especially with repeated pulsing, sometimes causing sub-micrometer patterns to fade with a single extra pulse.

Müller et al. (2021)[30] expand on this by showing the formation of flake-like structures on the copper surface after laser structuring, attributed to oxide formation. This effect was largely minimized by etching, which removed most of these oxide flakes. Chemical analysis showed oxide presence, with valleys having less oxide than peaks. After etching, oxide presence was effectively reduced on the surface.

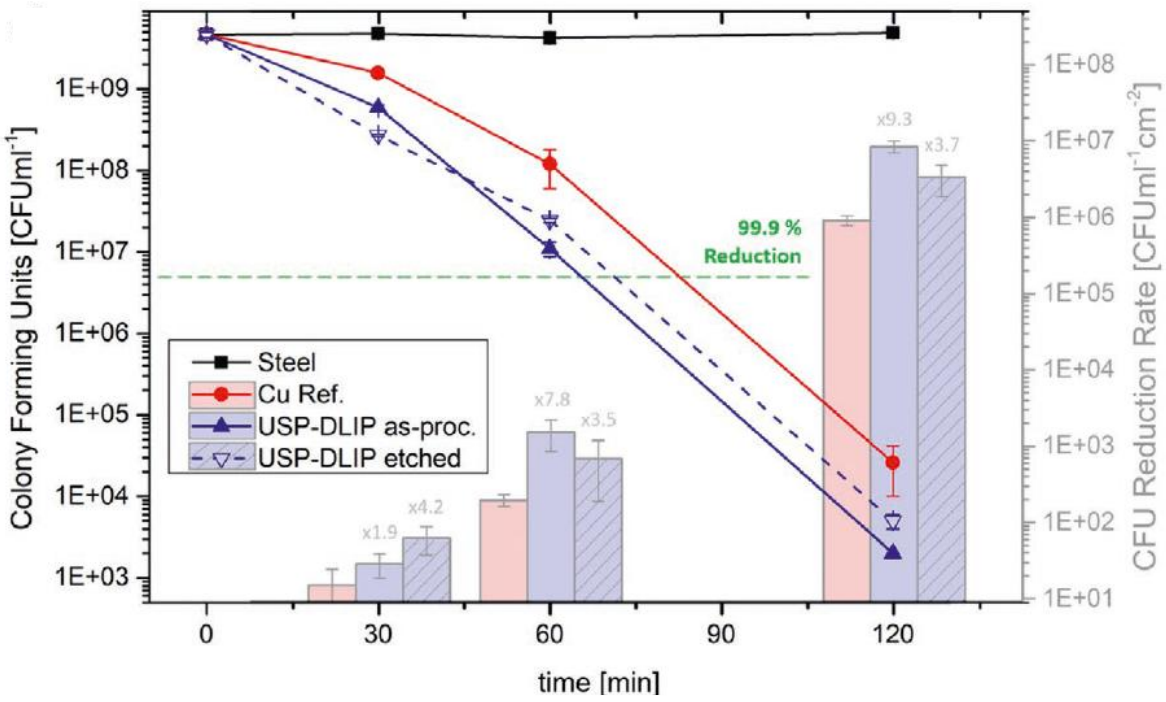

Figure 6: Contact-Killing results reproduced from Müller et al. (2021)[176] in its original form licensed under CC BY-NC 4.0.

In a subsequent study, Müller et al. (2021)[176] demonstrate that USP-DLIP-treated copper surfaces significantly improve antibacterial performance, with patterned surfaces showing up to a 15-fold increase in *E. coli* reduction (see Figure 6). Enhanced

bacterial killing is linked to stronger bacteria-surface interactions and elevated Cu ion release in the presence of bacteria, especially on as-processed laser-structured surfaces. Additionally, hydrophobic surfaces exhibited greater antibacterial efficacy than hydrophilic ones, emphasizing the influence of surface wettability and topography. These results underscore the potential of customized surface modifications to optimize copper's antibacterial effects beyond simple Cu ion release.

These findings establish a robust foundation for the current study. The extensive work on DLIP-treated pure copper in this last decade has yielded valuable insights into several aspects such as laser–material interaction, surface chemistry, and structure-dependent antibacterial behavior. This knowledge now provides the basis for a systematic investigation into copper-based alloys, where the role of alloying elements in defining antibacterial functionality through USP-DLIP processing remains largely unexplored.

2.6 Research Objectives

Building on the foundation established in the previous sections, this section outlines the research objectives that translate prior findings into a structured investigation of surface engineering strategies for antibacterial optimization. In recent years, various studies have provided valuable insights into the fundamental mechanisms behind copper's antibacterial activity. These investigations have been crucial in understanding copper acts in various forms, such as nanoparticles, nanowires, and different chemical compositions, including pure copper, copper oxides, and copper alloys. However, while these studies have addressed the initial layers of antibacterial potential through copper, further research is needed to optimize materials for large-scale, practical applications. This study aims to bridge the gap between this fundamental understanding and the real-world practical application. This can be achieved by developing copper-based surfaces that are tailored for such scalable antimicrobial use.

This doctoral research addresses the gap by employing USP-DLIP to fabricate microscale surface structures aligned with bacterial dimensions (single *E. coli* cell ~3

µm). It systematically investigates how alloy composition, surface chemistry and structural design influence antibacterial performance, as shown in Figure 7.

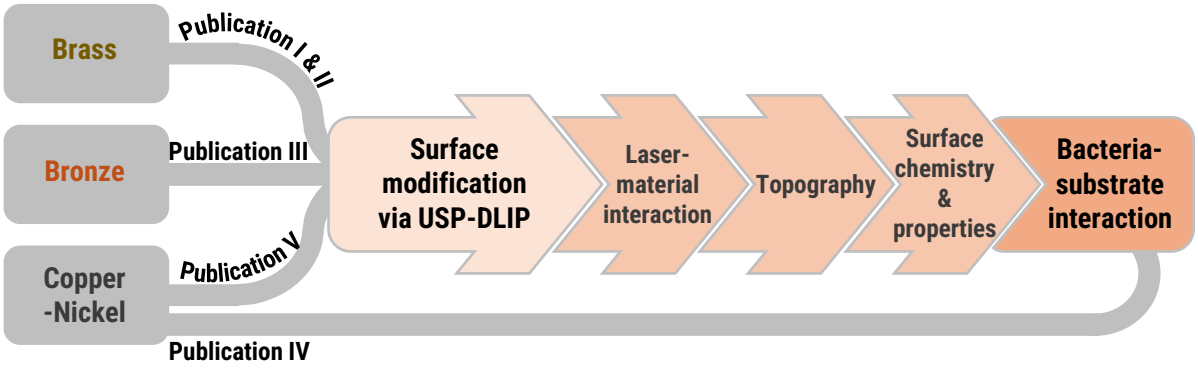

Figure 7: Research objectives — First, **surface modification** of copper-based binary alloys: brass (Publication I & II), bronze (Publication III), and copper-nickel alloys (Publication V). Second, to investigate the influence of bulk composition on **laser–material interaction**, **surface topography**, and **chemistry**. Finally, to evaluate how these factors collectively affect **bacteria–substrate interactions**.

The overarching goal is to establish design strategies for copper-based surfaces that exhibit enhanced and reproducible antibacterial activity, thereby advancing the integration of copper into real-world applications. The following chapters outline the experimental methodology, and present key findings that aim to address these unresolved questions.

3. Experimental Section

3.1 Materials and Preparation

A total of seven different materials, including two reference samples (stainless steel and pure copper), were selected for the experiments. The compositions and related information for all materials are provided in Table 1.

Table 1: Overview of materials used in the experiment, including composition, manufacturer, and preparation method.

Material	Label	Composition		Manufacturer	Preparation
Stainless steel	SS	304		*Brio*	cleaning
Pure copper	Cu	99 % pure Cu		*Wieland*	polishing
		Cu [wt-%]	*Zn [wt-%]*		
Brass 1	CuZn37	63	37	*Wieland*	grinding + polishing
Brass 2	CuZn15	75	15	*Wieland*	grinding + polishing
		Cu [wt-%]	*Sn [wt-%]*		
Bronze	CuSn6	94	6	*Wieland*	grinding + polishing
		Cu [wt-%]	*Ni [wt-%]*		
Copper-Nickel 1	CuNi10	90	10	*FEM*	grinding + polishing
Copper-Nickel 2	CuNi30	70	30	*FEM*	grinding + polishing

All materials, except for the copper-nickel alloys, are commercially available compositions and were obtained as sheets with a thickness of approximately 1 mm. These sheets were then cut into dimensions of roughly 25 × 10 mm². Copper-nickel alloys, however, are not readily available as binary alloys and were specially prepared by the "*Forschungsinstitut Edelmetalle + Metallchemie*"(*FEM*) in Schwäbisch Gmünd, Germany. For these alloys, the material was first cast from pure copper and pure nickel powders, then cold-rolled to a thickness of 1 mm. The final samples were cut to dimensions of 25 × 10 mm².

Considering that the structures to be prepared are at the microscale, the surfaces need to be smooth before laser processing. The stainless-steel samples were acquired with a mirror-quality finish and only required cleaning with acetone and isopropanol to remove the adhesive layer on the surface. Meanwhile, copper and copper-based alloys were metallographically prepared to obtain a mirror-quality finish. Before proceeding, the microhardness of the alloy samples was assessed using a Struers *Dura Scan 50* microhardness tester. This step is essential for determining the appropriate polishing parameters, given the significant copper content in the samples presents a difficulty due to its soft nature. The Vickers hardness (HV 0.1) was measured as 97 ± 5 for CuZn15, 107 ± 9 for CuZn37, and 181 ± 3 for CuSn6. While these values are higher than that of pure copper, they remain significantly lower than those of steel. To minimize significant deformations, the first step was fine grinding. Initially, SiC (silicon carbide) paper with a 15 μm grain size was used on a manual *Tegrapol system* (Struers) to eliminate the topmost layer of deformations. Following this, the surfaces were polished using an automated *TegraPol system* (Struers) to achieve a mirror-like finish. The polishing was carried out in three stages, utilizing diamond solutions with grain sizes of 6, 3, and 1 μm, respectively, in each step. Finally, all samples were cleaned with ethanol to remove any impurities before undergoing the laser process and the antibacterial testing.

3.2 Methods

3.2.1 Ultrashort Pulsed Direct Laser Interference Patterning

Ultrashort pulsed is defined as a range below the threshold of 10 ps. Laser processing, which is below this pulse duration, makes it possible to produce structures precisely down to a few micrometers[115]. In this study, a two-beam interference was used to produce periodic line-like structures on the sample surface. The periodicity of the structure was chosen according to the size of the bacteria for the antibacterial tests. For DLIP, a Ti:Sapphire laser emitting source was used with a wavelength of 800 nm, a

pulse duration of 100 fs, and a repetition rate of 1 kHz. The optical setup[25] is illustrated in Figure 8.

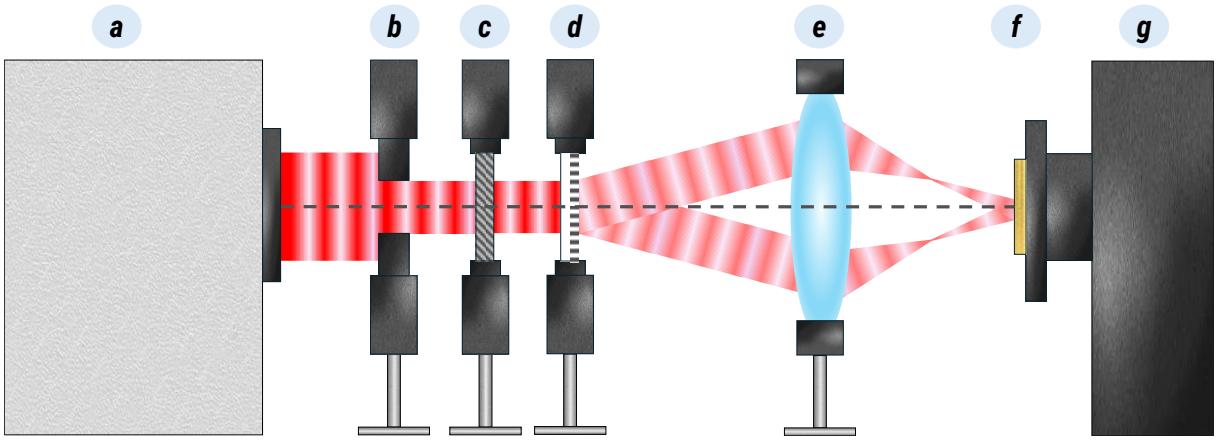

Figure 8: DLIP – Optical setup. a) laser source, b) aperture, c) wave plate, d) diffractive optical element (DOE), e) lens, f) sample, and g) sample stage.

A coherent beam is emitted via a laser source, and first it goes through an aperture, which can change the diameter of the working beam. Following that, through a wave plate to set the polarization of the beam perpendicular to the sample surface. This is then split with the help of a diffractive optical element (DOE) into two coherent beams, which are then focused on the sample with the help of the lens system. For three-beam interference, the setup remains largely the same, with the only difference being the use of a DOE designed to split the beam into three paths.

3.2.2 Static Contact Angle Measurement

Contact angle experiments were conducted using a *Drop Shape Analyzer DSA 100* (Krüss GmbH). This facilitated in monitoring the aging of USP-DLIP-structured surfaces over a period of three weeks[30]. The laser treated samples were stored in a box at room temperature (20 ± 2 °C) and a humidity level of 30 ± 7%. The initial measurement (Week 0) was taken 24 hours post-treatment. Subsequent measurements were performed at 7-day intervals up to the third week, with each week's test conducted on an alternative specimen under following conditions: a room temperature of 21.5 ± 0.5 °C and a humidity of 20 ± 1.3%.

A 3 µL droplet of distilled water was dispensed onto the sample surface using the falling droplet method with a micro-syringe. Each sample was tested with at least five droplets applied to different surface areas. Due to the anisotropic topography of the laser-structured samples, the contact angle of each droplet was measured both perpendicular and parallel to the lines of the structure. Furthermore, to ensure reproducibility, all measurements were taken within one minute of droplet application.

3.2.3 Antibacterial Test

The antibacterial activity on the sample surface was investigated using the droplet method as outlined by Müller et al. (2021)[30]. This investigation consists of several steps. Firstly, the preparation of the bacterial suspension, then the droplet application, and lastly wet plating to count the surviving colony-forming units (CFU), as well as a parallel ion release test to measure the concentration of copper ions (µg/L) released during the contact period. Figure 9 illustrates the antibacterial testing setup, including droplet deposition and contact zone confinement, with a detailed description provided in the following subsections.

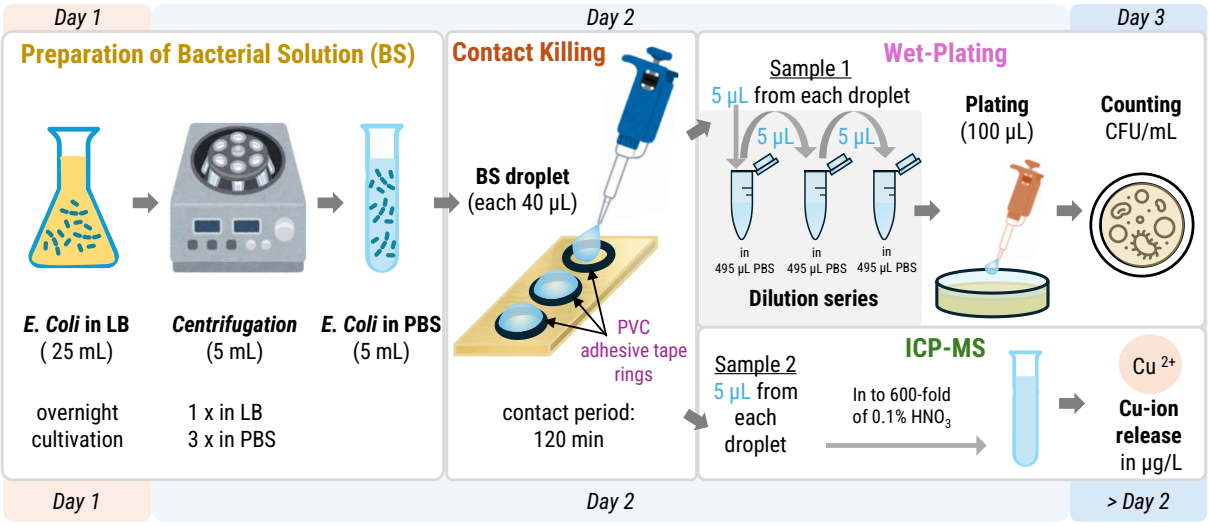

Figure 9: Schematic representation of the antibacterial testing setup used for surfaces. PVC adhesive tape rings are utilized to define the exposed area.

3.2.3.1 Bacterial Suspension Protocol

E. coli WT K12 (BW25113) strain was cultured aerobically overnight in Lysogeny broth (LB) medium in a water bath under the following conditions: at 37 °C and a speed set to 220 rpm. The bacterial culture was retrieved the following day and centrifuged at 5000 x g to remove the stationary cells. The centrifugation procedure was repeated three times using phosphate-buffered saline solution (PBS) under identical conditions. Lastly, the stationary cells were resuspended in PBS to make the bacterial suspension.

3.2.3.2 Contact Killing and Wet plating Method

A 40 μL droplet of the suspension was applied to the test surfaces. The experiment was conducted in a high-humid environment at room temperature for durations of 30, 60, 90 (in some cases) and 120 minutes. After each point, 5 μL of the suspension was withdrawn from the droplet following repetitive pipetting, serially diluted in PBS, and then spread onto LB agar plates. These were incubated at 37 °C for 24 hours. Finally, CFU were counted to determine the bacterial concentration in the suspension. The initial CFU/mL of the bacterial solution was used as the negative control.

3.2.3.3 Ion Release Test

Another 5 μL of the suspension was withdrawn from the droplet and added in to the 600-fold of 0.1 % nitric acid to measure the Cu-ion release during the contact. This measurement is done with inductively coupled plasma mass spectrometry (ICP – MS).

3.2.3.4 Solution Information

Phosphate-buffered saline (PBS) was prepared by dissolving NaH_2PO_4 $1H_2O$ (Merck, Germany, final concentration 0.01 M) and NaCl (VWR, Germany, final concentration 0.14 M) in purified water. The pH was adjusted to 7.4 using NaOH. The solution was then sterilized through autoclaving after preparation.

3.3 Characterization Techniques

3.3.1 Topographical and Morphological Analysis

3.3.1.1 Optical Microscopy

Surface modification was first analyzed with Confocal Laser Scanning Microscopy (CLSM) with the *LEXT OLS4100 3D Measuring Laser Microscope* (Olympus). CLSM is a non-contact, non-destructive technique that captures high-resolution images and measures surface roughness. The system used in this study offered a lateral resolution of 0.12 μm and a height resolution of 10 nm, enabling precise 3D imaging of the surface. The equipment features a laser with a 405 nm wavelength, providing accurate measurements of microroughness.

3.3.1.2 Scanning Electron Microscopy

This section explores the high-resolution method of Scanning Electron Microscopy (SEM) to study surface topography. This method uses the fundamental principle of electron beam and sample surface interaction to produce a signal, which is detected and used to create detailed images. This provides information on topography as well as chemical composition, depending on the type of interaction and the region from which the signal is detected[177]. In this study, two SEM/FIB Dual-station equipment were utilized: SEM/FIB, *Helios NanoLab 600*, FEI (at the Functional Materials Institute, Saarland University, Germany), and SEM/FIB, *Helios NanoLab 600i*, *FEI* (at Institut Jean Lamour (IJL, Nancy, France)).

3.3.1.3 SEM-Imaging

The SEM imaging was performed using a *Helios NanoLab 600*, FEI, operating in secondary electron (SE)contrast mode with an acceleration voltage of 5 kV and a current of 1.4 nA. To enhance the visualization of topographic features, the specimen was tilted at 45°. Additionally, to enhance the visibility of organic matter under characterization, samples containing bacteria were coated with a Gold-Palladium layer using the *MITECH* K950X sputter coater in a vacuum atmosphere of 2×10^{-2} mbar.

For higher-resolution imaging, at scales down to a few hundred nanometers, the detector was switched from the Everhart-Thornley Detector (ETD) to the Through Lens Detector (TLD). Additionally, backscattered electron contrast was employed at an acceleration voltage of 10 kV to capture images with enhanced Z-contrast (material contrast).

3.3.1.4 SEM - Focused Ion Beam

Cross-sections of the structures were examined using SEM/FIB (Focused Ion Beam) techniques. To begin, a platinum coating was applied to protect the samples, and the surface was tilted at 52° for precise material removal with a focused ion beam. This process was conducted at an acceleration voltage of 30 kV in two stages: an initial coarse milling step with a current of 0.28 nA, followed by a polishing step at a current of 21 nA.

Atom probe tomography (APT) specimen preparation was carried out in a FIB/SEM dual-beam workstation (*Helios NanoLab 600*, FEI) using the lift-out technique explained by Thompson et al.[178]. To preserve the region of interest, the analyzed surface was protected with a chromium layer deposited via physical vapor deposition (PVD). After lift-out and thinning, a final low-energy milling step at 2 kV was performed to reduce gallium-induced damage.

Furthermore, a *Helios NanoLab 600i*, FEI SEM, was used to fabricate lamellas perpendicular to the lines on the sample surface. These lamellas were then lifted out and mounted on a transmission electron microscopy (TEM) grid, where further ion-beam thinning was performed to achieve electron-beam transparency.

3.3.2 Chemical and Phase Analysis

3.3.2.1 SEM - Energy Dispersive X-ray Spectroscopy

An elemental analysis of the surfaces was performed with the FEI *Helios G4 PFIB CXe* system and the software EDAX APEX from Ametek Materials Analysis Division. This analysis provides qualitative and quantitative elemental information by detecting characteristic X-rays emitted from the sample. The detected signal originates primarily

from the upper surface and subsurface layers, and the depth of this information can be adjusted by varying the applied acceleration voltage[177]. As the surface modification was only a few micrometers, an acceleration voltage of 5 kV and a current of 5.5 nA were employed to confine the analysis to the superficial layer.

3.3.2.2 Grazing Incidence X-ray Diffraction

Quantitative phase analysis was conducted using high-resolution Grazing Incidence X-ray Diffraction (GI-XRD). This method is used to analyze thin films, surfaces, and nanoscale layers with high surface sensitivity. In GI-XRD, X-rays are directed at a very shallow angle to the sample (usually between 0.5° and 5°), limiting how deep they penetrate and focusing the analysis on the surface. This setup combines Bragg diffraction with total external reflection conditions, making it much more effective for studying surface layers than traditional methods. While standard Bragg diffraction typically examines the top few μm of material, GI-XRD reduces this range to a few nm, making it ideal for examining thin films and surface modifications[179].

In this study, the equipment was operated with a Cu Kα radiation source (wavelength of 1.5418 Å) at a grazing angle of 1°, using 40 kV and 40 mA on a *PANalytical X'Pert PRO-MPD* system. Additionally, the samples were aligned with the pattern direction so that the incident beam is parallel to the pattern. This minimizes obscuring effects from the pattern structure and enables detailed analysis of both peaks and valleys. Subsequently, the raw data were processed using X'pert HighScore software (version 5.1)[180], which included correction of the baseline and identification of the peaks for database comparison.

3.3.2.3 Scanning Transmission Electron Microscopy

Scanning Transmission Electron Microscopy (STEM) combined with Energy-Dispersive X-ray Spectroscopy (STEM-EDS) provides a highly effective method for nanoscale imaging and elemental analysis. The analysis was performed on a *JEOL ARM 200F* equipped with two Cs correctors to analyze and map the chemical

composition through elemental profiling. The sample preparation is described in section 3.3.1.4.

Furthermore, the microstructure of the modified area was characterized through electron diffraction imaging using Transmission Electron Microscopy (TEM). Selected Area Electron Diffraction (SAED) patterns were acquired and subsequently matched with corresponding interplanar spacing (*d*-spacing) values.

3.3.2.4 Atom Probe Tomography

Investigation of the surface and subsurface modifications was carried out using atom probe tomography (APT). This method is capable of 3D imaging and measurements of chemical composition at the atomic scale[178].

A *LEAP 3000X HR* (CAMECA) was used for this analysis. Regions containing oxides were examined using laser-pulsed mode, while subsurface composition analysis was conducted using voltage-pulsed mode. All the measurements were conducted at approximately 60 K, with a repetition rate of 100–200 kHz, a pressure below 1.33×10^{-8} Pa, and an evaporation rate of 2–5 atoms per 1000 pulses. The laser-pulsed mode was performed with pulse energies ranging from 0.5–0.6 nJ, while voltage-pulsed mode was performed using a 20% pulse fraction.

Data reconstruction and analysis were completed using IVAS3.6.8 (CAMECA) software. The composition calculations employed a peak decomposition algorithm, which separates overlapping peaks built on natural isotopic ratios. In this case, a key overlap of O_2^{+1} and Zn^{+2} peaks appears at 32 [Da] in the mass-to-charge spectrum, making it difficult to generate concentration profiles across the oxides.

3.3.2.5 X-ray Photon Spectroscopy

An analysis of the surface distribution of oxide phases was performed using X-ray Photoelectron Spectroscopy (XPS) combined with Ar^+-ion etching. This approach enables differentiation between the chemical states of elements present on the surface, allowing highly surface-sensitive analysis of oxides. By irradiating the sample with X-rays, XPS detects the kinetic energy of photoelectrons emitted from the sample surface,

providing detailed information on surface composition, oxidation states, and chemical environments. This technique is particularly valuable for studying materials, corrosion, catalysis, and surface modifications[181].

In this study, XPS, Vacuum Generators *ESCA MKII*, with a nonmonochromatic Al-Kα radiation, $\hbar\omega$ = 1486.6 eV, and normal emission was utilized. Data analysis was performed as explained in Müller et al. (2020)[31].

3.3.2.6 Raman Spectroscopy

Raman spectroscopy works by detecting the energy shifts in light scattered from a laser as it interacts with a sample's molecular vibrations, creating a unique spectrum that reveals molecular composition and structure. This technique is particularly useful for oxide analysis, as it can identify specific oxide phases, oxidation states, and surface composition with minimal sample preparation[182]. The study utilizes a Horiba Jobin, *HRLab* with a 532 nm laser.

3.3.2.7 Scanning Tunnel Microscopy and Spectroscopy

In this study, Scanning Tunneling Microscopy and Spectroscopy (STM/STS, using a *VT-STM* by Scienta Omicron) was employed to investigate the spatial distribution of the metal and oxide phases on brass samples.

3.3.2.8 HR-SIMS

A secondary ion mass spectrometer (SIMS) integrated with a *Zeiss Orion NanoFab* Helium Ion Microscope (HIM) system was used to perform surface chemical analysis. Initially, SE images were captured at a resolution of 2048 × 2048 pixels using 25 keV He^+ ions, a beam current of 4 pA, a dwell time of 10 μs per pixel, and an average of four scan lines. Following this, SIMS imaging was performed at 512 × 512 pixels with 25 keV Ne^+ ions, 5 pA current, and a dwell time of 2 ms per pixel, resulting in approximately 8 minutes per image. Key regions of interest (ROIs) were identified, including areas with line-like and honeycomb features on copper-nickel alloys, both in the presence and absence of bacterial cells. Sequential acquisition of SE and SIMS images from the same ROI enabled a direct correlation between surface morphology

and chemical composition. SIMS was operated in dynamic mode, involving continuous ion bombardment, which offered high spatial resolution (better than 15 nm) and exceptional sensitivity for elemental analysis. This approach was particularly effective in revealing nanoscale chemical patterns on laser treated surfaces and assessing copper uptake at bacterial contact sites.

4. Overview

To address the research objectives, a series of studies was conducted across different copper-based alloys, including brass[183,184], bronze[185], and copper-nickel alloys[186,187], each investigated in a specific set of publications.

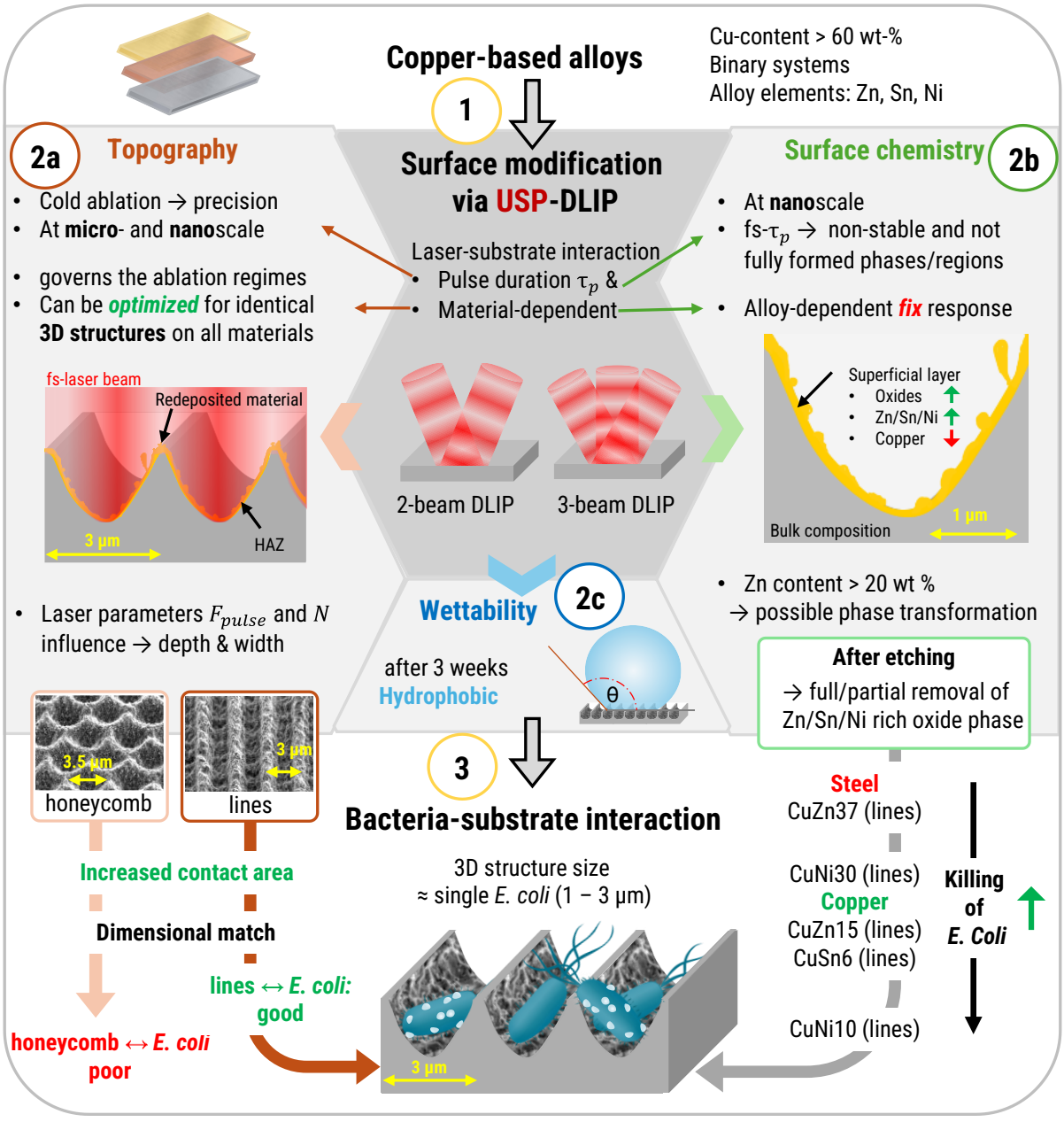

Figure 10: An overview of antibacterial properties of copper-based alloys (Cu > 60 wt-%) structured by USP-DLIP. **1)** Microscale structures, line-like and honeycomb patterns, were fabricated to match the dimensions of a single *E. coli* cell. **2)** Surface properties including topography, chemistry, and wettability were evaluated. USP-DLIP enabled precise micro-nanoscale structuring across materials, influencing oxide

formation enriched with alloy elements and resulting in a hydrophobic surface nature. **3)** Line-like structures demonstrated enhanced antibacterial activity, especially in alloys with higher copper content.

Brass was investigated in **Publications I**[183] and **II**[184], bronze in **Publication III**[185], and copper-nickel alloys in **Publications IV**[187] and **V**[186]. Each study targeted distinct aspects of surface engineering, including chemical composition, oxidation behavior, laser fluence, and surface structure geometry, encompassing line-like and point-honeycomb patterns. Together, these studies form a coherent investigation linking alloy design, laser structuring, surface chemistry, and antibacterial behavior.

The initial objective was the **fabrication of periodic microscale-structures** via USP-DLIP, which was successfully achieved across all studied alloys. A key part was understanding how alloy composition influences laser-material interaction, and for that a combination of complementary characterization techniques was employed. SEM, GI-XRD, and Raman spectroscopy were consistently used to investigate surface topography, phase formation, and oxide evolution. For brass, **Publications I** and **II** further utilized STEM-EDS, APT, and XPS to investigate chemical changes at the nanoscale, revealing modifications that had previously been considered negligible but proved critical for interpreting antibacterial behavior.

The influence of **alloy composition** on laser structuring emerged as a key factor in determining surface outcomes. For brass, variations in zinc content between 37 wt-% and 15 wt-% were explored, while copper-nickel alloys were studied with nickel contents of 10 wt-% and 30 wt-%. These studies demonstrated that the alloying element significantly affects laser-material interaction. While copper content above 60 wt-% is typically required by international standards, post-laser surface compositions deviated from this threshold, depending on alloying elements and phase transformations. Zinc-containing alloys require careful composition control to avoid phase transformations, whereas copper-nickel alloys, despite the presence of fully soluble phases, show a complex laser material interaction under laser irradiation.

Laser parameters also strongly influenced the topography of the surfaces and thereby impacted the antibacterial performance. In **Publication III**, bronze surfaces were systematically studied with varying laser fluences, demonstrating that changes in laser parameters modify the depth and width of surface features. The effect of topographical variation was tested against bacterial interaction, and it showed a good compatibility between the structure dimension and bacterial cell dimension.

A major chemical modification induced by USP-DLIP is the **formation of oxides**, which typically enriches the surface in the alloying element while reducing copper content. Citric acid post-treatment (5%) demonstrated that oxide-induced effects were reversible for copper alloys with lower alloying-element contents (CuZn15, bronze, and CuNi10), but less so for alloys with higher contents (CuZn37 and CuNi30). **Publications IV** revealed that annealing promoted stable cuprous oxide formation in copper–nickel alloys with lower copper content, which improved antibacterial activity. In contrast, in **Publication V**, oxide formation during laser structuring consistently diminished antibacterial performance, underscoring the complexity of processing–chemistry–function relationships.

Antibacterial performance testing provided initial insights into bacterial–substrate interactions. Overall, the laser-structured and citric-acid-etched alloy surfaces exhibited stronger bactericidal activity than the laser-structured surfaces alone. **Publications II, III**, and **V** revealed the first observations of bacterial-substrate interactions. **Publications I** and **II** employed ICP-MS to quantify copper ion release, whereas **Publication V** utilized HR-SIMS, which offered the first indication of copper ions within the bacterial cell wall. Another critical aspect explored was the compatibility of surface structure dimensions with bacterial size, observed across all laser-structured samples but studied in detail in **Publications III** and **V**. These studies demonstrated that the width of valleys is particularly important in governing bacterial adhesion. **Publication V** introduced honeycomb three-dimensional structures intended to isolate bacteria; however, the results indicated that line-like structures provided superior antibacterial performance against *E. coli*.

Collectively, the results of **Publications I–V** demonstrate that microscale surface structuring, combined with alloy composition, laser parameters, and surface chemistry, plays an important role in governing antibacterial activity, and contributes to the development of copper-based antimicrobial materials suitable for real-world applications. **Publication I** investigated the effect of zinc content on laser structuring and nanoscale chemical modifications in brass, while **Publication II** optimized brass surface structures and demonstrated the reversibility of oxide-induced modifications. **Publication III** extended these findings to bronze, highlighting the role of laser parameters on surface topography and the resulting effects on bacterial adhesion. **Publications IV** and **V** explored copper-nickel alloys, with Publication V highlighting the role of nickel content and structural design in bacterial interaction. Together, these studies provide a systematic framework for engineering copper-based surfaces with controlled structural and chemical properties that enhance antibacterial functionality, thereby bridging fundamental material design with practical applications.

5. Included Publications

- **Publication I:**

  This study demonstrated that USP-DLIP can fabricate periodic, line-like microscale structures on brass substrates (37 wt -% Zn), with periodicities (~3 μm) matching the size of *E. coli* cells. In this case, laser treatment not only changed surface topography but also induced localized chemical alterations within the heat-affected zone (HAZ). Consequently, a phase transformation from α- to β-brass and to oxide formation is observed, which resulted in increased zinc and decreased copper content on the superficial layer. Consequently, the antibacterial activity of the structured brass surfaces decreased, suggesting that both topography and laser-induced chemical modifications collectively contribute to bacterial inactivation.

- **Publication II:**

  Building on the findings from Publication I, this study evaluated the impact of zinc content (15 wt-% zinc) in brass alloys on the effectiveness of laser-induced antibacterial surfaces. The results revealed that even modest variations in zinc concentration affected the post-laser surface chemistry, particularly in HAZ, which in turn influenced bacterial interaction and survival. The work confirmed that low zinc content can significantly improve the antibacterial activity, highlighting the importance of alloy selection and surface composition in functional design.

- **Publication III:**

  This study focused on surface modification of tin-alloyed bronze surfaces, For that purpose, laser pulse fluence/pulse energy is optimized to produce diverse but consistent 3 μm periodic patterns matching the size of individual *E. coli* cells. The structured bronze surfaces were then evaluated for antibacterial

efficiency and wetting behavior, given the influence of wettability on bacterial adhesion. Findings indicated that the most effective surfaces were fabricated with moderate laser fluences, as these balanced structural integrity with biological activity. The results highlighted the need for parameter tuning to achieve a reproducible topography and showed that surface hydrophobicity influenced bacterial retention, but the compositional effects were dominant.

- **Publication IV:**

  This collaborative publication examined the role of surface oxidation on Cu-Ni alloy. The study demonstrated that controlled oxidation was shown to either enhance or impair antibacterial activity, depending on the alloy composition Specifically, when the surface copper concentration dropped below 60 wt-% due to oxidation or high nickel content, antibacterial efficiency declined significantly. These findings underline that surface copper availability is a key determinant for the contact-based bacterial killing. Therefore, oxidation strategies must be carefully managed depending on the alloy to modulate antibacterial functionality.

- **Publication V:**

  This study investigates surfaces of binary Cu-Ni alloys (10 and 30 wt-% Ni) structured with two distinct geometries: periodic line-like and honeycomb structures. Results show that line-like structures had a better antibacterial activity then the honeycomb. However, 30 wt-% Ni alloys exhibited reduced antibacterial activity across both pattern types compared with the non-structured surfaces, due to copper depletion at the surface. A significant enhancement in antibacterial activity was observed only for the 10 wt-% Ni alloys, correlating with preserved surface copper levels above 60 wt-%. This suggests that both copper concentration and structure geometry are critical to maximizing antibacterial performance.

PUBLICATION I

Surface Modification of Brass Via Ultrashort Pulsed Direct Laser Interference Patterning and its Effect on Bacteria-Substrate Interaction

Aisha Saddiqa Ahmed[a,b], Daniel Wyn Müller[a], Stephanie Bruyere[b], Anne Holtsch[c], Frank Müller[c], Jenifer Barrirero[a], Kristina Brix[d], Sylvie Migot[b], Ralf Kautenburger[d], Karin Jacobs[c], Jean-François Pierson[b], Frank Mücklich[a]

[a] *Chair of Functional Materials, Department of Material Science and Engineering, Saarland University, 66123 Saarbrücken, Germany*

[b] *Université de Lorraine, CNRS, IJL, F-54000 Nancy, France*

[c] *Experimental Physics and Center for Biophysics, Saarland University, 66123 Saarbrücken, Germany*

[d] *Department of Inorganic Solid-State Chemistry, Elemental Analysis, Saarland University, 66123 Saarbrücken, Germany*

Research article

Published in "**Applied Materials & Interfaces**" (2023)

Impact Factor: 8.2 (2025)

Reproduced with permission from 'American Chemical Society'

Accessible online at: https://doi.org/10.1021/acsami.3c04801

Own Contributions: Conceptualization, Investigation, Validation, Visualization, Writing – original draft.

Cite this article as: Ahmed, A. S.; Müller, D. W.; Bruyere, S.; Holtsch, A.; Müller, F.; Barrirero, J.; Brix, K.; Migot, S.; Kautenburger, R.; Jacobs, K.; Pierson, J.-F.; Mücklich, F. Surface Modification of Brass via Ultrashort Pulsed Direct Laser Interference Patterning and Its Effect on Bacteria-Substrate Interaction. *ACS Appl Mater Interfaces* **2023**, *15* (30), 36908–36921. https://doi.org/10.1021/acsami.3c04801.

Full article: https://pubs.acs.org/articlesonrequest/AOR-NWYGFIRMZIDK3PTZ9WCT

ACS APPLIED MATERIALS & INTERFACES

www.acsami.org

Research Article

Surface Modification of Brass via Ultrashort Pulsed Direct Laser Interference Patterning and Its Effect on Bacteria-Substrate Interaction

Aisha Saddiqa Ahmed,* Daniel Wyn Müller, Stephanie Bruyere, Anne Holtsch, Frank Müller, Jenifer Barrirero, Kristina Brix, Sylvie Migot, Ralf Kautenburger, Karin Jacobs, Jean-François Pierson, and Frank Mücklich

Cite This: https://doi.org/10.1021/acsami.3c04801

Read Online

ACCESS | Metrics & More | Article Recommendations | Supporting Information

ABSTRACT: In recent decades, antibiotic resistance has become a crucial challenge for human health. One potential solution to this problem is the use of antibacterial surfaces, i.e., copper and copper alloys. This study investigates the antibacterial properties of brass that underwent topographic surface functionalization via ultrashort pulsed direct laser interference patterning. Periodic line-like patterns in the scale range of single bacterial cells were created on brass with a 37% zinc content to enhance the contact area for rod-shaped *Escherichia coli* (*E. coli*). Although the topography facilitates attachment of bacteria to the surface, reduced killing rates for *E. coli* are observed. In parallel, a high-resolution methodical approach was employed to explore the impact of laser-induced topographical and chemical modifications on the antibacterial properties. The findings reveal the underlying role of the chemical modification concerning the antimicrobial efficiency of the Cu-based alloy within the superficial layers of a few hundred nanometers. Overall, this study provides valuable insight into the effect of alloy composition on targeted laser processing for antimicrobial Cu-surfaces, which facilitates the thorough development and optimization of the process concerning antimicrobial applications.

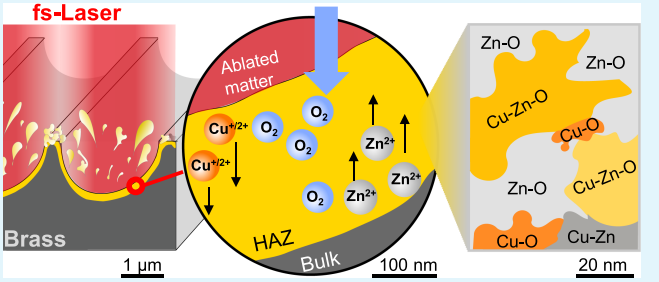

KEYWORDS: *ultrashort pulsed direct laser interference patterning, femtosecond pulse duration, brass, zinc oxide, copper oxides, nanoscale chemical modification, nanoscale heat-affected zone, antibacterial*

1. INTRODUCTION

Rapidly increasing infectious diseases remain a major social problem, and the threat of antibiotic resistance is a significant concern.[1] However, alternative strategies such as the use of antimicrobial surfaces offer a promising solution to effectively inhibit the growth and spread of harmful microorganisms.[2−4] Inspired by nature's morphological blueprints, researchers are constantly investigating new techniques to harness their beneficial properties.[5,35,36] The nanopillars on cicada wings are a primary example of a naturally occurring antibacterial effect owing to the surface structures.[6] On the contrary, the hydrophobic behavior of the *Lotus* leaf is a result of micro- and nanostructures as well as their surface chemistry, which gives them a self-cleaning function.[7]

A variety of techniques have been developed for the functionalization of surfaces to alter their characteristics. These include chemical or/and topographical alterations realized via methods like nanoparticle fabrication, micro- and nanostructuring, and creating photocatalytic surfaces.[3,8,9] Direct laser interference patterning (DLIP) technology[10] has been utilized for over a decade to modify surfaces down to the nanoscale. DLIP in combination with ultrashort pulse (USP) durations has proven to provide attainable precise nanostructures.[11−13] This is attributed to the curtailed melting zone by the virtue of shorter pulse durations.[14] As whole, the scope of DLIP application is defined remarkably wide including functions such as tribology,[15−17] electrical conductivity,[18] antibacterial properties,[3,19] and wettability.[20,21] Moreover, various materials ranging from metals to polymers, depending on the application, have been modified via laser technology.[22−26]

Metals like copper, copper alloys, cadmium, and silver have been the focus of investigation for their naturally occurring antibacterial properties.[3,4,22,27−29] Moreover, metal oxides like zinc oxide and titanium oxide, which show antibacterial

Received: April 4, 2023
Accepted: July 5, 2023

activities upon exposure to ultraviolet light, are also being investigated.[8,30] In the case of pure copper, surface modification via ultrashort pulsed direct laser interference patterning (USP-DLIP) was shown to further improve the already pronounced inherent antibacterial properties.[3,31,32] This involves an increased Cu-sensitivity alongside improved bacterial contact conditions.[3] The antimicrobial effect of Cu surface is directly related to the quantitative release of cytotoxic Cu-ions, which are known to deteriorate both bacteria and viruses by several modes of action, e.g., targeting the cell wall, proteins, and DNA.[31,33] Here, the presence of copper oxides can impact the antibacterial properties: excessive cupric oxide (CuO) was shown to reduce antibacterial efficiency, whereas, for predominant cuprous oxide (Cu_2O) composition, it is improved.[34]

Despite the advantageous antibacterial properties of copper, its limited mechanical properties, including low hardness and strength yield, restrict its widespread use, e.g., as antibacterial surfaces in public and private infrastructure to prevent the transmission of harmful microorganisms. In this case, alloying represents a powerful approach to optimize the properties according to the desired application.

For this study, a commercially available copper alloy with 37% zinc content (brass, CuZn37) is chosen. The zinc in brass adds to the hardness and durability of the material.[37] The aim is to use USP-DLIP to fabricate periodic line-like structures in the scale range of single bacteria cells, first to understand the laser-material interaction and second to test the impact of USP-DLIP processing on antibacterial efficiency. Various characterization methods are employed to determine the effect of the alloying on the degree of surface modification, which include scanning electron microscopy (SEM), high-resolution grazing incidence X-ray diffraction (GI-XRD), scanning transmission electron microscopy along with energy-dispersive X-rays spectroscopy (STEM-EDS), atom probe tomography (APT), electron diffraction (selected area electron diffraction, SAED, or fast Fourier transform image, FFT) via transmission electron microscopy (TEM), X-ray photoelectron spectroscopy (XPS), scanning tunnel microscopy and spectroscopy (STM and STS), and Raman spectroscopy. The structured surfaces are then tested for their antibacterial activity against *Escherichia coli* (*E. coli*) WT K12 (BW25113) to understand the correlation with surface modifications achieved via USP-DLIP.

2. MATERIALS AND METHODS

2.1. Materials and Preparation. The commercially available brass with 37 wt.-% zinc (M37; Wieland), CuZn37, was chosen for this work. It should be noted that, for Cu-Zn alloys, the composition given in wt.-% differs only marginally from the composition given in at.-%. Additionally, 99.95% pure copper (Wieland) and stainless steel (Brio) were utilized as references. The samples were acquired in the form of a sheet with a thickness of 1 mm and were then cut to a dimension of approx. 25 × 10 mm^2. Since a smooth initial surface topography is required for the subsequent laser process, the sample surfaces were prepared metallographically. Prior to that, microhardness of brass was measured with a Struers Dura Scan 50 microhardness tester, which is required to determine the polishing parameters, as the high copper content in the samples can present a challenge during preparation due to its softness. The Vickers hardness (HV 0.1) value for CuZn37 was recorded at 107 ± 9. This value is almost double that of pure copper, yet low compared to steel. For that reason and to avoid any big deformations, the process was started with fine grinding. First, SiC paper with a grain size of 15 μm was utilized on a manual Tegrapol system (Struers) to remove the uppermost layer of deformations. Next, the surfaces were polished with an automated TegraPol system (Struers) to finally obtain a mirror-quality finish. This was executed in a total of three steps, i.e., 6, 3, and 1 μm grain sizes, each using the respective all-in-one diamond solutions (Struers).

2.2. Ultrashort Pulsed Direct Laser Interference Patterning (USP-DLIP). USP-DLIP technology was utilized to produce line-like structures with a periodicity of 3 μm on the brass surface. For the surface modification, a Ti:sapphire Spitfire laser system (Spectra Physics) with ultrashort laser pulses (pulse duration of t_p = 100 fs, full width at half maximum—FWHM) was utilized. The centered wavelength λ was 800 nm. The optical setup was chosen as described by Müller et al.[38] The setup consists of a beam diameter aperture, wave plate, diffractive optical element (DOE), mask, and focusing lens system with a 100 mm focal length. First, the laser beam passes through an aperture, which adjusts the beam diameter and transforms the intensity profile from Gaussian to near Top Hat shape. The beam is then forwarded to a wave plate that changes the polarization angle of the beam perpendicular to the orientation of fabricated patterns. Subsequently, the DOE splits the beam into two coherent partial beams. These are then diverted by a lens to finally interfere on the sample surface. These create maxima and minima of intensities in the focal spot leading to the formation of line-like periodic structures via ablative processes. Looking at the superimposed profile in cross-section, a wave-like intensity distribution profile with broad valleys and narrow peaks emerges as described by Müller et al.[38] The periodicity of these line-like structures is linked to the incident angle of single laser beam on the sample surface. This interference setup hereby is similar to the Fresnel mirror setup,[39] which describes the periodicity p according to eq 1.

$$p = \frac{\lambda}{2 \times \tan \alpha} \tag{1}$$

where λ is the wavelength of a laser beam and α is the incident angle of a single partial beam. As the surface is irradiated with a laser beam, the energy is first absorbed by the electrons and then transferred onto the lattice until a thermal equilibrium is achieved.[15] The electron-lattice relaxation time hereby is in the range of a few picoseconds,[40] whereby the laser material interaction within and below this range is described involving a two-temperature model.[41−43] In the case of femtosecond pulses, the relaxation time is considerably longer than the pulse duration. Therefore, it is highly improbable to realize a thermal equilibrium in the lattice. As a result, a direct solid to vapor/plasma phase transformation is observed, instead.[44] Depending on the applied fluence regime, very thin melting depths are expected alongside ablation via spallation or phase explosion.[13,45] Due to averted thermal diffusion within this time scale, very high temperatures and pressure are experienced in the thermal response of irradiated matter. This results in thermal and mechanical lattice distortion of the material. Due to which, the uppermost surface undergoes topographical as well as chemical modifications. This includes remelting, rapid solidification, and redeposition of the previously ablated matter in the shape of oxidic particles.[22] In this work, a total of 24 samples were structured. Twelve of the laser structured samples were then etched to remove the process-induced oxides. For that purpose, samples were emerged in 5% citric acid, then placed in an ultrasonic bath for 2 min, and finally cleaned with ethanol. For any further experiments, the samples were aged at least for three weeks to ensure stable and reproducible wettability conditions.[3]

2.3. Surface Characterization. The topography of the samples was observed with confocal laser scanning microscopy (CLSM, LEXT OLS4100 3D Measuring Laser Microscope by Olympus). A quantitative phase analysis was performed via high-resolution grazing incidence X-ray diffraction (GI-XRD, Cu K_a source with a wavelength of 1.54 Å at a 1° grazing angle, PANalytical X'Pert PRO-MPD).

Scanning electron microscopy (SEM, Helios NanoLab 600, FEI) was used to acquire images in secondary electron contrast mode. An acceleration voltage of 5 kV at a current of 1.4 nA was applied, and the sample was tilted at 45° to improve visualization of topographic

https://doi.org/10.1021/acsami.3c04801
ACS Appl. Mater. Interfaces XXXX, XXX, XXX−XXX

pattern features. Subsequently, cross-sections of the line-like structures were examined by the means of SEM/FIB (Focused Ion Beam) Lamellas (perpendicular to the lines) that have been prepared on the sample surface before lift out and mounting on a TEM-grit for further ion-beam thinning to reach e-beam transparency. These are analyzed via scanning transmission electron microscopy (STEM) also including energy-dispersive X-ray spectroscopy (STEM-EDS, JEOL ARM 200F equipped with two Cs correctors) to determine the chemical composition via mapping and profiling. This characterization was further supplemented by the electron diffraction imaging via transmission electron microscopy.

The surface and subsurface effects of modification were characterized by atom probe tomography (APT). This was accomplished in a LEAP 3000X HR (CAMECA) with laser-pulsed mode for the regions with oxides and voltage-pulsed mode for the subsurface composition. All APT measurements were performed at a temperature of about 60 K, a repetition rate of 100−200 kHz, pressure lower than 1.33×10^{-8} Pa, and an evaporation rate of 2−5 atoms per 1000 pulses. Laser pulsed APT was carried out with a pulse energy of 0.5−0.6 nJ; and voltage measurements with 20% pulse fraction. The reconstruction and analysis of the datasets was done with the commercial software IVAS3.6.8 (CAMECA). Compositions were calculated by applying a peak decomposition algorithm included in the analysis software. As the name explains, this algorithm decomposes overlapping peaks based on the natural isotopic ratios. In the present case, the most important overlap occurs in the mass-to-charge spectrum at 32 [Da] due to the overlap of the most abundant peaks of O_2^{+1} and Zn^{+2}. Due to this overlap, it is not possible to construct concentration profiles across the different oxides in the reconstructions. APT specimens were prepared in a FIB/SEM dual-beam workstation (Helios NanoLab 600, FEI) by the lift-out technique described by Thompson et al.[46] The analyzed surface was covered by a chromium capping deposited by physical vapor deposition (PVD) to ensure the preservation of the region of interest. After lift-out and thinning of the specimens, a low-energy milling at 2 kV was performed to minimize gallium-induced damage.

Additionally, scanning tunneling microscopy and spectroscopy (STM/STS, VT-STM by Scienta Omicron) was utilized to further map the surface topography and investigate the electronic structure of the surface. Finally, the oxide characterization was done with Raman spectroscopy (Horiba Jobin, HRLab with a 532 nm laser) as well as X-ray photoelectron spectroscopy (XPS, Vacuum Generators ESCA MKII, nonmonochromatic Al-K_α radiation, $\hbar\omega$ = 1486.6 eV, normal emission, data analysis according to ref 22).

2.4. Wet Plating. The antibacterial activity of brass surfaces was tested via the wet plating method.[47] Bacteria of the strain *E. coli* WT K12 (BW25113) were implemented in the wet plating and were stored at 4 °C. The bacteria culture preparation was performed as described by Müller et al. and Luo et al.[3,4] The strain was grown overnight aerobically in a Lysogeny broth (LB) medium at 37 °C in a water bath with a speed of 220 rpm. The next day, the bacterial culture was taken out and centrifuged at 5000×*g* to separate the stationary cells. The centrifugation process was repeated three times with phosphate-buffered saline (PBS) using the same parameters. Finally, the stationary cells were resuspended in PBS to prepare the bacterial suspension. The bacterial suspension (40 μL) was applied on the tested surfaces in the shape of a droplet. The region of contact was defined by a polyvinyl chloride (PVC) ring.[3] The test was conducted in an environment of saturated humidity at room temperature for a duration of 30, 60, and 120 min. At the end of each respective time, two samples of 5 μL of the suspension were retreated from the droplet after repetitive pipetting. The first was then serially diluted in PBS and finally spread on LB agar plates. The plates were stored in an incubator at 37 °C for 24 h. Finally, the surviving colony-forming units (CFU) were counted to enumerate the viable bacteria of the sampled suspension. As a first reference, the original CFU/mL value of the suspension was chosen. As further references, mirror-polished surfaces of pure copper and stainless steel were tested simultaneously. The second 5 μL of droplet was diluted in to 600-fold of 0.1% HNO_3 to determine the Cu-ion release during the exposure time, which is measured with inductively coupled plasma mass spectrometry (ICP-MS, Agilent 8900 ICP-QQQ).

2.4.1. Solution Information. Phosphate-buffered saline (PBS) was prepared using NaH_2PO_4 $1H_2O$ (Merck, Germany, final concentration 0.01 M), NaCl (VWR, Germany, final concentration 0.14 M), and pure water for analysis, and its pH value was adjusted to 7.4 by adding NaOH. It was autoclaved after preparation for sterilization.

3. RESULTS AND DISCUSSION

3.1. Topography of the USP-DLIP Structures. Line-like structures with the periodicity of 3 μm were fabricated on CuZn37 using a fluence of 0.98 J/cm^2 with a total number of 9 pulses (N = 9). According to CLSM measurements, the aimed periodicity of 3.0 ± 0.1 μm and a depth of 1.30 ± 0.14 μm were achieved. Figure 1a shows the surface after laser

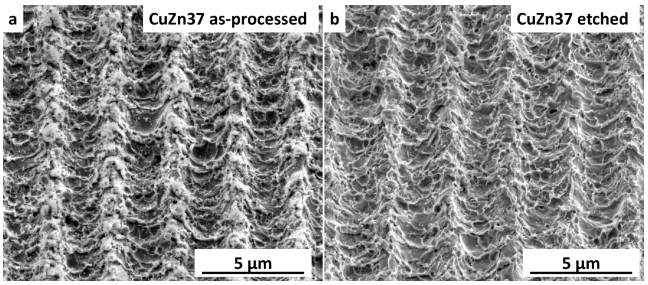

Figure 1. SEM-topography: the 3 μm periodic line-like structure with USP-DLIP on CuZn37 (a) as-processed and (b) after etching with citric acid (the images were obtained at a tilt angle of 45°).

treatment also referred to as the as-processed samples. As expected, the SEM micrographs exhibit line-like surface patterns comprising of narrow peaks and broad valleys.

The aim here is to allow the bacteria to settle well within the valleys and have contact area to the substrate regardless of the direction of placement. Furthermore, the deep valleys provide additional contact for the bacteria that accumulate on the monolayer, and overall, a larger contact area is achieved. Apart from that, a layer of flake-like substructures is observed that indicates the formation of oxides consequent to laser processing, as also shown by Müller et al.[3] The presence of oxides plays a vital role in altering the crucial parameters of antibacterial properties, i.e., Cu-ion release on contact and the adhesion of bacteria. First, depending on the oxidation state of pure copper, the release of Cu-ions is affected.[4] And second, the adhesion of bacterial droplets is impaired by the reduced wettability due to the topographical construct of the oxides but also due to the accumulation of carbon species during the aging process, i.e., carbon oxides, hydrocarbons, etc.

In the case of pure copper, it has been demonstrated that removing this layer can further alter the antibacterial efficacy.[3] To examine the effect of oxidation on brass, the structured samples were etched with citric acid to remove the possible oxides. Figure 1b shows an efficient removal of the substructures, making the surface morphology underneath more visible. As a result, the attention is drawn toward the actual geometry of the fabricated structures with a peak-valley ratio of 1:2.3 and, hence, a 2.3-fold increase in the actual surface area. Likewise, the concave shape of valleys is revealed, which provides favorable conditions for bacteria to settle in the valley. The SEM micrographs also show nanoroughness along the lines suggesting melting and redeposition together with the ablation. Ablation occurs as a result of locally high confined

https://doi.org/10.1021/acsami.3c04801
ACS Appl. Mater. Interfaces XXXX, XXX, XXX−XXX

stresses in the surface, which are produced via high temperature during laser irradiation.[48,49] The observed surface morphology points toward ablation predominantly in the phase explosion regime involving the ejection of the molten matter.[50] Parallel to ablation, the melted matter also creates multipulse ripples.[51] Another prominent feature is the small round nanoparticles mostly on the peaks formed due to the redeposition of exploded melted particles.[52,53] These further add to the depth of the crater. Overall, the morphology of the structures corresponds to the ones in previous studies.[3,22]

3.2. Morphological and Chemical Surface Modification. Lamellas were lifted out perpendicular to the line-like structures (see Figure S1 in the Supporting Information) from both structured samples and analyzed with STEM-EDS. The same procedure was repeated with numerous measurements of peaks and valleys of the structures to achieve the results (see Figure 2a,b).

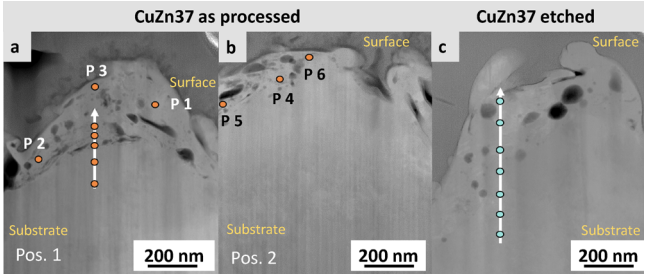

Figure 2. STEM high-angle annular dark field images of CuZn37 lamellas displaying the cross section of the peaks from: (a, b) as-processed and (c) etched with EDS-line scan (points on the arrow) as well as individual scan points.

The high-angle annular dark field-TEM images in Figure 2 reveal the nanoscale surface morphology of the surface with clear redeposition of the molten matter on the peaks. Since the fabrication is done via a multipulse laser irradiation, the multiple piling of redeposited matter is observed,[54] which, in this case, leads to the formation of pores within the layers as shown in Figure 2.

The results of EDS line scans for the as-processed sample (Table 1) show a drastic modification of the chemical composition for CuZn37 approx. 250 nm from the surface, which also includes the layers of the redeposited matter. The uppermost scan point of the line scan on position 1 (see Figure 2a and Table 1) shows that the surface has a reduced amount of copper (approx. 41 at.-%) in comparison to the bulk. On the contrary, zinc (39 at.-%) and oxygen (up to ∼20 at.-%) are detected in abundance, which suggests the formation of oxide-rich regions. At the same time, the Cu-Zn ratio of 2:3 (excluding oxygen) was recorded at a few points that suggest the diffusion of zinc toward the outer surface. It can be explained by the exceptionally high thermal energy as well as the kinetic energy in the near surface range caused by laser irradiation, which enables the diffusion of copper and zinc atoms in the subsurface. This indicates the occurrence of the Kirkendall effect.[55] Concurrently, additional mobility for the atoms can be anticipated in the redeposited matter during remelting, which is experienced due to the multipulse laser irradiation.

The results on position 2 (see Figure 2b), however, exhibit a nongradual alteration of the Cu-Zn-O ratio from the bulk to the surface. For that reason, few point scans were carried out

Table 1. STEM-EDS Results of CuZn37[a]

				at.-%		
sample	distance from the surface [nm]			Cu	Zn	O
as-processed	pos. 1	line scan	422	6.1	35.3	2.6
			314	63.1	35.2	1.8
			260	52.8	37.4	9.8
			206	50.4	37.1	12.5
			179	41.0	39.4	19.6
		P1	125	52.9	43.7	3.4
		P2	102	59.5	36.9	3.6
		P3	23	52.1	42.1	5.8
	pos. 2	P4	90	53.1	42.2	4.7
		P5	50	52.0	41.2	6.8
		P6	15	34.8	59.8	5.4

		at.-%		
sample	distance from the surface [nm]	Cu	Zn	O
etched	606	63.4	34.3	2.3
	505	64.3	35.0	0.7
	404	63.7	33.6	2.7
	303	62.1	35.1	2.8
	202	61.3	36.4	2.3
	101	58.6	37.0	4.4
	10	44.4	39.2	16.4

[a]This includes the line scan and point scans (P1−6) from Figure 2a,b on the as-processed and line scan from Figure 2c on the etched sample.

on both positions to investigate the discrepancies. Table 1 contains the results of point scans on position 1 (P1−3) and position 2 (P4−6) confirming varying distribution ratios in the modified surface area. Here, few points with lower oxygen at.-% have a Cu-Zn ratio that corresponds to the stoichiometry of the β phase of brass.[56,57]

After etching, the uppermost layer still has increased amounts of zinc and oxygen (see Figure 2c and Table 1). However, the chemical modification is only observed for ∼100 nm from the surface. Furthermore, the variation of the Cu-Zn ratio for points with less oxygen is not that significant. Overall, the total variation of chemical composition after etching suggests that a layer consisting of the zinc-rich phase with oxidic components was removed. This indicates that the uppermost surface consists mostly of zinc richer oxide areas, as it also agrees with the oxidation prone nature of zinc in comparison to copper.[58] The varying distribution ratios recorded for the modified area are further investigated in the next sections.

3.3. Determination of Local Elemental Distribution. APT is utilized to investigate the three-dimensional local distribution of elements in CuZn37 as-processed. Specimens from the peak and valley of the line-like structures were prepared and analyzed. The volumes reconstructed have a diameter of ∼30 nm and a depth between 20 and 50 nm and give an image of the surface oxidation of the sample.

The results confirm an inhomogeneous distribution of Zn, Cu, and O. All specimens depicting the oxidized surface show two regions with distinctive compositions. To determine the composition of each of these regions, the atoms corresponding to each of them were selected by the construction of iso-concentration surfaces for Zn and Cu and exporting the atoms inside (see Figure 3, Table 2).[59] In all cases, the iso-

https://doi.org/10.1021/acsami.3c04801
ACS Appl. Mater. Interfaces XXXX, XXX, XXX−XXX

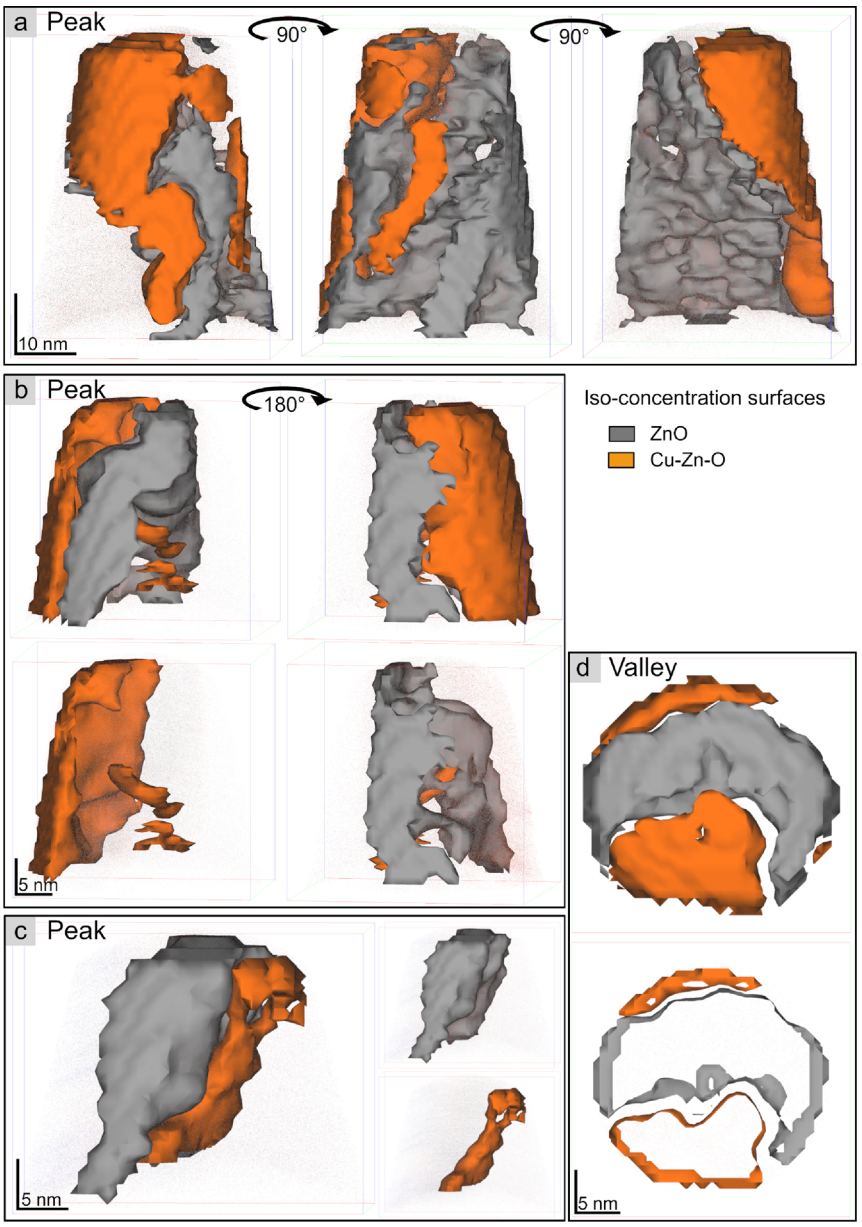

Figure 3. Atom probe tomography (APT) reconstructions of the oxidized surface in sample CuZn37 as-processed [iso-concentration values for gray surfaces 55−57 at.-% Zn and for orange surfaces 20−33 at.-% Cu depending on the composition of the Cu-Zn-O region]. (a−c) Peak and (d) valley of the line-like structure with their respective chemical composition in Table 2.

concentration values were chosen so that they enveloped intertwined volumes rich in Zn and rich in Cu separately.

Figure 3 shows four APT reconstructions giving an overview of the oxides' distribution. Besides the superficial measurements shown in Figure 3, two extra measurements were performed below the oxidized layer to measure the subsurface composition. Table 2 summarizes the composition of each of the oxidized regions in Figure 3 and the subsurface region.

The Zn-rich oxide (gray in Figure 3) shows a stoichiometry near ZnO with Zn:O ratios ranging from 1 to 1.3 and a low concentration of Cu of 2−5 at.-%. On the other side, the complementary regions (orange in Figure 3) show varying contents of the three elements Cu-Zn-O. Similar chemical compositions were also detected using STEM-EDS on CuZn37 as-processed (see Table 1). These compositions indicate the formation of a Cu-Zn-O transitional region. Two recent papers[60,61] discuss the formation of Cu-Zn-O nanoparticles and layers with varying compositions and discuss the diffusion of Cu atoms upon annealing. In this work, high

Table 2. APT Results of CuZn37 As-Processed

		at.-%		
position	Figure 3	Cu	Zn	O
peak	a	5.2 ± 0.1	54.0 ± 0.2	40.8 ± 0.1
		54.9 ± 0.3	34.3 ± 0.3	10.8 ± 0.1
peak	b	6.4 ± 0.1	46.1 ± 0.3	47.4 ± 0.1
		50.6 ± 0.2	19.8 ± 0.2	29.6 ± 0.1
peak	c	4.9 ± 0.1	49.7 ± 0.3	45.4 ± 0.1
		33.8 ± 0.6	43.0 ± 0.8	23.3 ± 0.3
valley	d	2.8 ± 0.2	52.5 ± 0.6	44.6 ± 0.1
		36.4 ± 0.5	35.5 ± 0.4	28.1 ± 0.1
subsurface		58.3 ± 0.1	41.2 ± 0.1	0.6 ± 0.1
		55.9 ± 0.2	42.6 ± 0.2	1.6 ± 0.1

https://doi.org/10.1021/acsami.3c04801
ACS Appl. Mater. Interfaces XXXX, XXX, XXX−XXX

temperature and stress are induced on the sample surface by USP-DLIP, followed by a rapid cooling that promotes the formation of metastable phases alongside crystallographic defects.

The results show the diffusion of elements along with ablation and redeposition through laser irradiation. The subsequent chemical modification at subsurface levels indicates that the thermal diffusion length is greater than the ablation depth in the valley. Moreover, there is an absorption of certain amounts of laser energy on the peaks. Although these regions are exposed to the minima of the interference modulated intensity profile, the absorption cannot be entirely excluded. This indicates that a nanoscale heat-affected zone (HAZ) is given due to residual thermal energy. This energy is sufficient to increase the mobility of elements, which presumably leads to oxygen penetration to a depth of a few hundred nanometers and forms the Cu-Zn-O regions. Moreover, the redeposited matter is also exposed to the residual thermal energy due to multipulse laser irradiation. This leads to high kinetic energy[54] exposing the redeposited matter to additional oxygen diffusion. Parallel to that, outward diffusion of Zn from this region can be anticipated, which is supported by the Kirkendall effect[55] as well as the oxide prone nature of zinc. Therefore, the formation of Zn-rich oxide phase is observed. It should also be noted that, in a thermodynamically stable state, the whole diffusion should lead to the formation of stable segregated phases. However, in this case, the pulse duration is ultrashort. Therefore, a rapid cooling of the surface most probably hinders the formation of stable phases. Hence, the occurrence of metastable Cu-Zn-O transitional regions is observed. The discrepancies recorded in the Cu-Zn-O ratio of these regions are probably due to variations in the amount of oxygen that diffuses into the HAZ as well as into the redeposited matter. Another factor could be the kinetic energy of the atoms, which can vary depending on the energy absorbed in the different regions. All these factors together affect the diffusion of all elements and hence the chemical composition.

Furthermore, the subsurface of the valley is analyzed (see Figure 3) and the recorded chemical compositions confirm the presence of the intermetallic β phase of brass. This indicates the formation of the β phase most credibly through the rapid cooling of the α phase in the heat affected zone as well as redeposited material. All these findings summarized propose nanoscale segregated regions consisting mainly of the zinc-rich oxide phase with either insignificant or a lower amount of Cu suggesting the existence of Zn-O and transitional Cu-Zn-O regions, respectively. Furthermore, the regions with an insignificant amount of oxygen suggest the existence of the intermetallic β phase.

3.4. Microstructural Characterization. The annular dark field STEM images (Figure 2) show a contrast in the modified area for both as-processed and etched samples. This suggests segregation of diverse regions and variation in the microstructure due to laser structuring. To investigate this, selected area electron diffraction (SAED) patterns were taken and indexed with the corresponding interplanar spacing (d-spacing) values.

Figure 4 displays the TEM micrographs of CuZn37 as-processed and its respective electron diffraction patterns. The first pattern was taken in the bulk area I (Figure 4a), which corresponds to the α-brass (220) diffraction spot and zone axis <101>. The respective SAED pattern is typical for a monocrystalline cubic structure.[62] This additionally indicates

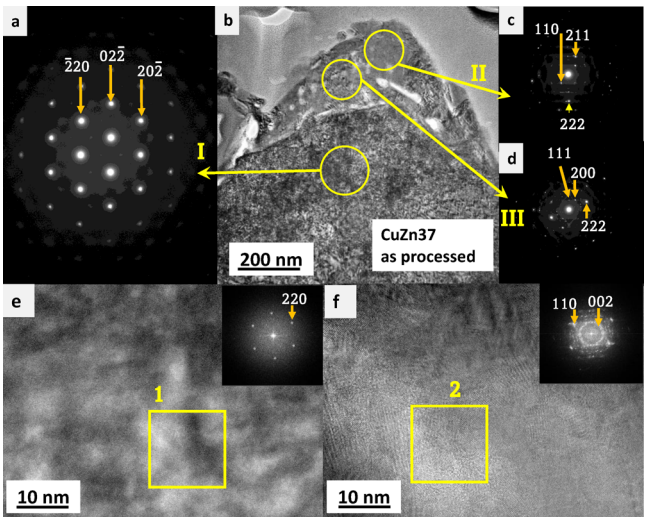

Figure 4. TEM-electron diffraction and images on CuZn37 as-processed. (a, c, d) SAED patterns taken from panel b. (e, f) HR-TEM images of the modified area with their respective binned FFT patterns of a selected area (yellow square).

that the measurement was carried out in a single grain implying a grain size of larger than 150 nm. However, the next patterns in the modified area (area II (c) and area III (d)) incorporate discrete spots revealing a polycrystalline structure,[63] which suggests grains with a smaller size. Here, area II represents β-brass (110), (211), and (222) diffraction spots, and area III represents the Cu_2O (111), (200), and (222) diffraction spots.

For a detailed understanding, higher resolution (HR) images were collected and evaluated with the Gatan software to acquire the patterns and respective d-spacing values. Figure 4e shows the result of the bulk region with diffraction spot correspondent to α-brass. An additional measurement is carried out in the visually lighter region of the modified surface (see Figure 4f), and the resulting appearance of the pattern indicates the presence of a polycrystalline structure. This pattern can be assigned to the ZnO (002) and (110) diffraction spots. Next, CuZn37 etched is taken under observation and similar results are obtained. The respective SAED patterns (see Figure S2) alongside a detailed discussion are presented in the Supporting Information. Overall, the position of α-brass in the bulk and β-brass on the surface correlates with the depth of modified areas observed with STEM-EDS analysis for both samples. The HR-TEM micrographs and their respective FFT patterns show mono- and polycrystalline structures for brass phases suggesting an inhomogeneous grain size distribution. Moreover, the presence of Cu_2O and ZnO is identified.

Similar results were achieved from all the above characterization methods. Besides the topographical surface modification, USP-DLIP processing has a localized effect on the composition of the alloy itself and leads to the occurrence of the β phase of brass, as suggested by the APT and TEM analysis. Additionally, the formation of zinc and copper oxide phases is proposed.

3.5. Phase Analysis with Grazing Incidence X-Ray Diffraction (GI-XRD). GI-XRD analysis was performed to identify the phases present on the structured surface, and the results were simultaneously compared to the polished sample. Figure 5 illustrates X-ray diffractograms for all CuZn37 samples. The polished surface (black diffractogram) has

https://doi.org/10.1021/acsami.3c04801
ACS Appl. Mater. Interfaces XXXX, XXX, XXX−XXX

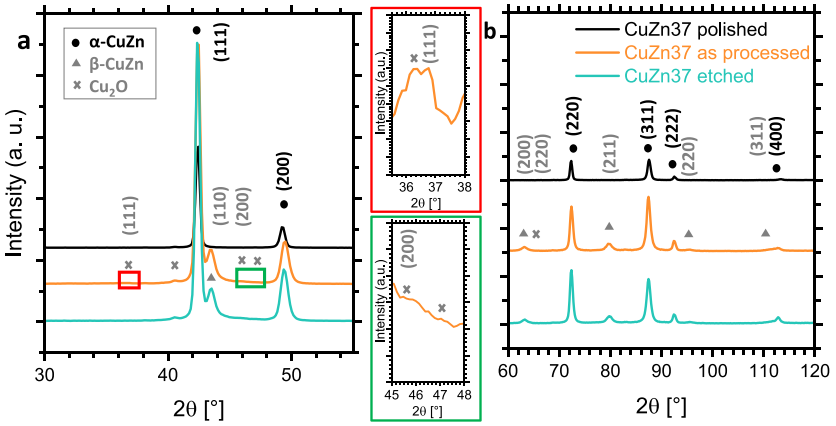

Figure 5. GI-XRD phase analyses of CuZn37 samples, i.e., polished (black), as-processed (orange), and etched (green). 2θ-range: (a) 30°−55°and (b) 60°−120°.

peaks at 42°, 49°, 72°, 87.4°, 92.4°, and 113°, which can be attributed to the α phase of brass with 63 wt.-% copper and 37 wt.-% zinc (ICDD: 04-003-2952). Simultaneously, additional peaks are observed for both CuZn37 structured samples, of which the peaks at 43.5°, 63°, 78.7°, 95.5°, and 111° can be assigned to the β phase of brass (LPF: 558003, ICDD: 04-006-6026). Furthermore, the peaks at 36.3° and 63° can be allocated to cuprous oxide (Cu_2O) (ICDD: 04-007-9767). It is to be noted that the position at 63° is an overlap of β-brass (200) at slightly lower and Cu_2O (220) at slightly higher 2θ values. The remaining additional peaks at 40.5°, 45.4°, and 47.1° are recorded for Cu_2O formed under especially high pressure (ICDD: 00-035-1091),[64] which are realized during ultrashort laser irradiation.[50] The results indicate a possible oxidation and validate the formation of an intermetallic phase during the laser process.

The formation of the intermetallic phase is entirely dependent on the bulk chemical composition. All the phases that can exist at various temperatures for any given chemical composition are shown in the Cu-Zn phase diagram in Figure S3. It shows that, above 30 ± 3 wt.-% of zinc, more than one phase can exist at various temperatures. At 37 wt.-% of zinc, the phase likely to form is the β phase in two modulations depending on the temperature. This is a result of, first, extreme temperatures achieved via high laser power applied for the process. Second, due to the ultrashort pulse duration, rapid cooling of the surface can be anticipated after the laser beam has interacted with the surface. As a result, the intermetallic β phase is formed, as confirmed by the GI-XRD diffractograms. At this stage, the complete identification and verification of the oxide phases present on the surface are still unresolved. The SEM micrographs suggest a successful removal of flake-like substructures via etching, but the XRD diffractograms show cuprous oxide peaks, which remain unaltered even after etching. This is further analyzed and verified in the following sections.

3.6. Identification of Oxide Phases on the Superficial Layer. To develop an understanding of the types of oxides, the results were complemented by Raman spectroscopy analysis. Figure 6 illustrates the Raman spectra of CuZn37 samples. Bands are observed at 61, 73, 83, 92, 147, 206, 473, 520, 572, and 643 cm^{-1} for CuZn37 as-processed (orange spectra). All the characteristic bands of ZnO are visible. However, a slight shift to lower values is noted for E_2^{low} (92 cm^{-1}) and LO (572 cm^{-1}) indicating an increase in the quantity of ZnO-defects.[65]

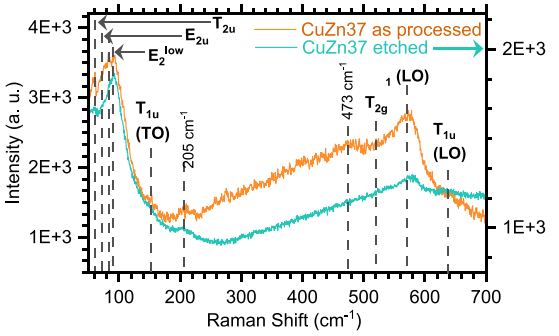

Figure 6. Raman spectra of CuZn37 as-processed (orange) represented by the left y-axis and etched (green, right y-axis).

The reason behind the existence of defects is perhaps the suppression of zinc oxide formation. Even though the oxidation of zinc is favored over copper, there is a potential concurrence between both due to the higher copper content. Besides that, the stress produced at higher temperatures and limited reaction time, in this case, can inhibit the full and thermodynamically stable formation of oxides.[66] Furthermore, a weak peak is observed at 473 cm^{-1}. A similar band in the range 450−500 cm^{-1} has been reported for a zinc-rich zone in an annealed brass sample with higher zinc content.[67] However, this literature does not provide an exact value or discussion on the existence of this band. Additionally in the same paper, this peak is not visible for brass samples with lower zinc content.[67] Since there is very broad band between 300 and 600 cm^{-1} with a tilted baseline, the weak characteristic bands of ZnO in this range are most probably suppressed. In addition to that, the silent and IR-active modes of Cu_2O as well as the T_{2g} band are detected at 516 cm^{-1}. These all results confirm the presence of ZnO and Cu_2O after the laser process. In total, the literature values of all the characteristic bands for the vibrational modes active in Raman as well as in IR and the silent modes for the oxides alongside the results of this paper are stated in Table S1 in the Supporting Information.

After etching the CuZn37 surface, the intensity of the band is reduced significantly, and the baseline appears to be flatter. Since the intensities of the bands are comparatively higher for the as-processed sample, CuZn37 etched is represented by the right y-axis. The reduced intensities can be attributed to the significant reduction of the intensive LO band of ZnO indicating a substantial loss of zinc oxide. Additionally, the

https://doi.org/10.1021/acsami.3c04801
ACS Appl. Mater. Interfaces XXXX, XXX, XXX−XXX

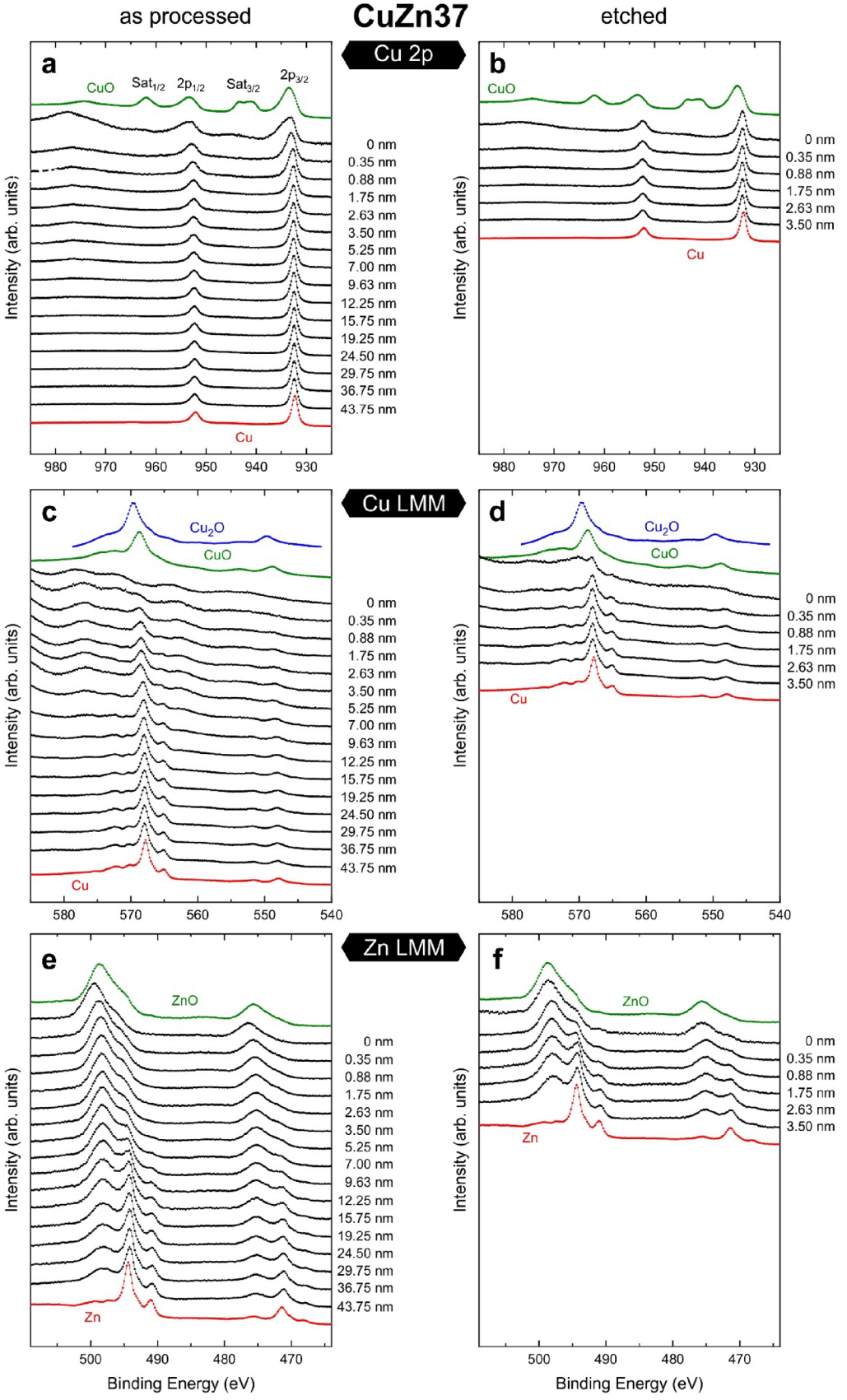

Figure 7. XPS results of CuZn37 with high-resolution spectra of (a, b) Cu 2p, (c, d) Cu LMM, and (e, f) Zn LMM of as-processed and etched samples.

https://doi.org/10.1021/acsami.3c04801
ACS Appl. Mater. Interfaces XXXX, XXX, XXX−XXX

band experiences a shift to a higher value suggesting a decline in ZnO-defects. Moreover, the band at 473 cm^{-1} is no longer visible. All the Cu_2O bands can still be observed, but now at lower Raman shifts. The reduction in intensities of the ZnO and Cu_2O bands for the etched sample suggests a lower oxide amount on the surface in comparison to the as-processed.

The results of Raman spectroscopy validate formation of cuprous and zinc oxide on the brass surface via laser processing. However, after etching the sample, partial removal of zinc oxide is observed.

3.7. Identification of Oxide Phases at Surface and Subsurface Layer. This section is concerned with the investigation of the subsurface distribution of oxides via XPS analyses combined with surface ablation by Ar^+-ion etching. The XPS-based elemental depth profiles suggest an increase in the zinc and oxygen concentrations on the laser structured surface. This validates the formation of zinc oxide by laser processing, which complements the results until now. A detailed discussion alongside the depth profiles is present in Figure S4 in the Supporting Information.

Besides C (as resulting from adsorbates), the XPS survey spectra indicate only the presence of Cu, Zn, and O. Therefore, XPS detailed spectra were recorded for O 1s, Cu 2p, Zn 2p, Cu LMM, and Zn LMM to reveal the elemental composition of the samples as well as the oxidation state of Cu and Zn. To distinguish Cu, Cu_2O, and CuO, both the Cu $2p_{3/2}$ spectra and the Cu LMM spectra are needed. In the Cu 2p spectra, CuO can be distinguished from Cu and Cu_2O via the chemical shift to higher binding energies as well as via the characteristic satellite at higher binding energy.[68−72] In the Cu LMM spectra, Cu can be distinguished from Cu_2O and CuO mainly via the low binding energy (=high kinetic energy) tail of the $L_3M_{45}M_{45}$ Auger peak. For ZnO and Zn, the Zn-$2p_{3/2}$ spectra display no difference. However, the Zn-LMM Auger peaks display distinct differences in the peak shape as well as in the peak position.[68,73,74]

The Cu $2p_{3/2}$ spectra of CuZn37 as-processed together with the reference CuO and Cu are plotted in Figure 7a. For the as-provided sample, i.e., before Ar^+-ion etching (0 nm ablation), the spectrum displays a superposition of Cu/Cu_2O and CuO (with the latter being identified via the weak satellite at about 940−945 eV). After ablation of approx. 0.35 nm, the CuO-related features, i.e., the satellite as well as the high binding energy shoulder of the $2p_{3/2}$ peak, disappear. This implies that the presence of CuO only applies to the uppermost surface layer. To reveal the distribution of Cu_2O, Figure 7c shows the Cu LMM Auger spectra in comparison with the spectra for Cu and CuO as probed on reference samples. The spectrum for Cu_2O is taken from Figure 5 in ref 70. With increasing ablation, the Cu LMM spectra in Figure 7c display a systematic decrease of Cu_2O (as seen by the increasing intensity of the Cu^0 characteristic $L_3M_{45}M_{45}$ Auger peak at about 565 eV). At this stage, it is not possible to give a distinct value for the subsurface range with Cu_2O contributions. However, when compared with the Cu LMM spectrum of the Cu reference sample in Figure 7c, the Cu LMM spectra at 9.63 or 12.25 nm are very similar to the Cu reference spectrum. Therefore, the "thickness" of the Cu2O layer can be approximated smaller than 10 nm, whereas CuO (according to the XPS results from Figure 7a) is mostly distributed on the uppermost layer of the surface.

The Zn LMM spectra (including the spectra from ZnO and Zn reference samples) are represented in Figure 7e. In contrast to CuO and Cu_2O, the presence of ZnO is not a surface or near subsurface related issue. In the whole range of ablation, i.e., up to approx. 44 nm into the bulk, the Zn LMM spectra display a superposition of the Zn and ZnO reference data. At the surface and in the topmost layers, the spectra indicate that the amount of ZnO is much larger than the amount of Zn. However, with each step of ablation, the ZnO:Zn ratio decreases, and the presence of Zn starts to dominate at depths between approx. 15 and 20 nm. Figure 7a,c,e gives clear evidence that Zn acts as an oxygen scavenger. This is also supported by the O 1s spectra in Figure S5 in the Supporting Information. With increasing depth, the O 1s intensity (with the binding energy matching with the O 1s binding energy for ZnO) decreases in the same way as the intensity of the ZnO-related contribution of the Zn LMM spectra.

After etching, the Cu 2p spectra in Figure 7b display no significant contributions of CuO. Even for zero ablation, the Cu 2p spectrum displays only marginal contribution of the CuO related satellite, i.e., even at the surface, there is nearly no CuO. Concerning the presence of Cu_2O, the Cu LMM spectrum at 0 nm (Figure 7d) shows a superposition of Cu and Cu_2O. Soon after ablation, i.e., approx. at 0.35 nm, a significant change in the intensity ratio is observed indicating the presence of mainly pure copper.

The Zn LMM spectra in Figure 7f show that, even after etching, there are still contributions of ZnO at the surface as well as in the subsurface range. However, compared to the as-processed CuZn37 sample in Figure 7c, the relative amount of ZnO is strongly decreased. In addition, there is a stronger decrease of ZnO with increasing depth (for example, the Zn LMM spectrum of CuZn37 etched at about 3.50 nm ablation in Figure 7f is comparable to the Zn LMM spectrum of CuZn37 as-processed at about 19.25 nm ablation in Figure 7e). Therefore, etching the CuZn37 sample reduced the thickness of the (mainly) ZnO layer by approx. half an order of magnitude.

Overall, the STEM-EDS, Raman, and XPS results are in good agreement. This is indicated by the presence of cupric, cuprous, and zinc oxide on the surface after structuring with USP-DLIP. All the results indicate a higher amount of zinc oxide than other oxides. The weak intensities of CuO peaks in XPS spectra indicate an occurrence in a remarkably lower quantity. Literature[67,75] reports that cuprous oxide formation is favored at higher/increasing temperatures because of the predominant lattice diffusion whereas cupric oxide is a result of grain diffusion at relatively lower temperatures. Thus, the Cu_2O formation can be deeper into the surface, and CuO is largely on the outer surface. The etching results suggest a partial removal of zinc oxide and full removal of CuO. On the other hand, it is evident that the Cu_2O formed is stable and is not altered via etching.

3.8. Spatial Distribution of Metal and Oxide Phases. Scanning tunneling microscopy and spectroscopy (STM and STS) measurements were used on all sample surfaces to investigate the spatial distribution of the metal and oxide phases. The STM result in the Supporting Information, Figure S6, exhibits a variation of the profile both perpendicular and parallel to the line-like structures, confirming the periodicity as well as the nanoroughness along the valleys, which is consistent with the CLSM results. Furthermore, STS is conducted on the peaks and valleys of the samples to investigate the local density of electron states (LDOS) as a function of electron energy, which, in this case, is the voltage applied between the sample

https://doi.org/10.1021/acsami.3c04801
ACS Appl. Mater. Interfaces XXXX, XXX, XXX−XXX

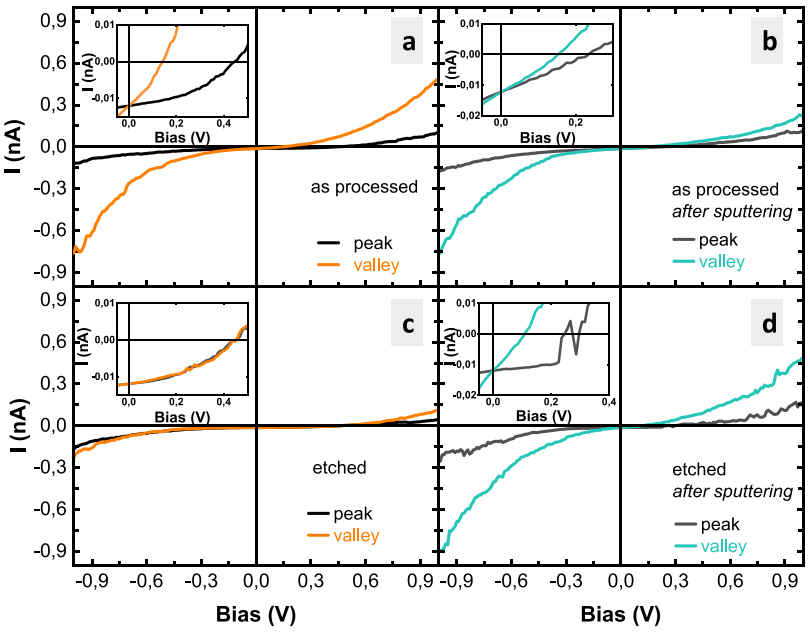

Figure 8. CuZn37 (a) as-processed and (c) etched before argon sputtering as well as (b) as-processed and (d) etched after argon sputtering.

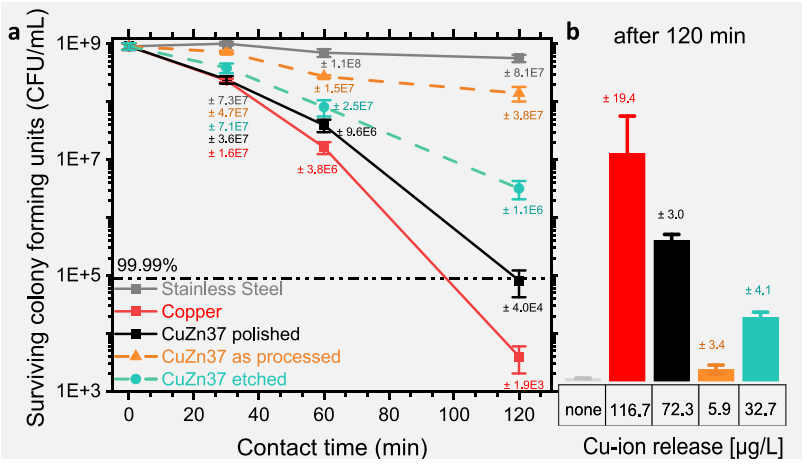

Figure 9. (a) Surviving colony-forming units as results of contact killing experiment with *E. coli* for 30, 60, and 120 min on the CuZn37 surface. (b) The respective Cu-ion release values after 120 min of exposure time in the form of a bar chart.

and tip. LDOS, hereby, is material-dependent and thus directly influences the slope of the $I(V)$ curve. The $I(V)$ curve is divided into two regimes, i.e., the ohmic regime (−0.2 to +0.2 V) with a linear behavior in dependence to the conductivity and the Fowler-Nordheim regime ($-0.2 < V > +0.2$) with an exponential-like behavior where the slope depends on the work function of the material.[22]

The $I(V)$ curves (averaged over several hundred measurements at various positions) of the peak and valley for both samples are displayed in Figure 8. The curve of CuZn37 as-processed in Figure 8a shows a significantly lower conductivity at the peak with a nearly flat behavior at voltages between $-0.5 < V < 0.5$ indicating the presence of a semiconductor phase. This is attributed to a much lower presence of oxide phases with a semiconducting behavior. Here, the larger band gaps (E_g) and work functions (Φ) of zinc oxide (E_g: 3.37 eV, Φ: 4.7−5.1 eV)[76,77] and copper oxides (E_g: 1.2−2.2 eV, Φ: 5.0−5.5 eV)[22] are responsible for the lower conductivity. At the same time, the valley exhibits an increased conductivity suggesting an enhanced contribution by a conductive metallic phase. This is attributed to the presence of copper and zinc phases with lower work functions (Φ(Cu): 4.5 eV, Φ(Zn): 3.6 eV).[22,76,77]

Additionally, argon ion etching was applied for both surfaces to examine the spatial distribution in the subsurface range. After sputtering (see Figure 8b), the peak and valley exhibit similar conductivity suggesting a higher concentration of conductive metallic phase alongside the semiconductor oxide phases in relatively lower quantity.

The etched CuZn37 exhibits identical conductivity behavior for the peak and valley indicating the presence of a semiconductor phase. However, after argon sputtering, the subsurface level shows an increase in conductivity on the valley confirming the reduction of the oxide phase. Overall, the results reveal the presence of a semiconductor oxide phase on the peaks, which is significantly deeper into the surface, whereas the valleys indicate the coexistence of metallic and oxide phases on the uppermost surface as well as the subsurface level for as-processed and etched samples, which is in agreement with the preceding results.

https://doi.org/10.1021/acsami.3c04801
ACS Appl. Mater. Interfaces XXXX, XXX, XXX−XXX

3.9. Antibacterial Tests. Contact killing tests were carried out on CuZn37 including USP-DLIP processed surfaces at a pattern periodicity of 3 μm in as-processed and etched surface state. Additionally, mirror-polished Cu and stainless steel were used as topographically smooth and inert reference surfaces. The results were evaluated taking into account the changed contact area due to surface modification and thereby also the altered wettability. On one hand, the patterned surfaces have a 2.3-fold increase in surface area. On the other hand, the wettability changes significantly within the first week after laser structuring, finally stabilizing after 3 weeks of aging. The wetting behavior changes from hydrophilic in the first week to hydrophobic after at least 3 weeks of aging.[22] As a result, when the droplet with the bacterial suspension was placed on the structured sample, it occupied only ∼33% of the PVC-ring area. However, on the etched surface, the wettability is slightly increased, and the droplet covered up to ∼47% of the ring area. Considering all these factors, the surviving CFU/mL over a contact period of 120 min is plotted in Figure 9a. In the same Figure, the respective Cu-ion releases for 120 min are charted as bars.

Predictably,[3] the stainless steel (gray graph) shows nearly no reduction in the CFU-value over the 120 min exposure. Simultaneously, a quick reduction in surviving CFU-value is noted for pure copper (red graph). Proceeding with CuZn37 polished (black graph in Figure 9), a fast reduction in CFU-value for the same exposure time but rather slower than that of pure copper is recorded. This is an expected result due to the lower concentration of copper,[4,78] which is confirmed by the attenuated Cu-ion release (Figure 9b). In the as-processed state (orange graph Figure 9), a considerably reduced killing and corresponding copper-ion release rate are observed, which denotes an inadequate antibacterial activity, despite the increased and improved contact area. This is attributed to chemical alteration of the surface via laser treatment resulting in depleted copper content and, therefore, zinc-rich phases/regions. While zinc does have a cytotoxic effect on bacterial cells, it is much less pronounced compared to copper. Furthermore, the presence of zinc oxide in these conditions is very stable chemically, making the release of Zn-ions improbable.

After etching, the surface exhibits an improved efficiency (see green graph Figure 9) with an increased Cu-ion release. This is ascribed to the partial removal of zinc-rich oxide phases resulting in exposure of certain copper-rich metallic or the more stable cuprous oxide phases that are susceptible to corrosion. However, it is not quite sufficient to even reach the level of the polished CuZn37 surface. The comparison between the antibacterial activities of as-processed and etched samples indicate that the higher amount of zinc oxide leads to higher corrosion resistance in wet conditions containing bacteria.

4. CONCLUSIONS

The present study investigates the nanoscale surface modification of brass by means of USP-DLIP and sheds light on the mechanisms involved in the alteration of the antibacterial properties. At first, USP-DLIP was employed to create the 3 μm line-like structures. GI-XRD, STEM-EDS, APT, and STM/STS analyses reveal topographical as well as chemical variation as a result of the laser process, which infuses a few hundred nm of depth. The results confirm the presence of zinc-rich zones and formation of an additional intermetallic β phase on the uppermost surface. Another interesting result observed is the formation of oxides via USP laser processing. The Raman and XPS results confirmed the presence of zinc oxide in abundance, followed by cuprous oxide and cupric oxide in a comparatively low concentration. Additionally, formation of transitional Cu-Zn-O regions is detected. The formation of the metastable phases is most presumably a consequence of the Kirkendall effect in combination with the rapid cooling of the melted and redeposited matter, as it hinders the formation of stable phases. After etching the laser-processed samples with citric acid, a partial removal of zinc oxide and a full removal of CuO are observed, whereas Cu_2O and β phase show no significant alteration.

The results of antibacterial efficiency against *E. coli* revealed a significant decrease in the killing rate on the laser-treated surfaces in comparison to that on the polished surface. This is first attributed to the reduced release of copper concentration on the modified surface. Second, it is due to a higher corrosion resistance of zinc-rich oxide phases in wet conditions. This property as well as the significantly reduced wettability can be very advantageous in the application of laser-structured brass underwater conditions to minimize the material damage, e.g., that occurs as a consequence of biofouling. However, this needs to be further investigated in future studies to acquire a full understanding of the corrosion resistance of the structured brass under wet conditions.

To summarize, it is essential to recognize that, while the ultrashort pulsed laser was utilized for the surface modification and the HAZ was at the nanoscale, it should not be neglected. The magnitude of chemical alteration profoundly depends on the chemical composition and phase diagram of the specimen. Furthermore, it is evident that an enhanced antibacterial through contact killing can be achieved with a well-defined topography in combination with a right surface chemistry. In future studies, brass samples with a bulk chemical composition lower than 30 wt.-% can be utilized to investigate the effect of zinc concentration on the formation of oxide and intermetallic phases and hence the resulting influence on antibacterial properties. Other important factors need to be investigated, i.e., surface contaminations and wettability to further gain a comprehensive understanding of the bacteria-substrate interaction.

■ ASSOCIATED CONTENT

Supporting Information

The Supporting Information is available free of charge at https://pubs.acs.org/doi/10.1021/acsami.3c04801.

TEM-electron diffraction images of CuZn37 etched (figure and description); Cu-Zn Phase diagram; Raman bands of CuZn37 samples (table); XPS-based elemental depth profiling (figure and description), XPS-spectra of CuZn37 in O 1s region (figure and description); and results of STM exhibiting the topography (figure) (PDF)

■ AUTHOR INFORMATION

Corresponding Author

Aisha Saddiqa Ahmed − *Chair of Functional Materials, Department of Material Science and Engineering, Saarland University, Saarbrücken 66123, Germany; Université de Lorraine, CNRS, IJL, Nancy F-54000, France;* orcid.org/

https://doi.org/10.1021/acsami.3c04801
ACS Appl. Mater. Interfaces XXXX, XXX, XXX−XXX

0000-0002-5908-2421; Email: aisha.ahmed@uni-saarland.de

Authors

Daniel Wyn Müller − *Chair of Functional Materials, Department of Material Science and Engineering, Saarland University, Saarbrücken 66123, Germany*
Stephanie Bruyere − *Université de Lorraine, CNRS, IJL, Nancy F-54000, France*
Anne Holtsch − *Experimental Physics and Center for Biophysics, Saarland University, Saarbrücken 66123, Germany*
Frank Müller − *Experimental Physics and Center for Biophysics, Saarland University, Saarbrücken 66123, Germany;* orcid.org/0000-0001-8955-5317
Jenifer Barrirero − *Chair of Functional Materials, Department of Material Science and Engineering, Saarland University, Saarbrücken 66123, Germany*
Kristina Brix − *Department of Inorganic Solid-State Chemistry, Elemental Analysis, Saarland University, Saarbrücken 66123, Germany*
Sylvie Migot − *Université de Lorraine, CNRS, IJL, Nancy F-54000, France*
Ralf Kautenburger − *Department of Inorganic Solid-State Chemistry, Elemental Analysis, Saarland University, Saarbrücken 66123, Germany*
Karin Jacobs − *Experimental Physics and Center for Biophysics, Saarland University, Saarbrücken 66123, Germany*
Jean-François Pierson − *Université de Lorraine, CNRS, IJL, Nancy F-54000, France;* orcid.org/0000-0001-8790-3162
Frank Mücklich − *Chair of Functional Materials, Department of Material Science and Engineering, Saarland University, Saarbrücken 66123, Germany*

Complete contact information is available at: https://pubs.acs.org/10.1021/acsami.3c04801

Author Contributions

A.S.A.: conceptualization, investigation, validation, visualization, writing—original draft; D. W.M.: investigation, validation, writing—review and editing; S.B.: investigation, validation, writing—review; A.H.: investigation, validation, writing—review; F.M.: investigation, validation, writing—review and editing; J.B.: investigation, validation, writing—review and editing; K.B.: investigation, validation, writing—review; S.M.: investigation; R.K.: supervision; K.J.: supervision; J.-F.P.: investigation, validation, writing—review and editing, resources, supervision; F.M.: funding acquisition, resources, supervision.

Funding

A.A. has been funded by the German Aerospace Center—Space Administration (DLR) within the project "Investigation of antimicrobial metal surfaces under space conditions—An effective strategy to prevent microbial biofilm formation" (project number 50WB1930). D.M. has been funded by the German Research Foundation (DFG) within the project "Controlled bacterial interaction to increase the antimicrobial efficiency of copper surfaces" (project number 415956642). K.J. and A.H. acknowledge support from the German Research Foundation (DFG) via the Collaborative Research Center SFB 1027.

Notes

The authors declare no competing financial interest.

■ ACKNOWLEDGMENTS

The Author would like to thank to the group of Prof. Rolf Müller from the Helmholtz Centre of Infection Research in Saarbrücken for providing *E. coli*.

■ ABBREVIATIONS

APT, atom probe tomography
CuZn37, brass with 37% zinc content
CLSM, confocal laser scanning microscopy
CFU, colony-forming units
Da, Dalton or unified atomic mass unit
E. coli, *Escherichia coli*
FFT, fast Fourier transform image
FWHM, full width at half maximum
GI-XRD, grazing incidence X-ray diffraction
HAZ, heat affected zone
HV, Vickers hardness
IR, infrared
LDOS, local density of electron states
PBS, phosphate-buffered saline
PVC, polyvinyl chloride
SAED, selected area electron diffraction
SEM, scanning electron microscopy
STEM-EDS, scanning transmission electron microscopy along with energy-dispersive X-ray spectroscopy
STM and STS, scanning tunnel microscopy and spectroscopy
TEM, transmission electron microscopy
USP-DLIP, ultrashort pulsed direct laser interference patterning
XPS, X-ray photoelectron spectroscopy

■ REFERENCES

(1) Davies, J. Origins and Evolution of Antibiotic Resistance. *Microbiol. Mol. Biol. Rev.* **2010**, 9−16.
(2) Hasan, J.; Crawford, R. J.; Ivanova, E. P. Antibacterial Surfaces: The Quest for a New Generation of Biomaterials. *Trends Biotechnol.* **2013**, *31*, 295−304.
(3) Müller, D. W.; Lößlein, S.; Terriac, E.; Brix, K.; Siems, K.; Moeller, R.; Kautenburger, R.; Mücklich, F. Increasing Antibacterial Efficiency of Cu Surfaces by Targeted Surface Functionalization via Ultrashort Pulsed Direct Laser Interference Patterning. *Adv. Mater. Interfaces* **2021**, *8*, 2001656.
(4) Luo, J.; Ahmed, A.; Pierson, J. F.; Mücklich, F. Tailor the Antibacterial Efficiency of Copper Alloys by Oxidation: When to and When Not To. *J. Mater. Sci.* **2022**, *57*, 3807−3821.
(5) Rößler, F.; Lang, V.; Günther, D.; Lasagni, A. F. Fabricating Three-Dimensional Periodic Micro Patterns on Photo-Resists Using Laser Interference Lithography. *Adv. Eng. Mater.* **2017**, *19* (), DOI: 10.1002/adem.201600855.
(6) Quirk, T. Insect Wings Shred Bacteria to Pieces. *Nature* **2013**, DOI: 10.1038/nature.2013.12533.
(7) Luís, Â.; Domingues, F.; Ramos, A. Production of Hydrophobic Zein-Based Films Bioinspired by the Lotus Leaf Surface: Characterization and Bioactive Properties. *Microorganisms* **2019**, *7* (), DOI: 10.3390/microorganisms7080267.
(8) Borda D'Água, R.; Branquinho, R.; Duarte, M. P.; Maurício, E.; Fernando, A. L.; Martins, R.; Fortunato, E. Efficient Coverage of ZnO Nanoparticles on Cotton Fibres for Antibacterial Finishing Using a Rapid and Low Cost: In Situ Synthesis. *New J. Chem.* **2018**, *42*, 1052−1060.

(9) Raffi, M.; Mehrwan, S.; Bhatti, T. M.; Akhter, J. I.; Hameed, A.; Yawar, W.; Ul Hasan, M. M. Investigations into the Antibacterial Behavior of Copper Nanoparticles against Escherichia Coli. *Ann. Microbiol* **2010**, *60*, 75−80.
(10) Lasagni, A. F.; Gachot, C.; Trinh, K. E.; Hans, M.; Rosenkranz, A.; Roch, T.; Eckhardt, S.; Kunze, T.; Bieda, M.; Günther, D.; Lang, V.; Mücklich, F. Direct Laser Interference Patterning, 20 Years of Development: From the Basics to Industrial Applications. In *Laser-based Micro- and Nanoprocessing XI*; SPIE, 2017; Vol. *10092*, p 1009211. DOI: 10.1117/12.2252595.
(11) Momma, C.; Nolte, S.; Chichkov, B. N.; Alvensleben, F. V.; Tunnermann, A. T. Precise Laser Ablation with Ultrashort Pulses. *Appl. Surf. Sci.* **1997**, *109*.
(12) Korte, F.; Serbin, J.; Koch, J.; Egbert, A.; Fallnich, C.; Ostendorf, A.; Chichkov, B. N. Towards Nanostructuring with Femtosecond Laser Pulses. *Appl. Phys. A: Mater. Sci. Process.* **2003**, *77*, 229−235.
(13) Nolte, S.; Momma, C.; Jacobs, H.; Tünnermann, A.; Chichkov, B. N.; Wellegehausen, B.; Welling, H. Ablation of Metals by Ultrashort Laser Pulses. *Journal of the Optical Society of America B* **1997**, *14*, 2716.
(14) Sonntag, S.; Roth, J.; Gaehler, F.; Trebin, H. R. Femtosecond Laser Ablation of Aluminium. *Appl. Surf. Sci.* **2009**, *255*, 9742−9744.
(15) Stark, T.; Alamri, S.; Aguilar-Morales, A. I.; Kiedrowski, T.; Lasagni, A. F. Positive Effect of Laser Structured Surfaces on Tribological Performance. *J. Laser Micro Nanoeng.* **2019**, *14*, 13−18.
(16) Rosenkranz, A.; Hans, M.; Gachot, C.; Thome, A.; Bonk, S.; Mücklich, F. Direct Laser Interference Patterning: Tailoring of Contact Area for Frictional and Antibacterial Properties. *Lubricants* **2016**, *4* (), DOI: 10.3390/lubricants4010002.
(17) Roch, T.; Benke, D.; Milles, S.; Roch, A.; Kunze, T.; Lasagni, A. Dependence between Friction of Laser Interference Patterned Carbon and the Thin Film Morphology. *Diamond Relat. Mater.* **2015**, *55*, 16−21.
(18) Heilmann, S.; Zwahr, C.; Knape, A.; Zschetzsche, J.; Lasagni, A. F.; Füssel, U. Improvement of the Electrical Conductivity between Electrode and Sheet in Spot Welding Process by Direct Laser Interference Patterning. *Adv. Eng. Mater.* **2018**, *20* (), DOI: 10.1002/adem.201700755.
(19) Lutey, A. H. A.; Gemini, L.; Romoli, L.; Lazzini, G.; Fuso, F.; Faucon, M.; Kling, R. Towards Laser-Textured Antibacterial Surfaces. *Sci. Rep.* **2018**, *8*, 1.
(20) Aguilar-Morales, A. I.; Alamri, S.; Voisiat, B.; Kunze, T.; Lasagni, A. F. The Role of the Surface Nano-Roughness on the Wettability Performance of Microstructured Metallic Surface Using Direct Laser Interference Patterning. *Materials* **2019**, *12* (), DOI: 10.3390/ma12172737.
(21) Fu, Y.; Soldera, M.; Wang, W.; Milles, S.; Deng, K.; Voisiat, B.; Nielsch, K.; Lasagni, A. F. Wettability Control of Polymeric Microstructures Replicated from Laser-Patterned Stamps. *Sci. Rep.* **2020**, *10* (), DOI: 10.1038/s41598-020-79936-1.
(22) Müller, D. W.; Holtsch, A.; Lößlein, S.; Pauly, C.; Spengler, C.; Grandthyll, S.; Jacobs, K.; Mücklich, F.; Müller, F. In-Depth Investigation of Copper Surface Chemistry Modification by Ultrashort Pulsed Direct Laser Interference Patterning. *Langmuir* **2020**, *36*, 13415−13425.
(23) Raillard, B.; Gouton, L.; Ramos-Moore, E.; Grandthyll, S.; Müller, F.; Mücklich, F. Ablation Effects of Femtosecond Laser Functionalization on Steel Surfaces. *Surf Coat Technol* **2012**, *207*, 102−109.
(24) Zhang, W.; Cheng, G.; Feng, Q.; Cao, L. Femtosecond Laser Machining Characteristics in a Single-Crystal Superalloy. *Rare Met.* **2011**, *30*, 639−642.
(25) Lang, V.; Roch, T.; Lasagni, A. F. High-Speed Surface Structuring of Polycarbonate Using Direct Laser Interference Patterning: Toward 1 M2 Min−1 Fabrication Speed Barrier. *Adv. Eng. Mater.* **2016**, *18*, 1342−1348.
(26) Prudent, M.; Iabbaden, D.; Bourquard, F.; Reynaud, S.; Lefkir, Y.; Borroto, A.; Pierson, J. F.; Garrelie, F.; Colombier, J. P. High-Density Nanowells Formation in Ultrafast Laser-Irradiated Thin Film Metallic Glass. *Nanomicro Lett.* **2022**, *14*, 1−15.
(27) Luo, J.; Hein, C.; Mücklich, F.; Solioz, M. Killing of Bacteria by Copper, Cadmium, and Silver Surfaces Reveals Relevant Physicochemical Parameters. *Biointerphases* **2017**, *12*, No. 020301.
(28) Hans, M.; Támara, J. C.; Mathews, S.; Bax, B.; Hegetschweiler, A.; Kautenburger, R.; Solioz, M.; Mücklich, F. Laser Cladding of Stainless Steel with a Copper-Silver Alloy to Generate Surfaces of High Antimicrobial Activity. *Appl. Surf. Sci.* **2014**, *320*, 195−199.
(29) Bieda, M.; Siebold, M.; Lasagni, A. F. Fabrication of Sub-Micron Surface Structures on Copper, Stainless Steel and Titanium Using Picosecond Laser Interference Patterning. *Appl. Surf. Sci.* **2016**, *387*, 175−182.
(30) Matias, M. L.; Nunes, D.; Pimentel, A.; Ferreira, S. H.; Borda D'Agua, R.; Duarte, M. P.; Fortunato, E.; Martins, R. Paper-Based Nanoplatforms for Multifunctional Applications. *J. Nanomater.* **2019**, *2019*, 1.
(31) Vincent, M.; Duval, R. E.; Hartemann, P.; Engels-Deutsch, M. Contact Killing and Antimicrobial Properties of Copper. *J Appl Microbiol* **2018**, *124*, 1032−1046.
(32) Grass, G.; Rensing, C.; Solioz, M. Metallic Copper as an Antimicrobial Surface. *Appl. Environ. Microbiol.* **2011**, *77*, 1541−1547.
(33) Meister, T. L.; Fortmann, J.; Breisch, M.; Sengstock, C.; Steinmann, E.; Köller, M.; Pfaender, S.; Ludwig, A. Nanoscale Copper and Silver Thin Film Systems Display Differences in Antiviral and Antibacterial Properties. *Sci. Rep.* **2022**, *12*, 1−10.
(34) Luo, J.; Hein, C.; Pierson, J. F.; Mücklich, F. Sodium Chloride Assists Copper Release, Enhances Antibacterial Efficiency, and Introduces Atmospheric Corrosion on Copper Surface. *Surfaces and Interfaces* **2020**, *20*, No. 100630.
(35) Nijhout, H. F. Elements of Butterfly Wing Patterns. *J. Exp. Zool.* **2001**, *291*, 213−225.
(36) Wilson, S. J.; Hutley, M. C. The Optical Properties of 'Moth Eye' Antireflection Surfaces. *Opt Acta* **1982**, *29*, 993−1009.
(37) Selvaraj, S.; Ponmariappan, S.; Natesan, M.; Palaniswamy, N. Dezincification of Brass and Its Controlan Overview. *Corros. Rev.* **2003**, *21*, 41−74.
(38) Müller, D. W.; Fox, T.; Grützmacher, P. G.; Suarez, S.; Mücklich, F. Applying Ultrashort Pulsed Direct Laser Interference Patterning for Functional Surfaces. *Sci. Rep.* **2020**, *10* (), DOI: 10.1038/s41598-020-60592-4.
(39) Malag, A. Simple Interference Method of Diffraction Grating Generation for Integrated Optics by the Use of a Fresnel Mirror. *Opt Commun* **1980**, *32*, 54−58.
(40) Wang, X. Y.; Riffe, D. M.; Lee, Y. S.; Downer, M. C. Time-Resolved Electron-Temperature Measurement in a Highly Excited Gold Target Using Femtosecond Thermionic Emission. *Phys. Rev. B* **1994**, *50*, 8016−8019.
(41) Kirkwood, S. E.; Tsui, Y. Y.; Fedosejevs, R.; Brantov, A. V.; Bychenkov, V. Y. Experimental and Theoretical Study of Absorption of Femtosecond Laser Pulses in Interaction with Solid Copper Targets. *Phys. Rev B Condens. Matter. Mater. Phys.* **2009**, *79* (), DOI: 10.1103/PhysRevB.79.144120.
(42) Hirayama, Y.; Obara, M. Heat-Affected Zone and Ablation Rate of Copper Ablated with Femtosecond Laser. *J. Appl. Phys.* **2005**, *97*, No. 064903.
(43) Anisimov, S. I.; Kapeliovich, B. L.; Perel'man, T. L. Electron Emission from the Metal Surfaces Induced by Ultrashort Lasers Pulses. *Zhurnal Ehksperimental'noj i Teoreticheskoj Fiziki* **1974**, *66* ().
(44) Chichkov, B. N.; Momma, C.; Nolte, S.; Von Alvensleben, F.; Tünnermann, A. Femtosecond, Picosecond and Nanosecond Laser Ablation of Solids. *Appl. Phys. A: Mater. Sci. Process.* **1996**, *63*, 109−115.
(45) Abdelmalek, A.; Bedrane, Z.; Amara, E.-H. Thermal and Non-Thermal Explosion in Metals Ablation by Femtosecond Laser Pulse: Classical Approach of the Two Temperature Model. *J Phys Conf Ser* **2018**, *987*, No. 012012.

https://doi.org/10.1021/acsami.3c04801
ACS Appl. Mater. Interfaces XXXX, XXX, XXX−XXX

(46) Thompson, K.; Lawrence, D.; Larson, D. J.; Olson, J. D.; Kelly, T. F.; Gorman, B. In Situ Site-Specific Specimen Preparation for Atom Probe Tomography. *Ultramicroscopy* **2007**, *107*, 131−139.
(47) Sanders, E. R. Aseptic Laboratory Techniques: Plating Methods. *J. Visualized Exp.* **2012**, *63*, 1−18.
(48) Fairand, B. P.; Clauer, A. H.; Jung, R. G.; Wilcox, B. A. Quantitative Assessment of Laser-Induced Stress Waves Generated at Confined Surfaces. *Appl. Phys. Lett.* **1974**, *25*, 431−433.
(49) Masse, J. E.; Barreau, G. Laser Generation of Stress Waves in Metal. *Surf Coat Technol* **1995**, *70*, 231−234.
(50) Zhigilei, L.; Garrison, B. J. Microscopic Mechanisms of Laser Ablation of Organic Solids in the Thermal and Stress Confinement Irradiation Regimes. *J. Appl. Phys.* **2000**, *88*, 1281−1298.
(51) Ionin, A. A.; Kudryashov, S. I.; Makarov, S. V.; Levchenko, A. O.; Rudenko, A. A.; Saraeva, I. N.; Zayarny, D. A.; Nathala, C. R.; Husinsky, W. Nanoscale Surface Boiling in Sub-Threshold Damage and above-Threshold Spallation of Bulk Aluminum and Gold by Single Femtosecond Laser Pulses. *Laser Phys. Lett.* **2016**, *13* (). DOI: 10.1088/1612-2011/13/2/025603.
(52) Zuhlke, C. A.; Anderson, T. P.; Alexander, D. R. Formation of Multiscale Surface Structures on Nickel via above Surface Growth and below Surface Growth Mechanisms Using Femtosecond Laser Pulses. *Opt. Express* **2013**, *21*, 8460.
(53) Leitz, K. H.; Redlingshöer, B.; Reg, Y.; Otto, A.; Schmidt, M. Metal Ablation with Short and Ultrashort Laser Pulses. *Phys. Procedia* **2011**, *12*, 230−238.
(54) Müller, D. W.; Lößlein, S.; Pauly, C.; Briesenick, M.; Kickelbick, G.; Mücklich, F. Multi-Pulse Agglomeration Effects on Ultrashort Pulsed Direct Laser Interference Patterning of Cu. *Appl. Surf. Sci.* **2023**, *611*, No. 155538.
(55) Kirkendall, E. O. Diffusion of Zinc in Alpha Brass. *Trans. Am. Inst. Min. Metall* **1942**, *147*, 104−110.
(56) Ataya, S.; El-Sayed Seleman, M. M. Microstructure Stability Of CuZn37 Brass. In *14th International Materials Symposium*; IMSP 2012.
(57) Kowalski, M.; Spencer, P. J. Thermodynamic Reevaluation of the Cu-Zn Syst m. *J. Phase Equilib.* **1993**, *14*, 432−438.
(58) Hasegawa, M. Ellingham Diagram. *Treatise Process Metall.* **2014**, *1*, 507−516.
(59) Lopes, A.; Brodlie, K. Interactive Approaches to Contouring and Isosurfacing for Geovisualization. *Exploring Geovisualization* **2005**, 345−361.
(60) Liu, T. H.; Hung, F. Y.; Chen, C. H.; Chen, K. J. Microstructure, Optical, Electrical, and Magnetic Properties of ZnO/CuO Thin Films Prepared Using Two-Stage Magnetron Sputtering and Diffusion Doping Process. *J. Mater. Sci.: Mater. Electron.* **2020**, *31*, 4017−4026.
(61) Feng, Y.; Li, Z.; Liu, H.; Dong, C.; Wang, J.; Kulinich, S. A.; Du, X. Laser-Prepared CuZn Alloy Catalyst for Selective Electrochemical Reduction of CO2 to Ethylene. *Langmuir* **2018**, *34*, 13544−13549.
(62) Huang, N.; Sun, C.; Zhu, M.; Zhang, B.; Gong, J.; Jiang, X. Microstructure Evolution of Zinc Oxide Films Derived from Dip-Coating Sol-Gel Technique: Formation of Nanorods through Orientation Attachment. *Nanotechnology* **2011**, *22* (), DOI: 10.1088/0957-4484/22/26/265612.
(63) Dhama, R.; Nayek, C.; Thirmal, C.; Murugavel, P. Enhanced Magnetic Properties in Low Doped La1-XBa XMnO3+δ (X=0, 0.1 and 0.2) Nanoparticles. *J. Magn. Magn. Mater.* **2014**, *364*, 125−128.
(64) Kalliomäki, M.; Meisalo, V.; Laisaar, A. High Pressure Transformations in Cuprous Oxide. *PHYS. STATUS SOLIDI A* **1979**, *56*, K127−K131.
(65) Momot, A.; Amini, M. N.; Reekmans, G.; Lamoen, D.; Partoens, B.; Slocombe, D. R.; Elen, K.; Adriaensens, P.; Hardy, A.; Van Bael, M. K. A Novel Explanation for the Increased Conductivity in Annealed Al-Doped ZnO: An Insight into Migration of Aluminum and Displacement of Zinc. *Phys. Chem. Chem. Phys.* **2017**, *19*, 27866−27877.
(66) Itoh, M. Time-Dependent Power Laws in the Oxidation and Corrosion of Metals and Alloys. *Sci. Rep.* **2022**, *12* (), DOI: 10.1038/s41598-022-10748-1.
(67) Zhu, Y.; Mimura, K.; Lim, J. W.; Isshiki, M.; Jiang, Q. Brief Review of Oxidation Kinetics of Copper at 350 °C to 1050 °C. *Metall. Mater. Trans.* **2006**, *37*, 1231−1237.
(68) Poulston, S.; Parlett, P. M.; Stone, P.; Bowker, M. Surface Oxidation and Reduction of CuO and Cu2O Studied Using XPS and XAES. *Surf. Interface Anal.* **1996**, *24*, 811−820.
(69) Barreca, D.; Gasparotto, A.; Tondello, E. CVD Cu2O and CuO Nanosystems Characterized by XPS. *Surf. Sci. Spectra* **2007**, *14*, 41−51.
(70) Schedel-Niedrig, T.; Neisius, T.; Böttger, I.; Kitzelmann, E.; Weinberg, G.; Demuth, D.; Schlögl, R. Copper (Sub)Oxide Formation: A Surface Sensitive Characterization of Model Catalysts. *Phys. Chem. Chem. Phys.* **2000**, *2*, 2407−2417.
(71) Wang, Y.; Lany, S.; Ghanbaja, J.; Fagot-Revurat, Y.; Chen, Y. P.; Soldera, F.; Horwat, D.; Mücklich, F.; Pierson, J. F. Electronic Structures of C U2 O, C U4 O3, and CuO: A Joint Experimental and Theoretical Study. *Phys. Rev. B* **2016**, *94*, 1−10.
(72) Armelao, L.; Barreca, D.; Bertapelle, M.; Bottaro, G.; Sada, C.; Tondello, E. A Sol−Gel Approach to Nanophasic Copper Oxide Thin Films. *Thin Solid Films* **2003**, *442*, 48−52.
(73) Tobin, J. P.; Hirschwald, W.; Cunningham, J. XPS and XAES Studies of Transient Enhancement of Cu1 at CuO Surfaces during Vacuum Outgassing. *Appl. Surf. Sci.* **1983**, *16*, 441−452.
(74) Wiame, F.; Jasnot, F. R.; Twiatowska, J.; Seyeux, A.; Bertran, F.; le Fèvre, P.; Taleb-Ibrahimi, A.; Maurice, V.; Marcus, P. Oxidation of α-Brass: A Photoelectron Spectroscopy Study. *Surf. Sci.* **2015**, *641*, 51−59.
(75) Mrowec, S.; Stokłosa, A. Oxidation of Copper at High Temperatures. *Oxid. Met.* **1971**, *3*, 291−311.
(76) Gutmann, S.; Conrad, M.; Wolak, M. A.; Beerbom, M. M.; Schlaf, R. Work Function Measurements on Nano-Crystalline Zinc Oxide Surfaces. *J. Appl. Phys.* **2012**, *111* (), DOI: 10.1063/1.4729527.
(77) Gordon, P. G.; Bačić, G.; Lopinski, G. P.; Barry, S. T. Work Function of Doped Zinc Oxide Films Deposited by ALD. *J. Mater. Res.* **2020**, *35*, 756−761.
(78) Mehtar, S.; Wiid, I.; Todorov, S. D. The Antimicrobial Activity of Copper and Copper Alloys against Nosocomial Pathogens and Mycobacterium Tuberculosis Isolated from Healthcare Facilities in the Western Cape: An in-Vitro Study. *Journal of Hospital Infection* **2008**, *68*, 45−51.

https://doi.org/10.1021/acsami.3c04801
ACS Appl. Mater. Interfaces XXXX, XXX, XXX−XXX

Surface modification of brass via ultrashort pulsed direct laser interference patterning and its effect on bacteria-substrate interaction

Aisha Saddiqa Ahmed[a,b], Daniel Wyn Müller[a], Stephanie Bruyere[b], Anne Holtsch[c], Frank Müller[c], Jenifer Barrirero[a], Kristina Brix[d], Sylvie Migot[b], Ralf Kautenburger[d], Karin Jacobs[c], Jean-François Pierson[b], Frank Mücklich[a]*

[a] Chair of Functional Materials, Department of Material Science and Engineering, Saarland University, 66123 Saarbrücken, Germany

[b] Université de Lorraine, CNRS, IJL, F-54000 Nancy, France

[c] Experimental Physics and Center for Biophysics, Saarland University, 66123 Saarbrücken, Germany

[d] Department of Inorganic Solid-State Chemistry, Elemental Analysis, Saarland University, 66123 Saarbrücken, Germany

* aisha.ahmed@uni-saarland.de

Content of SI

1 Position of lamella lifted out from the as-processed sample

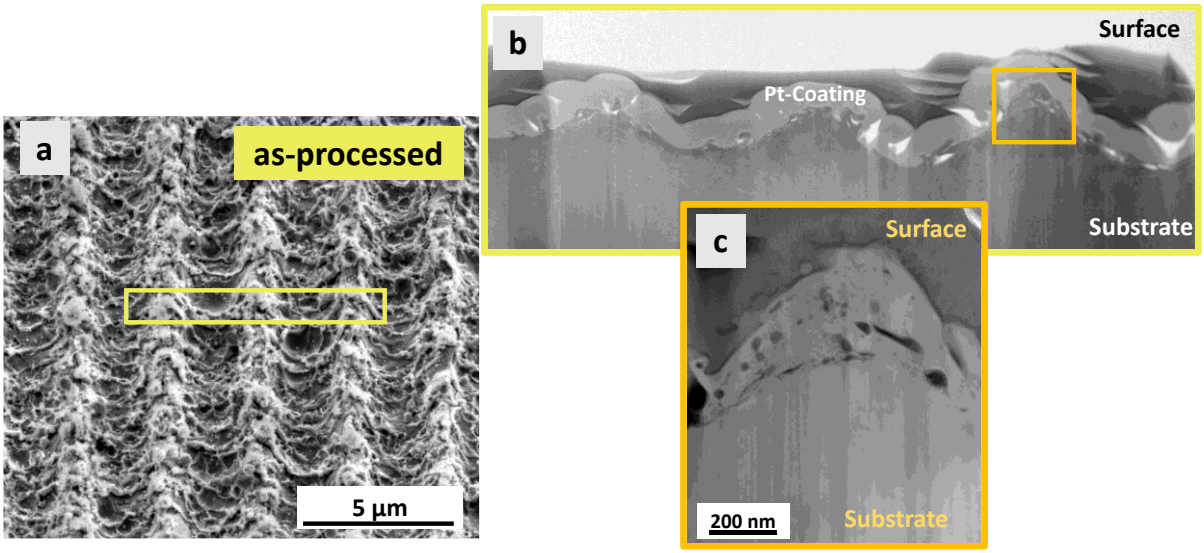

Figure S1: a) SEM Micrograph of the as-processed CuZn37 sample displaying the position of lamella in a yellow box perpendicular to the line-like structures. The STEM high angle annular dark field images display b) lamella with the position of the peak in the orange box, c) the magnification of the peak, as represented in Figure 2 a.of the manuscript.

2 TEM-Electron diffraction images of CuZn37 etched

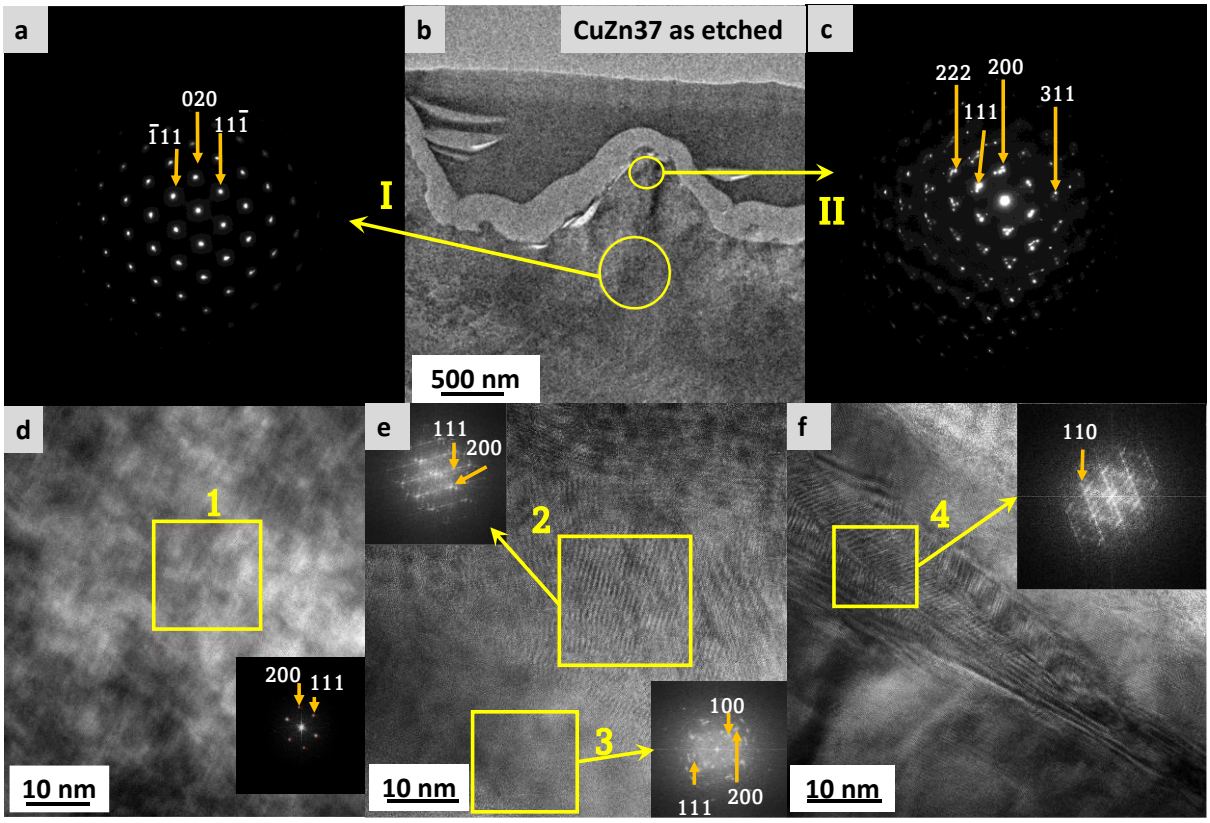

Figure S2: TEM-Electron diffraction imaging on CuZn37 etched. (a, c) SAED patterns taken from (b) and (d, e, f) HR-TEM images of the modified area with their respective binned FFT patterns of a selected area.

Description of Figure S2: CuZ37 etched is taken under observation. A monocrystalline pattern is noted for the bulk area I (Figure S1 a) and identified as α-brass (111), (020) diffraction spots, and zone axis <101>. This pattern was taken from a considerably larger area of the bulk region, which suggest a larger grain size. Subsequently, measurement is done closer to the surface and the presence of α-brass is still detected with identifiable zone axes (Figure S1 c). In this case, the discrete spots revealing polycrystalline structure suggest a decline of grain size from the bulk towards the surface with sizes much smaller in the range of a few nanometres. The inhibition of grain growth is potentially attached to the rapid cooling of the surface and the presence of defects in the structure.[1] The bulk itself has a grain size of roundabout 1 µm and

near surface a range of a few 100 nm, which is a result of pre laser surface preparation with polishing. Further analysis was carried out 100 nm region from the surface as shown in Figure S1 e and f. Here, area 2 represents Cu_2O (111), and (200) diffraction spots. Furthermore, the β-brass phase is detected as a polycrystalline structure in Area 3 represented by (100), (111), (200) diffraction spots as well as in the twin boundaries (Area 4) represented by (110) diffraction spot.

3 Cu-Zn Phase diagram

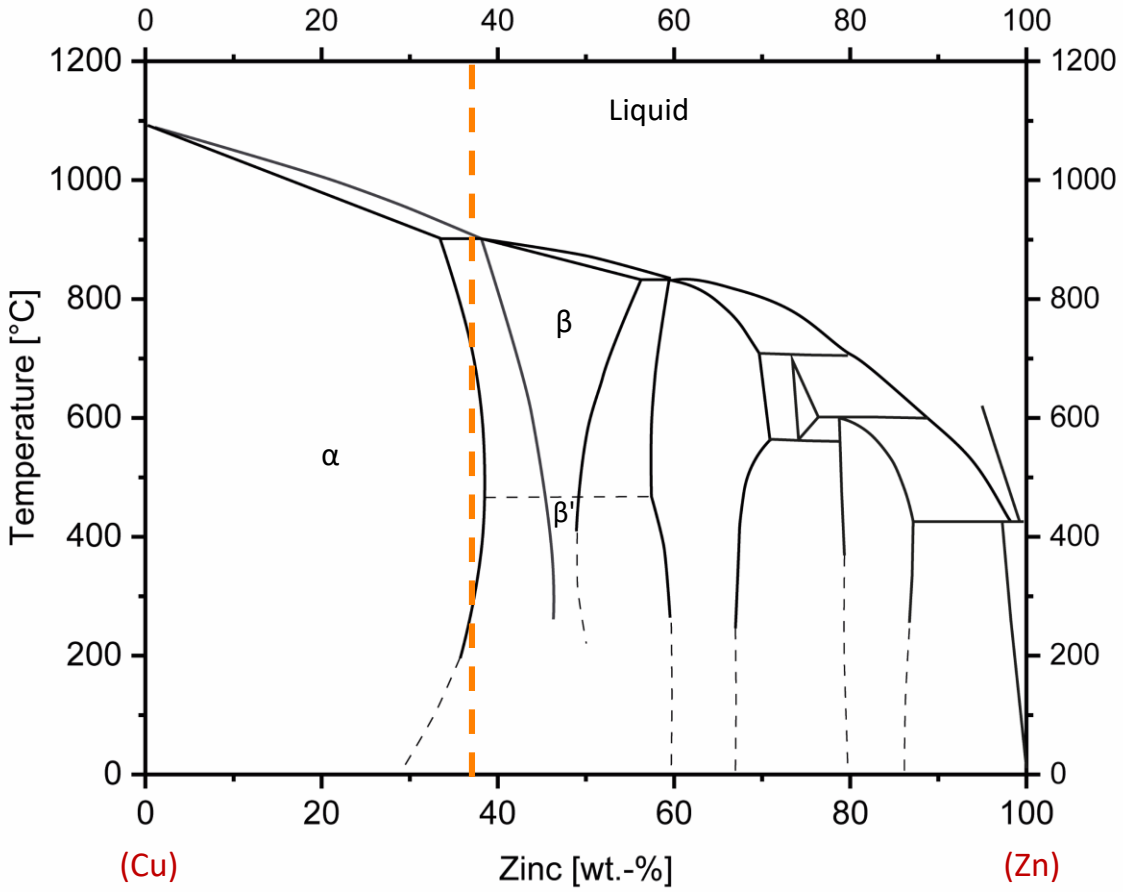

Figure S3: Cu-Zn phase diagram [2,3] according to Massalski et al [4] .The dashed orange line represents the position of chemical composition of CuZn37. This figure displays only the phases relevant to this study.

4 Table with Raman bands of all samples as well as the literature values of the bands.

Table S1: Results of Raman spectroscopy on CuZn37 in as-processed and etched condition. As a comparison the literature [5–15] values of ZnO, Cu_2O and CuO bands are stated as well.

symmetry	*activity*	*oxide*	Raman shift ω_e [cm^{-1}]		
			Literature	*CuZn37*	
				as-processed	*etched*
T_{2u}	silent	Cu_2O	60-94	61-62	58-60
E_u	silent	Cu_2O	72-110	73	76-77
				83	-
E_2^{low}	Raman	ZnO	99-101	89-92	91-92
T_{1u} *(TO)*	IR	Cu_2O		147-146	144-145
				206-210	205-211
AM 1	silent	Cu_2O	273-275	-	-
A_g	Raman	CuO			
B_g	Raman	CuO	327-382	300-600 (broad band with tilted baseline)	
A_1 *(TO)*	Raman	ZnO	378-380		
E_1 *(TO)*	Raman	ZnO	407-413		
E_2^{high}	Raman	ZnO	437-438		
AM 2	silent	Cu_2O	500-508		
				473-492	-
T_{2g}	Raman	Cu_2O	500-515	516-520	520-523
A_1 *(LO)*	Raman	ZnO	573-579	572	579-580
E_1 *(LO)*	Raman	ZnO	583-591		
T_{1u} *(LO)*	IR	Cu_2O	630-680	644-645	636-646
B_g	Raman	CuO	609-636	-	-

5 XPS-based elemental depth profiling

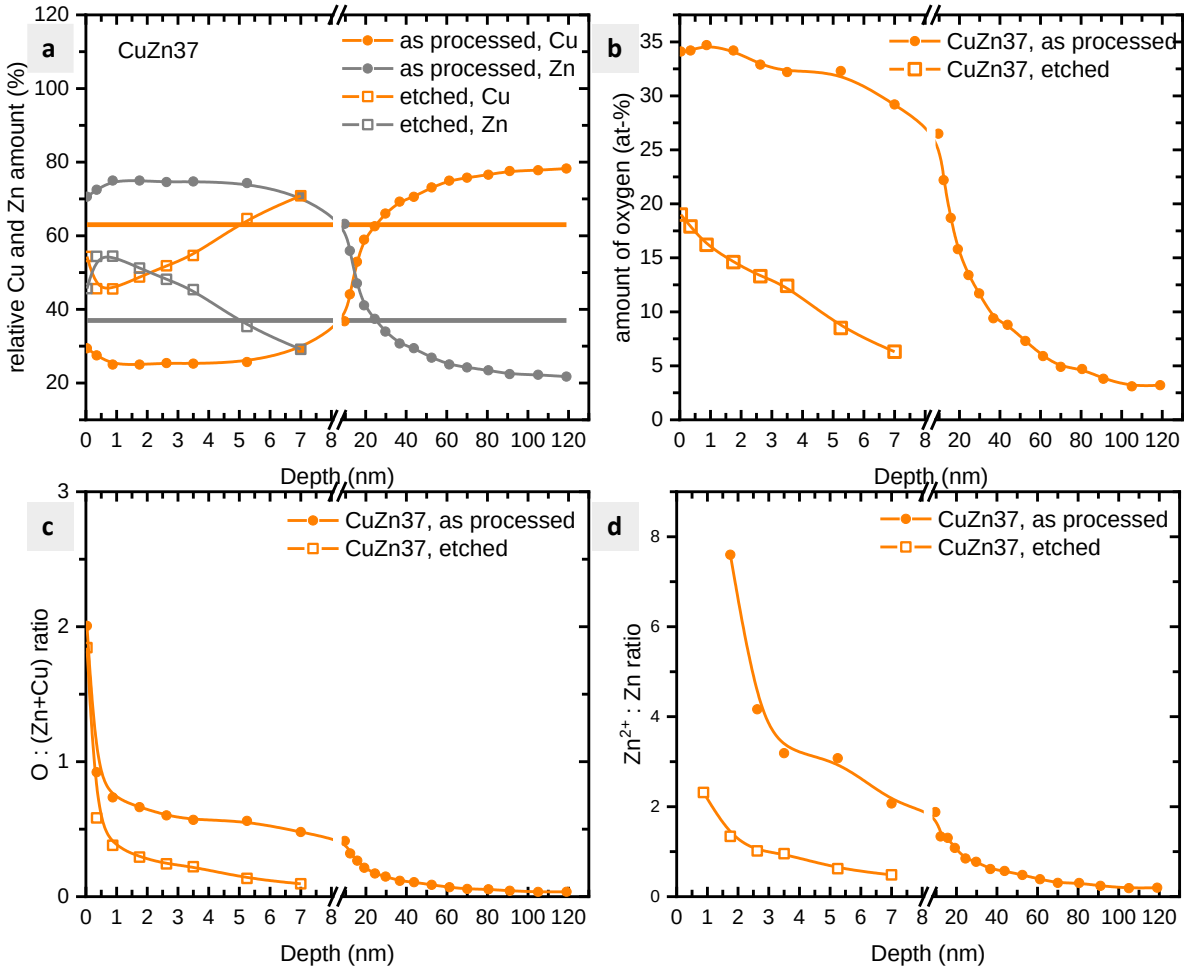

Figure S4: XPS-based elemental depth profiles with Cu and Zn at.-% on (a) CuZn37 in as processed and etched conditions each. Also represented are (b) the amount of oxygen in at.-%, (c) the oxygen to zinc ratio and (d) Zn^{2+} to Zn^{0} for both samples.

Description: Cu, Zn, and O concentrations are investigated for both samples and the results are displayed in Figure S3. The two horizontal reference lines represent the nominal bulk concentration (in at.-% ≈ wt.-%) for copper and zinc in CuZn37. The as processed sample (see Figure S3 a) shows reduced content of copper and an equally increased concentration of zinc towards the surface. The same effect is visible to a less extent on the etched sample. However, the depth of this variation is significantly less. This is connected to the presence of oxygen on

the sub-surface of the samples (see Figure S3 b), which is distributed deeper for the as-processed sample. As it is compared to the results of the oxygen to zinc ratio (see Figure S3 c) as well as the Zn^{2+} to Zn^{0} ratio (see Figure S3 d), it is evident that the laser process induces the formation of zinc oxide. As the surface is etched, the amount of oxygen alongside its ratio to zinc as well the Zn^{2+} to Zn^{0} ratio decreases in depth indicating a partial removal of zinc oxide via etching. These results add to the STEM-EDS results and validate the presence of zinc oxide.

6 XPS-spectrums of CuZn37 in O 1s region

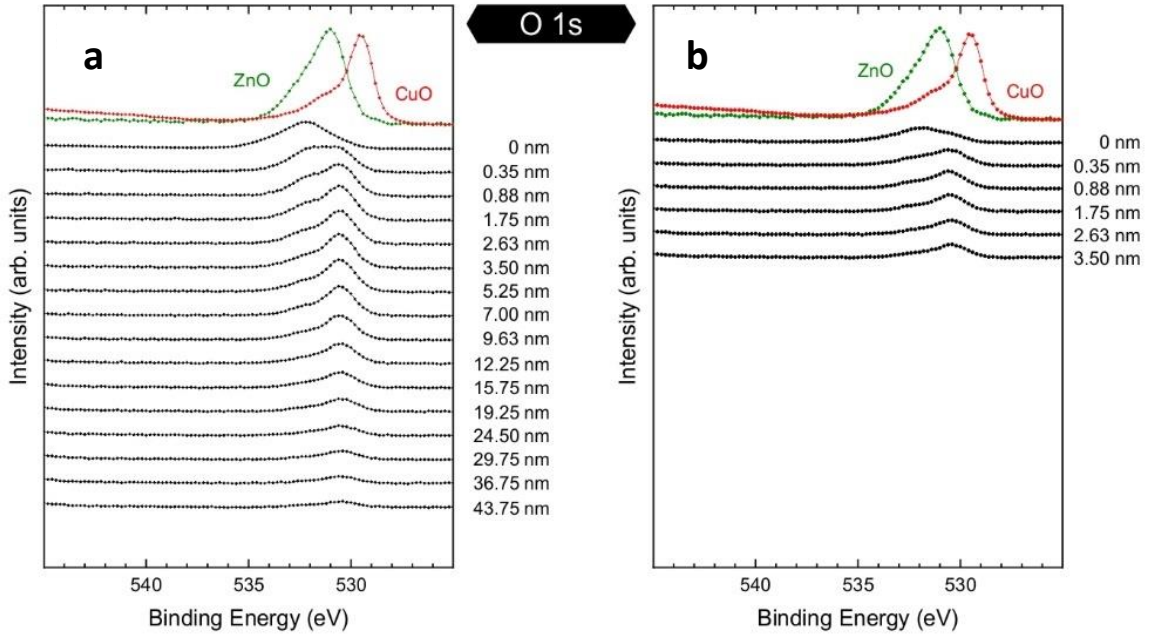

Figure S5: XPS - spectra of CuZn37 a) as processed and b) etched with high resolution spectra of O 1s region.

Description of Figure S5: The CuZn37 spectra discussed in the Manuscript are supported by the results of the O 1s region. The spectra related to CuO (529.6 eV) and ZnO (531 eV) are provided as references. For zero ablation (0 nm) Figure S5 a shows a broad peak between 534.2-529.2 eV, suggesting an overlap of various O 1s contributions resulting also from adsorbates. However, the maximum of the peak at BE 531.6 eV correlates rather with that of ZnO[16–18] than

CuO and Cu_2O since both oxidation states of copper appear at a lower BE.[19,20] The slightly higher BE is consequent to the presence of oxygen vacancies and loosely bonded O on the surface.[21,22] With increasing ablation, the intensities of the O 1s peaks decrease in the same way as the ZnO related contributions of the Zn LMM Auger spectra in Figures 7 e and 7 f for as-processed and for etched CuZn37, respectively.

7 Results of scanning tunnelling microscopy (STM) exhibiting the topography

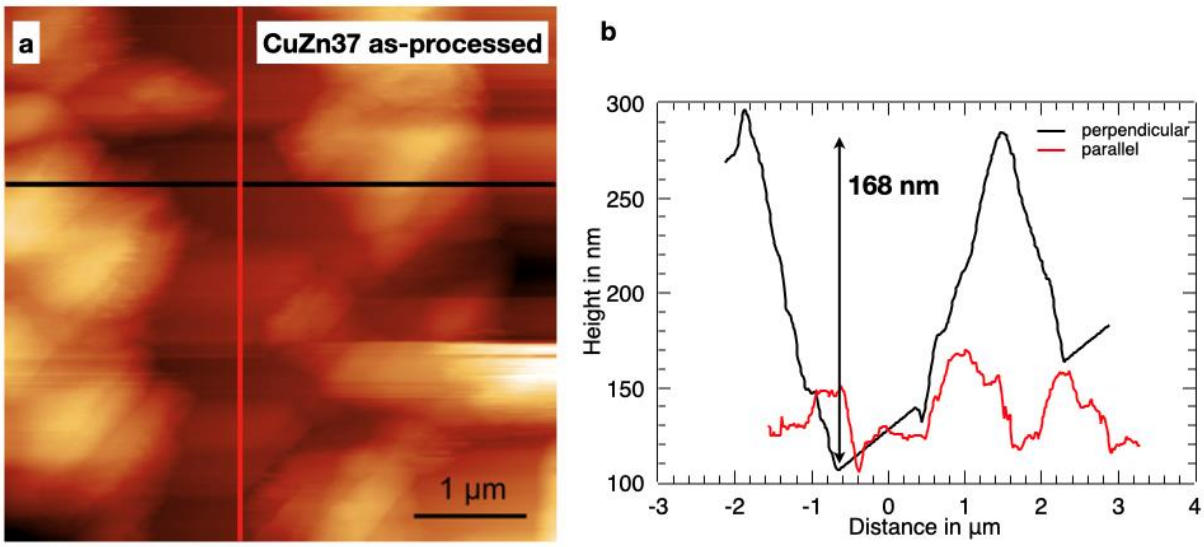

Figure S6: (a) 5× 5 µm² STM image of CuZn37 as processed after argon ion etching. (b) Cross section perpendicular (black) and parallel (red) to the linear structures.

8 References

(1) Huang, N.; Sun, C.; Zhu, M.; Zhang, B.; Gong, J.; Jiang, X. Microstructure Evolution of Zinc Oxide Films Derived from Dip-Coating Sol-Gel Technique: Formation of Nanorods through Orientation Attachment. *Nanotechnology* **2011**, *22* (26). https://doi.org/10.1088/0957-4484/22/26/265612.

(2) Kejzlar, P.; Machuta, J.; Nová, I. Comparison of the Structure of CuZn40MnAl Alloy Casted into Sand and Metal Moulds. *Manufacturing Technology* **2017**, *17* (1), 15–15. https://doi.org/10.21062/ujep/x.2017/a/1213-2489/MT/17/1/44.

(3) Kowalski, M.; Spencer, P. J. Thermodynamic Reevaluation of the Cu-Zn Syst m. *Journal of Phase Equilibria* **1993**, *14* (4), 432–438.

(4) Massalski, T. B.; Okamoto, H.; Subramanian, P.; Kacprzak, L.; Scott, W. W. Binary Alloy Phase Diagrams. *American society for metals* **1986**, *1* (2).

(5) Damen, T. C.; Porto, S. P. S.; Tell, B. Raman Effect in Zinc Oxide. *Physical Review* **1966**, *142* (2), 570–574. https://doi.org/10.1103/PhysRev.142.570.

(6) Russo, V.; Ghidelli, M.; Gondoni, P.; Casari, C. S.; Li Bassi, A. Multi-Wavelength Raman Scattering of Nanostructured Al-Doped Zinc Oxide. *J Appl Phys* **2014**, *115* (7). https://doi.org/10.1063/1.4866322.

(7) Debbichi, L.; Marco De Lucas, M. C.; Pierson, J. F.; Krüger, P. Vibrational Properties of CuO and Cu 4O 3 from First-Principles Calculations, and Raman and Infrared Spectroscopy. *Journal of Physical Chemistry C* **2012**, *116* (18), 10232–10237. https://doi.org/10.1021/jp303096m.

(8) Xu, Z.; Tang, K.; Zhu, S.; Ma, J.; Ye, J.; Gu, S. Identification and Tuning of Zinc-Site Nitrogen-Related Complexes in ZnO Material. *Journal of Vacuum Science & Technology A: Vacuum, Surfaces, and Films* **2018**, *36* (2), 021503. https://doi.org/10.1116/1.4996617.

(9) Momot, A.; Amini, M. N.; Reekmans, G.; Lamoen, D.; Partoens, B.; Slocombe, D. R.; Elen, K.; Adriaensens, P.; Hardy, A.; van Bael, M. K. A Novel Explanation for the Increased Conductivity in Annealed Al-Doped ZnO: An Insight into Migration of Aluminum and Displacement of Zinc. *Physical Chemistry Chemical Physics* **2017**, *19* (40), 27866–27877. https://doi.org/10.1039/c7cp02936e.

(10) Zhu, X.; Wu, H.; Yuan, Z.; Kong, J.; Shen, W. Multiphonon Resonant Raman Scattering in N-Doped ZnO. *Journal of Raman Spectroscopy* **2009**, *40* (12), 2155–2161. https://doi.org/10.1002/jrs.2385.

(11) Zhu, Y.; Sow, C. H.; Yu, T.; Zhao, Q.; Li, P.; Shen, Z.; Yu, D.; Thong, J. T. L. Co-Synthesis of ZnO-CuO Nanostructures by Directly Heating Brass in Air. *Adv Funct Mater* **2006**, *16* (18), 2415–2422. https://doi.org/10.1002/adfm.200600251.

(12) Morales, C.; del Campo, A.; Méndez, J.; Prieto, P.; Soriano, L. Re-Oxidation of ZnO Clusters Grown on HOPG. *Coatings* **2020**, *10* (4). https://doi.org/10.3390/coatings10040401.

(13) Ivanda, M.; Waasmaier, D.; Endriss, A.; Ihringer, J.; Kirfel, A.; Kiefer, W. Low-Temperature Anomalies of Cuprite Observed by Raman Spectroscopy and x-Ray Powder Diffraction. *Journal of Raman Spectroscopy* **1997**, *28* (7), 487–493. https://doi.org/10.1002/(sici)1097-4555(199707)28:7<487::aid-jrs115>3.0.co;2-v.

(14) Zhu, Y.; Mimura, K.; Lim, J. W.; Isshiki, M.; Jiang, Q. Brief Review of Oxidation Kinetics of Copper at 350 °C to 1050 °C. *Metall Mater Trans A Phys Metall Mater Sci* **2006**, *37* (4), 1231–1237. https://doi.org/10.1007/s11661-006-1074-y.

(15) Meyer, B. K.; Polity, A.; Reppin, D.; Becker, M.; Hering, P.; Kramm, B.; Klar, P. J.; Sander, T.; Reindl, C.; Heiliger, C.; Heinemann, M.; Müller, C.; Ronning, C. The Physics of Copper Oxide (Cu2O). *Semiconductors and Semimetals* **2013**, *88*, 201–226. https://doi.org/10.1016/B978-0-12-396489-2.00006-0.

(16) Amor, S. ben; Jacquet, M.; Fioux, P.; Nardin, M. XPS Characterisation of Plasma Treated and Zinc Oxide Coated PET. *Appl Surf Sci* **2009**, *255* (9), 5052–5061. https://doi.org/10.1016/j.apsusc.2008.12.067.

(17) Du, Y.; Zhang, M. S.; Hong, J.; Shen, Y.; Chen, Q.; Yin, Z. Structural and Optical Properties of Nanophase Zinc Oxide. *Appl Phys A Mater Sci Process* **2003**, *76* (2), 171–176. https://doi.org/10.1007/s003390201404.

(18) Claros, M.; Setka, M.; Jimenez, Y. P.; Vallejos, S. Aacvd Synthesis and Characterization of Iron and Copper Oxides Modified Zno Structured Films. *Nanomaterials* **2020**, *10* (3). https://doi.org/10.3390/nano10030471.

(19) Barreca, D.; Gasparotto, A.; Tondello, E. CVD Cu2O and CuO Nanosystems Characterized by XPS. *Surface Science Spectra* **2007**, *14* (1), 41–51. https://doi.org/10.1116/11.20080701.

(20) Poulston, S.; Parlett, P. M.; Stone, P.; Bowker, M. Surface Oxidation and Reduction of CuO and Cu2O Studied Using XPS and XAES. *Surface and Interface Analysis* **1996**, *24* (12), 811–820. https://doi.org/10.1002/(SICI)1096-9918(199611)24:12<811::AID-SIA191>3.0.CO;2-Z.

(21) Koo, C. Y.; Song, K.; Jung, Y.; Yang, W.; Kim, S. H.; Jeong, S.; Moon, J. Enhanced Performance of Solution-Processed Amorphous LiYInZnO Thin-Film Transistors. *ACS Appl Mater Interfaces* **2012**, *4* (3), 1456–1461. https://doi.org/10.1021/am201701v.

(22) Kim, S. Y.; Park, H.-G.; Cho, M.-J.; Jeong, H.-C.; Kim, D.-H.; Seo, D.-S. Liquid Crystal Aligning Capabilities in Solution-Processed HfZrO Layers Created via Ion-Beam Irradiation. *ECS Journal of Solid State Science and Technology* **2014**, *3* (11), R212–R215. https://doi.org/10.1149/2.0111411jss.

PUBLICATION II

Antibacterial Property Alterations Induced by Low Zinc Content in Laser-Structured Brass

Aisha Saddiqa Ahmed[a,b], Daniel Wyn Müller[a], Stephanie Bruyere[b], Anne Holtsch[c], Frank Müller[c], Kristina Brix[d], Sylvie Migot[b], Ralf Kautenburger[d], Karin Jacobs[c], Jean-François Pierson[b], Frank Mücklich[a]

[a] *Chair of Functional Materials, Department of Material Science and Engineering, Saarland University, 66123 Saarbrücken, Germany*

[b] *Université de Lorraine, CNRS, IJL, F-54000 Nancy, France*

[c] *Experimental Physics and Center for Biophysics, Saarland University, 66123 Saarbrücken, Germany*

[d] *Department of Inorganic Solid-State Chemistry, Elemental Analysis, Saarland University, 66123 Saarbrücken, Germany*

Research article

Published in "**Applied Surface Science**" (2024)

Impact Factor: 6.9 (2025)

Accessible online at: https://doi.org/10.1016/J.APSUSC.2024.160338

Own Contributions: Conceptualization, Investigation, Validation, Visualization, Writing – original draft.

Cite this article as: Ahmed, A. S.; Müller, D. W.; Bruyère, S.; Holtsch, A.; Müller, F.; Brix, K.; Migot, S.; Kautenburger, R.; Jacobs, K.; Pierson, J. F.; Mücklich, F. Antibacterial Property Alterations Induced by Low Zinc Content in Laser-Structured Brass. *Appl Surf Sci* **2024**, *665*, 160338. https://doi.org/10.1016/J.APSUSC.2024.160338.

Applied Surface Science 665 (2024) 160338

Contents lists available at ScienceDirect

Applied Surface Science

journal homepage: www.elsevier.com/locate/apsusc

Full Length Article

Antibacterial property alterations induced by low zinc content in laser-structured brass

Aisha Saddiqa Ahmed [a,b,*], Daniel Wyn Müller [a], Stéphanie Bruyère [b], Anne Holtsch [c], Frank Müller [c], Kristina Brix [d], Sylvie Migot [b], Ralf Kautenburger [d], Karin Jacobs [c], Jean–François Pierson [b], Frank Mücklich [a]

[a] Chair of Functional Materials, Department of Material Science and Engineering, Saarland University, 66123 Saarbrücken, Germany
[b] Université de Lorraine, CNRS, IJL, F-54000 Nancy, France
[c] Experimental Physics and Center for Biophysics, Saarland University, 66123 Saarbrücken, Germany
[d] Department of Inorganic Solid-State Chemistry, Elemental Analysis, Saarland University, 66123 Saarbrücken, Germany

ARTICLE INFO

Keywords:
Femtosecond pulsed direct laser interference patterning
Brass
Nanoscale modification
Antibacterial
Bacteria-substrate contact
Escherichia coli

ABSTRACT

Brass, along with other copper-based alloys, exhibits advantageous antibacterial properties that can be further enhanced by altering the surface topography to increase bacterial adhesion. This enhancement is achievable through a higher contact area created by precise periodic structures, each approximately the size of a single bacterial cell. One method for generating these structures is ultrashort pulsed direct laser interference patterning (USP-DLIP). However, this process may induce chemical alterations in addition to topographical changes, depending on the substrate's composition. To mitigate unfavorable chemical alterations, brass with a 15% zinc content was selected for this study. The antibacterial effectiveness of the modified surfaces was tested against *Escherichia coli*, providing initial insights into the interaction between bacteria and the substrate. The results indicate that modified brass with a 15% zinc content shows improved antibacterial activity. Overall, this research demonstrates that by modifying a surface with the appropriate chemical composition, effective bacterial elimination through contact can be achieved.

1. Introduction

Excessive consumption of antibiotics over the last few decades has created multidrug resistance among several pathogens. The spread of such pathogens has resulted in an increased number of incurable infections leading to a higher mortality rate, especially in hospitals. [1] Nosocomial or hospital-acquired infections are transmitted either through direct or indirect contact. [2,3] As soon as any microorganism or pathogens encounter another living organism or a surface, they tend to adhere to the host, build colonies, and form biofilms, which can be a source of further infections. [4] Therefore, the first step is to prevent transmission e.g., via isolation of the patient or extensive sanitization of the surfaces, which can be achieved with physical cleaning. However, a smarter option is to use surfaces with antibacterial and self-cleaning properties that require considerably less maintenance. [5].

The antibacterial effects of copper and its alloys have garnered significant attention in the scientific community over the past few decades. Numerous studies have been conducted to explore their potential as an antibacterial agent. [6] Recent studies [7] show that it is related to the Cu-ion release from the surface, which is responsible for the degradation of bacterial cells. [8,9] Further studies have demonstrated the formation of reactive oxygen species in the presence of copper oxide nanoparticles and hydrogen peroxide as well as other reactants. These reactive oxygen species induce oxidative stress, leading to the deterioration of bacterial cells. [10,11] Additionally, the use of ultrashort pulsed direct laser interference patterning to produce superficial structures in the dimension of the bacteria provides a larger contact area. The increased surface area enhances the bacterial killing on copper surfaces further. DLIP is a

Abbreviations: CuZn15, Brass with 15% zinc content; CLSM, confocal laser scanning microscopy; CFU, colony-forming units; *E. coli*, *Escherichia coli*; FWHM, full width at half maximum; GI-XRD, grazing incidence X-ray diffraction; HAZ, heat-affected zone; PBS, phosphate-buffered saline; SEM, scanning electron microscopy; STEM-EDS, scanning transmission electron microscopy along with energy dispersive X-rays spectroscopy; TEM, transmission electron microscopy, USP-DLIP, ultrashort pulsed direct laser interference patterning; XPS, X-ray photoelectron spectroscopy.

* Corresponding author at: Chair of Functional Materials, Department of Material Science and Engineering, Saarland University, 66123 Saarbrücken, Germany.
E-mail address: aisha.ahmed@uni-saarland.de (A.S. Ahmed).

https://doi.org/10.1016/j.apsusc.2024.160338
Received 18 December 2023; Received in revised form 20 April 2024; Accepted 19 May 2024
Available online 20 May 2024

very well-known high-speed technique for creating superficial periodic structures down to the nanoscale that are very precise and can alter the surface properties. [12] Nature is a primary example of micro- and nanoscale features in different species, demonstrating how such superficial structures have evolved over the years according to their functionalities i.e., light absorption, wettability, adhesion, friction, mechanical strength, etc. [13–16] These examples are an inspiration for DLIP method, which is used for surface modification of various materials to obtain specific properties with diverse applications. [12,17].

The DLIP technique combined with the ultrashort pulsed (USP) duration causes the matter to ablate with heat-affected zones (HAZ) only at the nano-scale. [18] In the case of copper, it leads to topographical and chemical modification of the surface, which works in favor of the antibacterial properties. [7,19] However, a recent study [20] on USP-DLIP treatment of brass with 37 % zinc shows that these nano-scale HAZ cannot be completely neglected, as they led to some major chemical modifications of the surface, i.e. not only the formation of oxide phases but also the intermetallic β-phase of brass. Therefore, a decrease in the release of copper ions is observed, which significantly reduces the antibacterial efficacy.

This study aims to investigate the correlation between the chemical modification of HAZ by USP-DLIP and the bulk chemical composition of brass and to understand its influence on antibacterial properties. While pure copper surfaces possess beneficial antibacterial properties, they also face mechanical limitations in application. Alloying, particularly with zinc, offers a feasible solution to expand applications by enhancing durability and corrosion resistance. For that purpose, commercially available brass with 15 % zinc (CuZn15) is chosen. Since it has a zinc content below 30 ± 3 wt-%, the probability of the formation of any intermetallic phases is low. [21] Given that earlier investigations [20] with elevated zinc content revealed the emergence of both intermetallic and oxide phases following USP-DLIP modification, this study aims to enhance our understanding of the consequences of preventing intermetallic phase formation on the alteration of antibacterial efficacy. In brief, periodic line-like structures in the dimension of the single bacterial cell, *Escherichia coli* (*E. coli*), are fabricated, characterized, and finally tested for their antibacterial efficacy.

2. Materials and methods

2.1. Materials

This study uses brass with 15 % zinc (CuZn15, *Wieland*) together with two references i.e., 99 % pure copper (*Wieland*), and stainless steel 304 (*Brio*). The sample sheets, each measuring approximately 1 mm in thickness, were trimmed to dimensions of around 25 x 10 mm^2 followed by a metallographic preparation as described in Ahmed *et al.* [20] to acquire a mirror-quality finish. For that purpose, the sample surface was first ground with SiC paper (15 μm grain size) on a manual Tegrapol system (*Struers*). It was then polished using an all-in-one diamond solution (Dia Duo 2 from *Struers*) on an automated TegraPol system (*Struers*), which involved three steps using the following grain sizes: 6 μm, 3 μm, and 1 μm.

2.2. Ultrashort pulsed direct laser interference patterning

Line-like structures with a periodicity of 3 μm were fabricated on the CuZn15 surface as described in Ahmed *et al.*[20] For that purpose, USP-DLIP with the following laser system and parameters was employed: a Ti:sapphire Spitfire laser system (*Spectra Physics*) with ultrashort laser pulses (pulse duration of t_p = 100 fs, full width at half maximum, FWHM) and centered wavelength $\lambda = 800$ nm. The optical configuration was selected in accordance with the description provided by Müller *et al.* [22] A fluence of 0.84 J/cm^2 with a total number of approx.10 pulses were applied to produce the structures. Following the laser treatment, the samples underwent a minimum aging period of three weeks to guarantee stable and reproducible wettability conditions. [7] For the characterization and the tests, the structured samples were observed in as-processed and etched conditions. “As-processed” denotes samples that have undergone laser processing and aging, whereas “etched” indicates structured samples immersed in a 5 % citric acid solution in an ultrasonic bath for 2 min, then cleaned with ethanol to eliminate any process-induced oxides and subsequently aged for 3 weeks.

2.3. Characterization

At first, confocal laser scanning microscopy (CLSM, *LEXT OLS4100 3D Measuring Laser Microscope by Olympus*) was utilized to verify the topography of structures followed by scanning electron microscopy (SEM, *Helios NanoLab 600™, FEI Company*) to acquire images in secondary electron contrast mode. For that an acceleration voltage of 5 kV and a current of 1.4 nA were used, whereas the sample was tilted at 45° to obtain a better image of the line-like structures. Subsequently, a quantitative phase analysis was performed via a high-resolution grazing incidence X-ray diffractometer (GIXRD, Cu K_α source with a wavelength of 1.5418 Å at 1° grazing angle, *PANalytical X'Pert PRO-MPD*). The raw data underwent processing with the X'pert HighScore software (version 5.1), [23] which encompassed baseline correction and peak identification for comparison with the database.

Scanning transmission electron microscopy also including energy-dispersive X-ray spectroscopy (STEM-EDS, JEOL ARM 200F cold FEG equipped with two Cs correctors) was applied to determine the chemical composition via mapping and profiling. Wherefore, thin foil lamellas (perpendicular to the lines) were produced by using a focused ion beam (FIB) SEM dual beam system *FEI Helios NanoLab 600i*.

The oxides characterization was carried out with X-ray photoelectron spectroscopy (XPS, Vacuum Generators ESCA MKII, non-monochromatic Al-K_α radiation (1486.6 eV), normal emission).

2.4. Antibacterial tests

Wet plating method [24] is used in this work to test the antibacterial activity on all three brass surfaces (polished, as-processed, etched) including the copper and stainless-steel references. The bacteria of strain *E. coli* WT K12 (BW25113) were used in the wet plating. The preparation of the bacterial culture was conducted following the method outlined in Luo *et al.* [6] The bacterial suspension was applied in the form of a 40 μL droplet to perform the contact-killing experiment as described in previous studies. [7,20] The experiment was carried out across three distinct durations: 30 min, 60 min, and 120 min. At the conclusion of each period, two droplets of 5 μL each were collected. One is diluted in a phosphate buffer saline (PBS) solution to then spread on an agar plate consisting of lysogeny broth (LB), which is later stored in an incubator at 37 °C. Following a 24-hour period, the total count of surviving colony units (CFU/mL) was determined. The second droplet was diluted into 600-fold of 0.1 % HNO_3 to assess the release of Cu ions during 120 min of contact. The measurement is carried out with inductively coupled plasma mass spectrometry (ICP-MS, Agilent 8900 ICP-QQQ). When evaluating the results, the increase in the contact area and the variation in wettability were taken into account as described in Ahmed *et al.* [20].

3. Results and discussion

3.1. Topographical modification

Fig. 1 shows the topography with the line-like structures on CuZn15. By subjecting the surface to ultrashort pulsed laser irradiation, high temperatures, and localized stress are generated, resulting in the material ablating in the form of a phase explosion and the ejection of molten material. [25,26] This process creates periodic line-like structures, as observed in this work where the periodicity is 3 μm and the depth is 1.3 ± 0.1 μm. The increase in surface area is 2.3-fold, with the valleys

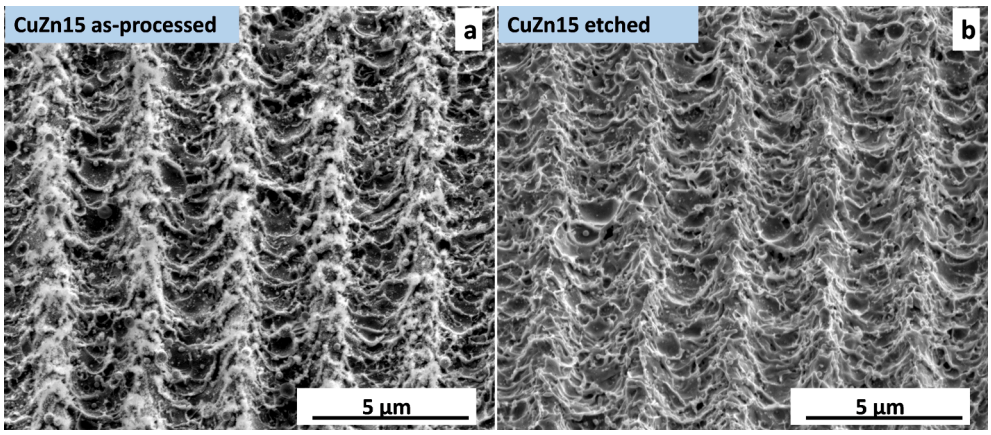

Fig. 1. SEM-images of line-like structures fabricated by USP-DLIP on CuZn15 (a) in as-processed state and (b) after etching with citric acid. The structures have a periodicity of 3 µm.

exhibiting a concave form that is approx. 2 times larger surface area than that of the peaks. Overall, the aim is to enhance the bacteria-substrate contact via this structure form.

The formation of oxides is evident in the flake-like sub-structures observed on the as-processed sample shown in Fig. 1 a. This occurrence is particularly beneficial for pure copper as it leads to a heightened antimicrobial effect by promoting corrosion and subsequently releasing more copper ions. [7] On the contrary, brass with higher zinc content experience the formation of predominantly zinc-rich phases with oxygen when irradiated with a USP laser. Correspondingly, a higher corrosion resistance is achieved resulting in lower Cu-ions release. [20].

The interaction between bacteria and the substrate is significantly influenced by the release of Cu ions and surface wettability, and both are affected by oxide formation. [6] In order to investigate the effect of oxide formation on brass with low zinc content, the surfaces were etched. This results in the removal of the flake-like sub-structures revealing the actual structure underneath (see Fig. 1 b). The structures exhibit nanoroughness along the lines, likely due to the presence of melting zones and the resulting multi-ripples. This is further aided by redepositioning the molten material as nanoparticles. The structures obtained in this study agree well with those in recent studies. [7,20].

3.2. Phase analysis

This section deals with phase analysis of brass surfaces in the polished state and after laser structuring in the as-processed and etched state. The black diffractogram in Fig. 2 shows peaks at 43°, 50°, 73.6°, 89°, 94.1°, and 115.2° that are designated characteristic peaks of an α-phase in brass with 85 wt-% copper and 15 wt-% zinc (LPF:1826484, ICDD:04–018-5556). Likewise, similar peaks with no significant distinctions are recorded for the structured surfaces. These results show no phase alteration of α-brass for CuZn15 via laser treatment. However, the SEM images (see Fig. 1) indicate the removal of flake-like sub-structures on the surface, which will be further investigated in the subsequent sections.

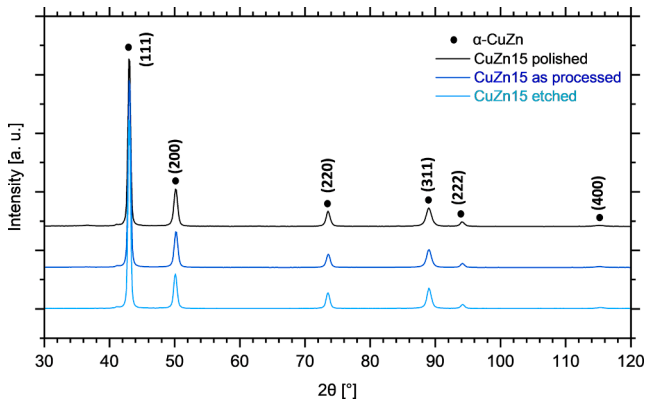

Fig. 2. Results of GI-XRD on brass with 15% zinc content: polished (black diffractogram), as-processed (dark blue diffractogram), etched (light blue diffractogram). (For interpretation of the references to color in this figure legend, the reader is referred to the web version of this article.)

3.3. Chemical modification

STEM-EDS analysis was carried out on the structured CuZn15 surfaces. To conduct the investigation, a cross-section was prepared perpendicular to the line-like structures, followed by the extraction of lamella from the prepared cross-section.

Fig. 3 illustrates the elementary mapping on a peak (tilted clockwise at 90°) of the CuZn15 as–processed sample. The map indicates unaltered chemical composition until the last 65 nm from the surface. In these last ca.65 nm towards the uppermost surface, a substantial variation in the mapping suggests a depleted copper content with an increased quantity of zinc alongside oxygen. This proposes the formation of zinc oxide through laser processing. In comparison to the GI-XRD results, no oxide phases were discernible in the XRD spectra. One potential explanation for this could be that the oxide formed in this case is of an amorphous nature, making it challenging to detect via XRD.

For further analysis, line scans containing seven points were carried out from the bulk towards the surface. The results are summarized in Table 1 showing that the values are in agreement with the bulk composition until the second last position. However, a drastic change in the composition was recorded for the last position close to the surface. Here, the copper content is reduced from about 84 to 27 at-%. In parallel, an increase is recorded for zinc from about 14.5 to 57 at-% as well as for oxygen from a negligible value to 15.5 at-%. Hence, the occurrence of oxides on the surface is confirmed. The chemical composition suggests the formation of a mixture of zinc and copper oxides. Excluding oxygen, the Cu/Zn atomic ratio on the topmost surface is now approx. 0.48.

Additionally, the chemical composition of CuZn15 etched is shown in Table 2 The results show a decrease in oxygen content from 15.5 to 8.7 at-% implying a successful, but partial removal of oxides through etching. Simultaneously, the reduction in zinc and oxygen confirms the formation of a zinc-rich oxide layer through laser structuring. The preferential formation of zinc oxide is related to the fact that zinc requires, comparatively, lower Gibbs energy change for the oxide formation.[27].

As the new layer is revealed after etching, it now has a Cu to Zn

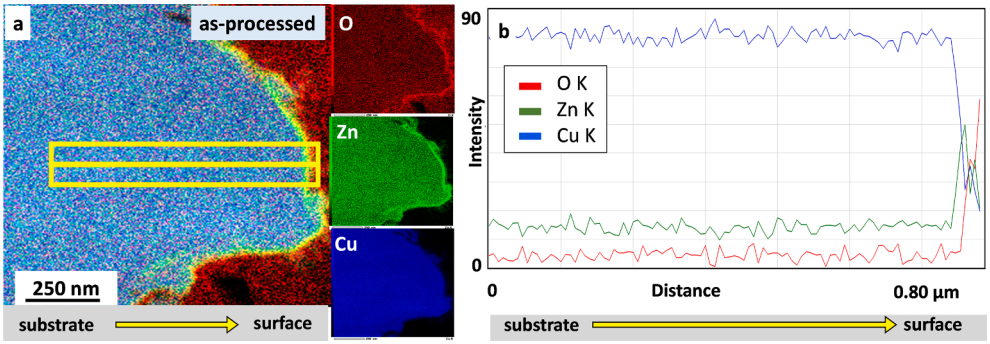

Fig. 3. Results of STEM-EDS mapping on as-processed CuZn15: (a) color elemental map of a peak (clockwise rotation at 90°, substrate (left) to surface (right)); (b) the intensity profile of the yellow line scan in a). (For interpretation of the references to color in this figure legend, the reader is referred to the web version of this article.)

Table 1
Results of STEM-EDS on CuZn15 as-processed.

Distance from the surface [nm]	at-%		
	Cu	Zn	O
709	84.8	14.5	0.7
592	84.8	14.4	0.8
475	83.9	14.9	1.2
358	84.3	14.6	1.1
242	85.6	14.3	0.1
125	84.2	14.6	1.2
0	27.3	57.2	15.5

Table 2
Results of STEM-EDS on CuZn15 etched.

Distance from the surface [nm]	at-%		
	Cu	Zn	O
509	84.8	14.3	0.9
426	84.7	14.6	0.7
339	84.9	14.4	0.7
256	84.8	14.3	0.9
175	83.6	14.7	1.7
85	84.0	15.0	1.0
0	66.4	24.9	8.7

atomic ratio of about 2.7 indicating a copper-rich uppermost layer (see Table 2). Fig. 4 shows the TEM-EDS map and profile of an etched sample and as it is compared with the profile of the as-processed sample in Fig. 3, it shows that a few tens of nanometers has been removed from the surface through etching. The elevated thermal and kinetic energy near the surface, induced by laser irradiation, plays a key role in facilitating the diffusion of copper and zinc atoms in the subsurface, providing an explanation for this occurrence. As the sample is etched and the zinc-rich phase with oxygen is removed, the inner layer into which the copper has diffused becomes visible.

3.4. Characterization of oxide phases

In this section, XPS analysis combined with surface ablation by Ar-ion etching is utilized to further investigate the chemical composition as well as the oxidation state of Cu and Zn at the surface and subsurface levels.

First, XPS-based elemental depth profiles are recorded and the results are displayed in Fig. 5 a. Here, the two horizontal reference lines represent the bulk concentration (in at-%) for copper (orange) and zinc (blue). The as-processed CuZn15 sample shows a reduced content of copper and an equally increased concentration of zinc towards the surface. The same effect is visible on the etched sample. However, the depth of this variation is significantly less. This is connected to the presence of oxygen on the subsurface of the samples (see Fig. 5 b and c), which is deeper for the as–processed samples. For the as-processed sample, the nearly 1: 1 ratio of Cu and Zn in Fig. 5 a is not in contrast to Table 1 where an enrichment of Zn is observed. In Table 1 the increase of Zn content is observed at the peak positions of the line structures while in Fig. 5 the XPS data display intensities as averaged over nearly 1 cm^2. These distinctions are likely attributable to the uneven distribution of chemical composition at the ten-nanometer range.[20] Nevertheless, the commonality lies in the increase of zinc content in the modified surface area relative to the bulk composition.

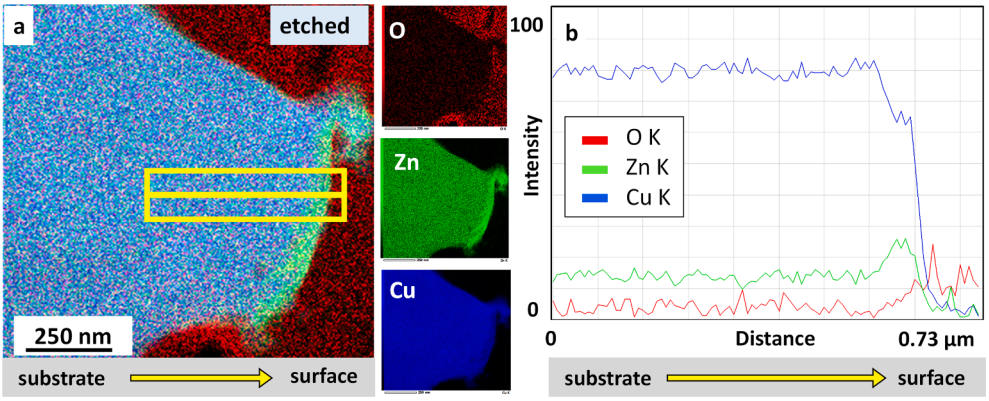

Fig. 4. Results of STEM-EDS mapping on etched CuZn15: (a) color elemental map of a peak (clockwise rotation at 90°, substrate (left) to surface (right)); (b) the intensity profile of the yellow line scan in a). (For interpretation of the references to color in this figure legend, the reader is referred to the web version of this article.)

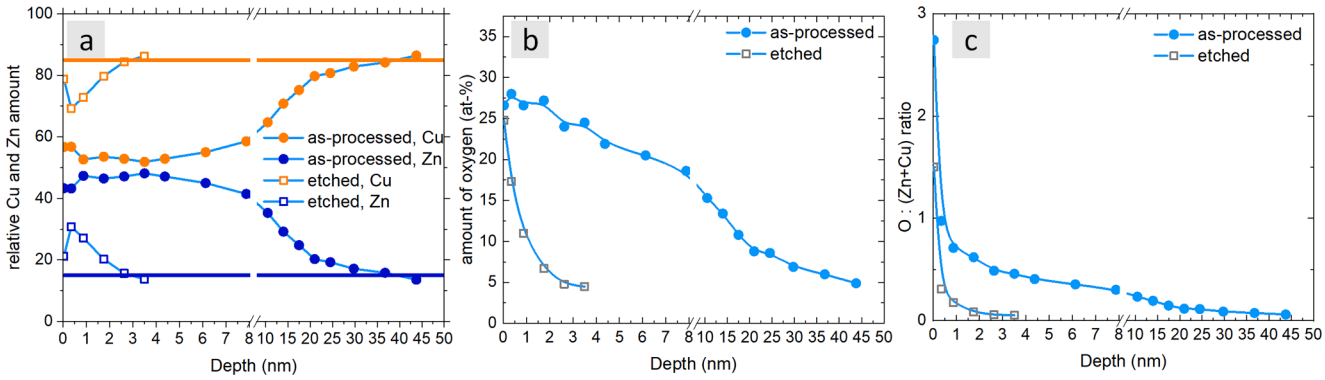

Fig. 5. (a) Atomic Cu:Zn ratio (b) amount of oxygen in at.% and (c) atomic O:(Zn + Cu) ratio as obtained by elemental depth profiling in XPS for CuZn15.

The survey data of the as-received samples (i.e., before Ar ion ablation) showed the presence of Cu, Zn, and O (as well as C from adsorbates). For quantitative analysis (i.e., distribution of elements, oxidation state of Zn and Cu), high-resolution spectra were recorded for O 1 s, Cu 2p, Zn 2p, Cu LMM, and Zn LMM. The analysis approach was the same as described in Ahmed *et al.* [20] In the Cu-2p spectra in Fig. 6 a and b contributions from Cu and Cu_2O cannot be distinguished. However, CuO differs from Cu and Cu_2O by two spectral features. For CuO, there is a shift to higher binding energy and there is the characteristic satellite at higher binding energy. [28–31] Contributions from Cu can be distinguished from contributions of Cu_2O and CuO by the low binding energy part (approx. 565 eV) of the $L_3M_{45}M_{45}$ peak in the Cu-LMM spectra in Fig. 6 c and d. Zn-2p spectra in general display no characteristic features to distinguish Zn from ZnO. Contributions from Zn and ZnO can be distinguished by the differences in peak shape and peak position in the Zn-LMM spectra in Fig. 6 e and f. [28,32,33].

Fig. 6 a shows the Cu-2p spectra for the CuZn15 (as-processed) sample as well as for Cu and CuO reference samples. In the initial state (no Ar ion etching, ablation 0 nm), the double Cu-$2p_{3/2}$ and Cu-$2p_{1/2}$ peaks as well as the CuO-like satellites ($Sat_{3/2}$, $Sat_{1/2}$) predict contributions of CuO and Cu/Cu_2O. After ablation of only 0.35 nm, no spectral features of CuO are visible, i.e. there is e.g. a single Cu-$2p_{3/2}$ peak at 932.4 eV as representing Cu and/or Cu_2O. [28,32] Since the thickness of the ablated surface layer is in the range of atomic distances in Cu or Cu oxides, the absence of any CuO-related spectral features gives evidence that the formation of CuO only affects the 1–2 outmost atomic layers. Fig. 6 c illustrates the Cu LMM spectra compared to the spectra from Cu and CuO reference samples. For Cu_2O the reference spectrum is taken from Fig. 5 in Schedel *et al.* [30] (since the spectra for Cu and CuO shown there are very similar to the spectra of Cu and CuO as probed with our setup). In the as-provided state (0 nm) and after ablation of 0.35 nm, the spectra display a superposition of the Cu, Cu_2O, and CuO spectra. At further ablation (i.e., $\geq$ 0.88 nm) the Cu contribution starts to increase (see e.g., the Cu-characteristic peak at 565 eV), and with each new step of ablation, the spectra adapt more and more the Cu reference data. According to Fig. 6 a and c, CuO is present only at the surface (and maybe the subsurface layer) while Cu_2O is distributed only up 3–4 nm into the bulk.

Fig. 6 e shows the Zn LMM spectra for CuZn15 in the as-processed state. When compared to spectra as probed on ZnO and Zn reference samples it is evident that ZnO is distributed much deeper into the bulk than CuO and Cu_2O. Even after an ablation of approx. 44 nm the Zn-LMM spectrum still represents a superposition of Zn and ZnO. The amount of ZnO exceeds the amount of Zn in depths ranging down to 15 nm. Below 15 nm the amount of Zn starts to dominate but even in the deepest bulk range that was probed (i.e., approx. 44 nm) the Zn LMM spectrum still displays contributions from ZnO. Compared to the distribution of CuO and Cu_2O, the distribution of ZnO in Fig. 5 c and Fig. 6 e evidently show that Zn traps oxygen. This is also supported by the amount of oxygen in Fig. 5 b that is distributed in line with the amount of Zn in Fig. 5 a.

After etching CuZn15 samples with citric acid, the chemical composition of the surface and the subsurface regime is strongly different. Fig. 5 b shows a significant decrease in the oxygen content. In Fig. 6 b nearly no CuO-related satellite is visible in the Cu-2p spectrum for zero ablation, i.e., there is nearly no CuO even at the surface. The Cu-LMM in Fig. 6 d shows that there is also no large contribution of Cu_2O in the subsurface regime. Only at the surface (0 nm ablation), the Cu-LMM displays an overlap of the Cu and Cu_2O reference data, but at 0.35 nm ablation, the Cu-LMM spectrum strongly resembles the spectrum of the Cu reference sample. After etching, ZnO is still present in the bulk. However, the Zn-LMM spectra in Fig. 6 f show that the contributions of ZnO are strongly reduced in comparison to the as-processed sample. The amount of ZnO is much strongly reduced with increasing depth as in the case of the as-processed sample. This is shown by e.g., the comparable weak ZnO-related peak intensities at 498 eV in comparison to the Zn-related peak intensities at about 495 eV. In the Zn-LMM spectrum of CuZn15 etched at about 3.50 nm ablation in Fig. 6 f shows that the ZnO-related peak is smaller as in the Zn-LMM spectrum of CuZn15 as-processed at about 43.75 nm ablation in Fig. 6 e. Etching of the CuZn15 sample therefore results in a decrease of the thickness of the (mainly) ZnO layer by more than one order of magnitude. As observed in comparison with the STEM-EDS results, it is evident that a layer measuring a few tens of nanometers has been removed from the surface through etching.

The findings indicate the presence of cupric oxide primarily at the topmost layer, while the formation of zinc oxide and cuprous oxide occurs in the underlying layers beneath the surface. Additionally, the much higher concentration of zinc throughout the modified thickness and towards the upper surface of CuZn15 as-processed suggests an asymmetrical diffusion. Therefore, a non-equilibrium transport of the lattice is observed, where the diffusion of the zinc atoms towards the surface is significantly faster than the diffusion of the copper atoms away from the surface. This phenomenon is commonly known as the Kirkendall effect.[34] After etching, there is a decrease in the levels of zinc and oxygen, leading to the emergence of a copper-rich oxide phase. This observation implies the partial elimination of the zinc oxide phase.

3.5. Antibacterial tests

This section is concerned with the results of contact killing tests on brass with 15 % zinc (CuZn15). In total, three different surfaces of CuZn15 in the polished, as-processed, and etched state were tested, along with mirror-polished copper and stainless steel as references.

Fig. 7 a exhibits the surviving CFU/mL values over a contact period of 120 min for all samples. Furthermore, these results are complemented by the corresponding release of Cu-ions after 120 min (see the bars in Fig. 7 b). The references show an expected antibacterial behavior i.e.,

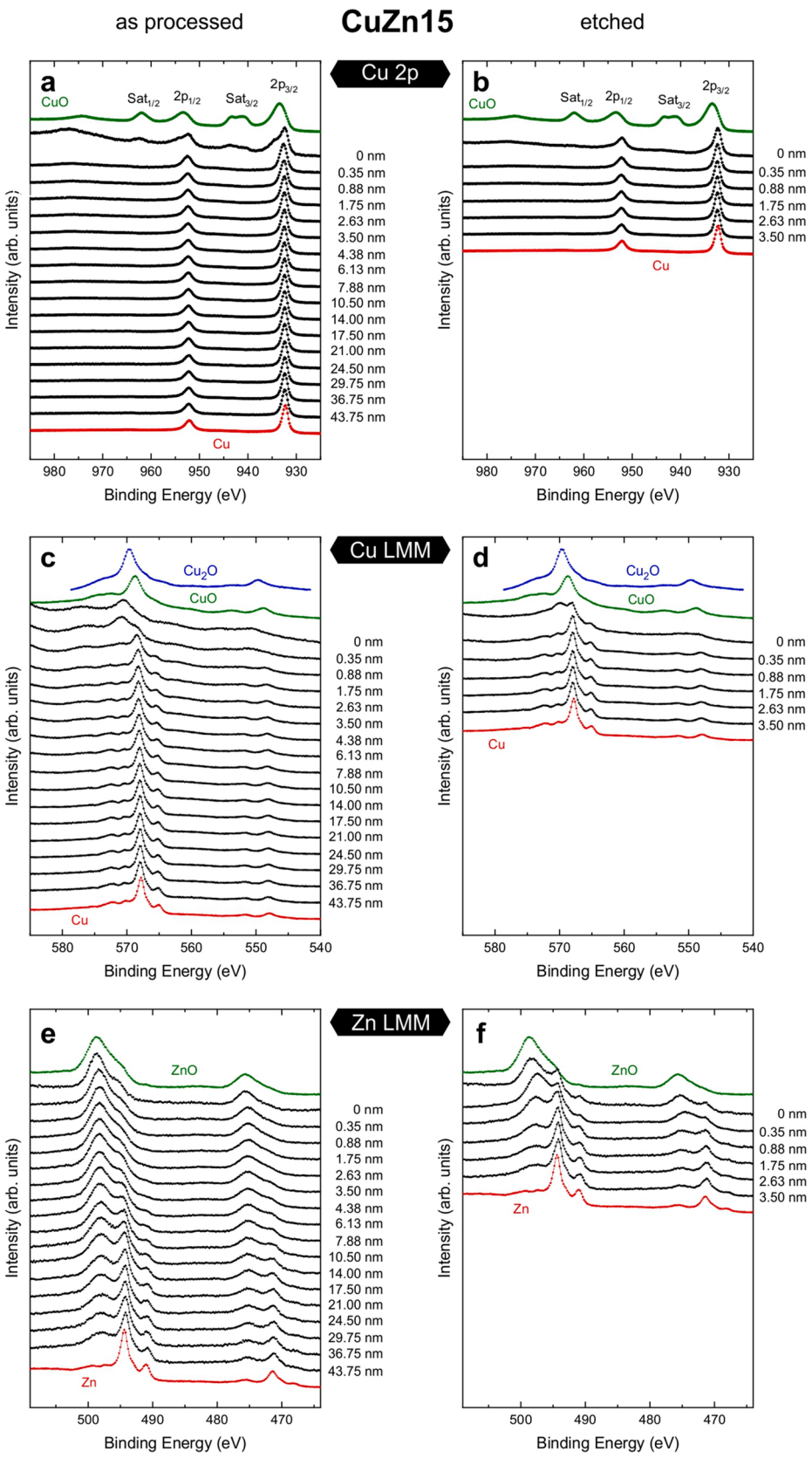

Fig. 6. High-resolution XPS-spectra of (a, b) Cu 2p, (c, d) Cu LMM and (e, f) Zn LMM of as-processed (a, c, e) and etched samples (b, d, f), respectively. This also includes the reference spectra for CuO (green), Cu_2O (dark blue), Cu (red), ZnO (green) and Zn (red). (For interpretation of the references to color in this figure legend, the reader is referred to the web version of this article.)

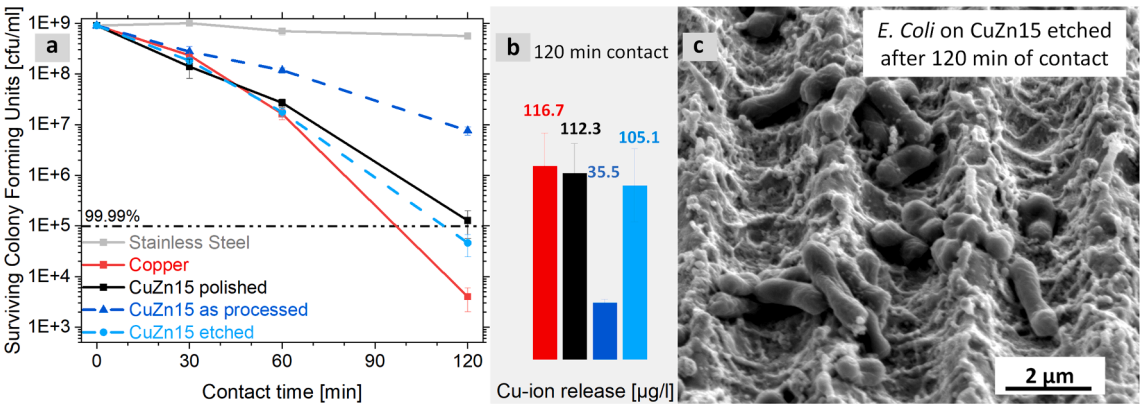

Fig. 7. Results of contact killing experiment with *E. coli*: (a) Surviving colony-forming units for 30, 60 and 120 min on reference surfaces (steel and copper) and all three CuZn15 surfaces (polished, as-processed and etched). (b) The Cu-ion release values at 120 min are represented in form of a bar chart. (c) SEM image of *Escherichia coli* in the line-like structures of the etched CuZn15 surface. The image was taken at 52° tilt.

the poor killing of *E. coli* by stainless steel (grey) and an excellent one by the copper surface (red). [7,20] Simultaneously, the polished CuZn15 (black) displays a similar behavior until the first 60 min of exposure as compared to the copper reference. However, in the following 60 min, it shows a relatively reduced killing of *E. coli*. This can be attributed to the lower concentration of copper in brass,[6,35] which was validated by the slightly reduced Cu-ion release concentration after 120 min. Meanwhile, a drastic change in antibacterial behavior is observed for the as-processed CuZn15 (dark blue). In the initial 60 min of contact, the number of surviving CFU/mL is one magnitude higher compared to the polished brass surface. However, with the increasing exposure time, the killing rate on the as-processed surface is attenuated resulting in a bigger difference. This is attributed to the fact that the copper content has reduced by half (as also shown by STEM-EDS results), which explains the lowered Cu-ions release and thence decreased killing of *E. coli.* At the same time, the zinc content has increased. A previous study suggests an antibacterial effect of ZnO nanostructures on *E. coli*, attributed to the release of zinc ions under UV irradiation. [36] However, the experiments in this study were conducted on bulk material under ambient conditions, and there are no studies demonstrating an antibacterial effect of zinc without UV irradiation. However, etching the surface results in an improved efficiency, which in the case of CuZn15 etched (light blue graph in Fig. 7 a) is instantly better than that of polished CuZn15 (black graph). This can be attributed to the removal of the unwanted oxide layer, exposing the layer beneath with more favorable conditions to release copper ions. It is to be noticed that the Cu-ion release for the etched sample is similar to that for the polished and yet the killing on the etched surface is enhanced. This is a possible result of the topographical modification, which is further examined in the next section.

3.6. State of surface after bacteria-substrate contact

Fig. 7 c displays the bacterial-substrate contact, revealing that the bacteria mainly reside in the valleys of the structures. This contact results in a significant alteration of both the surface and the bacteria. In order to investigate this further, a comparison of the surface topography was conducted before and after contact with the bacteria. Fig. 8 a and c illustrate the surface prior to contact with *E. coli*, showing a rapid cooling of the melted material along with the redeposition of ablated material in the form of round nanoparticles, as well as smooth surface areas in between.

After contact with the bacteria (Fig. 8 b and d), the surface exhibits nano roughness, which is indicative of corrosion and subsequent release of Cu ions. This effect is particularly prominent in the valleys. Furthermore, the Cu ion release observed for the etched surface (light blue) in Fig. 7 a is comparable to that of polished CuZn15 (black). This suggests that the improved ability to kill *E. coli* on the etched surface is due to both the release of copper ions and the surface's topography.

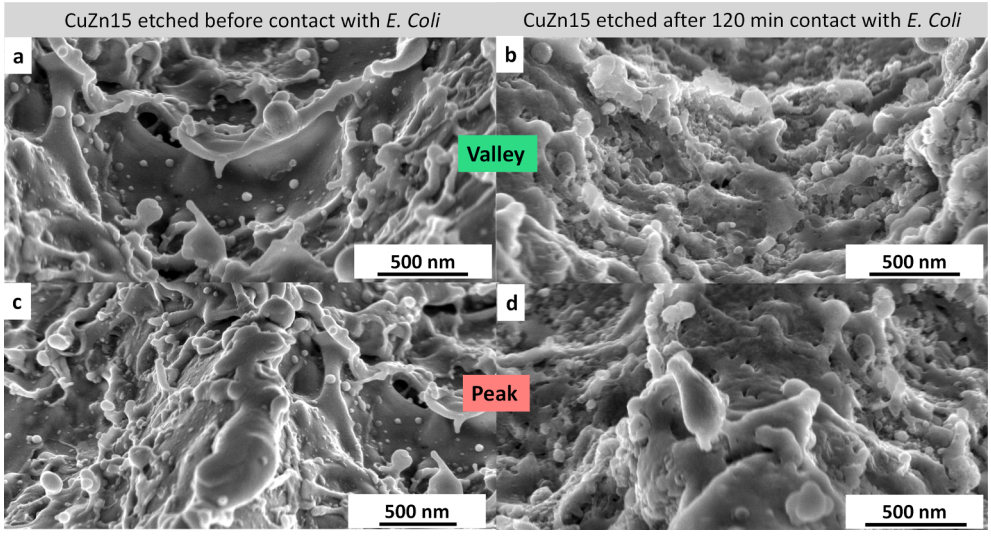

Fig. 8. SEM images of the etched CuZn15 surface exhibiting valley and peak of line-like structures each (a, c) before and (b, d) after 120 min contact with *E. coli*. The images were taken at 52° tilt.

Chemical analysis was conducted using SEM-EDS to further examine the samples. The results in Fig. 9 b show that the peak (red, position 2 in Fig. 9 a) contains higher zinc and oxide content compared to the valley (green, position 1 in Fig. 9 a). This might explain why the peaks have greater resistance to corrosion in the bacterial solution with PBS and experience less alteration on their surfaces after coming into contact with bacteria. However, further investigations need to be done to determine the corrosion resistance of the brass surface modified via DLIP.

When the bacteria are taken under observation one interesting aspect noticed here is the presence of nano agglomerates on the cell membrane (see Fig. 9 a). These agglomerates were identified as part of the bacterial cell membrane upon closer examination (magnified in the yellow circle in Fig. 9 a). This is potentially associated with the penetration of Cu-ions into the bacterial cells. To investigate the chemical composition of these agglomerates, SEM-EDS analysis was conducted (see position 3, pink spectra in Fig. 9 b). However, it should be noted that the characterization method has limitations, and therefore the results may also contain information from the substrate beneath the bacteria. The exact interaction mechanism between ions and bacteria still remains inconclusive. However, previous studies [8,9,37] suggest that when the cell membrane is ruptured, there is a leakage of intracellular components leading to the death of bacterial cell. Alternatively, there is a chance that before cell membrane rupture, copper ions deposit onto the membrane and are subsequently absorbed into the cell through respiratory processes. These Cu-ions are likely to react with these components as well as DNA, leading to the formation of copper complexes. These complexes hinder any potential repair processes, contributing to the eventual deterioration of bacterial cells.

To further observe the bacteria-substrate contact, FIB cross-sections were performed perpendicular to the line-like structures containing *E. coli*. Fig. 10 a shows that the bacterium on the right side exhibits strong adhesion, with the bacterial cell membrane appearing to merge with the substrate. On the left, the bacterium has detached a portion of the surface, revealing underlying surface corrosion. Furthermore, backscattered electron (BSE) imaging was utilized to detect the contrast between bacteria with different chemical compositions. In Fig. 10 b, the BSE image shows varying contrasts within the bacteria. Bacterium no. 1 displays no contrast, while bacterium no. 2 exhibits a uniform distribution of brighter and darker zones. Bacterium no. 3 exhibits the most distinct contrast between the inner part of the bacterium and the nano agglomerates formed within the cell membrane. The presence of copper, which is a heavier element than other elements in the chemical composition of *E. coli*, may cause it to appear brighter in the image. By comparing the FIB-SEM and BSE images, it is evident that different bacteria are likely in different stages of adhesion and contact with Cu-ions. To gain a better understanding of these phenomena, further investigation methods will be necessary for future studies.

4. Conclusion

This study investigates and compares the importance of zinc content in brass for surface modification using USP-DLIP to previous studies. A chemical composition with zinc content lower than 30 ± 3 wt-% was chosen to lower the possibility of the formation of intermetallic phases in brass. As expected, the only chemical modification observed is the formation of oxide phases. The results reveal a profound modification on a nanoscale, with a significant presence of zinc oxide in both superficial and subsurface layers.

After laser processing, the reduced copper content in the brass leads to a slower killing rate compared to a polished brass sample. However, after etching, the amount of zinc oxide decreases, followed by the complete removal of cupric oxide from the uppermost layer. This exposes a copper-rich layer, resulting in a higher release of Cu-ions and consequently a higher killing rate of *E. coli* on the etched brass with 15 % zinc compared to the polished brass sample.

The SEM images and EDS analysis suggest an alteration of the surface as well as bacteria upon contact with each other. It is noticeable that the valleys have a higher level of corrosion in the presence of bacterial solution with PBS compared to the peaks. This difference in corrosion may be attributed to the higher zinc and oxide content in the peaks, i.e., possibly higher corrosion resistance, which needs to be investigated in future. The bacteria, on the other hand, show the formation of nano agglomerates on their cell membrane. This indicates a possible presence of Cu-ions in the bacteria, as also suggested by the BSE imaging. The findings suggest that the enhanced antibacterial activity is attributed to a higher quantitative bacteria-substrate contact accompanied by a higher Cu-ion release. However, further investigations using high-resolution methods are needed to fully understand the bacteria-substrate interaction and the killing mechanism of Cu-ions. Additionally, exploring other etching solutions can help remove zinc oxide fully from the structured surfaces and analyze its impact on the bacteria-substrate contact.

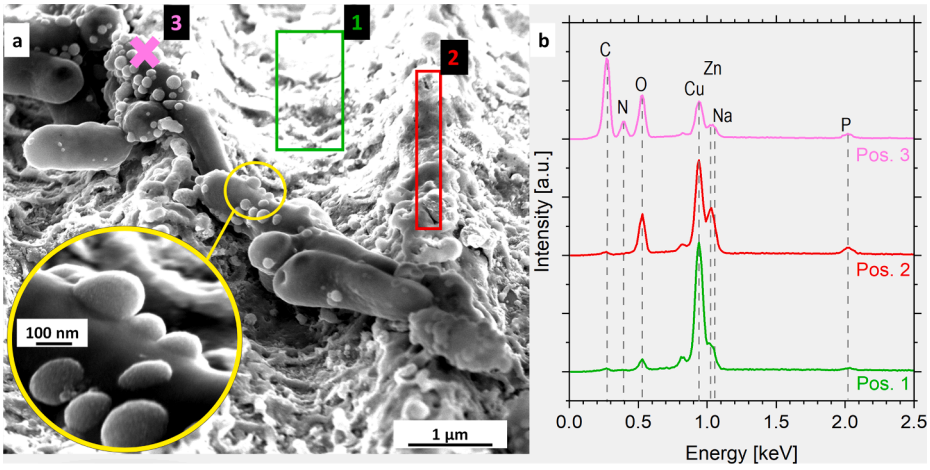

Fig. 9. (a) SEM image of *E. coli* on the structured and etched CuZn15 surface after two hours exposure time. The yellow circle represents the position of magnified image of the bacteria with nano agglomerates. The squares and cross shape show the position of EDS measurements. The images were taken at a tilt of 52°. The corresponding EDS spectra are displayed in (b). (For interpretation of the references to color in this figure legend, the reader is referred to the web version of this article.)

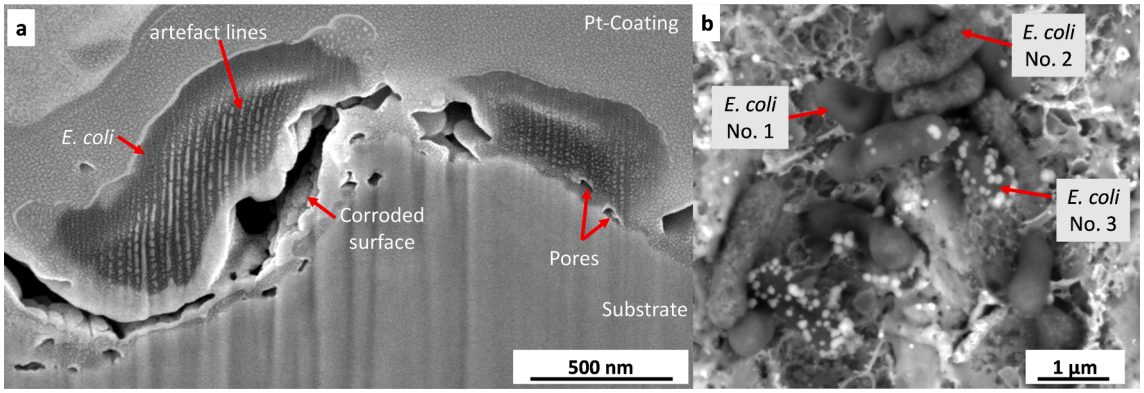

Fig. 10. (a) SEM image of bacteria on substrate. The FIB cross section was done perpendicular to the line-like structures. The artefact lines in the bacteria are a result of FIB cross section. (b) BSE image of *E. coli* on CuZn15 etched.

CRediT authorship contribution statement

Aisha Saddiqa Ahmed: Conceptualization, Investigation, Validation, Visualization, Writing – original draft. **Daniel Wyn Müller:** Investigation, Validation, Writing – review & editing. **Stéphanie Bruyère:** Investigation, Validation, Writing – review. **Anne Holtsch:** Investigation, Validation, Writing – review & editing. **Frank Müller:** Investigation, Validation, Writing – review & editing. **Kristina Brix:** Investigation, Validation, Writing – review. **Sylvie Migot:** Investigation. **Ralf Kautenburger:** Supervision. **Karin Jacobs:** Writing – review & editing, Supervision. **Jean–François Pierson:** Writing – review & editing, Resources, Supervision. **Frank Mücklich:** Funding acquisition, Resources, Supervision.

Declaration of competing interest

The authors declare that they have no known competing financial interests or personal relationships that could have appeared to influence the work reported in this paper.

Data availability

Data will be made available on request.

Acknowledgments

The Author would like to thank to the group of Prof. Rolf Müller from the Helmholtz Centre of Infection Research in Saarbrücken for providing the *E. coli*. The authors would like to thank the technical platforms “Microscopies, Microprobes and Metallography (3 M)” and “Optic and Lasers” at Institut Jean Lamour (IJL, Nancy, France) for access to FIB and TEM facilities.

References

[1] CDC, Antibiotic Resistance Threats in The United States 2019, Cdc 10 (2019). doi: https://doi.org/10.15620/cdc:82532.
[2] A.U.M. Khan, A. Torelli, I. Wolf, N. Gretz, AutoCellSeg: Robust automatic colony forming unit (CFU)/cell analysis using adaptive image segmentation and easy-to-use post-editing techniques, Sci Rep 8 (2018), https://doi.org/10.1038/s41598-018-24916-9.
[3] K.A. Davis, J.J. Stewart, H.K. Crouch, C.E. Florez, D.R. Hospenthal, Methicillin-resistant Staphylococcus aureus (MRSA) nares colonization at hospital admission and its effect on subsequent MRSA infection, Clinical Infectious Diseases 39 (2004) 776–782, https://doi.org/10.1086/422997.
[4] R.M. Donlan, Biofilm formation: A clinically relevant microbiological process, Clinical Infectious Diseases 33 (2001) 1387–1392, https://doi.org/10.1086/322972.
[5] J. Hasan, R.J. Crawford, E.P. Ivanova, Antibacterial surfaces: The quest for a new generation of biomaterials, Trends Biotechnol 31 (2013) 295–304, https://doi.org/10.1016/j.tibtech.2013.01.017.
[6] J. Luo, A. Ahmed, J.F. Pierson, F. Mücklich, Tailor the antibacterial efficiency of copper alloys by oxidation: when to and when not to, J Mater Sci 57 (2022) 3807–3821, https://doi.org/10.1007/s10853-022-06879-5.
[7] D.W. Müller, S. Lößlein, E. Terriac, K. Brix, K. Siems, R. Moeller, R. Kautenburger, F. Mücklich, Increasing Antibacterial Efficiency of Cu Surfaces by targeted Surface Functionalization via Ultrashort Pulsed Direct Laser Interference Patterning, Adv Mater Interfaces 8 (2021), https://doi.org/10.1002/admi.202001656.
[8] M. Raffi, S. Mehrwan, T.M. Bhatti, J.I. Akhter, A. Hameed, W. Yawar, M.M. Ul Hasan, Investigations into the antibacterial behavior of copper nanoparticles against Escherichia coli, Ann Microbiol 60 (2010) 75–80, https://doi.org/10.1007/s13213-010-0015-6.
[9] G. Tong, M. Yulong, G. Peng, X. Zirong, Antibacterial effects of the Cu(II)-exchanged montmorillonite on Escherichia coli K88 and Salmonella choleraesuis, Vet Microbiol 105 (2005) 113–122, https://doi.org/10.1016/J.VETMIC.2004.11.003.
[10] F.A. Bezza, S.M. Tichapondwa, E.M.N. Chirwa, Fabrication of monodispersed copper oxide nanoparticles with potential application as antimicrobial agents, Sci Rep 10 (2020), https://doi.org/10.1038/s41598-020-73497-z.
[11] C. Angelé-Martínez, K.V.T. Nguyen, F.S. Ameer, J.N. Anker, J.L. Brumaghim, Reactive oxygen species generation by copper(II) oxide nanoparticles determined by DNA damage assays and EPR spectroscopy, Nanotoxicology 11 (2017), https://doi.org/10.1080/17435390.2017.1293750.
[12] A.F. Lasagni, C. Gachot, K.E. Trinh, M. Hans, A. Rosenkranz, T. Roch, S. Eckhardt, T. Kunze, M. Bieda, D. Günther, V. Lang, F. Mücklich, Direct laser interference patterning, 20 years of development: from the basics to industrial applications, in: Laser-Based Micro- and Nanoprocessing XI, SPIE, 2017: p. 1009211. doi: 10.1117/12.2252595.
[13] X. Li, G.S. Cheung, G.S. Watson, J.A. Watson, S. Lin, L. Schwarzkopf, D.W. Green, The nanotipped hairs of gecko skin and biotemplated replicas impair and/or kill pathogenic bacteria with high efficiency, Nanoscale 8 (2016) 18860–18869, https://doi.org/10.1039/c6nr05046h.
[14] K. Liu, L. Jiang, Bio-inspired design of multiscale structures for function integration, Nano Today 6 (2011) 155–175, https://doi.org/10.1016/j.nantod.2011.02.002.
[15] R.J. Crawford, E.P. Ivanova, S.H. Nguyen, H.K. Webb, Natural Superhydrophobic Surfaces, Superhydrophobic Surfaces (2015) 7–25, https://doi.org/10.1016/B978-0-12-801109-6.00002-1.
[16] E. Arzt, H. Quan, R.M. McMeeking, R. Hensel, Functional surface microstructures inspired by nature – From adhesion and wetting principles to sustainable new devices, Prog Mater Sci 120 (2021) 100823, https://doi.org/10.1016/J.PMATSCI.2021.100823.
[17] F. Rößler, V. Lang, D. Günther, A.F. Lasagni, Fabricating Three-Dimensional Periodic Micro Patterns on Photo-Resists Using Laser Interference Lithography, Adv Eng Mater 19 (2017), https://doi.org/10.1002/adem.201600855.
[18] J. Bonse, J. Krüger, Probing the heat affected zone by chemical modifications in femtosecond pulse laser ablation of titanium nitride films in air, J Appl Phys 107 (2010), https://doi.org/10.1063/1.3311552.
[19] D.W. Müller, A. Holtsch, S. Lößlein, C. Pauly, C. Spengler, S. Grandthyll, K. Jacobs, F. Mücklich, F. Müller, In-Depth Investigation of Copper Surface Chemistry Modification by Ultrashort Pulsed Direct Laser Interference Patterning, Langmuir 36 (2020) 13415–13425, https://doi.org/10.1021/acs.langmuir.0c01625.
[20] A.S. Ahmed, D.W. Müller, S. Bruyere, A. Holtsch, F. Müller, J. Barrirero, K. Brix, S. Migot, R. Kautenburger, K. Jacobs, J.-F. Pierson, F. Mücklich, Surface Modification of Brass via Ultrashort Pulsed Direct Laser Interference Patterning and Its Effect on Bacteria-Substrate Interaction, ACS Appl Mater Interfaces (2023), https://doi.org/10.1021/acsami.3c04801.
[21] P. Kejzlar, J. Machuta, I. Nová, Comparison of the Structure of CuZn40MnAl Alloy Casted into Sand and Metal Moulds, Manufacturing Technology 17 (2017) 15, https://doi.org/10.21062/ujep/x.2017/a/1213-2489/MT/17/1/44.
[22] D.W. Müller, T. Fox, P.G. Grützmacher, S. Suarez, F. Mücklich, Applying Ultrashort Pulsed Direct Laser Interference Patterning for Functional Surfaces, Sci Rep 10 (2020), https://doi.org/10.1038/s41598-020-60592-4.

[23] T. Degen, M. Sadki, E. Bron, U. König, G. Nénert, The high score suite, Powder Diffr (2014), https://doi.org/10.1017/S0885715614000840.
[24] E.R. Sanders, Aseptic laboratory techniques: Plating methods, Journal of Visualized Experiments (2012) 1–18, https://doi.org/10.3791/3064.
[25] L.V. Zhigilei, B.J. Garrison, Microscopic mechanisms of laser ablation of organic solids in the thermal and stress confinement irradiation regimes, J Appl Phys 88 (2000) 1281–1298, https://doi.org/10.1063/1.373816.
[26] J.E. Masse, G. Barreau, Laser generation of stress waves in metal, Surf Coat Technol 70 (1995) 231–234, https://doi.org/10.1016/0257-8972(95)80020-4.
[27] M. Hasegawa, Ellingham Diagram, Treatise on, Process Metallurgy 1 (2014) 507–516, https://doi.org/10.1016/B978-0-08-096986-2.00032-1.
[28] S. Poulston, P.M. Parlett, P. Stone, M. Bowker, Surface oxidation and reduction of CuO and Cu2O studied using XPS and XAES, Surface and Interface Analysis 24 (1996) 811–820, https://doi.org/10.1002/(SICI)1096-9918(199611)24:12<811::AID-SIA191>3.0.CO;2-Z.
[29] D. Barreca, A. Gasparotto, E. Tondello, CVD Cu2O and CuO Nanosystems Characterized by XPS, Surface Science Spectra 14 (2007) 41–51, https://doi.org/10.1116/11.20080701.
[30] T. Schedel-Niedrig, T. Neisius, I. Böttger, E. Kitzelmann, G. Weinberg, D. Demuth, R. Schlögl, Copper (sub)oxide formation: A surface sensitive characterization of model catalysts, Physical Chemistry Chemical Physics 2 (2000) 2407–2417, https://doi.org/10.1039/b000253o.
[31] L. Armelao, D. Barreca, M. Bertapelle, G. Bottaro, C. Sada, E. Tondello, A sol–gel approach to nanophasic copper oxide thin films, Thin Solid Films 442 (2003) 48–52, https://doi.org/10.1016/S0040-6090(03)00940-4.
[32] J.P. Tobin, W. Hirschwald, J. Cunningham, XPS and XAES studies of transient enhancement of Cu1 at CuO surfaces during vacuum outgassing, Applications of Surface Science 16 (1983) 441–452, https://doi.org/10.1016/0378-5963(83)90085-5.
[33] F. Wiame, F.R. Jasnot, J. Wiatowska, A. Seyeux, F. Bertran, P. le Fèvre, A. Taleb-Ibrahimi, V. Maurice, P. Marcus, Oxidation of α-brass: A photoelectron spectroscopy study, Surf Sci 641 (2015) 51–59, https://doi.org/10.1016/j.susc.2015.05.013.
[34] E.O. Kirkendall, Diffusion of zinc in alpha brass, Trans. Am. Inst Min. Metall 147 (1942) 104–110.
[35] S. Mehtar, I. Wiid, S.D. Todorov, The antimicrobial activity of copper and copper alloys against nosocomial pathogens and Mycobacterium tuberculosis isolated from healthcare facilities in the Western Cape: an in-vitro study, Journal of Hospital Infection 68 (2008) 45–51, https://doi.org/10.1016/j.jhin.2007.10.009.
[36] R. Goyal, P. Roy, P. Jeevanandam, Antibacterial activity studies of ZnO nanostructures with different morphologies against E, in: Coli and S. Aureus, Appl Phys A Mater Sci Process 129, 2023, https://doi.org/10.1007/s00339-023-06530-3.
[37] J. Luo, C. Hein, J. Ghanbaja, J.F. Pierson, F. Mücklich, Bacteria accumulate copper ions and inhibit oxide formation on copper surface during antibacterial efficiency test, Micron 127 (2019), https://doi.org/10.1016/j.micron.2019.102759.

PUBLICATION III

Femtosecond-DLIP on Tin-Alloyed Bronze: Effect of Pulse Fluence on Surface Topography for Antibacterial Application

Aisha Saddiqa Ahmed[a,b], Diego Sancio[a], Daniel Wyn Müller[a], Jean-François Pierson[b], Frank Mücklich[a]

[a] *Chair of Functional Materials, Department of Material Science and Engineering, Saarland University, 66123 Saarbrücken, Germany*

[b] *Université de Lorraine, CNRS, IJL, F-54000 Nancy, France*

Research article

Published in "**Materials Today Advances**" (2025)

Impact Factor: 8.0 (2025)

Accessible online at: https://doi.org/10.1016/j.mtadv.2025.100596

Own Contributions: Conceptualization, Investigation, Validation, Visualization, Writing – original draft.

Cite this article as: Ahmed, A. S.; Sancio, D.; Müller, D. W.; Pierson, J. F.; Mücklich, F. Femtosecond-DLIP on Tin-Alloyed Bronze: Effect of Pulse Fluence on Surface Topography for Antibacterial Application. *Mater Today Adv* **2025**, *27*. https://doi.org/10.1016/j.mtadv.2025.100596.

Materials Today Advances 27 (2025) 100596

Contents lists available at ScienceDirect

Materials Today Advances

journal homepage: www.journals.elsevier.com/materials-today-advances/

Femtosecond-DLIP on tin-alloyed bronze: Effect of pulse fluence on surface topography for antibacterial application

Aisha Saddiqa Ahmed [a,b,*], Diego Sancio [a], Daniel Wyn Müller [a], Jean-François Pierson [b], Frank Mücklich [a]

[a] Functional Materials, Saarland University, 66123, Saarbrücken, Germany
[b] Université de Lorraine, CNRS, LJL, F-54000, Nancy, France

ARTICLE INFO

Keywords:
Bronze
Copper alloy
Direct laser interference patterning
Ultrashort pulse duration
Femtosecond
Surface modification
Antibacterial

ABSTRACT

The rise of antibiotic resistance has prompted the exploration of other strategies, including the use of material surfaces, to prevent the spread of contagious microorganisms. Copper, renowned for its antimicrobial properties, holds potential in this area. However, its application is often limited from a materials perspective. Therefore, it is crucial to investigate copper alloys to assess their effectiveness in these promising new approaches. For that purpose, the surface of the bronze with 6 % tin content was modified using ultrashort-pulsed direct laser interference patterning (USP-DLIP) to produce 3 μm periodic line-like structures aimed at enhancing antibacterial properties. This study examines how pulse fluence impacts surface topography and subsequently, the killing of *Escherichia coli (E. coli)*. The results show a variation in topography with varied peak-to-valley width ratios. Chemical analyses confirmed an increased copper content and the formation of tin- and copper-rich oxides. Subsequently, the flake-like oxide structures, formed due to laser treatment, were removed via etching with 5 % citric acid. The wettability tests showed increased hydrophobicity over 3 weeks, with etched surfaces exhibiting lower hydrophobicity than as-processed ones. Overall, the etched laser-processed surfaces demonstrated an *E. coli* killing rate of an order of magnitude higher than polished bronze and comparable to pure copper. This enhancement is attributed to the increased contact area and optimized topography achieved through USP-DLIP. This approach presents a promising strategy for antimicrobial surface design.

1. Introduction

To address the growing spread of pathogenic microorganisms, antimicrobial surfaces have become a major focus of research due to their potential to reduce microbial transmission [1,2]. Copper, long known for its antimicrobial properties, remains one of the most promising materials due to its ability to release metallic ions that disrupt bacterial membranes and degrade RNA/DNA upon contact [3–6]. Although copper's antibacterial performance can be significantly enhanced using laser-based surface treatments such as Direct Laser Interference Patterning (DLIP) [7], its limited mechanical strength constrains broader application. Alloying copper with elements like tin improves properties such as hardness, strength, corrosion resistance, and wear resistance. [8], making copper alloys—such as brass and bronze—viable candidates for antimicrobial infrastructure in public spaces like hospitals, schools, and transport systems [9–11]. Bronze, in particular, is suitable for high-touch components (e.g., door handles, railings, bed rails) where its antibacterial properties can help mitigate pathogen spread.

Over recent decades, several strategies have been developed to improve the antibacterial performance of surfaces. One common approach involves the use of copper-based nanoparticles, which release ions and generate reactive oxygen species that damage bacterial membranes and DNA [12,13]. Surface coatings offer another route, combining protective and antimicrobial properties; copper coatings applied by cold gas spraying or onto textiles have shown effective bacterial inhibition [14,15]. In addition to nanoparticles and surface coatings, laser surface structuring has emerged as a powerful technique for enhancing antibacterial activity by modifying the physical and chemical characteristics of material surfaces [7,16–20]. These textures can reduce

Abbreviations: CFU, colony forming units; CLSM, confocal laser scanning microscopy; *E. coli*, *Escherichia coli*; fs, femtosecond; GI-XRD, grazing incidence X-ray diffractometer; LIPSS, laser induced periodic surface structures; SEM, scanning electron microscopy; USP-DLIP, ultrashort-pulsed direct laser interference patterning.

* Corresponding author. Functional Materials, Saarland University, 66123, Saarbrücken, Germany.
E-mail address: aisha.ahmed@uni-saarland.de (A.S. Ahmed).

https://doi.org/10.1016/j.mtadv.2025.100596
Received 1 March 2025; Received in revised form 8 June 2025; Accepted 9 June 2025
Available online 11 June 2025

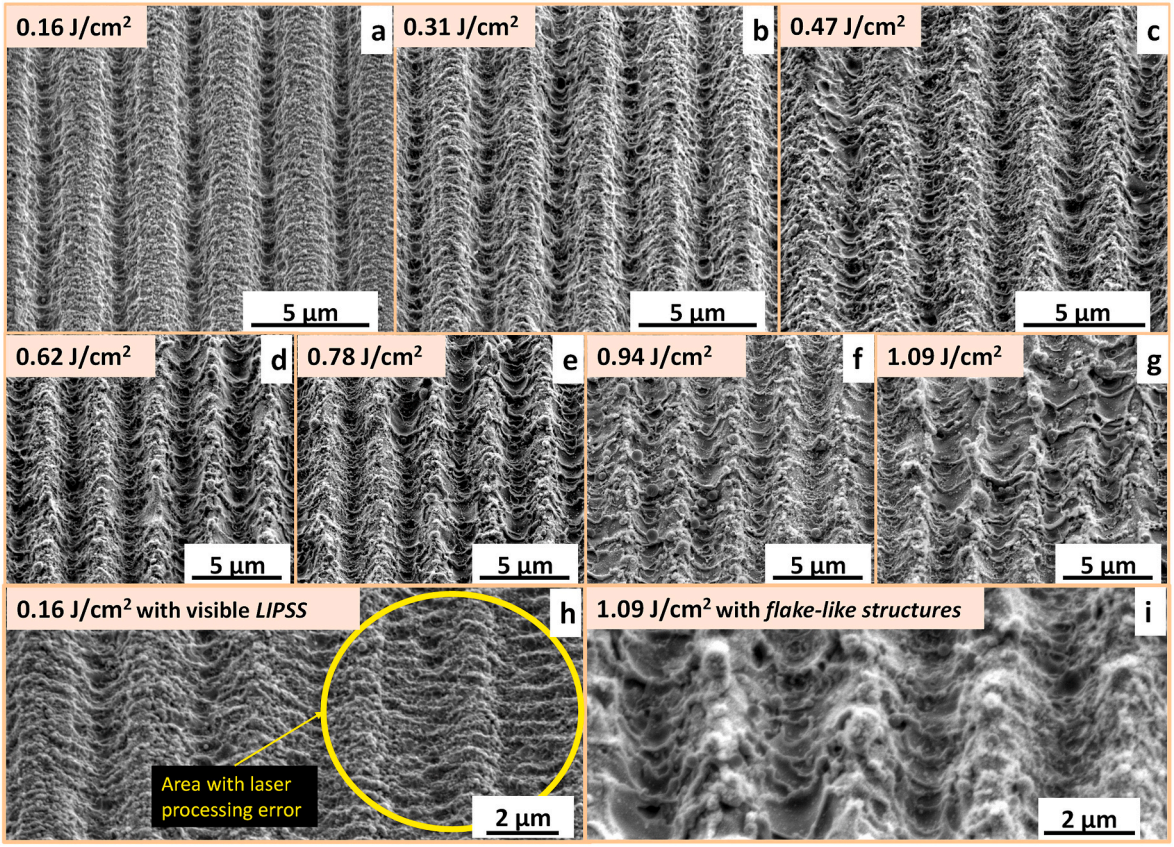

Fig. 1. SEM images of laser treated bronze surfaces with an accumulated fluence of 10 J/cm^2. Each sample varies in their single pulse fluence F_{pulse}: (a) 0.16 J/cm^2 (b) 0.31 J/cm^2 (c) 0.47 J/cm^2 (d) 0.62 J/cm^2 (e) 0.78 J/cm^2 (f) 0.94 J/cm^2 (g) 1.09 J/cm^2. Additionally, SEM images of (h) 0.16 J/cm^2 showing laser processing errors that enhance the visibility of LIPSS, and (i) 1.09 J/cm^2 with higher magnification of the flake-like structures.

bacterial adhesion or physically damage cells through increased roughness or sharp features [17,18]. Some studies focus solely on topographical effects to deter bacterial colonization [16,17], while others exploit combined chemical and morphological changes induced by laser processing, such as altered oxidation states or elemental distribution, to enhance antimicrobial activity [19,20]. For example, hierarchical micro- and mesoporous copper surfaces created via laser texturing have demonstrated superior bactericidal activity due to a combination of increased surface area, specific oxide phases, and topographic features [20].

Among the various laser structuring techniques, Direct Laser Interference Patterning (DLIP) is a particularly promising approach. DLIP utilizes the interference of coherent laser beams to create controlled surface modifications, with periodical features down to the nanoscale [21]. Recent studies [22,23] have shown that ultrashort pulsed DLIP (USP-DLIP) can significantly enhance bacterial-killing properties in copper and its alloys. Furthermore, Müller et al. [24] investigated various structure periodicities fabricated with USP-DLIP and their effects on different bacteria. It highlights that the impact of surface topography on bacterial adhesion differs among bacterial species, which in turn affects the antibacterial effectiveness of Cu surfaces.

While most research has focused on how surface topography influences antibacterial activity, few studies have examined how material composition in conjunction with laser parameters affect the antibacterial killing via the contact mechanism. This study addresses that gap by investigating the role of tin in ultrashort-pulsed laser-induced surface modifications on bronze.

Bronze containing 94 wt% copper and 6 wt% tin is selected to isolate the influence of tin, excluding other typical alloying elements such as phosphorus, aluminum, zinc, and nickel [8]. Using only tin as the alloying element allows a focused investigation of its specific effect on laser-material interaction and surface structure. The objective is to fabricate periodic line-like structures with a 3 µm spacing, matching the dimensions of *Escherichia coli* (*E. coli*) cells, using a two-beam DLIP setup [22,23,25].

The first phase of the study involves identifying optimal parameters for fabricating the line-like structures by evaluating the effects of pulse energy (E_{pulse}) or pulse fluence (F_{pulse}) on the topography. A fixed accumulated fluence (F_{acc})—the total laser energy delivered per unit area—based previous studies [23,25], is used to replicate the successful fabrication of these structures. In the second phase, the fabricated surfaces are characterized to assess how laser parameters influence topography, followed by evaluation of their antibacterial performance via contact-killing tests [26]. Additionally, the wetting behaviour of the surfaces is briefly examined due to its relevance in antibacterial efficacy.

2. Results and discussion

2.1. Topography of line-like structures

Fig. 1 reveals that the desired periodicity of 3 µm was achieved in all the samples. However, a variation in topography is observed involving the width of the valleys and peaks. Samples a and b were produced with lower pulse irradiation energies, resulting in a significantly higher number of pulses required for the predetermined value of F_{acc}. In this case, the valleys appear notably slender with a width of approx. 1 µm and broad peaks resembling plateaus. Presumably, the irradiation energy was insufficient to induce ablation in the form of a complete intensity profile. Instead, it appears that the ablation was confined to the maximum of the intensity profile.

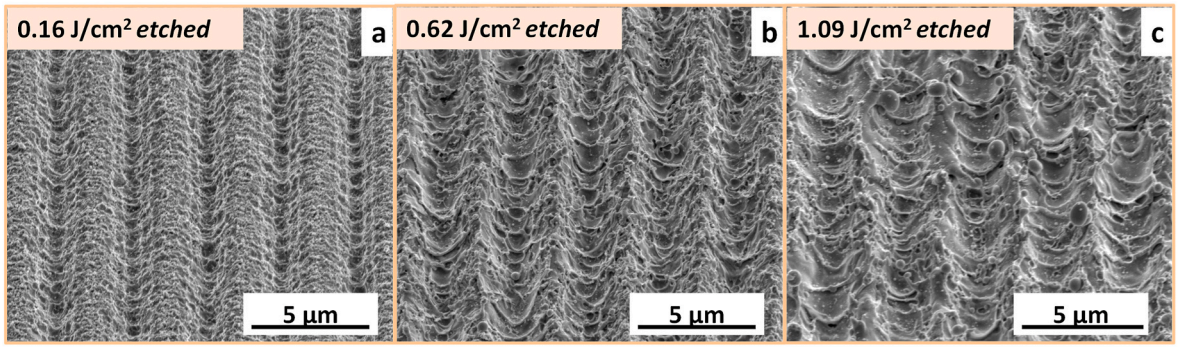

Fig. 2. SEM images of laser treated bronze surfaces with an accumulated fluence of 10 J/cm^2 and subsequently etched with 5 % citric acid. Each sample varies in their single pulse fluence F_{pulse}: (a) 0.16 J/cm^2 (b) 0.62 J/cm^2 (c) 1.09 J/cm^2.

Additionally, the valleys in Fig. 1 a and b exhibit roughness at sub-µm scale along the line-like structures. A closer examination reveals that this roughness is not random but periodic in nature. Fig. 1 h of the surface processed at 0.16 J/cm^2, due to the laser processing error, clearly shows that the structures are perpendicular to the surface, with a spatial periodicity of approximately 575 nm. This can be attributed to the formation of laser induced periodic surface structures (LIPSS), which arise from the irradiation of surfaces with a linearly polarized laser beam and are strongly influenced by factors such as laser fluence, number of pulses, and laser wavelength [27,28]. These observations are consistent with a recent study on copper, where similar periodic structures were observed under the same DLIP setup with an s-polarized laser beam, particularly at low pulse fluences, due to multi-pulse structuring [29]. Given that the copper content in the bronze investigated in this study is also very high, these findings align well with previous observations.

As the pulse fluence increases, the sub- µm periodic structures gradually lose its defined pattern, adopting a more random appearance and less visibility of the LIPSS. This results from the increased amount of melted and redeposited material. This indicates a shift from spallation to phase explosion as the predominant ablation mechanism. This transition occurs due to an increase in pulse energy on the surface, resulting in temperatures exceeding the material's boiling point. Under these conditions, the system approaches the critical temperature, inducing extensive homogeneous nucleation within the irradiated surface region [30].

Although the accumulated number of pulses becomes smaller, the higher pulse energy leads to broader valleys and narrower peaks. The line-like structures in Fig. 1a–e, with a laser pulse fluence ranging from 0.16 J/cm^2 to 0.72 J/cm^2, show a rather defined structure. In contrast, the topography in Fig. 1 f and g reveals less defined lines, with a notable accumulation of redeposited molten and ablated matter in the valleys and on the peaks. In the case of 1.09 J/cm^2 (see Fig. 1 g), the valleys are a lot wider in comparison to the structures produced with lower pulse fluences. In this case, the melting and ablation mechanisms result in significant variations in both the morphology of the peak tips and the structure depth.

An additional interesting observation is the presence of flake-like structures, initially appearing in the topography created with 0.47 J/cm^2 and become most prominent on the surface treated with 1.09 J/cm^2 surface (see Fig. 1 i). These structures are linked to the formation of oxides on the surface [7,25]. A recent study [29] demonstrates that the formation of these structures is highly dependent on the laser parameters. The results indicate that the threshold pulse fluence for the formation of flake-like structures lies between 0.31 and 0.47 J/cm^2, as these structures are already evident at 0.47 J/cm^2. Furthermore, the occurrence of these flake-like structures correlates with the laser pulse fluence, highlighting an increase in their abundance. Previous studies suggest that working with femtosecond laser pulses should result in a negligible heat-affected zone and cold ablation, reducing the probability of chemical alterations [31,32]. However, some literature indicates that the extent of alteration is heavily affected by the chemical composition of the sample. In the case of copper, it tends to predominantly form oxides [7]. Nevertheless, the presence of alloy elements can significantly impact the degree of alteration, depending on their concentration, leading to additional chemical changes [25].

Table 1
Depth of the line-like structures of the samples with following single pulse fluence F_{pulse}: 0.16 J/cm^2, 0.62 J/cm^2 and 1.09 J/cm^2.

Sample set	a	d	g
F_{pulse} [J/cm^2]	0.16	0.62	1.09
Depth [µm]	0.8 ± 0.2	1.0 ± 0.2	1.2 ± 0.2

In this study, topographies exhibit a relatively lower occurrence of flake-like structures compared to previous research [22,25]. This is most likely due to the high copper content in the bronze sample, as copper requires relatively high enthalpy for oxide formation—ranging from approximately −155 to −170 kJ/mol [33,34]. In contrast, tin requires significantly lower enthalpy, with tin oxide formation ranging from approx. −280 to −577 kJ/mol depending on its oxidation state [35]. However, since the tin content in the alloy is much lower than that of copper, the observed behaviour likely results from a combined effect of both the elemental composition and their respective oxide formation energetics [36]. Notably, the surface exposed to 1.09 J/cm^2 displays the highest concentration of flake-like structures. This is consistent with findings from a previous study on copper [29], which showed that laser fluence is directly proportional to the concentration of these flake-like structures. For further in-depth analysis, three distinct sets representing three diverse topographical trends were selected. These sets comprised samples fabricated using the following laser pulse fluences: 0.16 J/cm^2, 0.62 J/cm^2, and 1.09 J/cm^2.

According to previous studies [25,26], the formation of oxides can influence antibacterial properties significantly. To investigate its possible impact on the antibacterial activity of the bronze samples, these were etched with 5 % citric acid to eliminate any existing oxides. Fig. 2 shows the SEM images of the etched laser-processed samples. The samples exposed to higher laser pulse fluences no longer display flake-like structures.

Subsequently, the depths of the three chosen structures were measured by confocal laser scanning microscopy (CLSM) and are presented in Table 1. It is evident that the samples subjected to higher single-pulse fluences have deeper valleys. To investigate the overall alterations, the samples were characterized in both their as-processed and etched states.

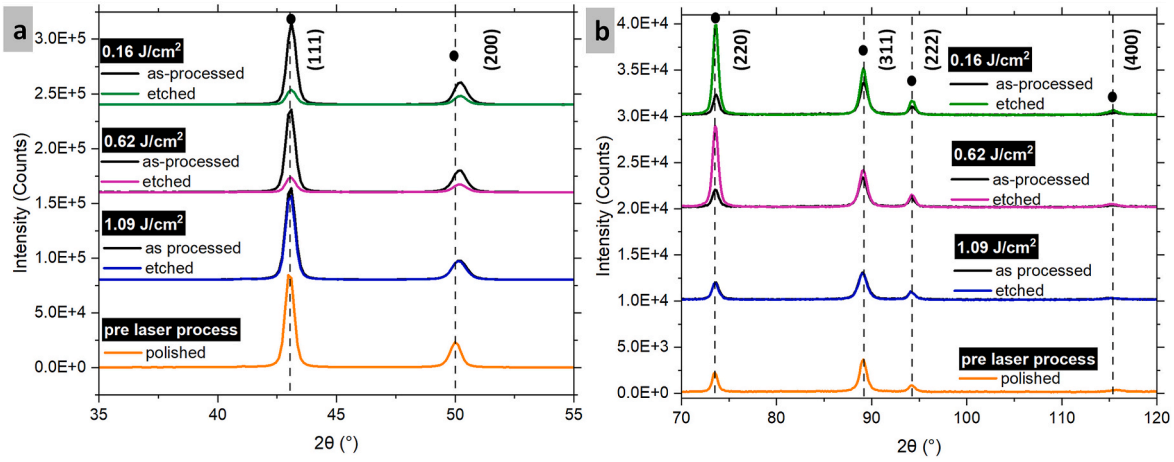

Fig. 3. XRD-Diffractograms of laser treated and the polished bronze for 2Θ range of (a) 35–55° and (b) 70–120°.

2.2. Characterization

2.2.1. Phase analyses

First, grazing incidence X-ray diffractometer GI-XRD is utilized to investigate the chemical alterations induced via laser processing. Simultaneously, it is compared with the results of a reference polished bronze surface. The findings are illustrated in the form of diffractograms in Fig. 3. The 2Θ-range of 55–70° showed no peaks (see Fig. S1) and, therefore, was not included in Fig. 3. The orange diffractogram in Fig. 3 depicts the polished bronze surface. For this reference sample, only the diffraction peaks corresponding to the fcc phase are evidenced. According to existing literature [37] and the International Center for Diffraction Data (ICDD 01-071-784, ICDD 00-044-1477) on bronze with 5–10 wt% tin, the 2Θ-values of the peaks are indicative of α-phase of bronze containing 6 wt% tin. Due to the lower atomic radius of copper (135 p.m.) compared to tin (145 p.m.), an observed trend reveals that as the copper content in bronze increases, there is a visible shift in peak positions towards higher 2Θ-values, a phenomenon consistent with literature [38] and ICDD 00-004-0836 values for pure copper samples. The comparison between the polished sample and all structured samples in an as-processed state shows a notable shift in peak positions. Specifically, the (111) and (200) peaks have shifted by 0.2° in their respective 2Θ-values. This shift suggests an elevated copper concentration on the surface subsequent to the laser-structuring.

Following the etching process, noticeable alterations in peak intensities are observed, particularly in samples exposed to 0.16 and 0.62 J/cm^2. The (111) and (200) peaks exhibit a considerable reduction in intensity, approaching nearly a fivefold decrease. On the contrary, the (220) peaks demonstrate an enhanced intensity after etching, while the (311) and (222) peaks remain constant after etching. These results suggest a change in grain orientation on the surface for the samples treated with 0.16 and 0.62 J/m^2. Additionally, it is evident that the 2Θ-values of the (400) peak lack consistency. This inconsistency is likely attributed to the peak's broad form and weak intensity, leading to an indistinct position of the peak maximum. Furthermore, for the GI-XRD geometry, it is not unexpected that the (400) signal is not proportional, as intensity variations can arise from differences in crystal plane orientation and the characteristics of the X-ray diffraction process [39]. Overall, the results show a possible increase in copper content and a change in preferred orientation on the surface through laser processing.

2.2.2. Characterization of the oxides

The results of the last section reveal the presence of flake-like structures on the surfaces modified with higher pulse fluences. The existence of these is related to the presence of oxides [7]. However, the XRD results did not show any additional oxide peaks for the 0.62 and

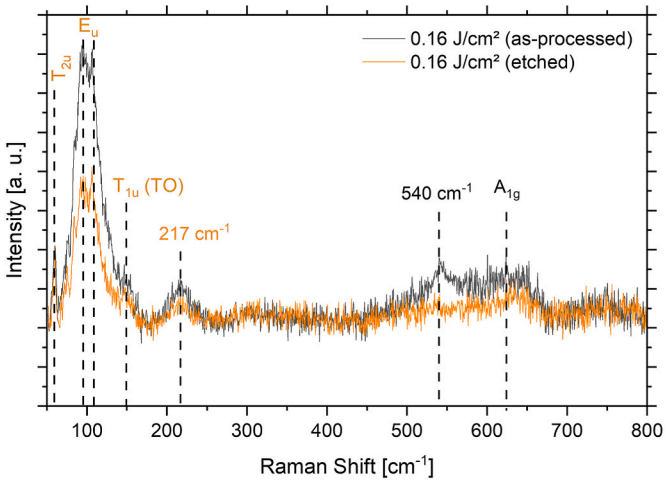

Fig. 4. Raman-spectra of bronze surfaces treated with 0.16 J/cm^2 in as-processed (black spectra) and etched (orange spectra).

1.09 J/cm^2 samples. To develop an understanding of this occurrence, Raman spectroscopy is applied to investigate oxides. All three sample sets were analyzed and the as-processed had identical spectra. This similarity was also observed for all the etched samples. For that purpose, only one set of samples is compared in their as-processed and etched state.

Fig. 4 displays the spectra of bronze surfaces treated with 0.16 J/cm^2. Bands are observed at 60, 94, 106, 147, 217, 540, 623, and 653 cm^{-1} for the as-processed surface (black spectra). Notably, characteristic Raman bands associated with cuprous or cupric oxide are absent. However, the bands from 60 to 147 cm^{-1} can be attributed to defects, non-stoichiometry and resonant excitation of cuprous oxide [40]. Yet, in cases where a phase has defects in the form of vacancies, or it is doped with other elements, these vibrational modes become visible in Raman [41]. Additionally, a band at 217 cm^{-1} lacks identification with any known oxides. However, a band in a similar range has been observed in the previous study for fs-laser structured copper-alloy [25].

Although no bands related to bulk SnO_2 are visible, two weak bands at 540 and 623 cm^{-1} can be assigned to SnO_2/Sn-O vibrations [42,43]. Literature indicates the occurrence of such a band in a range of 500–600 cm^{-1} for Sn-O particles at a nanoscale [44]. Given that the samples were treated with an ultrashort pulse duration, it is highly possible that there is a chemical alteration at the nanoscale [25,26]. Furthermore, processing under an ultrashort time period at very high local temperature/pressure and rapid cooling afterward can lead to the formation of

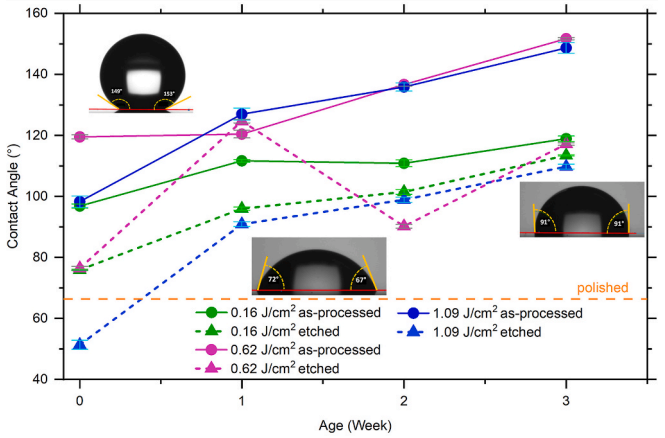

Fig. 5. Wetting behavior of various bronze surfaces (0.16 J/cm^2 (green), 0.62 J/cm^2 (purple), and 1.09 J/cm^2 (blue)) in as-processed (● solid line) and etched (▲ dashed line) state. Additionally, polished bronze (dashed orange line) is chosen as reference. The results are presented as calculated average values of the contact angle.

not fully/stably formed oxides [45]. This correlates with the observation of copper oxide bands that only occur as a result of defects in the oxide phase.

After etching (orange spectra), the intensity of cuprous oxide bands reduces by half. Whereas the band at 217 cm^{-1} remains constant. The Sn oxide bands are no longer visible, particularly the band at 540 cm^{-1}. Since the defect bands of Cu_2O remain evident after etching, the disappearance of the 540 cm^{-1} band suggests that it is not associated with Cu_2O and is, therefore, specifically related to SnO_2. These findings reveal the removal of cuprous oxide phases partially and tin oxide fully through etching. Furthermore, Raman spectra were also recorded for 0.62 and 1.09 J/cm^2 samples. The results showed identical spectra for all as-processed as well as etched surfaces.

Comparing the characterization results, it can be concluded that the observed increase in copper content in XRD spectra is possibly a result of copper ions diffusion towards the surface, forming oxides as indicated by the acquired Raman spectra. However, the absence of distinct XRD bands and the presence of only silent bands from copper oxides in Raman spectra suggest that the oxide formation is probably located only on the top surface of the bronze samples. In summary, the formation of a nanoscale tin oxide phase and a copper-rich oxide phase, possibly including tin ions, may be suggested as seen in previous studies [22,25].

2.3. Wetting behavior

The antibacterial test performed in this study involves the placement of the bacterial solution in the form of a droplet on the surfaces. To evaluate the results of the contact-killing tests, it is essential to first examine the wetting behavior of the different surfaces, including the polished bronze reference. For that purpose, the experiment is performed over a period of three weeks utilizing the sessile falling droplet method.

The calculated average values of the static contact angle are shown Fig. 5. Over the course of three weeks, a clear trend is observed for all the structured samples, except for the 0.62 J/cm^2 etched sample (▲ purple) at one week, which is a result of a processing error. This variation was noted since only the batch used for wettability experiments experienced the error in laser processing (similar to that shown in Fig. 1 h). By including this, the intention was to show how even slight variations in laser structuring, caused by missed laser processing, can affect the wettability. In general, an increasing contact angle is noted. This change from hydrophilic to hydrophobic nature after the laser processing with ultrashort pulses over a period of a few weeks has been noted in previous studies for pure metal surfaces [23,46]. Furthermore, these results are consistent with the findings of a previous study that tested the wetting behaviour of laser-processed phosphor bronze [47]. This study validates that irrespective of the bulk composition this trend is visible for all laser processed samples.

Comparing the initial and last results, the initial hydrophilic nature can be attributed to the micro roughness of the surface, which allows for the droplet to stick to the surface. However, at week 0, a significant difference is visible between the as-processed samples (● solid line) and the etched samples (▲ dashed line). It is evident that the etched samples show a more hydrophilic behavior in contrast. Previous studies [48,49] showed that this difference on the surfaces is closely related to the formation of oxygen, C–C, and C–H bonds, which depend on the atmospheric conditions. In this study, the laser process was conducted under ambient conditions, making it highly likely that such contaminants were present. Since the etched samples were treated with citric acid, most oxides and likely other surface contaminants were removed, which led to a change in the wetting behavior.

As the weeks progress, the samples become increasingly

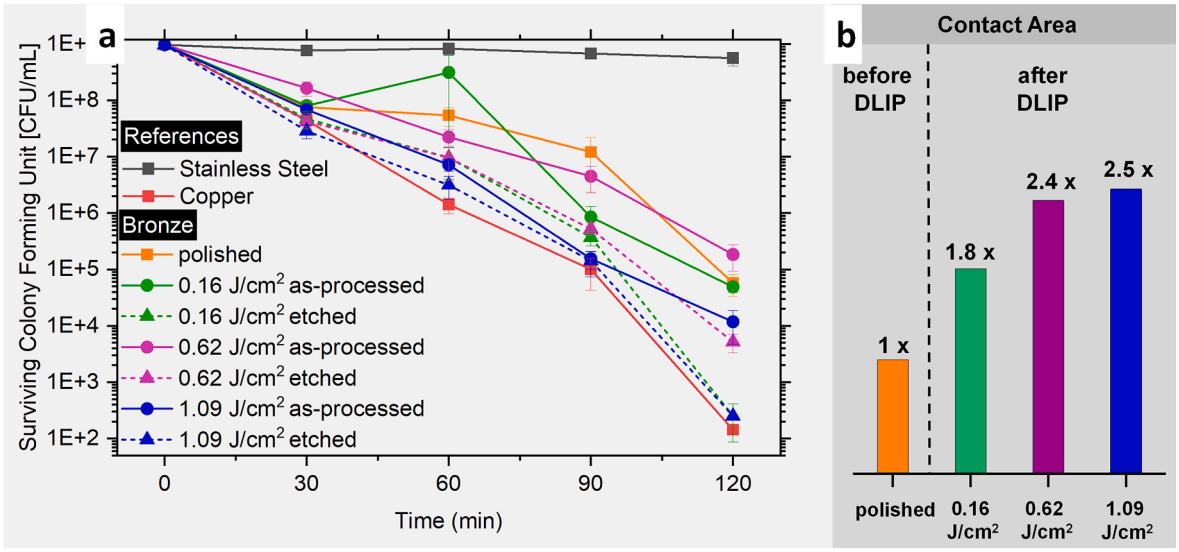

Fig. 6. a) Surviving colony forming units (CFU/mL) of all bronze surfaces in comparison to polished references, copper (red graph) and steel (grey graph). b) Increase in contact area after direct laser patterning with different pulse fluences on bronze.

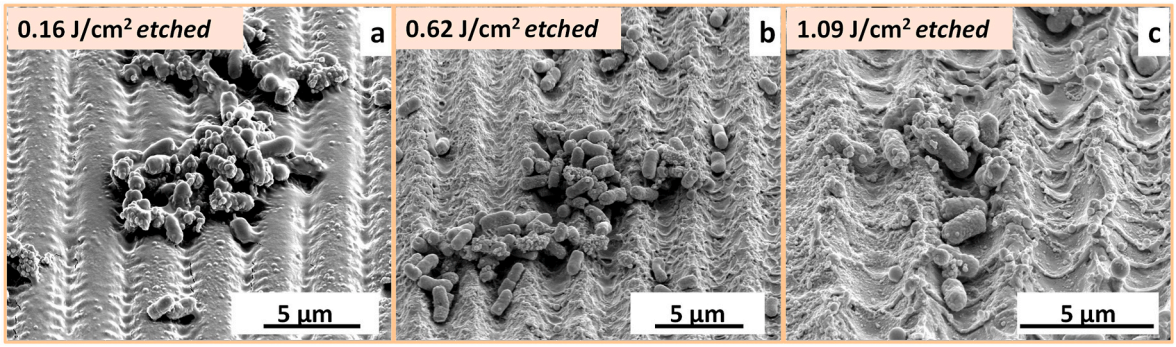

Fig. 7. Micrographs of etched laser-samples with *E. coli*. The samples were coated with Au-Pd to achieve a better contrast in presence of biological matter.

hydrophobic. By week 3, all etched samples display contact angles between 100° and 110°, while the as-processed samples reach around 150°, nearly approaching superhydrophobicity (>150°). However, the 0.16 J/cm^2 as-processed sample (● green) shows behavior like the etched samples by week 3, possibly due to its unique topography (see Fig. 2a). The plateau-like peaks in the surface structure may facilitate droplet adhesion in a way that reflects a combined effect of both polished and other structured surfaces, although further research is needed to confirm this. Future studies should evaluate droplet adhesion using contact angle hysteresis to gain a better understanding of this phenomenon. Overall, an increase in hydrophobicity is highly related to the absorption of organic matter [7] during the aging period of 3 weeks, as the samples were stored in an ambient atmosphere. Overall, the change in wetting behavior can be attributed to microroughness and surface aging.

2.4. Contact-killing and bacteria-substrate interactions

Next, the antibacterial activity of all these samples is examined against *E. coli*. Fig. 6 a displays surviving colony forming units (CFU)/mL over a contact period of 30, 60, 90, and 120 min. As expected, steel (■ grey graph) shows no killing of *E. coli* and, on the other side, the surviving CFU/mL on copper (■ red graph) reduces by 99 % in a contact period of 2 h [23]. In comparison, the polished bronze (■ orange graph) shows a significantly slower killing of *E. coli* than on pure copper. This can be explained by the lower copper content in bronze as previously observed for brass [22].

As this is compared to the laser-treated samples, regardless of the pulse fluence (all graphs with ● solid line), it is visible that within the first 30 min of contact, the killing rate is similar to that of polished bronze and copper. However, after 60 min, a discrepancy becomes visible for the 0.16 J/cm^2 sample. Due to one of the test results with a low killing rate the standard deviation in this case is bigger. This variation can be ascribed to different experimental errors, i.e., improper placement of the droplet leading to incomplete or insufficient duration of contact between bacteria and substrate, improper retrieval of the bacterial sample from the surface after contact, etc. These minor procedural variations were acknowledged to provide a more transparent and realistic interpretation of the data.

After 90 min, the 1.09 J/cm^2 sample kills significantly better than polished bronze and is almost similar to that of copper. After an increased contact duration, the killing of *E. coli* 1.09 J/cm^2 continues at a consistent rate. Whereas, in contrast, copper exhibits a notable surge in the killing rate within the final 30 min of contact. Overall, 0.16 J/cm^2 (● green graph) and 0.62 J/cm^2 (● purple graph) as-processed samples have similar killing within the 120 min contact duration as the polished bronze.

Simultaneously, the etched samples are assessed for their antibacterial activity, with the results presented in Fig. 6 (all graphs with ▲ dashed lines). During the initial 60 min, all samples exhibit similar behavior, surpassing polished bronze and their respective as-processed counterparts by one magnitude. By the 120-min mark, it becomes apparent that approximately 99 % of *E. coli* is killed on all etched samples. In the case of 0.16 J/cm^2 (▲ green graph) and 1.09 J/cm^2 (▲ blue graph) etched, the CFU/mL values are similar to that of copper. This indicates an improved antibacterial activity on the laser-treated samples with etching. This enhancement is likely due to the removal of surface layers formed during laser treatment, as these layers did not contribute as much to the increased antibacterial activity.This correlates with the results seen in previous studies on brass with USP-DLIP [22,25]. Fig. 6 b shows that all surfaces exhibited an increase in contact area between 1.8 and 2.5-fold, suggesting that, in the case of contact-killing, the topographical changes leading to this increase in contact area are as significant as the surface's chemical composition.

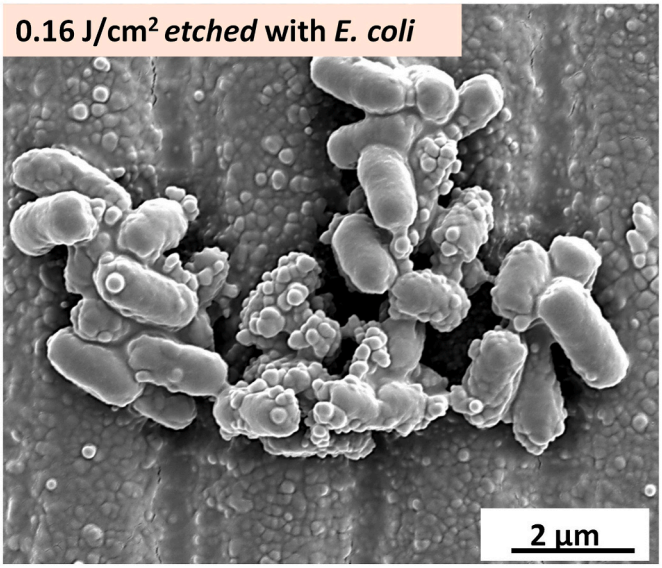

Fig. 8. Micrograph of an etched laser-treated sample with 0.16 J/cm^2 pulse fluence, showing interaction with *E. coli* and displaying the surface morphology.

Fig. 7 shows the interaction between *E. coli* and all three etched laser-treated surfaces. The surfaces exhibit a noticeable change in morphology after contact with bacteria. This is due to corrosion on the surface, which leads to the release of copper ions into the bacterial solution, as observed in a recent study [22]. It's also worth noting Fig. 7 a provides a valuable visual comparison of bacteria-surface interaction across the different surfaces. While the morphology is less visible due to the slightly thicker Au-Pd coating on the 0.16 J/cm^2 sample, the higher magnification SEM-image without tilting (see Fig. 8) offers a clearer view of the morphology.

A significant observation from the results is that, irrespective of the topographic enhancements achieved through different laser parameters for 3 μm periodic line-like structures, an improved killing of *E. coli* is observed for all etched samples. This is most likely due to the dimension of the single bacterial cell, which, in the case of *E. coli*, ranges between 1 and 3 μm. Since the width of the valleys across the varied sets also falls within this range, and an overall increase in contact area is observed (see Fig. 6 b), bacterial-substrate contact is enhanced as displayed in Fig. 7, resulting in a general increase in activity.

The findings further signify that the line-like structures, without any flake-like structures, facilitate a bacteria-substrate interaction, resulting in higher *E. coli* killing. The increased bacterial adhesion and killing on the etched surfaces can be attributed to several interacting factors. The removal of oxides reduced surface roughness, which likely enhanced bacterial attachment. Additionally, the oxides present on the as-processed surfaces created a hydrophobic layer, hindering bacterial adhesion. Etching improved wettability by removing this oxide layer, thus promoting better bacterial attachment. This reduction in roughness and improved wettability contribute significantly to the observed antibacterial performance.

Additionally, an important factor promoting this increased killing is the elevated copper content, as indicated by the XRD results, which show an overall higher copper concentration after laser processing. The increased bacterial killing is primarily due to the enhanced contact area and the alignment of the structures with bacterial size. Previous studies have shown that when surface structures match bacterial dimensions, but the chemical composition is unsuitable, reduced or no antibacterial effect occurs [25]. Since copper is known to be antibacterial while tin is not, both surface composition and contact area are critical for effective antibacterial performance.

3. Conclusion

This study demonstrates the enhancement of bronze surfaces with 6 wt.-% tin using ultrashort-pulsed direct laser interference patterning (USP-DLIP) to create 3 μm periodic line-like structures, improving antibacterial activity against *E. coli*.

The key findings from this research confirm the successful fabrication of the desired surface structures on bronze, with pulse fluence playing a significant role in determining the depth and width of valleys, which, in turn, increased the contact area by 1.8–2.5 times. Chemical analyses showed an increase in copper content and the formation of tin- and copper-rich oxide phases after laser processing. These oxide phases were effectively removed by etching with 5 % citric acid. The processed surfaces exhibited increased hydrophobicity over time, and the additional etching of the samples demonstrated *E. coli* killing rates comparable to pure copper, significantly outperforming polished bronze. Importantly, despite differences in topography, the increased antibacterial activity can be attributed to the larger contact area and the compatibility of the periodic structure dimensions with the size of *E. coli* bacteria, leading to improved bacterial killing.

The results show significant progress in optimizing the antibacterial properties of bronze for high-contact surface applications. Future research should focus on assessing long-term performance through repeated bacterial colonization, cleaning, and re-colonization cycles, exploring the effects of additional alloying elements and laser parameters, and conducting extensive investigations into wettability and bacterial adhesion to better understand the bacteria-substrate interaction.

Overall, this work shows that USP-DLIP, combined with etching, can effectively enhance the antibacterial performance of bronze. These findings offer a promising approach for developing antimicrobial surfaces suitable for a wide range of applications, including public transport, hospitals, schools, and other high-contact areas where hygiene and bacterial contamination are of significant concern. The insights gained from the binary copper-tin system provide a solid foundation for future work, enabling the exploration of more complex alloy systems for use in these applications.

4. Materials and methods

4.1. Materials

Bronze with 6 wt.-% tin (*Wieland*) was chosen for this study. In addition to that 99 % pure copper (*Wieland*) and stainless steel 304 (*Brio*) surfaces were used as references. The samples were received in the form of a 1 mm thin sheet, which is then trimmed to coupons measuring 10 × 25 mm^2. Subsequently, the sample surfaces were prepared metallographically to obtain a polished mirror finish as described in Ahmed et al. [25].

4.2. Direct laser interference patterning

Periodic line-like structures with a periodicity of 3 μm were created on bronze surfaces via direct laser interference patterning. This was achieved using a Ti:sapphire Spitfire laser system from Spectra Physics. A centered wavelength of 800 nm and an ultrashort pulsed duration of 150 fs (full width at half maximum) was utilized. The optical setup consisting of five key elements: a beam diameter aperture, a wave plate, a diffractive optical element, a mask, and a focusing lens system (100 mm focal length), was chosen as described in Ahmed et al. [25]. A spot diameter of 70 μm was achieved as a result of the two-beam DLIP on bronze. For this study, the laser-treated samples were tested in an as-processed and etched state. The samples were etched using a 5 % citric acid solution and subsequently cleaned with ethanol.

4.3. Experimental Procedure

In general, the laser process is characterized by scanning parameters aimed at achieving a uniform topographical alteration across the sample surface [50]. In this case, various input laser parameters play a role in defining these calculable scanning parameters. The first one is laser pulse fluence (F_{pulse}), which is determined by single pulse energy (E_{pulse}) or laser power (P). Laser pulse fluence is defined as energy per area for pulse irradiation (A_{spot}) and is calculated in Equation (1) according to Fox et al. [51].

$$F_{pulse} = \frac{E_{pulse}}{A_{spot}} \quad \text{Eq. (1)}$$

Furthermore, this energy can be calculated for a defined area of the processed surface as shown in equation (2) and is known as accumulated fluence (F_{acc}) [51].

$$F_{acc} = \frac{E_{pulse}}{\Delta x^{*} \Delta y} \quad \text{Eq. (2)}$$

Here, Δx is the pulse overlap in the scan direction (x-axis) and Δy is the step size also known as hatch distance in the y-axis [51]. Moreover, equations (1) and (2) lead to another calculable parameter (see equation (3)), which is the number of accumulated pulses (n_{acc}) for this defined area of the processed surface [51].

$$n_{acc} = \frac{F_{cc}}{F_{pulse}} \quad \text{Eq. (3)}$$

3 μm periodic line-like structures were fabricated and defined by an identical accumulated fluence (F_{acc}) of 10 J/cm^2. For that purpose, the repetition rate (f) and the overlap in y-direction (Δy: also, the hatch distance between two scan lines) were kept constant at 1000 Hz and 24 μm, respectively. The chosen repetition rate is consistent with previous studies [23,25], and the overlap value was selected accordingly for bronze to produce structures comparable to those earlier results. The input laser power (P) was varied intentionally to achieve a wide range of E_{pulse}. For each selected power, the number of accumulated pulses (n_{acc})

Table 2
Laser parameters — pulse energy (E_{pulse}), number of accumulated pulses (n_{acc}) and pulse fluence (F_{pulse}) — for 7 sets of samples with 3 μm line-like structures fabricated with femtosecond (fs)-DLIP technique using constant F_{acc} of 10 J/cm^2. The values of variables were calculated using equations (1) - (3).

Sample set	a	b	c	d	e	f	g
E_{pulse} [μJ]	6	12	18	24	30	36	42
n_{acc}	64	32	21	16	12	11	9
F_{pulse} [J/cm^2]	0.156	0.311	0.468	0.623	0.779	0.935	1.091

had to be adjusted to get the set constant value for F_{acc}. This is defined by the overlap and stage speed in the *x*-direction along the scan line [51]. In total, 7 different sets of samples were prepared. The parameters including the respective F_{pulse} are given in Table 2.

The samples were evaluated for their wetting properties over a period of three weeks following laser structuring. Subsequently, all further characterization and contact-killing experiments were conducted after this three-week aging period.

4.4. Wettability

Contact angle experiments were performed using a Drop Shape Analysator DSA 100 (*Krüss GmbH*) to observe the aging of laser-structured samples during a span of three weeks. After the laser treatment, the samples are stored in a box at a room temperature of 20 ± 2 °C and a humidity of 30 ± 7 %. The first measurement (Week 0) is done 24 h after the laser treatment. The remaining measurements up to the third week were carried out at 7-day intervals. Every week's measurement is performed on a different sample at room temperature of 21.5 ± 0.5 °C and a humidity of 20 ± 1.3 %. A droplet of distilled water with a volume of 3 μL is dosed on the sample with a micro-syringe using the sessile falling droplet method. Each sample is dosed with at least 5 droplets on different regions of the surface. Since the laser-structured samples show an anisotropic topography, the contact angle of each droplet was measured orthogonal and parallel to the line-like structures. To achieve reproducible results, the measurements were done within 1 min of droplet dosage.

4.5. Surface characterization

Confocal laser scanning microscopy (CLSM, LEXT OLS4100 3D Measuring Laser Microscope, *Olympus*) was employed to measure the dimensions of the structures, with the depth calculated based on a sequence of 10 peaks and valleys. Furthermore, scanning electron microscopy (SEM, Helios NanoLab 600™, *FEI Company*) in secondary contrast mode was utilized to observe the topography. The SEM images were obtained using an acceleration voltage of 5 kV and a current of 1.4 nA, with the sample surface positioned at a 45° tilt.

Phase analysis is carried out using a high-resolution grazing incidence X-ray diffractometer (GIXRD, Cu K_α source with a wavelength of 1.5418 Å at 1° grazing angle, *PANalytical X'Pert* PRO-MPD). Next, the characterization of oxides is carried out with Raman spectroscopy (Horiba Jobin, HRLab with a 532 nm laser).

4.6. Antibacterial efficiency determination

The antibacterial efficiency of the samples is investigated via a contact-killing experiment followed by the wet plating method [52]. For that purpose, a bacterial suspension of *E. coli* WT K12 (BW25113) is prepared with Phosphate-buffered saline (PBS) according to Luo et al. [26]. A total of three droplets (volume: 40 μL each) of the bacterial suspension are then placed on each sample surface. Each sample is tested at least thrice to achieve reproducible results. After 30 min, 5 μL are retrieved from one of the droplets after repetitive pipetting. The same volume is retrieved from the second and third droplets after 60 min and 120 min, respectively. These 5 μL are then serially diluted, spread on Lysogeny broth (LB) agar plates, and stored in an incubator at 37 °C for 24 h. To conclude, the number of surviving colony forming units is enumerated for all the samples as well as the original bacterial suspension prior to contact with any surface.

CRediT authorship contribution statement

Aisha Saddiqa Ahmed: Writing – original draft, Visualization, Validation, Investigation, Conceptualization. **Diego Sancio:** Writing – review & editing, Validation, Investigation. **Daniel Wyn Müller:** Writing – review & editing. **Jean-François Pierson:** Writing – review & editing, Validation, Supervision, Resources, Investigation. **Frank Mücklich:** Writing – review & editing, Supervision, Resources, Funding acquisition.

Funding

A.A. has been funded by the German Aerospace Center - Space Administration (DLR) within the project "Investigation of antimicrobial metal surfaces under space conditions - An effective strategy to prevent microbial biofilm formation" (project number 50WB1930). This work was funded by the German Research Foundation (DFG) within the project "Controlled bacterial interaction to increase the antimicrobial efficiency of copper surfaces" (project number 415956642).

Declaration of competing interest

The authors declare that they have no known competing financial interests or personal relationships that could have appeared to influence the work reported in this paper.

Acknowledgement

The authors would like to thank to the group of Prof. Rolf Müller from the Helmholtz Centre of Infection Research in Saarbrücken for providing the *E. coli*. The authors acknowledge financial support in the project "MatInnovat" supported by the Saarland State Ministry of Economics with resources from the European Fund for Regional Development (EFRE) and funding by the German Research Foundation for the Femtosecond Pulsed Laser System (DFG, INST 256/562 FUGG). The authors would also like to thank the technical platform "Optic and Lasers" at Institut Jean Lamour (IJL, Nancy, France) for access to Raman facility. Diego Sancio would like to thank the CUAA-DAHZ for the scholarship in the frame of project I.DEAR-Materials (Project ID: 57597084).

Appendix A. Supplementary data

Supplementary data to this article can be found online at https://doi.org/10.1016/j.mtadv.2025.100596.

Data availability

Data will be made available on request.

References

[1] J. Konieczny, Z. Rdzawski, Antibacterial properties of copper and its alloys, Archives of Materials Science and Engineering 56 (2012).

[2] J. Luo, C. Hein, F. Mücklich, M. Solioz, Killing of bacteria by copper, cadmium, and silver surfaces reveals relevant physicochemical parameters, Biointerphases 12 (2017) 020301, https://doi.org/10.1116/1.4980127.

[3] M. Hans, S. Mathews, F. Mücklich, M. Solioz, Physicochemical properties of copper important for its antibacterial activity and development of a unified model, Biointerphases 11 (2016) 018902, https://doi.org/10.1116/1.4935853.

[4] G. Borkow, J. Gabbay, Copper, an ancient remedy returning to fight microbial, fungal and viral infections, Curr. Chem. Biol. 3 (2009), https://doi.org/10.2174/187231309789054887.

[5] G. Grass, C. Rensing, M. Solioz, Metallic copper as an antimicrobial surface, Appl. Environ. Microbiol. 77 (2011) 1541–1547, https://doi.org/10.1128/AEM.02766-10.

[6] I.C. Lee, J.W. Ko, S.H. Park, J.O. Lim, I.S. Shin, C. Moon, S.H. Kim, J.D. Heo, J. C. Kim, Comparative toxicity and biodistribution of copper nanoparticles and cupric ions in rats, Int. J. Nanomed. 11 (2016), https://doi.org/10.2147/IJN.S106346.

[7] D.W. Müller, A. Holtsch, S. Lößlein, C. Pauly, C. Spengler, S. Grandthyll, K. Jacobs, F. Mücklich, F. Müller, In-depth investigation of copper surface chemistry modification by ultrashort pulsed direct laser interference patterning, Langmuir 36 (2020) 13415–13425, https://doi.org/10.1021/acs.langmuir.0c01625.

[8] J.R. Davis, ASM Speciality Handbook, Copper and Copper Alloys, 2001.

[9] H. Michels, W. Moran, J. Michel, Antimicrobial properties of copper alloy surfaces, with a focus on hospital-acquired infections, Int. J. Metalcast. (2008), https://doi.org/10.1007/BF03355432.

[10] A. Rózańska, A. Chmielarczyk, D. Romaniszyn, G. Majka, M. Bulanda, Antimicrobial effect of copper alloys on Acinetobacter species isolated from infections and hospital environment, Antimicrob. Resist. Infect. Control 7 (2018), https://doi.org/10.1186/s13756-018-0300-x.

[11] T.J. Karpanen, A.L. Casey, P.A. Lambert, B.D. Cookson, P. Nightingale, L. Miruszenko, T.S.J. Elliott, The antimicrobial efficacy of copper alloy furnishing in the clinical environment: a crossover study, Infect. Control Hosp. Epidemiol. 33 (2012), https://doi.org/10.1086/663644.

[12] M. Raffi, S. Mehrwan, T.M. Bhatti, J.I. Akhter, A. Hameed, W. Yawar, M.M. Ul Hasan, Investigations into the antibacterial behavior of copper nanoparticles against Escherichia coli, Ann. Microbiol. 60 (2010) 75–80, https://doi.org/10.1007/s13213-010-0015-6.

[13] U. Bogdanović, V. Lazić, V. Vodnik, M. Budimir, Z. Marković, S. Dimitrijević, Copper nanoparticles with high antimicrobial activity, Mater. Lett. 128 (2014), https://doi.org/10.1016/j.matlet.2014.04.106.

[14] F.S. da Silva, N. Cinca, S. Dosta, I.G. Cano, J.M. Guilemany, C.S.A. Caires, A. R. Lima, C.M. Silva, S.L. Oliveira, A.R.L. Caires, A.V. Benedetti, Corrosion resistance and antibacterial properties of copper coating deposited by cold gas spray, Surf. Coat. Technol. 361 (2019), https://doi.org/10.1016/j.surfcoat.2019.01.029.

[15] T. Suryaprabha, M.G. Sethuraman, Fabrication of copper-based superhydrophobic self-cleaning antibacterial coating over cotton fabric, Cellulose (Lond.) 24 (2017), https://doi.org/10.1007/s10570-016-1110-z.

[16] A. Rosenkranz, M. Hans, C. Gachot, A. Thome, S. Bonk, F. Mücklich, Direct laser interference patterning: tailoring of contact area for frictional and antibacterial properties, Lubricants (Basel) 4 (2016), https://doi.org/10.3390/lubricants4010002.

[17] Q. Pan, Y. Cao, W. Xue, D. Zhu, W. Liu, Picosecond laser-textured stainless steel superhydrophobic surface with an antibacterial adhesion property, Langmuir 35 (2019), https://doi.org/10.1021/acs.langmuir.9b01333.

[18] D. Patil, S. Aravindan, M.K. Wasson, P. Vivekanandan, P.V. Rao, Fast fabrication of superhydrophobic titanium alloy as antibacterial surface using nanosecond laser texturing, J Micro Nanomanuf 6 (2018), https://doi.org/10.1115/1.4038093.

[19] A.H.A. Lutey, L. Gemini, L. Romoli, G. Lazzini, F. Fuso, M. Faucon, R. Kling, Towards laser-textured antibacterial surfaces, Sci. Rep. 8 (2018), https://doi.org/10.1038/s41598-018-28454-2.

[20] V. Selvamani, A. Zareei, A. Elkashif, M.K. Maruthamuthu, S. Chittiboyina, D. Delisi, Z. Li, L. Cai, V.G. Pol, M.N. Seleem, R. Rahimi, Hierarchical micro/mesoporous copper structure with enhanced antimicrobial property via laser surface texturing, Adv. Mater. Interfac. 7 (2020), https://doi.org/10.1002/admi.201901890.

[21] A.F. Lasagni, C. Gachot, K.E. Trinh, M. Hans, A. Rosenkranz, T. Roch, S. Eckhardt, T. Kunze, M. Bieda, D. Günther, V. Lang, F. Mücklich, Direct laser interference patterning, 20 years of development: from the basics to industrial applications, in: Laser-Based Micro- and Nanoprocessing, vol. XI, SPIE, 2017 1009211, https://doi.org/10.1117/12.2252595.

[22] A.S. Ahmed, D.W. Müller, S. Bruyère, A. Holtsch, F. Müller, K. Brix, S. Migot, R. Kautenburger, K. Jacobs, J.F. Pierson, F. Mücklich, Antibacterial property alterations induced by low zinc content in laser-structured brass, Appl. Surf. Sci. 665 (2024) 160338, https://doi.org/10.1016/J.APSUSC.2024.160338.

[23] D.W. Müller, S. Lößlein, E. Terriac, K. Brix, K. Siems, R. Moeller, R. Kautenburger, F. Mücklich, Increasing antibacterial efficiency of Cu surfaces by targeted surface functionalization via ultrashort pulsed direct laser interference patterning, Adv. Mater. Interfac. 8 (2021), https://doi.org/10.1002/admi.202001656.

[24] D.W. Müller, C. Pauly, K. Brix, R. Kautenburger, F. Mücklich, Modifying the antibacterial performance of Cu surfaces by topographic patterning in the micro- and nanometer scale, Biomater. Adv. 169 (2025) 214184, https://doi.org/10.1016/J.BIOADV.2025.214184.

[25] A. Ahmed, D. Müller, S. Bruyère, A. Holtsch, F. Müller, J. Barrirero, K. Brix, S. Migot, R. Kautenburger, K. Jacobs, J.-F. Pierson, F. Mücklich, Surface Modification of Brass via Ultrashort Pulsed Direct Laser Interference Patterning and Its Effect on Bacteria-Substrate Interaction, ACS Appl. Mater. Interfaces 15 (n.d.) 36908–36921. https://doi.org/10.1021/acsami.3c04801.

[26] J. Luo, A. Ahmed, J.F. Pierson, F. Mücklich, Tailor the antibacterial efficiency of copper alloys by oxidation: when to and when not to, J. Mater. Sci. 57 (2022) 3807–3821, https://doi.org/10.1007/s10853-022-06879-5.

[27] A.I. Aguilar-Morales, S. Alamri, A.F. Lasagni, Micro-fabrication of high aspect ratio periodic structures on stainless steel by picosecond direct laser interference patterning, J. Mater. Process. Technol. 252 (2018) 313–321, https://doi.org/10.1016/j.jmatprotec.2017.09.039.

[28] Y. Zhang, Q. Jiang, M. Long, R. Han, K. Cao, S. Zhang, D. Feng, T. Jia, Z. Sun, J. Qiu, H. Xu, Femtosecond laser-induced periodic structures: mechanisms, techniques, and applications, Opto-Electronic Science 1 (2022), https://doi.org/10.29026/oes.2022.220005.

[29] D.W. Müller, S. Lößlein, C. Pauly, M. Briesenick, G. Kickelbick, F. Mücklich, Multi-pulse agglomeration effects on ultrashort pulsed direct laser interference patterning of Cu, Appl. Surf. Sci. 611 (2023) 155538, https://doi.org/10.1016/J.APSUSC.2022.155538.

[30] J. Cheng, C.S. Liu, S. Shang, D. Liu, W. Perrie, G. Dearden, K. Watkins, A review of ultrafast laser materials micromachining, Opt Laser. Technol. 46 (2013) 88–102, https://doi.org/10.1016/j.optlastec.2012.06.037.

[31] S.S. Harilal, J.R. Freeman, P.K. Diwakar, A. Hassanein, Femtosecond laser ablation: fundamentals and applications, Springer Opt. Sci. 182 (2014), https://doi.org/10.1007/978-3-642-45085-3_6.

[32] R.E. Russo, X. Mao, J.J. Gonzalez, S.S. Mao, Femtosecond laser ablation ICP-MS, J Anal At Spectrom (2002), https://doi.org/10.1039/b202044k.

[33] V.A. Lukyanova, S.M. Pimenova, D.Y. Ilin, A.I. Druzhinina, E.A. Morozova, A. S. Alikhanyan, Standard enthalpy of formation of copper(II) pivalate, J. Chem. Thermodyn. 131 (2019) 336–339, https://doi.org/10.1016/J.JCT.2018.11.016.

[34] R.D. Holmes, A.B. Kersting, R.J. Arculus, Standard molar Gibbs free energy of formation for Cu2O: high-resolution electrochemical measurements from 900 to 1300 K, J. Chem. Thermodyn. 21 (1989) 351–361, https://doi.org/10.1016/0021-9614(89)90136-5.

[35] E.G. Lavut, B.I. Timofeyev, V.M. Yuldasheva, E.A. Lavut, G.L. Galchenko, Enthalpies of formation of tin (IV) and tin (II) oxides from combustion calorimetry, J. Chem. Thermodyn. 13 (1981) 635–646, https://doi.org/10.1016/0021-9614(81)90034-3.

[36] S.M. Howard, Standard gibb ' s energies of formation for, J. Soc. Chem. Ind. (London) 63 (1971).

[37] Z. Li, G. Zhao, H. Wang, G. Gao, S. Chen, D. Yang, Y. Fan, G. Zhang, H. Xu, Microstructure and tribological behaviors of diffusion bonded powder sintered Cu-Sn based alloys, Mater. Res. Express 8 (2021), https://doi.org/10.1088/2053-1591/ac31ff.

[38] H. Khalid, S. Shamaila, N. Zafar, R. Sharif, J. Nazir, M. Rafique, S. Ghani, H. Saba, Antibacterial behavior of laser-ablated copper nanoparticles, Acta Metall. Sin. 29 (2016), https://doi.org/10.1007/s40195-016-0450-x.

[39] S.L. Chang, Thin-film characterization by grazing incidence X-ray diffraction and multiple beam interference, J. Phys. Chem. Solid. 62 (2001), https://doi.org/10.1016/S0022-3697(01)00109-3.

[40] L. Debbichi, M.C. Marco De Lucas, J.F. Pierson, P. Krüger, Vibrational properties of CuO and Cu 4O 3 from first-principles calculations, and Raman and infrared spectroscopy, J. Phys. Chem. C 116 (2012) 10232–10237, https://doi.org/10.1021/jp303096m.

[41] H.K. Yadav, K. Sreenivas, R.S. Katiyar, V. Gupta, Defect induced activation of Raman silent modes in rf co-sputtered Mn doped ZnO thin films, J. Phys. D Appl. Phys. 40 (2007) 6005–6009, https://doi.org/10.1088/0022-3727/40/19/034.

[42] N. Sergent, M. Epifani, E. Comini, G. Faglia, T. Pagnier, Interactions of nanocrystalline tin oxide powder with NO2: a Raman spectroscopic study, Sens Actuators B Chem 126 (2007) 1–5, https://doi.org/10.1016/j.snb.2006.10.013.

[43] Gyanendra Prakash Shukla, Mukesh Chandra Bhatnagar, SnO2 fiber: morphology, optical property, J. Mater. Sci. Eng. A (2015) 5, https://doi.org/10.17265/2161-6213/2015.9-10.006.

[44] A. Kuzume, M. Ozawa, Y. Tang, Y. Yamada, N. Haruta, K. Yamamoto, Ultrahigh sensitive Raman spectroscopy for subnanoscience: direct observation of tin oxide clusters, Sci. Adv. 5 (2019) 1–8, https://doi.org/10.1126/sciadv.aax6455.

[45] M. Itoh, Time-dependent power laws in the oxidation and corrosion of metals and alloys, Sci. Rep. 12 (2022), https://doi.org/10.1038/s41598-022-10748-1.

[46] A.M. Kietzig, M.N. Mirvakili, S. Kamal, P. Englezos, S.G. Hatzikiriakos, Laser-patterned super-hydrophobic pure metallic substrates: cassie to Wenzel wetting transitions, J. Adhes. Sci. Technol. 25 (2011), https://doi.org/10.1163/016942410X549988.

[47] B.S. Yilbas, Laser ablation of phosphor bronze for superhydrophobic surface, Surf. Eng. 32 (2016), https://doi.org/10.1179/1743294414Y.0000000325.

[48] B. Yan, J. Tao, C. Pang, Z. Zheng, Z. Shen, C.H.A. Huan, T. Yu, Reversible UV-light-induced ultrahydrophobic-to-ultrahydrophilic transition in an α-Fe2O3 nanoflakes film, Langmuir 24 (2008), https://doi.org/10.1021/la801900r.

[49] J. Long, M. Zhong, P. Fan, D. Gong, H. Zhang, Wettability conversion of ultrafast laser structured copper surface, J. Laser Appl. 27 (2015), https://doi.org/10.2351/1.4906477.

[50] A.I. Aguilar-Morales, S. Alamri, T. Kunze, A.F. Lasagni, Influence of processing parameters on surface texture homogeneity using Direct Laser Interference

Patterning, Opt Laser. Technol. 107 (2018) 216–227, https://doi.org/10.1016/j.optlastec.2018.05.044.
[51] T. Fox, F. Mücklich, Development and validation of a calculation routine for the precise determination of pulse overlap and accumulated fluence in pulsed laser surface treatment, Adv. Eng. Mater. (2022) 2201021, https://doi.org/10.1002/adem.202201021.
[52] E.R. Sanders, Aseptic laboratory techniques: plating methods, JoVE J. (2012) 1–18, https://doi.org/10.3791/3064.

Femtosecond-DLIP on Tin-Alloyed Bronze: Effect of Pulse Fluence on Surface Topography for Antibacterial Application

Aisha Saddiqa Ahmed[a,b*], Diego Sancio[a], Daniel Wyn Müller[a], Jean-François Pierson[b], Frank Mücklich[a]

[a] Functional Materials, Saarland University, 66123 Saarbrücken, Germany

[b] Université de Lorraine, CNRS, IJL, F-54000 Nancy, France

Corresponding Author: Aisha Saddiqa Ahmed[*]

* Email address: aisha.ahmed@uni-saarland.de

Content of SI

1 XRD-Diffractograms

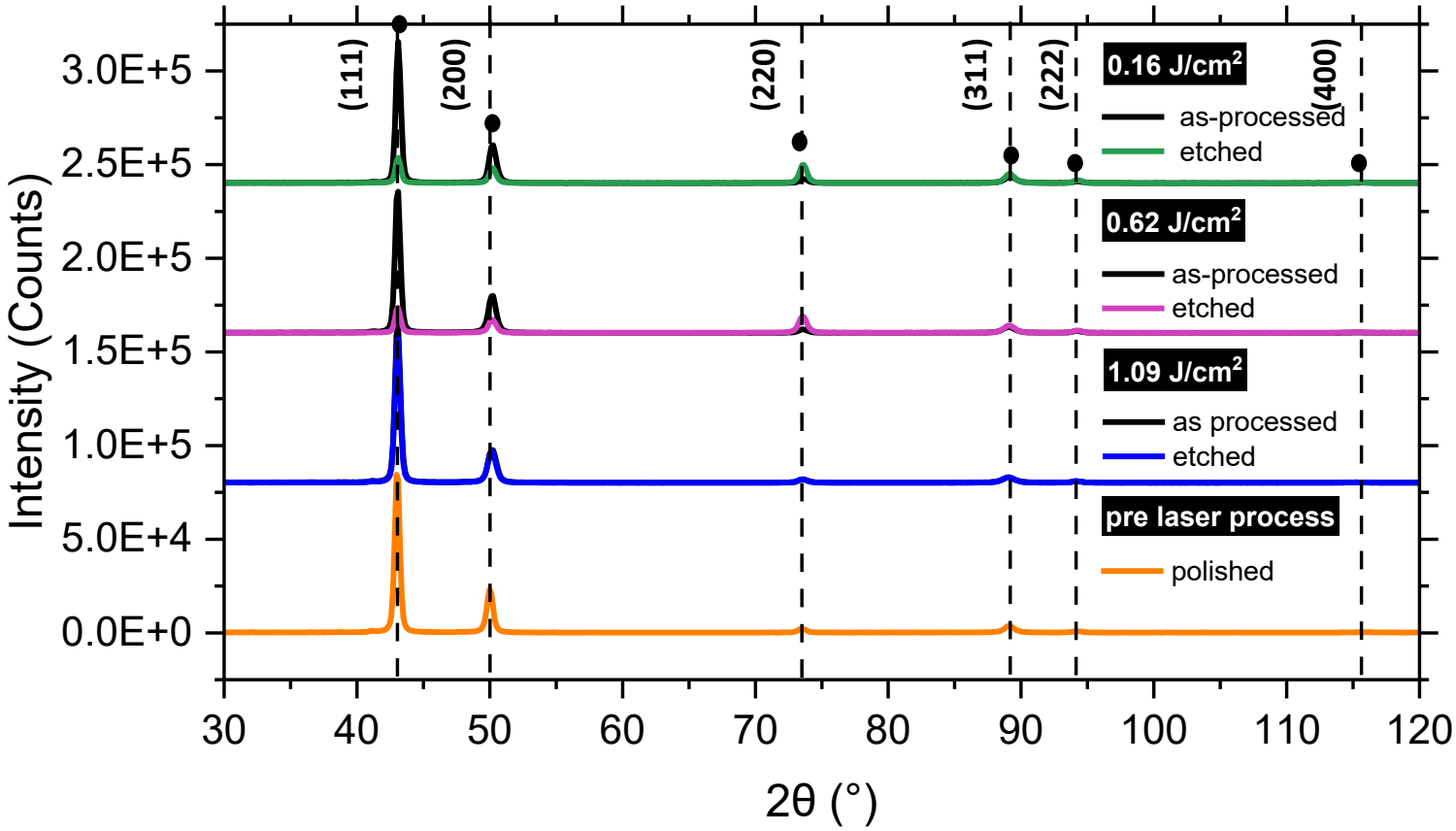

Figure S 1: XRD-Diffractograms of laser treated and the polished bronze for 2Θ range of 35-120°.

PUBLICATION IV

Tailor the Antibacterial Efficiency of Copper Alloys by Oxidation: when to and when not to

Jiaqi Luo[a,b], **Aisha Ahmed**[a,b], Jean-François Pierson[b], Frank Mücklich[a]

[a] *Chair of Functional Materials, Department of Material Science and Engineering, Saarland University, 66123 Saarbrücken, Germany*

[b] *Université de Lorraine, CNRS, IJL, F-54000 Nancy, France*

Research article

Published in "**Journal of Materials Science**" (2022)

Impact Factor: 3.9 (2025)

Accessible online at: https://doi.org/10.1007/s10853-022-06879-5

Own Contributions: Investigation, Validation, Visualization, Writing – original draft.

Cite this article as: Luo, J.; Ahmed, A.; Pierson, J. F.; Mücklich, F. Tailor the Antibacterial Efficiency of Copper Alloys by Oxidation: When to and When Not To. *J Mater Sci* **2022**, *57* (5), 3807–3821. https://doi.org/10.1007/s10853-022-06879-5.

J Mater Sci

Metals & corrosion

Tailor the antibacterial efficiency of copper alloys by oxidation: when to and when not to

Jiaqi Luo[1,2,3,*], Aisha Ahmed[1,2], Jean-François Pierson[2], and Frank Mücklich[1]

[1] *Functional Materials, Saarland University, 66123 Saarbruecken, Germany*
[2] *Université de Lorraine, CNRS, IJL, 54000 Nancy, France*
[3] *Present address: The Open Innovation Hub for Antimicrobial Surfaces, Surface Science Research Centre, Department of Chemistry, University of Liverpool, Liverpool L69 3BX, UK*

Received: 21 August 2021
Accepted: 5 January 2022

ABSTRACT

Copper and its relevant species, such as oxides and many alloys, have been recognised as potential antibacterial surfaces. Despite the relatively low antibacterial efficacy of cuprous oxide (Cu_2O) compared to pure copper, it is still worth consideration in some scenarios. Taking copper-nickel co-sputtered thin films with two copper contents (55 and 92 at.%) as examples, this work investigated the potential of oxidation in altering the antibacterial behaviour of copper alloy surfaces. By heat treatment at 200–250 °C for 20–24 h, a layer mainly composed of Cu_2O was successfully fabricated on the top of the Cu-Ni alloys. Antibacterial efficiency against *Escherichia coli* in 1 h was obtained by the droplet method and further compared. The coupons with 92 at.% copper became less effective after oxidation: the reduction rate declines from 97.0 to 74.3%; whereas the coupons with 55 at.% copper showed a large increase after oxidation, rising from 15.0 to 66.8%. The experiments described herein reveal a promising concept of oxidation in enhancing the less effective copper alloy surfaces for antibacterial applications.

Handling Editor: P. Nash.

Address correspondence to E-mail: jiaqi.luo@liverpool.ac.uk

https://doi.org/10.1007/s10853-022-06879-5

Published online: 20 January 2022

GRAPHICAL ABSTRACT

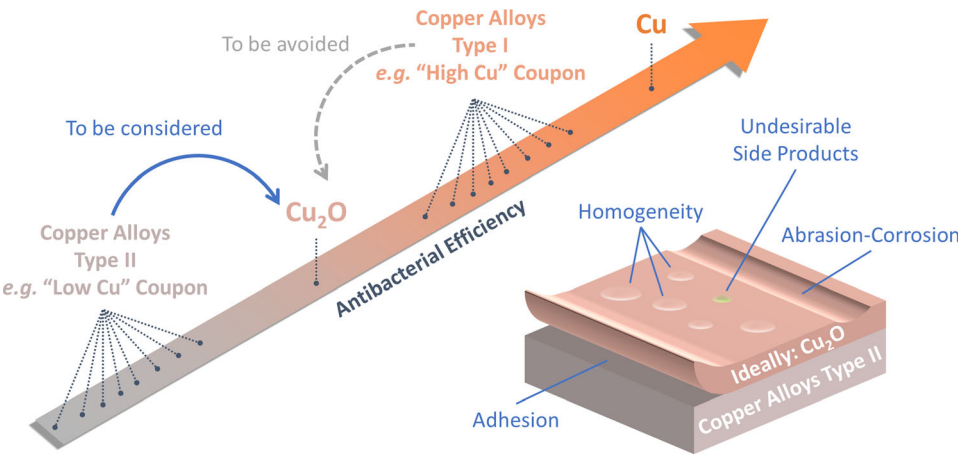

Introduction

Copper and copper alloys have been extensively investigated in recent years in terms of their antibacterial activity [1–3]. These metallic copper surfaces are excellent candidates in many scenarios, amongst which frequently touched surfaces have been highlighted, as they can be contaminated and further transmit deadly pathogens [4–7]. In our daily lives, antibacterial surfaces installed in public environments such as in transportations and buildings would be extremely helpful since timely cleaning is not always available. For the same reason, there is high expectation and demand in health care facilities, as it could become the decisive factor in combating with healthcare-associated infections (HAIs) that are strongly related to cross-contamination on surfaces.

The knowledge regarding antibacterial mechanisms of copper is being developed, which most of the time, is linked with the ionic copper released from the surfaces. Cuprous ions (Cu^{+}) could directly damage enzymes by replacing iron in their iron-sulphur clusters [8] or exhibit antibacterial effect indirectly by forming reactive oxygen species (ROS) [9]. Therefore, the antibacterial efficiency presented by the metallic copper surfaces, to a considerable degree, depends on how efficiently copper ions are released from the surfaces. This efficiency is certainly environment-dependent, for example, it can be evidently enhanced in a relatively corrosive environment in the existence of chloride [10]. Nevertheless, the chemical composition of the surfaces also plays an important role, as some alloying elements are originally designed to reduce the global corrosion tendency [11]. As a result, a phenomenon has been frequently observed on copper alloys: their antibacterial efficiency is poorer than the one of pure copper [12]. A huge range of metallic copper surfaces prepared with antibacterial properties have been assessed, including pure copper [13], Cu-Sn [14], Cu-Ag [15], Cu-Zr [16], Cu-Zr-Ag [17, 18], etc.

In addition to the metallic copper surfaces, copper oxides, regardless of their oxidation state: cupric oxide (CuO) or cuprous oxide (Cu_2O), have both shown antibacterial activity, although usually being considered less effective than pure copper [19–21]. As copper oxides can also release copper ions, even though by dissolution instead of corrosion, they do share similar antibacterial mechanisms as the metallic copper surfaces. Besides, extra amount of ROS could be produced via photocatalytic effect introduced by their semiconductor characteristics [22], assisting the antibacterial process. Copper oxide surfaces with antibacterial activity have been successfully synthesised by various methods, *e.g.* chemical vapour deposition [20], sputtering [21], wet chemical method

[23], hydrothermal method [24], and spin coating [25].

Apart from depositing an extra oxide layer on the pre-existing objects, such oxides can be obtained by directly transforming the metallic copper surfaces through specific oxidation processes. Several attempts have been recently reported, in order to evaluate the impacts of such sort of oxidation on the metallic copper alloys as well as their antibacterial efficiency [26, 27]. More precisely, it is usually the potential undesirable degradation of antibacterial efficiency that draws the attention of researchers. However, considering that the antibacterial efficiency of copper alloys could actually vary on a quite large scale [1], there might be several copper alloys that own poorer antibacterial efficacy than copper oxides. In these cases, oxidation of these surfaces would not necessarily become an unwelcome phenomenon. Instead, it can be the key to improve the antibacterial activity of those copper alloy surface, meanwhile preserving the advantage of metallurgical processing or mechanical properties introduced by alloying elements.

Consequently, we designed a scenario to verify this hypothesis. Copper-nickel thin films were produced by co-sputtering method, with two different copper contents, representing copper alloys with antibacterial efficiency in two ranges: intrinsically better or worse than Cu_2O. These thin films were thermally oxidised, aiming to form a layer of Cu_2O on the surface. Their antibacterial efficacy against *E. coli* was analysed, confirming the potential of this strategy.

Materials and methods

Thin film deposition

Copper-nickel thin films were deposited on microscope glass slides by magnetron co-sputtering technique. Before being transferred into the sputtering chamber, the substrates were cleaned with ethanol in an ultrasonic bath. During deposition, the sputtering pressure was maintained at 0.4 Pa, whilst the flow rate of argon was 50 sccm. The distance between the substrate and the Cu target (2″ diameter and 99.99% purity) and Ni target (2″ diameter and 99.99% purity) were 59 and 66 mm, respectively. The Cu content was controlled by adjusting the sputtering current of the Cu target by a DC generator (MDX-1.5 K, Advanced Energy): it was 0.20 A for high Cu content coupons (hereafter "High Cu") and 0.05 A for low Cu content coupons (hereafter "Low Cu"). Sputtering of Ni target was performed with a constant current 0.10 A for both sets, by a pulsed-DC generator (Pinnacle, Advanced Energy), whose frequency and off time were 50 kHz and 4 ms, respectively. The total deposition time was 10 min for the High Cu and 20 min for the Low Cu. These thin films were deposited without intentional heating of the substrate holder.

Heat treatment

Formation of oxides on the above-mentioned thin films were processed in a heating oven (UT 6120, Heraeus). Coupons were placed in the oven at room temperature, and the heat treatment was counted from the time the oven reached the specific temperatures. There were two sets of heat treatment parameters: (1) 200 °C for 20 h and (2) 250 °C for 24 h. At the end of this time, the oven was shut down and the coupons were taken out after the oven reached room temperature. The ventilation of the oven was maintained at the lowest level before the oven was shut down. According to their original copper contents, they are called "High Cu HT" and "Low Cu HT" hereafter.

Solutions

Phosphate-buffered saline (PBS) was prepared using NaH_2PO_4. $1H_2O$ (Merck, Germany, final concentration 0.01 M), NaCl (VWR, Germany, final concentration 0.14 M) and pure water for analysis, and its pH value was adjusted by adding NaOH to 7.4. It was sterilised after preparation.

Surface characterisation

High resolution grazing incidence X-ray diffractometer (GIXRD, Cu Kα source with a wavelength of 1.54 Å at 1° grazing angle, PANalytical X'Pert PRO-MPD) was used to determine the phases of as-deposited and heat-treated thin films. The following diffraction data are used to index: JCDPS#04-0836 for Cu, JCPDS#75-1531 for Cu_2O, and JCPDS#04-0835 for NiO. Different functions of scanning electron microscope (SEM, Helios NanoLab600, FEI) were employed at 5 kV: both Everhart–Thornley detector and Through-the-Lens detector were applied to

examine the top-surface of the coupons, whilst their global or local chemical composition was obtained by energy-dispersive X-ray spectroscopy (EDS). Image classification and analysis was processed with Fiji [28], with which the "Find Maxima" algorithm was applied.

Antibacterial efficiency determination

The antibacterial activity on the coupon surface was tested via the droplet method [29]. *E. coli* WT K12 (BW25113) strain were grown overnight aerobically in Lysogeny broth (LB) medium at 37 °C in a water bath with a speed of 220 rpm. Next day, the bacterial culture was taken out and centrifuged at 5000 × g to separate the stationary cells. The centrifugation process was repeated three times with PBS using the same parameters. Finally, the stationary cells were resuspended in PBS to prepare the bacterial suspension. Following this, 20 µL of the suspension was applied on the tested surfaces in the form of droplet. The test was carried out in a high humid environment at room temperature for a 1 h duration. At the end of this time, 10 µL of the suspension was retreated from the droplet after repetitive pipetting, then serially diluted in PBS and finally spread on LB agar plates. The plates were stored in an incubator at 37 °C for 24 h. Finally, the colony-forming units (cfu) were counted to enumerate the bacteria of the suspension taken. For negative control, the cfu/ml value from the test on the stainless steel was chosen for the section "Heat treatment at 200 °C is only successful for the High Cu" and the original cfu/ml value of the suspension for the section "Heat treatment at 250 °C turned the Low Cu to Cu_2O". Reduction rate is calculated by dividing the number of deactivated bacteria (i.e. difference of the cfu between the values of negative control and the values obtained in 1 h) by the values of negative control.

Results and discussion

Characterisation of as-deposited Copper-nickel thin films

Prior to investigating the effects of heat treatment, it is important to understand the features of the as-deposited thin films. Figure 1a presents the elemental analysis of the Cu-Ni co-sputtered thin films prepared with two currents applied to the Cu target. In the spectrum obtained from the High Cu, the CuL peak dominates the X-ray distribution, whilst the NiL peak can hardly be distinguished. On the other hand, the NiL peak becomes obvious in the case of the Low Cu. Quantification of these two elements after ZAF correction can be found in the inset: 92 at.% for the High Cu and 55 at.% for the Low Cu. However, it must be noticed that, these values may not precisely represent the actual composition because of the overlap of these two peaks, especially in the case of the High Cu (find detailed explanation in SI Fig. 1).

X-ray diffractograms shown in Fig. 1b further reveal the phase composition of the coupons. The broad diffraction peaks located from 15 to 40° originate from the amorphous glass substrate. This peak was less obvious for the High Cu, simply due to the greater thickness of the thin film (SI Fig. 2). For the same reason, the other diffraction peaks that can be indexed to Cu, are more intense in the diffractogram of the High Cu. Besides, on the diffractogram of the Low Cu, shift of the Cu diffraction peaks to higher angle can be observed as highlighted in the inset. This phenomenon is associated to the substitution of Cu atoms by Ni atoms in the fcc solid solution. Because the metallic Ni atoms is smaller than the Cu ones, an increase of Ni content leads to a decrease of the fcc lattice constant, causing a shift towards higher diffraction angle according to Bragg's law.

Figure 1c–e further compare the morphology of the as-deposited thin films. It is clear that a larger grain size is observed on the High Cu, whereas that shown on the Low Cu already reaches the limit of resolution at that operating conditions. For the same reason, the statistics from image processing indicate a relatively high fraction in the ultrasmall region, which could come from the inevitable error introduced by the blurry boundaries. The discrepancy of two thin films could be attributed to the thickness, *i.e.* the growth process of thin films, where the Low Cu could be closer to its nucleation regime and therefore with a finer microstructure.

To conclude, the Cu content is not the sole difference existing between two set of Cu-Ni thin films. However, it can be seen from the following sections that the influence of other parameters is not concerning in the present study.

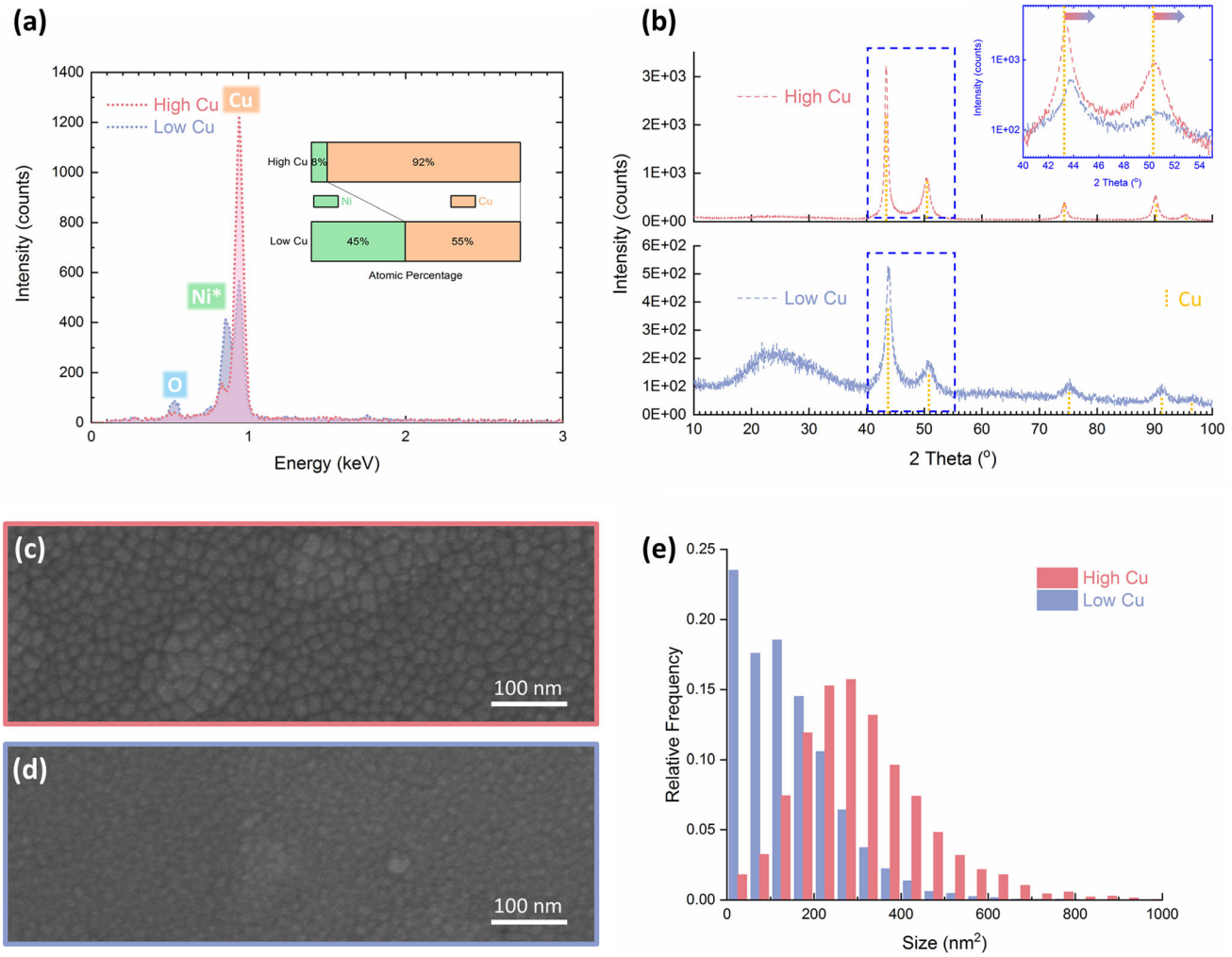

Figure 1 EDS spectra (**a**) collected from the coupons, with inset indicating the quantitative results after ZAF correction where Ni and Cu were selected. The label of Ni is marked with star in order to remind the readers of the likely overlap between NiL and CuL. High resolution GIXRD results (**b**) of as-deposited coupons, with inset that compares the positions of (111) and (200) diffractions with pure copper (JCDPS#04-0836). Representative high resolution SEM images of as-deposited the High Cu (**c**) and the Low Cu (**d**). Histogram (**e**) summaries the distribution of the lateral size of the grains calculated from SEM images.

Heat treatment at 200 °C is only successful for the High Cu

Heat treatment in ambient atmosphere at 200 °C has been demonstrated to form a layer of Cu_2O on top of pure Cu samples [19]. As a result, heat treatment at this temperature was firstly applied on Cu-Ni co-sputtered thin films, aiming to oxidise their outermost part and to obtain a layer mainly composed of Cu_2O.

Phase analysis of the heat-treated thin films can be found in Fig. 2a. For the High Cu HT, heat treatment introduces three extra and distinct peaks in its diffractogram, namely the (110), (111), and (220) diffraction peaks of Cu_2O. However, it has to be admitted that the formation of nickel oxide (NiO) should not be ruled out, based on the greater affinity of Ni atoms for oxygen [30]. The fact that it is hardly detectable can be attributed to the low Ni concentration in the alloy.

On the other hand, the attempt to form Cu_2O on the Low Cu HT seems to be unsuccessful: no additional diffraction peaks can be identified clearly or indexed to Cu_2O (or NiO). The reason why the current heat treatment parameters might not be effective enough to form an observable amount of Cu_2O could be associated with the addition of Ni. Previous research performed at elevated temperature (around

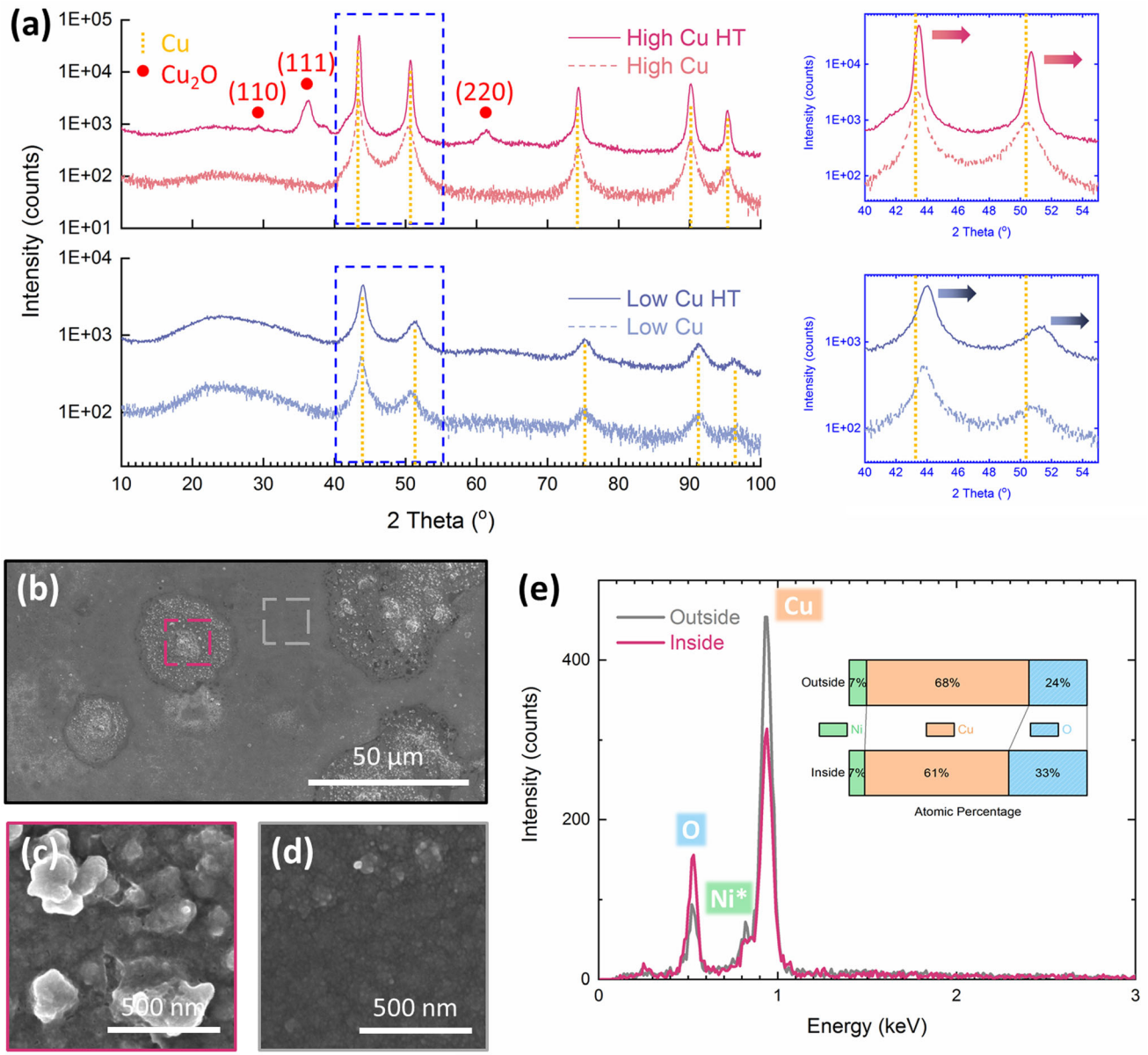

Figure 2 High resolution GIXRD results (**a**) of 200 °C heat-treated coupons ("High Cu HT" and "Low Cu HT") and their original as-deposited coupons ("High Cu" and "Low Cu" that have been shown in Fig. 1) for comparison. Cu_2O (JCPDS#75-1531) was applied to index the additional peaks. Enlarged spectra at the right side compare the positions of (111) and (200) diffractions with pure copper (JCDPS#04-0836). Representative SEM image (**b**) and high resolution SEM images (**c, d**) of two different regions found on the High Cu HT. EDS spectra (**e**) were collected from the regions that marked by squares in (**b**), with inset indicating the average quantitative results based on the data shown in SI Fig. 3. The label of Ni is marked with star in order to remind the readers of the likely overlap between NiL and CuL.

450 °C) has observed a prolonged nucleation period for Cu_2O as the concentration of Ni rises in the low copper content regime [31].

In addition, in both cases, the diffraction peaks from Cu can still be easily recorded, meaning that a substantial portion of these heat-treated thin films is still in the unreacted metallic state. These Cu diffraction peaks exhibit a shift to higher angle. As discussed in the above section, the shift of these metallic diffraction peaks corresponds to the shrinkage of fcc lattice. It is true that annealing tends to enhance diffusion, remove defects, improve the crystallinity, and thus results in relaxation of the internal stress. But if the shrinkage of glass substrate

due to annealing is more significant than that of thin films, then an external compressive state would still be introduced on the thin films. Alternatively, this compressive state can be related to the formation of oxides. The Pilling–Bedworth ratio of Cu_2O and NiO are both greater than 1, implying that an increase in volume is expected once Cu or Ni transforms to its oxide. It could therefore introduce compressive stress to the unreacted metallic thin films.

Although the formation of Cu_2O on the High Cu HT was successful, interestingly, the oxidation is not homogeneous. Figure 2b–e compare the evident morphological features: there are some (mostly round) regions owning coarser and upheaved particles, whereas the other regions are finer and flatter. Besides, stronger X-ray signal of oxygen can be found in the former region, representing the formation of thicker or denser oxide. It has to be noted that the atomic percentages calculated (as well as those to be shown in the following section) do not represent the chemical composition of any phases in any regions. This is because the X-ray signal could originate from both the oxide layer and the underneath co-sputtered thin films, and it therefore does not satisfy the premise of quantification under ZAF correction. Although these micron-scale features are not going to be further discussed with the global antibacterial activity, recent studies from different research groups did imply their possible roles in assisting bacteria deactivation [32, 33].

As for the antibacterial behaviour, previous studies have shown the significant effect of oxide formation on pure copper surfaces [19, 27]. Similar tests were now conducted on both Cu-Ni thin films, both the as-deposited state and the heat-treated state. Figure 3 shows the survival and reduction rate of *E. coli* after 1 h contact time compared to stainless steel. The results show that the High Cu killed bacteria most efficiently (96.8%), whilst its heat-treated state, the High Cu HT became less efficient (77.9%). This can be attributed to the formation of Cu_2O on the High Cu HT: the intrinsic antibacterial efficiency of the High Cu is higher than that of Cu_2O, thus the oxide coverage on the surface compromises the antibacterial behaviour.

The Low Cu, on the other hand, exhibits a relatively poor antibacterial efficacy: the reduction rate increases from 33.7% to 44.2% after heat treatment. This could be a neglectable enhance, given that the standard deviations are relatively huge. This can be attributed to the insufficient oxidation of the surface: if the surface was completely transformed into Cu_2O only (as in the case of the High Cu HT), then an antibacterial efficiency or reduction rate similar to the High Cu HT should have been observed. That being said, other modifications in terms of microstructural or surface properties introduced by the thermal oxidation process (*i.e.* annealing process) could also contribute to this neglectable change in antibacterial efficiency. To sum up, it is still necessary to find another approach that can lead to a sufficient Cu_2O formation on the Low Cu, in order to accomplish verification of the concept proposed.

Heat treatment at 250 °C turned the Low Cu to Cu_2O

Since the heat treatment parameters described in the above section failed to oxidise the Low Cu (even with prolonged period, see SI Fig. 4), thermal oxidation at a slightly high temperature (250 °C) was proceeded as it often increases the tendency to form oxides [34, 35], meanwhile avoiding the formation of less-desirable CuO [36]. Although it is unnecessary to carry out this heat treatment on the High Cu (as the designed Cu_2O was already obtained at 200 °C and served its purpose), it was still included here for better comparison.

The diffractograms in Fig. 4a demonstrate the efficacy of this heat treatment at 250 °C on both coupons. Cu_2O oxide still dominates the oxide species formed on the High Cu HT, but most excitingly, the very same oxide finally appears on the Low Cu HT. Additionally, a relatively tiny and broad diffraction peak was recorded and can be assigned to (220) diffraction of NiO. And again, such an annealing process introduces a shift of Cu diffraction peaks to higher angle for similar reasons discussed in the previous section.

Similarly, Fig. 4b–d show the localised strong oxidation phenomenon observed on the Low Cu HT (and the High Cu HT as well, see SI Fig. 6). The regions outside are also oxidised, but less in amount. Since in the case of the Low Cu HT, X-ray radiation of CuL and NiL can be easily differentiated, it is thus clear that a drop of NiL intensity can be recognised inside the strong oxidation regions. This revealed the preferred oxidation of Cu in these regions.

Regarding the antibacterial behaviour shown in Fig. 5, similar to the results in the previous section,

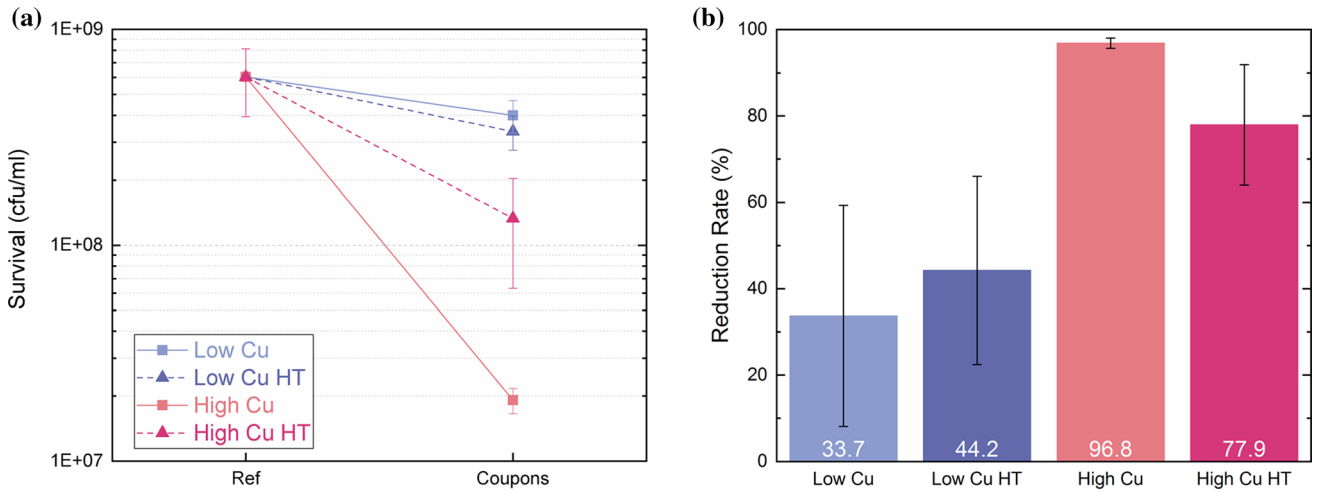

Figure 3 Antibacterial efficiency tests with *E. coli* on the 200 °C heat-treated coupons ("High Cu HT" and "Low Cu HT") and their original as-deposited coupons ("High Cu" and "Low Cu"): (**a**) surviving colony-forming units and (**b**) the reduction rate in 1 h. The cfu obtained on stainless steel is set as the negative control. The error bars indicate the standard deviation calculated from three measurements. The straight lines in (**a**) are only added for guiding the eyes.

the High Cu shows the best antibacterial efficiency (97.0%) amongst the tested coupons, whilst the High Cu HT endures a decrease (to 74.3%) due to surface oxidation. On the other hand, unlike the heat treatment at 200 °C, the number of surviving bacteria on the Low Cu HT decreases significantly this time. The reduction rate thus mounts from 15.0% to 66.8%, which is very close to that obtained from the High Cu HT. This trend is exactly as expected, as it reflects the successful Cu_2O formation on the surface of the Low Cu HT, which thus should show a comparable antibacterial efficiency as the High Cu HT. Formation of NiO could be a contributory factor of the slight difference between two heat-treated coupons, because it has not been considered to share comparable antibacterial property as Cu_2O. Besides, the antibacterial efficiency of the heat-treated coupons from this study and the sputtered Cu_2O coating (around 50% in 1 h) from our previous study [21] are just comparable but not entirely identical. This once again suggests that the antibacterial property does not depend on chemical/phase composition only, but possibly also on the minor effects of the microstructural or surface parameters, which may still require further investigation.

It is true that there are some discrepancies compared to the reduction rates obtained in the first heat treatment trial, *e.g.* the same Low Cu showed only 15% in this trial but 33.7% in the first trial. This could be introduced by the selection of the negative control (stainless steel or the original suspension), or the possible difference in the original concentration of the bacterial suspension [37, 38], etc. The slight decrease obtained from the High Cu HT (74.3% in this trial but 77.9% in the first trial) could be attributed to the same reason, or other slight intrinsic differences between two High Cu HT surfaces. Nevertheless, none of these affects the concept to be verified: oxidation on certain metallic copper alloy surfaces can truly improve their antibacterial efficiency.

Discussion on this promising strategy and practical insights

From the above comparison, it is clear that oxidation opens a powerful and simple pathway to tailor the antibacterial performance of the metallic copper alloy surfaces. This is summarised in Fig. 6, where antibacterial efficiency of pure copper and Cu_2O are set as benchmarks. For the alloys that already show a better reduction rate than Cu_2O (grouped as "Copper Alloys Type I"), oxidation should be avoided as it impairs their intrinsic antibacterial efficiency, although whether it can be effectively avoided is another issue. On the contrary, for those intrinsically less potent than Cu_2O (grouped as "Copper Alloys Type II"), measures that lead to surface oxidation should be considered. By transforming the metallic surfaces into Cu_2O, their antibacterial efficiency can be replaced by that of Cu_2O.

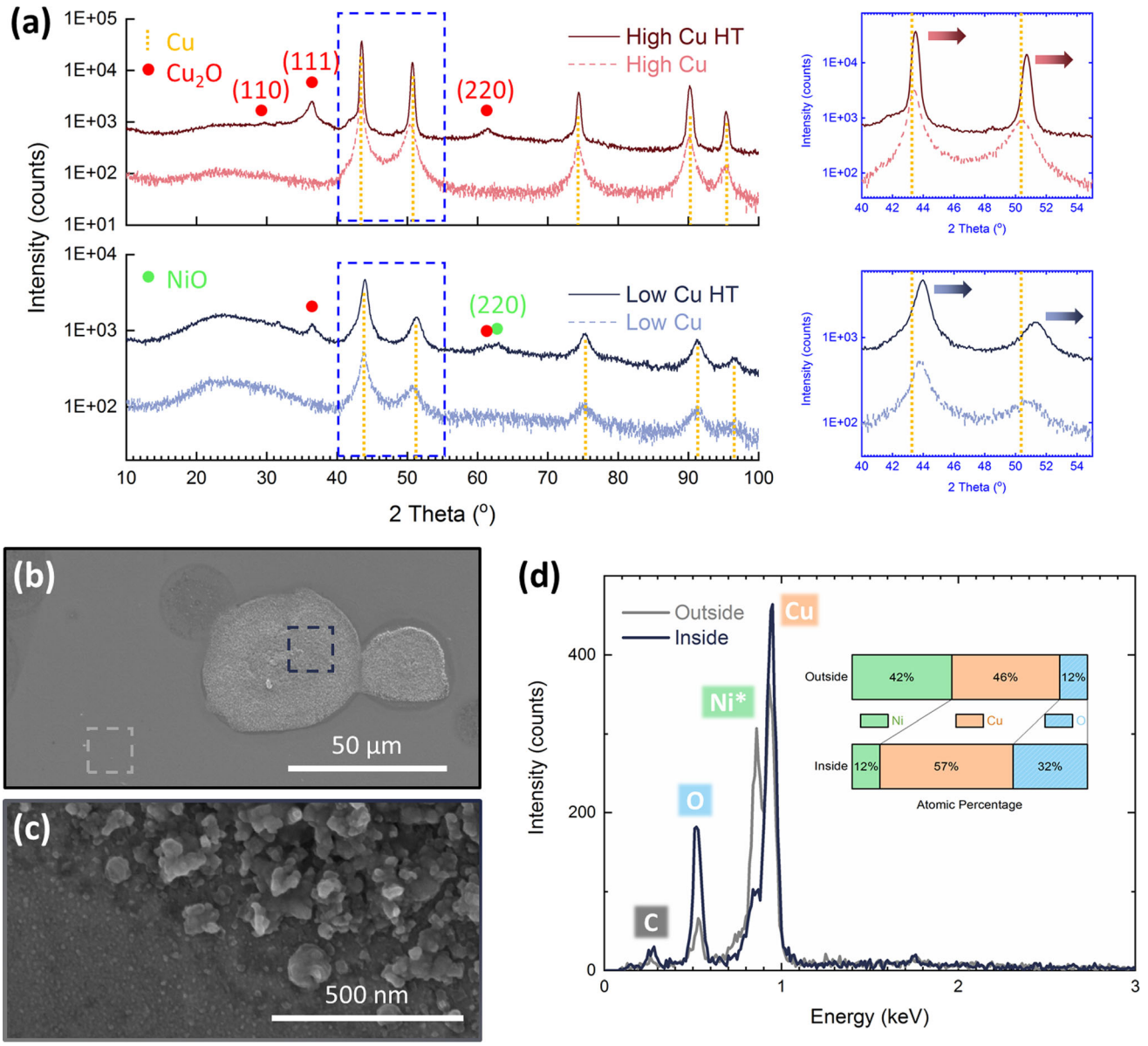

Figure 4 High resolution GIXRD results (**a**) of 250 °C heat-treated coupons ("High Cu HT" and "Low Cu HT") and their original as-deposited coupons ("High Cu" and "Low Cu" that have been shown in Fig. 1) for comparison. Cu_2O (JCPDS#75-1531) and NiO (JCPDS#04-0835) were applied to index the additional peaks. Enlarged spectra at the right side compare the positions of (111) and (200) diffractions with pure copper (JCDPS#04-0836). Representative SEM image (**b**) and high resolution SEM image (**c**) from the edge of two different regions found on the Low Cu HT. EDS spectra (**d**) were collected from the regions that marked by squares in (**b**), with inset indicating the average quantitative results based on the data shown in SI Fig. 5. The label of Ni is marked with star in order to remind the readers of the likely overlap between NiL and CuL.

It should be noted that, although in the present work, Copper Alloys Type I is represented by the High Cu whilst Copper Alloys Type II by the Low Cu, alloys with relatively lower copper contents do not necessarily always exhibit a poorer antibacterial efficacy [26, 39]. In other words, whether to oxidise an alloy or not should rely on its intrinsic antibacterial efficiency (which can be measured from trials), but not simply on its chemical composition (*e.g.* how high the copper content is).

The proof of concept presented in this work was accomplished by Cu-Ni co-sputtered thin films, because sputtering is without a doubt one of the most effective and effortless methods to obtain a defined

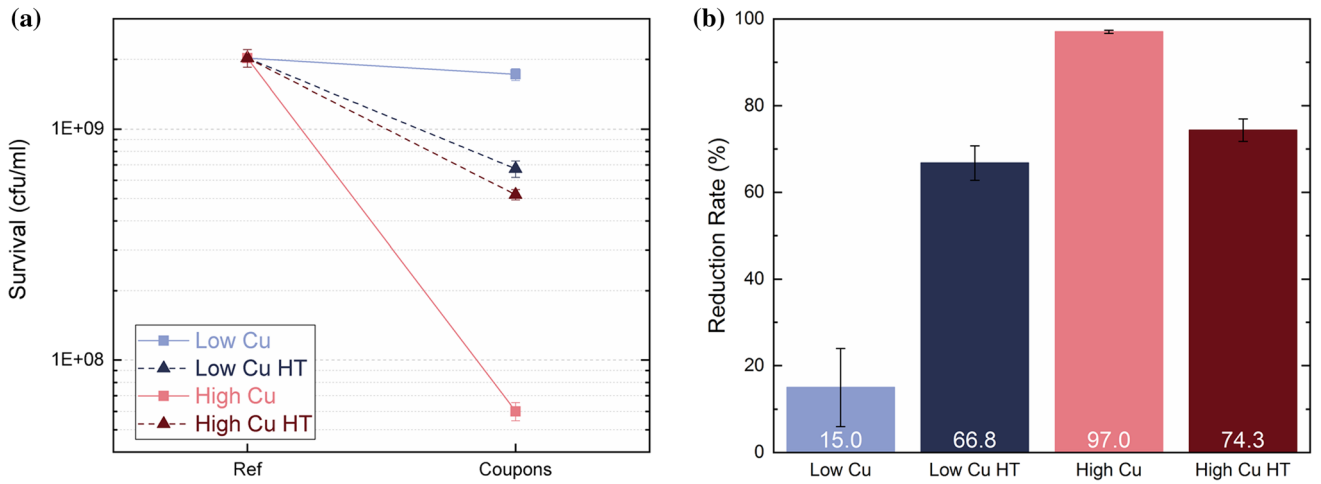

Figure 5 Antibacterial efficiency tests with *E. coli* on the 250 °C heat-treated coupons ("High Cu HT" and "Low Cu HT") and their original as-deposited coupons ("High Cu" and "Low Cu"): (**a**) surviving colony-forming units and (**b**) the reduction rate in 1 h. The cfu obtained from the original suspension is set as the negative control. The error bars indicate the standard deviation calculated from three measurements. The straight lines in (**a**) are only added for guiding the eyes.

surface with certain chemical composition or crystallinity. Many recent studies have applied this method to design functional surfaces and explored their antibacterial potentials [14, 17, 18]. But the very same idea is certainly applicable or even more meaningful in bulk copper alloys that can be fabricated in conventional metallurgical ways, no matter whether it is with commercial alloying elements or newly developed compositions [40, 41]. Its adaptability to a wide range of existing commercial copper alloys is worth being emphasised in the future studies.

Meanwhile, exclusive formation of Cu_2O could be a challenge, just like the formation of NiO on the Low Cu HT shown in this study. One could also imagine as more/different alloying elements are included, undesirable by-products could form during oxidation process [42], undermining the coverage of antibacterial Cu_2O or even suppressing its formation. Extensive investigation is thus needed in the selection of alloy composition in each applying scenario, even though coexistence of oxides might be inevitable subject to the oxygen affinity. Suitable temperature (as already shown in the present work) together with ambience composition might be two important parameters in guiding a desirable oxidation process. Nevertheless, apart from thermal oxidation, there are also other feasible approaches to introduce oxide that might be adapted accordingly, *e.g.* anodic oxidation [43] or laser surface treatment [32, 44, 45].

No matter which oxidation method is selected, there are other features of the oxidised layer that are essential to application and therefore should also be examined if possible. One of them is the horizontal homogeneity of oxidation. Localised strong oxidation spots that are observed in this work, however, did not introduce too much concern in antibacterial efficiency test, as it actually represents inhomogeneity in depth whilst the droplet method for 1 h is an evaluation based on the global antibacterial performance of the outermost surface in short term. Moreover, only if the amount of copper released into the droplet is sufficient to deactivate the microbes, the locations where release occurs could be less important. But this may not always suit the actual scenarios: there might be no aqueous environment covering the entire surface, and therefore it is important to ensure every position that is contaminated by microbes can present equally excellent antibacterial effect. In addition to chemical composition, homogeneity could be required in other aspects such as microstructure and micro/nano-roughness. To better investigate the localised antibacterial behaviour, recently developed tests with dry or quasi-dry inoculum [46, 47] are certainly important alternatives.

On the other hand, inhomogeneity in depth, namely the effective oxidation depth is still an important variable. Usually, one advantage of applying copper and its alloys in daily touched surfaces is their quasi self-healing properties: abrasion-corrosion introduced by touching or cleaning [48]

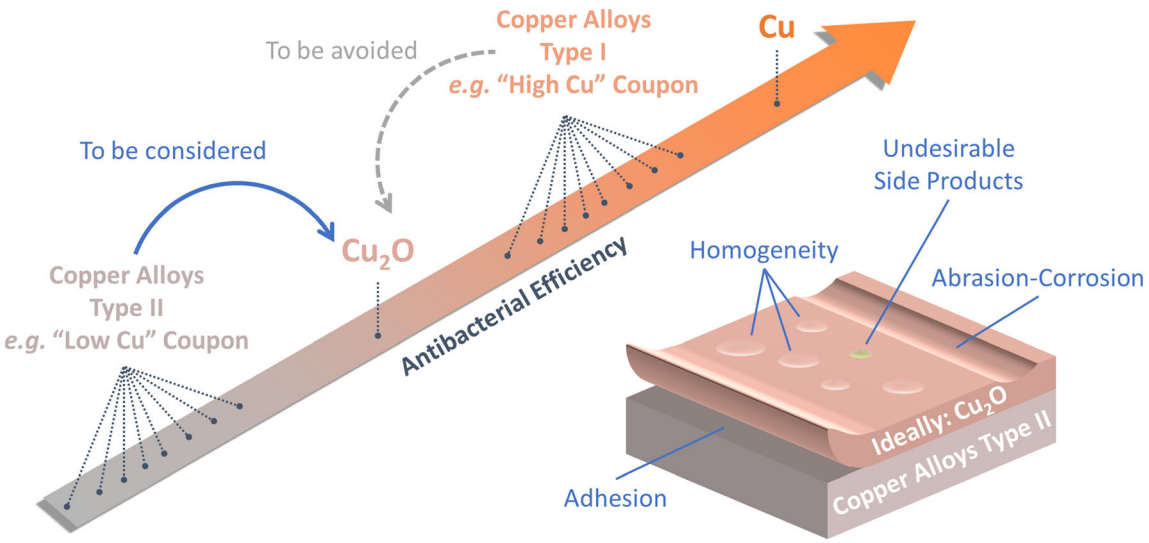

Figure 6 Schematic illustration of the potential of oxidation in altering the antibacterial efficiency of copper alloys and some practical insights of this concept.

could help releasing the topmost layer as well as the adhered microbes. This exposes the "new" surface underneath, maintaining the similar antibacterial efficacy. However, when surface oxidation is applied, the desired antibacterial effect only exists in the oxidised part, meaning within a certain depth. It is therefore important to evaluate the loss rate of the oxides in each specific circumstance in order to determine the desired depth of oxidation for an aimed lifespan. Along with this perspective, adhesion of the oxidised layer should be assessed or improved when necessary, since weak adhesion might cause early failure of the antibacterial layer.

Furthermore, adoption of oxidation strategy also shifts the mechanism of antibacterial copper ion release: from corrosion of the original metallic phases [49] to dissolution of Cu_2O [21], which can be influenced by temperature, pH value, etc. [50]. As a result, specifying the environmental factors in the evaluations will ensure much applicable implication and persuasive conclusion. Given that the outermost surface will be oxidised on purpose, the deterioration induced by atmospheric corrosion might not be as troublesome as that on the metallic copper surfaces [10, 42], but it could still be worthwhile tracking the stability of the oxidised surface, *e.g.* together with daily disinfection events [51].

Last but not the least, although it was only the antibacterial efficiency against *E. coli* that was investigated in the present study, copper surfaces have actually shown capability against a very broad range of bacteria [3, 7, 52], viruses [53–55], and fungi [25, 52, 56]. Therefore, the strategy proposed here is also encouraging in many scenarios where the general antimicrobial property is needed.

Conclusion

Thermal oxidation of Cu-Ni co-sputtered thin films are served as examples to illustrate the potential roles of oxidation on antibacterial copper alloy surfaces. Some concluding remarks are listed as follows:

- Critical oxidation temperature depends on the copper content of the thin films. To form a layer of Cu_2O on the surface in 20–24 h, thin films with higher copper content (92 at.%) require only 200 °C, whilst a relatively higher temperature (250 °C) is required for those with lower copper content (55 at.%).
- Although the atomic percentage of oxygen increased globally, some relatively strongly oxidised regions are found on both oxidised thin films, together with distinct sub-micron topography.
- Successful oxidation of the investigated thin films introduces dramatic changes in their antibacterial performance against *E. coli* evaluated by the droplet method: the high copper content thin films get degraded (reduction rate in 1 h declines from 97.0% to 74.3%) whilst the low copper

content ones get significantly improved (from 15.0% to 66.8%).
- The concept of enhancing antibacterial efficiency of less effective copper alloy surfaces by means of surface oxidation is verified.

Acknowledgements

The authors would like to thank Johannes Webel for the meaningful introduction in SEM image classification, and Dr. Christoph Pauly for constructive discussion in interpretation of EDS results.

Author contribution

JL contributed to conceptualization, investigation, validation, visualization, and writing – original draft. AA contributed to investigation, validation, visualization, and writing – original draft. J-FP contributed to funding acquisition, resources, supervision, and writing – review and editing. FM contributed to funding acquisition, resources, and supervision.

Funding

This study was supported by Erasmus Mundus Joint European Doctoral Programme in Advanced Materials Science and Engineering (DocMASE, 512225-1-2010-1-DE-EMJD, European Commission) and the PhD-Track-Programme (PhD02-14, Franco-German University). A.A. has been funded by the German Aerospace Center—Space Administration (DLR) within the project "Investigation of antimicrobial metal surfaces under space conditions—An effective strategy to prevent microbial biofilm formation" (Project Number 50WB1930), and German Research Foundation (DFG) within the project "Controlled bacterial interaction to increase the antimicrobial efficiency of copper surfaces" (Project Number 415956642). Open Access funding enabled and organized by Projekt DEAL.

Data availability

The data that support the findings of this study are available from the corresponding author on request.

Declarations

Conflict of interest The authors declare that they have no conflict of interest.

Supplementary Information: The online version contains supplementary material available at https://doi.org/10.1007/s10853-022-06879-5.

References

[1] Michels H, Moran W, Michel J (2008) Antimicrobial properties of copper alloy surfaces, with a focus on hospital-acquired infections. Int J Metalcast 2:47–56

[2] Salgado CD, Sepkowitz KA, John JF, Cantey JR, Attaway HH, Freeman KD, Sharpe PA, Michels HT, Schmidt MG (2013) Copper surfaces reduce the rate of healthcare-acquired infections in the intensive care unit. Infect Control Hosp Epidemiol 34:479–486

[3] Michels HT, Keevil CW, Salgado CD, Schmidt MG (2015) From laboratory research to a clinical trial: copper alloy surfaces kill bacteria and reduce hospital-acquired infections. HERD Health Environ Res Des J 9:64–79

[4] Souli M, Antoniadou A, Katsarolis I, Mavrou I, Paramythiotou E, Papadomichelakis E, Drogari-Apiranthitou M, Panagea T, Giamarellou H, Petrikkos G, Armaganidis A (2017) Reduction of environmental contamination with multidrug-resistant bacteria by copper-alloy coating of surfaces in a highly endemic setting. Infect Control Hosp Epidemiol 38:765–771

[5] Ibrahim Z, Petrusan AJ, Hooke P, Hinsa-Leasure SM (2018) Reduction of bacterial burden by copper alloys on high-touch athletic center surfaces. Am J Infect Control 46:197–201

[6] Różańska A, Chmielarczyk A, Romaniszyn D, Majka G, Bulanda M (2018) Antimicrobial effect of copper alloys on *Acinetobacter* species isolated from infections and hospital environment. Antimicrob Resist Infect Control 7:10

[7] Dauvergne E, Lacquemant C, Adjidé C, Mullié C (2020) Validation of a worst-case scenario method adapted to the healthcare environment for testing the antibacterial effect of brass surfaces and implementation on hospital antibiotic-resistant strains. Antibiotics 9:245

[8] Macomber L, Imlay JA (2009) The iron-sulfur clusters of dehydratases are primary intracellular targets of copper toxicity. Proc Natl Acad Sci 106:8344–8349

[9] Santo CE, Taudte N, Nies DH, Grass G (2008) Contribution of copper ion resistance to survival of *E. coli* on metallic copper surfaces. Appl Environ Microbiol 74:977–986

[10] Luo J, Hein C, Pierson J-F, Mücklich F (2020) Sodium chloride assists copper release, enhances antibacterial efficiency, and introduces atmospheric corrosion on copper surface. Surf Interfaces 20:100630

[11] Davis JR (2001) Copper and copper alloys. ASM international, Ohio

[12] Hong R, Kang TY, Michels CA, Gadura N (2012) Membrane lipid peroxidation in copper alloy-mediated contact killing of *E. coli*. Appl Environ Microbiol 78:1776–1784

[13] Kocaman A, Keles O (2019) Antibacterial efficacy of wire arc sprayed copper coatings against various pathogens. J Therm Spray Technol 28:504–513

[14] Kang Y, Park J, Kim D-W, Kim H, Kang Y-C (2016) Controlling the antibacterial activity of CuSn thin films by varying the contents of Sn. Appl Surf Sci 389:1012–1016

[15] Ciacotich N, Din RU, Sloth JJ, Møller P, Gram L (2018) An electroplated copper–silver alloy as antibacterial coating on stainless steel. Surf Coat Technol 345:96–104

[16] Villapún VM, Lukose CC, Birkett M, Dover LG, González S (2018) Tuning the antimicrobial behaviour of Cu85Zr15 thin films in "wet" and "dry" conditions through structural modifications. Surf Coat Technol 350:334–345

[17] Etiemble A, Der Loughian C, Apreutesei M, Langlois C, Cardinal S, Pelletier JM, Pierson JF, Steyer P (2017) Innovative Zr-Cu-Ag thin film metallic glass deposed by magnetron PVD sputtering for antibacterial applications. J Alloy Compd 707:155–161

[18] Comby-Dassonneville S, Venot T, Borroto A, Longin E, der Loughian C, ter Ovanessian B, Leroy M-A, Pierson J-F, Steyer P (2021) ZrCuAg thin-film metallic glasses: toward biostatic durable advanced surfaces. ACS Appl Mater Interfaces 13:17062–17074

[19] Hans M, Erbe A, Mathews S, Chen Y, Solioz M, Mücklich F (2013) Role of copper oxides in contact killing of bacteria. Langmuir 29:16160–16166

[20] Hassan IA, Parkin IP, Nair SP, Carmalt CJ (2014) Antimicrobial activity of copper and copper(i) oxide thin films deposited via aerosol-assisted CVD. J Mater Chem B 2:2855–2860

[21] Luo J, Hein C, Pierson J-F, Mücklich F (2019) Early-stage corrosion, ion release, and the antibacterial effect of copper and cuprous oxide in physiological buffers: Phosphate-buffered saline vs Na-4-(2-hydroxyethyl)-1-piperazineethanesulfonic acid. Biointerphases 14:061004

[22] Katwal R, Kaur H, Sharma G, Naushad M, Pathania D (2015) Electrochemical synthesized copper oxide nanoparticles for enhanced photocatalytic and antimicrobial activity. J Ind Eng Chem 31:173–184

[23] Ekthammathat N, Thongtem T, Thongtem S (2013) Antimicrobial activities of CuO films deposited on Cu foils by solution chemistry. Appl Surf Sci 277:211–217

[24] Eswar NK, Gupta R, Ramamurthy PC, Madras G (2018) Influence of copper oxide grown on various conducting substrates towards improved performance for photoelectrocatalytic bacterial inactivation. Mol Catal 451:161–169

[25] Shim G-I, Kim S-H, Eom H-W, Choi S-Y (2015) Concentration- and roughness-dependent antibacterial and antifungal activities of CuO thin films and their Cu ion cytotoxicity and elution behavior. J Ind Microbiol Biotechnol 42:735–744

[26] Horton DJ, Ha H, Foster LL, Bindig HJ, Scully JR (2015) Tarnishing and Cu ion release in selected copper-base alloys: implications towards antimicrobial functionality. Electrochim Acta 169:351–366

[27] Walkowicz M, Osuch P, Smyrak B, Knych T, Rudnik E, Cieniek Ł, Różańska A, Chmielarczyk A, Romaniszyn D, Bulanda M (2018) Impact of oxidation of copper and its alloys in laboratory-simulated conditions on their antimicrobial efficiency. Corros Sci 140:321–332

[28] Schindelin J, Arganda-Carreras I, Frise E, Kaynig V, Longair M, Pietzsch T, Preibisch S, Rueden C, Saalfeld S, Schmid B, Tinevez J-Y, White DJ, Hartenstein V, Eliceiri K, Tomancak P, Cardona A (2012) Fiji: an open-source platform for biological-image analysis. Nat Methods 9:10999

[29] Molteni C, Abicht HK, Solioz M (2010) Killing of bacteria by copper surfaces involves dissolved copper. Appl Environ Microbiol 76:4099–4101

[30] Wagner C (1952) Theoretical analysis of the diffusion processes determining the oxidation rate of alloys. J Electrochem Soc 99:369

[31] Heinemann K, Rao DB, Douglass DL (1977) In situ oxidation studies on (001) copper-nickel alloy thin films. Oxid Met 11:321–334

[32] Selvamani V, Zareei A, Elkashif A, Maruthamuthu MK, Chittiboyina S, Delisi D, Li Z, Cai L, Pol VG, Seleem MN, Rahimi R (2020) Hierarchical micro/mesoporous copper structure with enhanced antimicrobial property via laser surface texturing. Adv Mater Interfaces 7:1901890

[33] Müller DW, Lößlein S, Terriac E, Brix K, Siems K, Moeller R, Kautenburger R, Mücklich F (2021) Increasing antibacterial efficiency of Cu surfaces by targeted surface functionalization via ultrashort pulsed direct laser interference patterning. Adv Mater Interfaces 8:2001656

[34] Wallwork GR (1976) The oxidation of alloys. Rep Prog Phys 39:401–485

[35] Lawless KR (1974) The oxidation of metals. Rep Prog Phys 37:231–316

[36] Unutulmazsoy Y, Cancellieri C, Chiodi M, Siol S, Lin L, Jeurgens LPH (2020) In situ oxidation studies of Cu thin films: growth kinetics and oxide phase evolution. J Appl Phys 127:065101

[37] Noyce JO, Michels H, Keevil CW (2006) Potential use of copper surfaces to reduce survival of epidemic meticillin-resistant Staphylococcus aureus in the healthcare environment. J Hosp Infect 63:289–297

[38] Hahn C, Hans M, Hein C, Mancinelli RL, Mucklich F, Wirth R, Rettberg P, Hellweg CE, Moeller R (2017) Pure and oxidized copper materials as potential antimicrobial surfaces for spaceflight activities. Astrobiology 17:1183–1191

[39] Różańska A, Chmielarczyk A, Romaniszyn D, Sroka-Oleksiak A, Bulanda M, Walkowicz M, Osuch P, Knych T (2017) Antimicrobial properties of selected copper alloys on *Staphylococcus aureus* and *E. coli* in different simulations of environmental conditions: with vs without organic contamination. Int J Environ Res Public Health 14:813

[40] Fowler L, Janson O, Engqvist H, Norgren S, Öhman-Mägi C (2019) Antibacterial investigation of titanium-copper alloys using luminescent *Staphylococcus* epidermidis in a direct contact test. Mater Sci Eng, C 97:707–714

[41] Tao SC, Xu JL, Yuan L, Luo JM, Zheng YF (2020) Microstructure, mechanical properties and antibacterial properties of the microwave sintered porous Ti–3Cu alloys. J Alloys Compd 812:152142

[42] Chang T, Butina K, Herting G, Rajarao GK, Richter-Dahlfors A, Blomberg E, Wallinder IO, Leygraf C (2021) The interplay between atmospheric corrosion and antimicrobial efficiency of Cu and Cu5Zn5Al1Sn during simulated high-touch conditions. Corros Sci 185:109433

[43] Kunze J, Maurice V, Klein LH, Strehblow H-H, Marcus P (2001) In situ scanning tunneling microscopy study of the anodic oxidation of Cu(111) in 0.1 M NaOH. J Phys Chem B 105:4263–4269

[44] Villapún VM, Qu B, Lund PA, Wei W, Dover LG, Thompson JR, Adesina JO, Hoerdemann C, Cox S, González S (2020) Optimizing the antimicrobial performance of metallic glass composites through surface texturing. Mater Today Commun 23:101074

[45] Müller DW, Holtsch A, Lößlein S, Pauly C, Spengler C, Grandthyll S, Jacobs K, Mücklich F, Müller F (2020) In-depth investigation of copper surface chemistry modification by ultrashort pulsed direct laser interference patterning. Langmuir 36:13415–13425

[46] McDonald M, Wesgate R, Rubiano M, Holah J, Denyer SP, Jermann C, Maillard JY (2020) Impact of a dry inoculum deposition on the efficacy of copper-based antimicrobial surfaces. J Hosp Infect 106:465–472

[47] Chang T, Sepati M, Herting G, Leygraf C, Rajarao GK, Butina K, Richter-Dahlfors A, Blomberg E, Wallinder IO (2021) A novel methodology to study antimicrobial properties of high-touch surfaces used for indoor hygiene applications—a study on Cu metal. PLoS ONE 16:e0247081

[48] Bryce EA, Velapatino B, Khorami HA, Donnelly-Pierce T, Wong T, Dixon R, Asselin E (2020) In vitro evaluation of antimicrobial efficacy and durability of three copper surfaces used in healthcare. Biointerphases 15:011005

[49] Luo J, Hein C, Pierson J-F, Mücklich F (2019) Localised corrosion attacks and oxide growth on copper in phosphate-buffered saline. Mater Charact 158:109985

[50] Palmer D (2011) Solubility measurements of crystalline Cu2O in aqueous solution as a function of temperature and pH. J Solut Chem 40:1067–1093

[51] Steinhauer K, Meyer S, Pfannebecker J, Teckemeyer K, Ockenfeld K, Weber K, Becker B (2018) Antimicrobial efficacy and compatibility of solid copper alloys with chemical disinfectants. PLoS ONE 13:e0200748

[52] Mehtar S, Wiid I, Todorov SD (2008) The antimicrobial activity of copper and copper alloys against nosocomial pathogens and Mycobacterium tuberculosis isolated from healthcare facilities in the Western Cape: an in-vitro study. J Hosp Infect 68:45–51

[53] Noyce JO, Michels H, Keevil CW (2007) Inactivation of influenza a virus on copper versus stainless steel surfaces. Appl Environ Microbiol 73:2748–2750

[54] Warnes SL, Keevil CW (2013) Inactivation of norovirus on dry copper alloy surfaces. PLoS ONE 8:e75017

[55] van Doremalen N, Bushmaker T, Morris DH, Holbrook MG, Gamble A, Williamson BN, Tamin A, Harcourt JL, Thornburg NJ, Gerber SI, Lloyd-Smith JO, de Wit E, Munster VJ (2020) Aerosol and surface stability of SARS-CoV-2 as compared with SARS-CoV-1. N Engl J Med 382:1564–1567

[56] Lucas MDI, Botef I, Reid RG, van Vuuren SF (2020) Laboratory-based study of novel antimicrobial cold spray coatings to combat surface microbial contamination. Infect Control Hosp Epidemiol 41:1378–1383

Supplementary Information

Tailer the antibacterial efficiency of copper alloys by oxidation: when to and when not to

Jiaqi Luo[a,b,*], Aisha Ahmed[a,b], Jean-François Pierson[b], Frank Mücklich[a]

[a] Functional Materials, Saarland University, Germany
[b] Université de Lorraine, CNRS, IJL, F-54000 Nancy, France
[*] Current corresponding address: The Open Innovation Hub for Antimicrobial Surfaces, Surface Science Research Centre, Department of Chemistry, University of Liverpool, Liverpool L69 3BX, UK

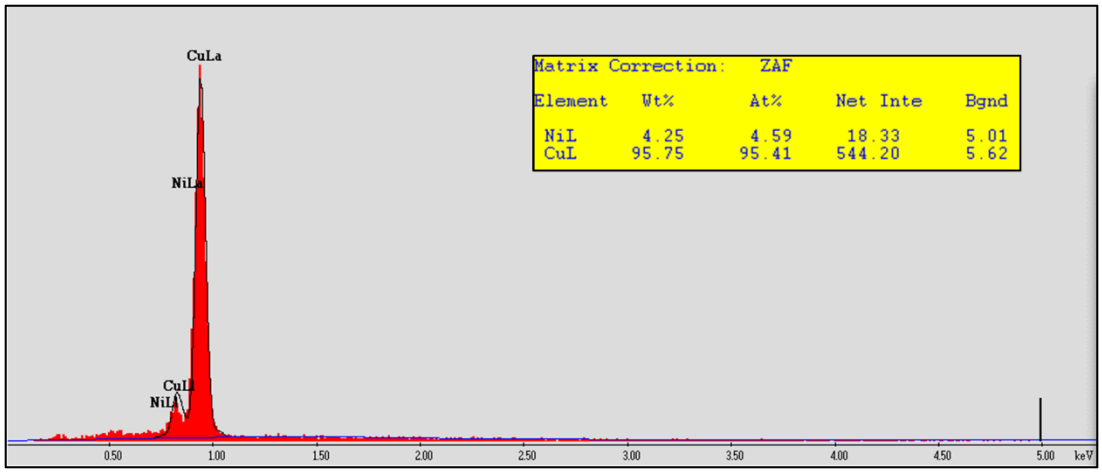

Supplementary Figure 1 | Typical EDS spectrum collected from pure copper, where quantitative analysis with ZAF correction was done with Ni and Cu.

Brief interpretation: This illustrates the impact of overlap between CuL and NiL in quantification: there will be a minimum of 4% to 5% of Ni presenting in the result if Ni is considered and manually selected, even though there is actually no Ni in the couple at all. An alternative to better quantify Cu and Ni would be considering their K_α peaks at 8.04 and 7.48 keV, respectively. This, however, can only be done with a higher acceleration voltage of the electron beam, which means thicker thin films are also required to ensure the electrons cannot reach the substrate and do not excite the irrelevant elements.

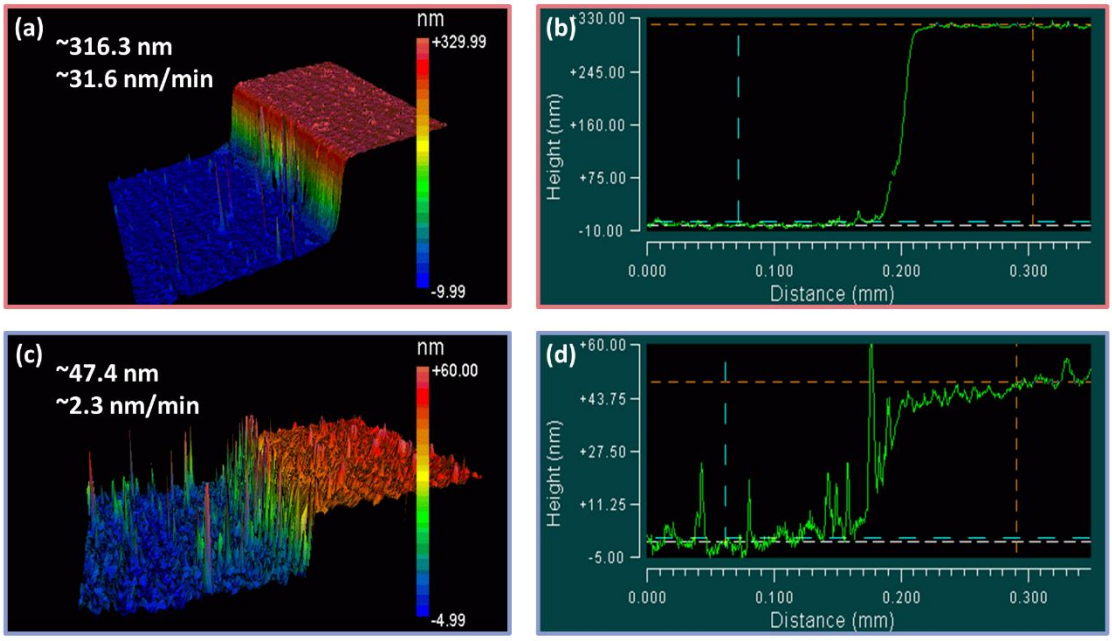

Supplementary Figure 2 | Profile and thickness measurement by white light interferometer (NewView 7300, Zygo, 20X) of as-deposited coupons: high copper content thin films **(a, b)** and low copper content thin films **(c,d)**.

Brief interpretation: Higher sputtering current of Cu was applied, resulting in an 8 times thicker thin films within half of the sputtering time, however, the values shown in **(b)** and **(d)** do not necessarily represent an average thickness as the lateral inhomogeneity cannot be totally avoided.

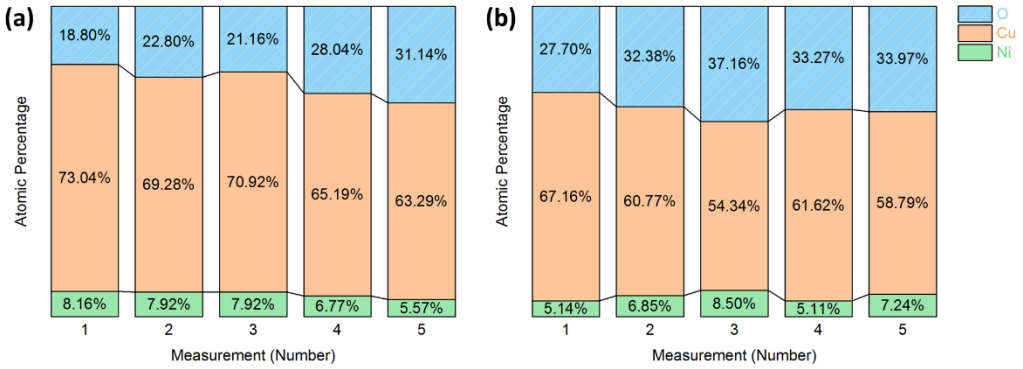

Supplementary Figure 3 | Quantitative results (after ZAF correction where Ni, Cu and O were selected) of two different regions found on the 200° C heat-treated high copper content coupon: outside the strong oxidation regions **(a)** and inside these regions **(b)**.

Brief interpretation: Five individual measurements on different locations were performed on each type of region. Average values of these data are calculated and presented in the main text Figure 2.

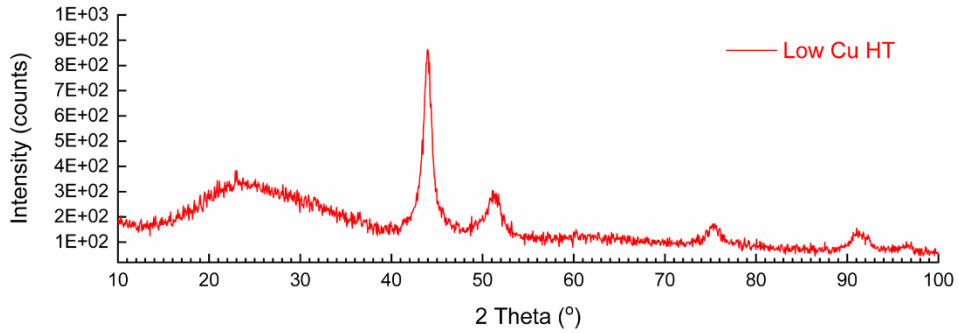

Supplementary Figure 4 | High resolution GIXRD results of low copper content thin films heat treated at 200° C for 72 h.

Brief interpretation: Prolonged heat treatment period does not introduce obvious oxide formation on low copper content thin films.

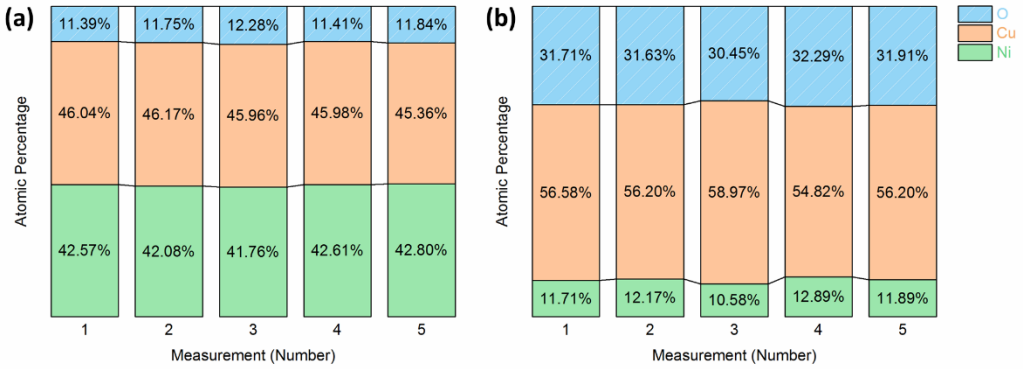

Supplementary Figure 5 | Quantitative results (after ZAF correction where Ni, Cu and O were selected) of two different regions found on the 250° C heat-treated low copper content coupon: outside the strong oxidation regions **(a)** and inside these regions **(b)**.

Brief interpretation: Five individual measurements on different locations were performed on each type of region. Average values of these data are calculated and presented in the main text Figure 4.

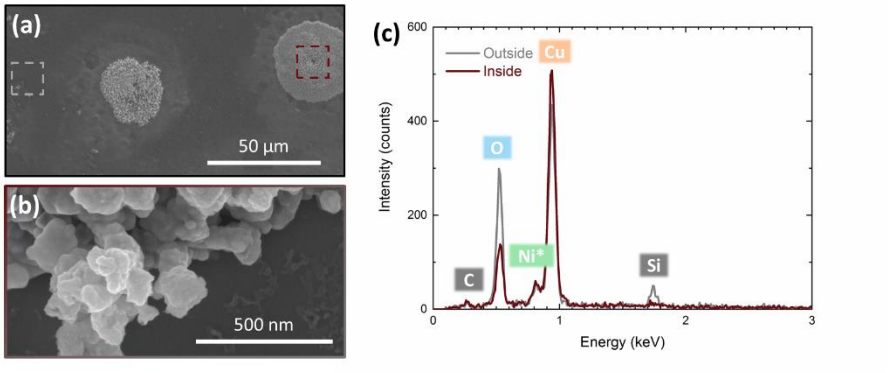

Supplementary Figure 6 | Typical SEM image **(a)** and high resolution SEM image **(b)** from the edge of two different regions found on the 250° C heat-treated high copper content coupon. EDS spectra **(c)** were collected from the regions that marked by squares in (a). The label of Ni is marked with star in order to remind the readers of the likely overlap between NiL and CuL.

Brief interpretation: Quantification has not been performed as one could already find the signal originated from Si. This could represent two scenarios: Si atom diffused from the glass substrate and entered the thin film, and/or X-ray emitted by the glass substrate reached the surface and therefore was connected. If the latter is the actual situation, then ZAF correction will not work properly as it assumes a mixture of homogenous distributed elements rather than a layer structure.

PUBLICATION V

3D Periodic Microscale Structures on Binary Copper-Nickel Alloys via fs-DLIP: Impact on *E. coli*-Substrate Interaction

Aisha Saddiqa Ahmed[a,b], Sebastian Wältermann[a], Pablo María Delfino,[c,d] Daniel Wyn Müller[a], Jean-Nicolas Audinot[c], Jean-François Pierson[b], Frank Mücklich[a]

[a] *Chair of Functional Materials, Department of Material Science and Engineering, Saarland University, 66123 Saarbrücken, Germany*

[b] *Université de Lorraine, CNRS, IJL, F-54000 Nancy, France*

[c] *Advanced Instrumentation for Nano-Analytics (AINA), Luxembourg Institute of Science and Technology (LIST), L-4422 Belvaux, Luxembourg*

[d] *University of Luxembourg, 4365 Esch-sur-Alzette, Luxembourg*

Research article

Published in "**Materials & Design**" (2025)

Impact Factor: 7.9 (2025)

Accessible online at: https://doi.org/10.1016/j.matdes.2025.114545

Own Contributions: Conceptualization, Investigation, Validation, Visualization, Writing – original draft.

Cite this article as: A.S. Ahmed, S. Wältermann, P.M. Delfino, D.W. Müller, J. Audinot, J.-F. Pierson, F. Mücklich, 3D periodic microscale structures on binary copper-nickel alloys via fs-DLIP: impact on E. coli-substrate interaction. *Mater Des* 258, 114545 **2025**. https://doi.org/10.1016/j.matdes.2025.114545.

Materials & Design 258 (2025) 114545

Contents lists available at ScienceDirect

Materials & Design

journal homepage: www.elsevier.com/locate/matdes

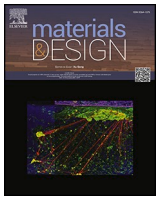

3D periodic microscale structures on binary copper-nickel alloys via fs-DLIP: impact on *E. coli*-substrate interaction

Aisha Saddiqa Ahmed [a,b,*], Sebastian Wältermann [a], Pablo María Delfino [c,d], Daniel Wyn Müller [a], Jean–Nicolas Audinot [c], Jean-François Pierson [b], Frank Mücklich [a]

[a] Functional Materials, Saarland University, 66123 Saarbrücken, Germany
[b] Université de Lorraine, CNRS, IJL F-54000 Nancy, France
[c] Advanced Instrumentation for Nano-Analytics (AINA), Luxembourg Institute of Science and Technology (LIST), L-4422 Belvaux, Luxembourg
[d] University of Luxembourg, 4365 Esch-sur-Alzette, Luxembourg

ARTICLE INFO

Keywords:
Femtosecond
Direct laser interference patterning
Copper-nickel alloy
Antibacterial
Periodic three-dimensional structures
Line-like structures
Honeycomb structures

ABSTRACT

In response to the rise of multidrug-resistant infections, researchers are increasingly focusing on modifying material surfaces through chemical or topographical changes to limit microbial spread. Copper and its alloys are particularly valued for their antimicrobial properties, playing a key role in combating pathogen transmission. To explore the potential of enhancing the antibacterial performance of copper-based alloys, this study focuses on surface modification of binary copper-nickel alloys. The goal is to create periodic microstructures at the scale of a single bacterial cell (*Escherichia coli*) and explore the bacteria-substrate interaction. Two copper-nickel alloy compositions with 10 and 30 wt-% nickel are selected to assess the impact of nickel on laser-material interaction. Additionally, two surface structures, lines and honeycomb, are fabricated to evaluate how structure type affects bacterial interaction. Results show that the line-like structures on the 10 wt-% nickel alloy enhance bacterial killing, while honeycomb structures show no improvement. Conversely, both laser-structured copper-nickel alloys with 30 wt-% nickel exhibit decreased bacterial killing, attributed to the reduced surface copper concentration (below 60 wt-%) as confirmed by chemical analyses. These findings highlight the importance of copper content and structural compatibility for effective contact-killing performance.

1. Introduction

Copper and its alloys are widely recognized for their ability to combat microorganisms, making them valuable materials in the fight against pathogen transmission [1,2]. With the growing threat of multidrug-resistant infections and the increasing prevalence of deadly microorganisms [3], research has expanded beyond conventional antibiotic development [4]. One promising approach is the modification of material surfaces via techniques that include chemical or topographical alterations to limit microbial spread through contact [5–7].

This study explores direct laser interference patterning (DLIP) [8], a surface modification technique that utilizes multiple laser beams to generate periodic micro- and nanoscale structures. DLIP has been widely employed to develop nature-inspired surface structures that enhance properties e.g., wettability, friction, electrical conductivity, and antibacterial activity [9–13]. When combined with ultrashort pulse laser processing, this technique enables precise modifications at the microscale and nanoscale that can effectively inhibit bacterial adhesion and proliferation [5,14].

While copper itself exhibits strong antibacterial properties, it is normally alloyed to meet the properties required in practical applications [15]. Nickel is a commonly used alloying element in copper-based materials, particularly in high-humidity and underwater environments, where it improves strength and corrosion resistance [16,17]. Commercial Cu-Ni alloys typically contain multiple alloying elements; however, in laser-based surface modifications, it is important to isolate and understand the interaction between the laser and the material while minimizing other variables. For that purpose, only binary copper-nickel systems are investigated in this study.

Recent studies suggest that a copper alloy must contain at least 60 wt-% copper to exhibit significant antibacterial properties [2,18]. Based on this criterion, two binary Cu-Ni alloys with 10 % and 30 % nickel by weight were selected for this investigation. The surfaces of these alloys are modified using ultrashort pulsed DLIP (USP-DLIP) to create

* Corresponding author at: Functional Materials, Saarland University, 66123 Saarbrücken, Germany.
E-mail address: aisha.ahmed@uni-saarland.de (A.S. Ahmed).

https://doi.org/10.1016/j.matdes.2025.114545
Received 29 April 2025; Received in revised form 27 June 2025; Accepted 8 August 2025
Available online 10 August 2025

microstructures tailored for bacterial interaction and increase the contact surface area. Furthermore, two distinct surface structures are studied: first, a line-like structure, previously investigated for its antibacterial properties on copper and other copper-based alloys [5,14,19,20]; and second, a honeycomb structure was designed to offer a varied contact area for bacteria and isolate them within the valleys to prevent bacterial growth. The antibacterial efficacy of both Cu-Ni alloys, along with their respective surface structures, is assessed against *Escherichia coli* (*E. coli*) to determine the role of modification in bacteria-substrate interaction.

2. Materials and methods

2.1. Materials

Two compositions of copper-nickel alloys were tested in this study. Most commercially available copper-nickel alloys contain additional alloying elements beyond copper and nickel. The primary goal of this study is to examine the specific effect of the nickel element and its weight percentage on the properties of the alloy. To achieve this, binary alloys consisting solely of copper and nickel were fabricated by the Forschungsinstitut Edelmetalle + Metallchemie in Germany, eliminating the influence of other alloying elements. The alloys were cast and then cold-rolled to a thickness of one millimeter. Subsequently, the sheets were cut to dimensions of 10 × 25 mm^2 to prepare the samples. These samples were then metallographically prepared for the laser process to achieve a mirror finish on the surfaces. For this purpose, the surfaces were first ground and then polished in three steps, as outlined in Ahmed *et al.* [19].

2.2. Direct laser interference patterning

A Ti:sapphire Spitfire laser system from Spectra Physics, featuring a femtosecond pulse duration, is used to modify surfaces at the microscale. Direct laser interference patterning is employed to create periodic structures at the scale of bacteria for this study. This technique involves two coherent laser beams that intersect through a lens and are then focused onto the sample surface, generating an intensity profile that leads to the formation of the desired 3D structures. An 800 nm centered wavelength and an ultrashort pulse duration of 150 fs (full width at half maximum) were employed. The optical configuration was chosen according to Ahmed *et al.* [19]. It comprises of five main components: a beam diameter aperture, a wave plate, a diffractive optical element, a mask, and a focusing lens system with a 100 mm focal length. In this study, two distinct structures are created. A line-like structure is produced using two-beam interference, while a honeycomb structure is generated using three-beam interference, both with a pulse fluence (F_{pulse}) of 0.65 J/cm^2 and an accumulated number of 18–19 pulses (n_{acc}).

Finally, the samples are immersed in 10 % citric acid to remove any process-related oxides. They are then stored at room temperature under ambient conditions for a minimum of 3 weeks to ensure stable wetting properties [5]. Subsequent examinations and tests are conducted after this 3-week period. For this study, samples that have undergone laser structuring are referred to as "as-processed," while those that have undergone both laser structuring and etching are referred to as "etched.

2.3. Surface characterization

The surface topography was examined using confocal laser scanning microscopy (CLSM) with the LEXT OLS4100 3D Measuring Laser Microscope (Olympus) and scanning electron microscopy (SEM) in secondary contrast mode (Helios NanoLab 600™, FEI/Thermo Fisher Company). SEM images were captured at an acceleration voltage of 5 kV, with a current of 1.4nA, and the sample surface was tilted at a 45° angle.

Surface elemental analysis was conducted using the FEI/Thermo Fisher Helios G4 PFIB CXe system, along with EDAX APEX software from Ametek Materials Analysis Division. Since the surface modification penetrated only a few micrometers, an acceleration voltage of 5 kV and a current of 5.5nA were used to limit the analysis to the outermost layer.

Phase analysis is performed using a high-resolution grazing incidence X-ray diffractometer (GI-XRD), equipped with a Cu K_α source (wavelength 1.5418 Å) and operated at a 1° grazing angle, utilizing the PANalytical X'Pert PRO-MPD system. Additionally, Raman spectroscopy (Horiba Jobin, Lab RAM HR with a 532 nm laser) is employed to characterize oxides.

Surface chemical analysis was performed using a secondary ion mass spectrometer (SIMS) integrated to a Zeiss Orion NanoFab Helium Ion Microscope (HIM).[21] First, secondary electron (SE) images were acquired with 2048x2048 pixels, 25 keV He^+, 4 pA, dwell time of 10 µs/pixel, 4 lines average. Subsequently, SIMS images were acquired with 512x512 pixels, 25 keV Ne^+, 5 pA, dwell time of 2 ms/pixel leading to a total of 8 min per image. Representative Regions Of Interest (ROIs) were selected for line-like and honeycomb structures with and without bacteria. Successive in situ SE and SIMS acquisitions provide morphological and chemical correlation from the same ROI.

The SIMS analysis was performed in dynamic mode, which operates under continuous ion bombardment. This configuration provides both a high spatial resolution (down to sub-15 nm) and an excellent detection limit for elemental analysis, making it particularly suitable for resolving nanoscale chemical distributions on structured surfaces and for detecting copper uptake at the bacterial interface as it is shown in section 3.3.2.

2.4. Contact killing and wet plating method

Contact killing followed by wet plating is used to determine the antibacterial activity on the surfaces. *E. coli* is grown aerobically overnight in Lysogeny broth (LB), and the bacterial suspension is prepared in a phosphate-buffered saline (PBS) according to Ahmed *et al.* [14]. Droplets with a volume of 40 µL each are placed on sample surfaces for 30 min, 60 min and 90 min. After the respective contact time, 5 µL of each droplet is retrieved, further diluted, and placed on LB-agar plates. After 24 h of incubation at 37 °C, the number of colony forming units (CFU) is counted to enumerate the surviving CFU/mL. The experiment was repeated three times for each material and contact time to ensure the results were reproducible.

3. Results and discussion

3.1. Topographical modifications

The surfaces were initially examined using secondary electron microscopy to assess the topographical changes. Fig. 1 a and b demonstrate that the desired periodicity of 3 µm for the line-like structures, with a depth of approx. 1 ± 0.2 µm, is achieved. As expected, the line-like structures (Fig. 1 a and b) show wide valleys and narrow peaks [14,19,22]. The periodicity aligns with literature values for the structure, which show an increased killing rate of *E. coli* on structured copper and brass [5,14].

The three-beam interference generates an intensity profile that forms honeycomb-like point structures. The interference minima of the three beams create a region with hexagonal peaks range, while the interference maxima form a region with point valleys, resulting in a hexagonal pattern. Previous studies [23,24] demonstrate the fabrication of similar point structures using DLIP, though with different pulse durations, wavelengths, periodicities and materials. According to the findings of Mulko *et al,*.[23] the crater/valley width increases with higher fluence, and the shape of this ablated regions transitions from circular to hexagonal. In this study, the structures have a periodicity of 3.5 µm and a depth of 1 ± 0.2 µm, as shown in Fig. 1 c and d. With these dimensions, the valley width is approximately in the range of individual *E. coli* cells,

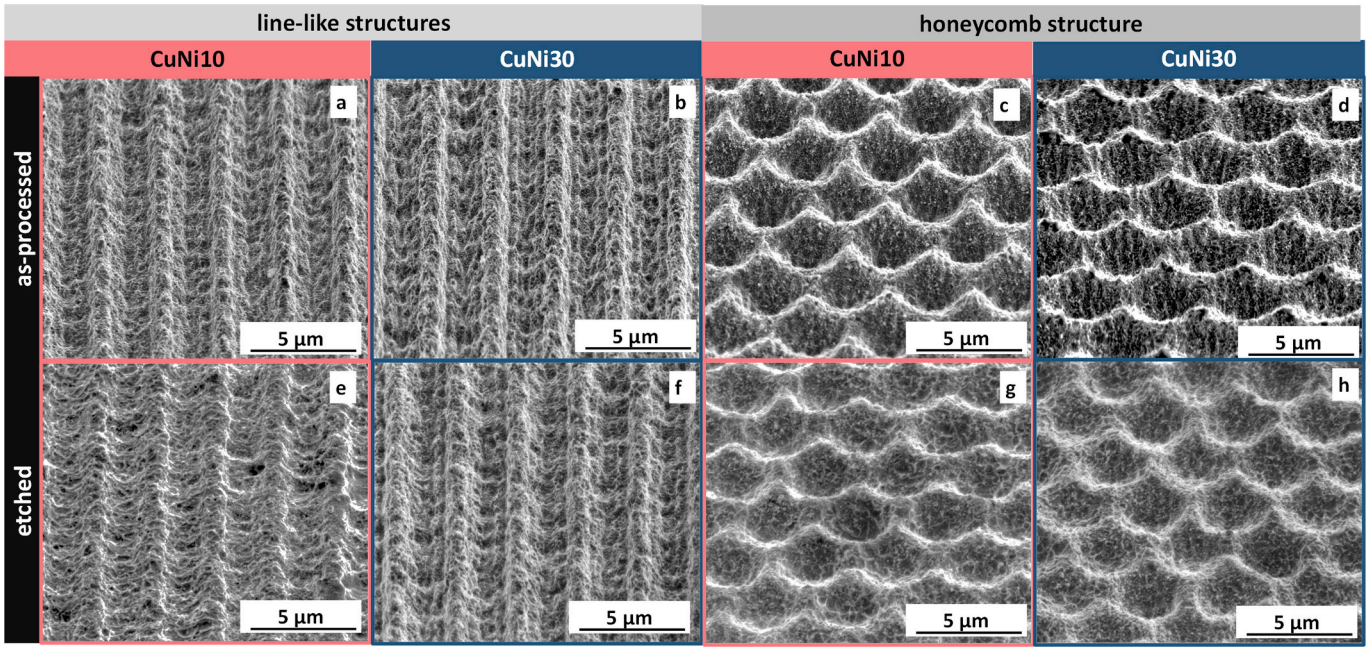

Fig. 1. SEM-images of 3D-microscale periodic structures on CuNi10 and CuNi30. As-processed surfaces: a) and b) represent the line-like structures. c) and d) represent the honeycomb structures on both alloys in their as-processed state, respectively. Etched surfaces: e) and f) correspond to the line-like structures, and g) and h) to the honeycomb structures.

which is ideal for contact with bacteria and similar to the line-like structure observed in this study and previous ones [5,14].

Overlapping beams create an intensity profile with maxima and minima, forming either a line-like (two-beam) or honeycomb (three-beam) pattern in the absorbed energy. Regardless of whether it is a two-beam or three-beam setup, the laser-material interaction remains similar for both structure types, as it is dependent on the pulse duration. In the case of femtosecond-pulsed DLIP, the pulse duration is shorter than the electron-lattice relaxation time (1–10 picoseconds) [25]. As a result, the high energy absorption leads to cold material ablation, primarily through phase explosion, which involves the creation of vapor and plasma phases that expand into the atmosphere, along with spallation [26,27]. This process is accompanied by a minimal heat-affected zone, resulting in little to no melting of the material [28–30]. Ultimately, it results in the formation of precise, periodic structures [31]. Due to the ultrashort pulse duration, the process is followed by rapid cooling of the molten matter and the redeposition of ablated material [32,33]. Additionally, since the phase explosion and evaporation occur outward from the interference maxima, the redeposition of ablated material predominantly happens on the peak regions of the structures, contributing to the roughness at the sub-micron scale [19].

In addition, another topographical feature at sub-µm is the formation of laser-induced periodic surface structures (LIPSS) [34,35]. The formation of LIPSS has been observed in previous studies using femtosecond laser processing on various materials and is reported to be dependent on several laser parameters, including wavelength, polarization, and scanning velocity [26,36,37]. Both alloys exhibit similar topographical features including LIPSS formation. In the case of line-like structures, the LIPSS are parallel to the lines, while in the honeycomb structure, they align with the vertical axis of the SEM images shown in Fig. 1 c and d.

Another notable difference is that the alloy with higher nickel content displays a small amount of flake-like structures that are associated with oxide formation [22]. The formation of these flake-like structures is directly related to the laser fluence [38]. Since both alloys have different chemical compositions, their laser-material interactions vary, which directly influences the chemical modification [39]. As a result, the threshold laser fluence required to form these flake-like structures may differ depending on the alloy composition. Given that the pulse fluence used for both alloys are identical, it is highly likely that this is the reason for the variation in the concentration of these flake-like structures. Moreover, after etching these flake-like structures are removed from the surface and both alloys depict the same topography (see Fig. 1 e-h).

3.2. Chemical modifications

3.2.1. Elemental analysis

Chemical analysis was performed using multiple methods, beginning with SEM-EDS for elemental analysis of both peak (black spectra) and valley (red spectra) regions of as-processed samples. The results are displayed in Fig. 2 and summarized in Table 1 for both alloy compositions.

In the laser-processed CuNi10 samples (Fig. 2 a and c), both regions, peak and valley, show the presence of the same elements. One noticeable difference is the intensities of the spectra, likely caused by height differences in the measured area, which directly affects the information depth. The signal is in particular weak within the valley regions of the honeycomb structures, which are surrounded on all sides by the peak regions. This is probably due to the obstruction of both the irradiated beam and the emitted beam from reaching the detector. In the case of the line-like structures, the lines were aligned with the detector, allowing it to receive a comparatively stronger signal from the valleys. However, when comparing the weight percentages of the valleys for both structures, the compositions are similar.

Overall, compared to the bulk chemical composition, there is a slight increase in oxygen content and a significant increase in nickel content, approximately 7–8 wt-%, are noted. Oxygen content is slightly higher on the peaks of the lines, consistent with previous research on line-like structures [22]. Notably, the highest increase in nickel content, around 11 wt-%, is observed in the valleys of the honeycomb structures (see Table 1). It is important to note that, although the wt-% of oxygen listed in Table 1 is quite low, the measured increase in at-% is somewhat higher, ranging between approximately 4–7 at-%. This indicates that the surface contains a higher concentration of oxygen atoms, even though its overall mass contribution to the material is relatively small, given oxygen's lower atomic weight compared to the metals in the alloy.

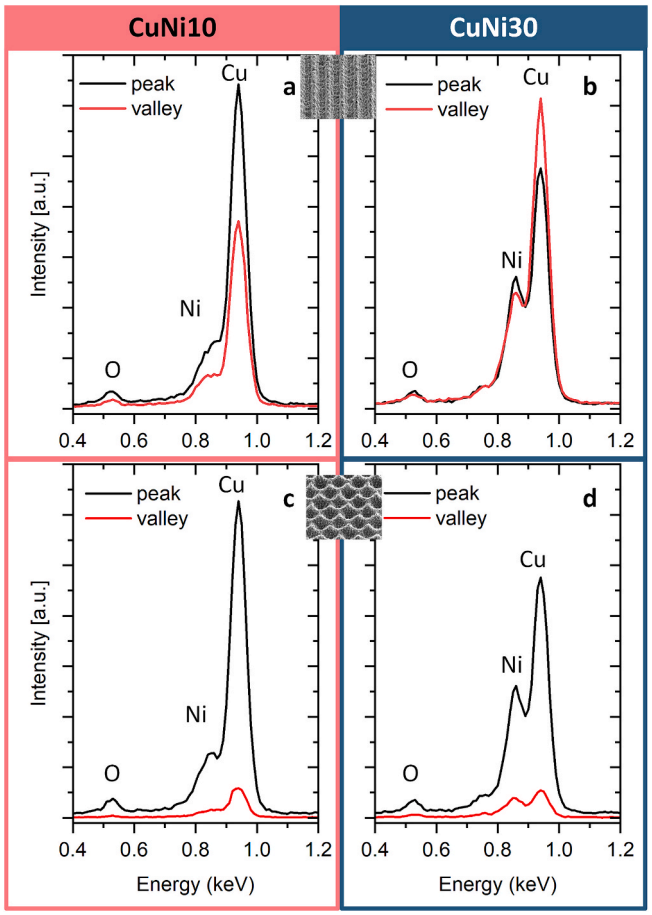

Fig. 2. EDX-spectra of laser-structured CuNi10 and CuNi30: a) & b) line-like structures c) & d) honeycomb structure. Each sample was analysed on the peak (black spectra) and in the valley (red spectra). (For interpretation of the references to colour in this figure legend, the reader is referred to the web version of this article.)

Oxygen might be forming a thin oxide layer or could be adsorbed onto the surface.

CuNi30 samples in Fig. 2 b and d also exhibit the presence of the same elements. Compared to the bulk chemical composition, the peaks (black spectra) of both structured surfaces show a slight increase in oxygen content and an increase in nickel content ranging from approx. 4–5 wt-%. However, significant compositional differences are evident between peaks and valleys. The valleys (red spectra in Fig. 2 b) of line-like structures exhibit a slight decrease in nickel and oxygen content, aligning closely with the known bulk composition of polished samples in terms of copper and nickel wt-%. The difference in oxygen content between peaks and valleys correlates with the results observed in CuNi10 lines.

Furthermore, the valleys of honeycomb structures for CuNi30 demonstrate a slight increase in oxygen content and a significant increase in nickel content, up to approx. 12 wt-%. This led to a decrease in copper content to approx. 54 wt-%. These findings suggest the presence of an oxide phase with high nickel content. According to the Ellingham diagram [40], the energy released during the formation of nickel oxide is more negative than that of copper, suggesting that the formation of a nickel-rich oxide phase is thermodynamically favored.

3.2.2. Phase analysis

Subsequently, phase analysis was performed on both polished and as-processed samples using GI-XRD. The resulting diffractograms are shown in Fig. 3 and Fig. 4, highlighting the prominent peaks: (111), (200), (220), (311), and (222) which appear in all samples. Fig. 3 a shows the diffractogram of polished CuNi10 with peaks at 43.65°, 50.67°, 74.59°, 90.45°, and 95.78°. In comparison, the peaks of CuNi30 are observed at 43.91°, 50.93°, 75.11°, 91.23°, and 96.56° (see Fig. 4 a). Since the atomic radii of nickel is lower than that of copper, the increase of the nickel content induces a shift in the peak positions towards higher 2θ values. These results are consistent with literature values [41–43] for pure copper, pure nickel, and binary copper-nickel alloys, confirming the correlation with known diffractograms.

Additionally, it is visible that for CuNi10 polished, the (111) and (200) peaks are more intense. According to the literature [44], both face-centered-cubic copper and nickel exhibit similar intensity ratios in between the peaks with (111) being the dominant one. While for CuNi30 polished, the (220) and (311) peaks are relatively more pronounced. This difference in relative intensities depends on various factors that influence the crystalline structure and texture of the sample, i.e. the agents and conditions used during sample fabrication, as well as the preparation of the sample surface [45–48].

The diffractograms of both CuNi10 as-processed samples, lines (Fig. 3 b) and honeycomb (Fig. 3 d) structures, are identical. However, as this is compared to the polished surface, a new low-intensity peak is visible at 36.63°. This can be attributed to the presence of copper or nickel oxide. According to literature [49–51], the 2Θ-value of (111) peak for cuprous oxide is at 36.42° and for nickel oxide at around 37.25°. However, there are no further peaks visible for any oxides and the most dominant peak in the case of nickel oxide is (200) at 43.28° (Ref.: PDF # 00–044-1159). Furthermore, a study [52] shows the presence of (003) peak at 36.79° for nickel oxide with nickel vacancies (Ref. ICCD 04–011-2340). This suggests the presence of copper oxide, likely with defects, and the shift to a higher 2Θ value compared to the literature value indicates that this may be related to the presence of nickel content. Another notable distinction is approx. a 0.1° shift observed in the (111) peak towards a lower value, and in the (200) peak towards a higher value. Additionally, there is a noticeable alteration in the relative intensities. Figures b and d illustrate that the (220) peak exhibits relatively high intensity, suggesting a preferred orientation of the CuNi10 surfaces after structuring.

The structured samples are also etched to remove any laser-process related oxide, as it has been shown in previous studies to enhance the killing of *E. coli* in the case of laser-structured copper alloys [14,19]. Fig. 3 c and e present the diffractograms of both etched laser-structured CuNi10 samples. These diffractograms are similar to their respective as-processed diffractograms with one exception, which is no visible sign of the oxide peak. This suggests the removal of oxides on laser-structured CuNi10 samples via etching.

Table 1
Weight percentages (wt-%) of copper and nickel in CuNi10 and CuNi30 samples after structuring, as determined by EDX analysis.

wt-%	CuNi10				CuNi30			
	lines		honeycomb		lines		honeycomb	
	peak	valley	peak	valley	peak	valley	peak	valley
Cu	79.5	80.5	78.9	74.7	60.7	68.4	62.4	53.9
Ni	17.8	17.4	16.8	21.0	36.3	29.2	34.9	41.8
O	1.91	1.28	1.86	1.54	1.76	1.34	1.74	2.57

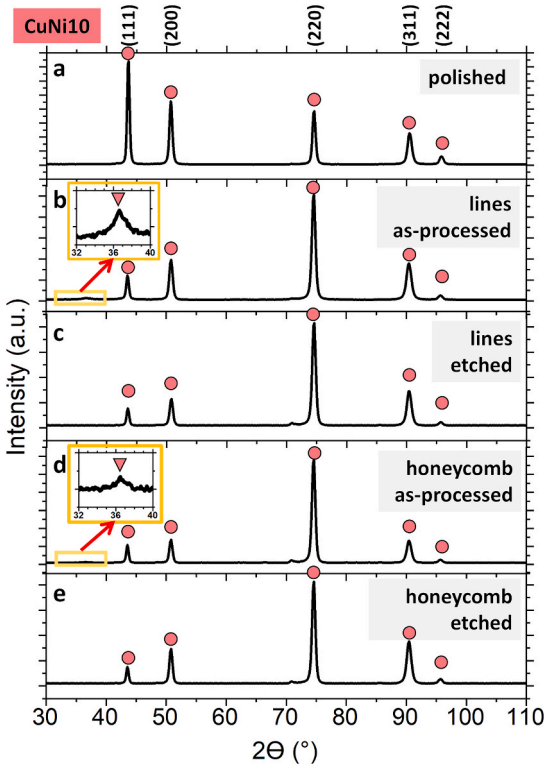

Fig. 3. X-ray diffractogram of CuNi10 a) polished, b) lines as-processed, c) lines etched, d) honeycomb as-processed, and e) honeycomb etched.

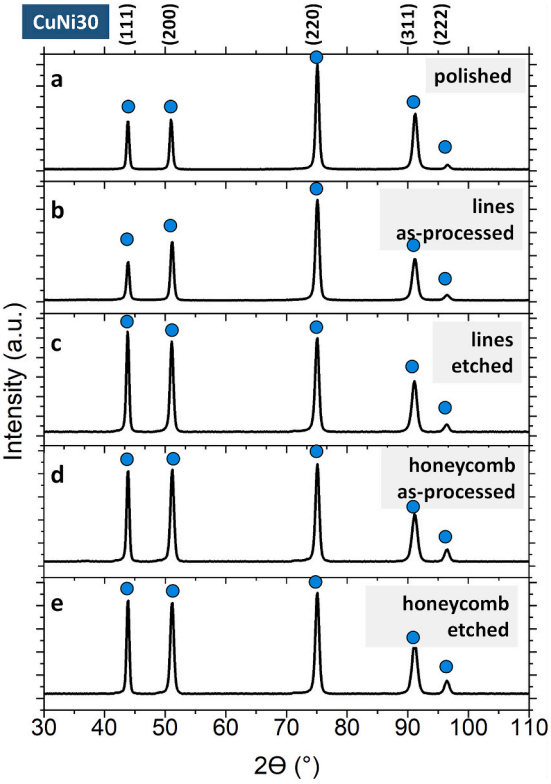

Fig. 4. X-ray diffractogram of CuNi30 a) polished, b) lines as-processed, c) lines etched, d) honeycomb as-processed, and e) honeycomb etched.

Fig. 4 displays the diffractograms of CuNi30 samples. First, as-processed samples are compared to the polished CuNi30. The diffractogram for the lines as-processed (Fig. 4 b) appears to be the same as that of the polished surface (Fig. 4 a). However, in the case of honeycomb as-processed (Fig. 4 d), a significant difference in the relative intensities is observed. The diffractogram shows that the (111), (200), and (220) peaks have similar intensities, suggesting a uniform distribution of these orientations. Furthermore, there are no new additional peaks related to oxides visible.

After etching laser-structured CuNi30, the diffractograms (Fig. 4 c and e) are similar in their peak positions and intensities, showing no change in chemical composition. However, a notable difference is observed in the relative intensity ratios of the peaks between the lines etched sample (Fig. 4 c) and the as-processed sample (Fig. 4 b). This suggests that the surface layer removed through etching exposes a layer with a different preferred orientation, which shows a uniform distribution of the (111), (200), and (220) peaks.

Overall, GI-XRD results indicate the formation of oxide phases solely on laser-structured CuNi10. However, compared with EDX results, an increased oxygen content is also observed on the laser-structured CuNi30 surface, particularly prominent in the valleys of honeycomb structures. A previous study [14] demonstrates similar effects on laser-structured brass surfaces, where the oxide phase was non-detectable via GI-XRD.

3.2.3. Oxide analysis

Next, Raman spectroscopy is utilized to identify the type of oxide present on both alloys. Since the GI-XRD results for laser-structured lines and honeycomb for CuNi10 as well as CuNi30 are identical, this section focuses exclusively on analyzing the line-like structures of each alloy. The resulting spectra are presented in Fig. 5, with the recorded band values summarized in Table 2.

A common feature across all spectra is the presence of bands in the 74–106 cm^{-1} range. According to the literature [53], these bands can be attributed to the silent modes of Cu_2O, and the appearance of these bands is likely the result of defects in the oxide phase. Furthermore, the spectrum of as-processed samples in Fig. 5 a and b show a band at 219 cm^{-1} and 240 cm^{-1}, respectively. This band cannot be assigned to any oxides relevant to this study. However, previous studies [19] have identified a similar band in laser-structured copper alloys. Since copper is the common factor in these studies, it suggests that this band may be related to a vibration of the bond involving copper.

The Raman spectrum of the CuNi10 lines in the as-processed state (black spectrum in Fig. 5 a) reveals a low-intensity band at 291 cm^{-1}, which can be attributed to the A_g mode of cupric oxide [48]. A

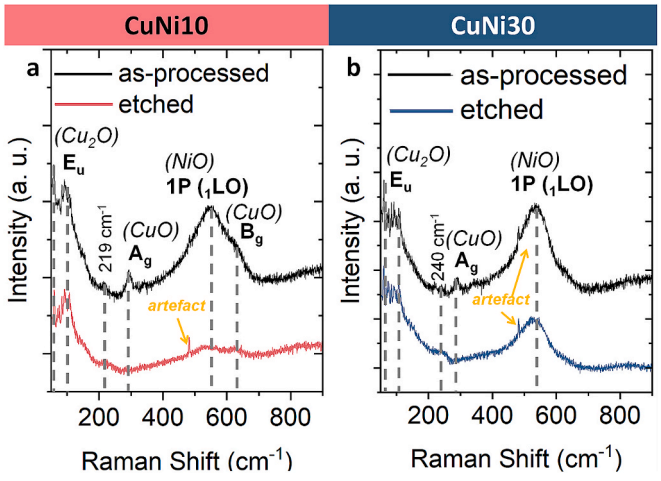

Fig. 5. Results of Raman spectroscopy on line-like structures of a) CuNi10 and b) CuNi30, each in as-processed and etched states.

Table 2
Results of Raman spectroscopy on CuNi10 and CuNi30 in as-processed and etched conditions. As a comparison, the literature-values of copper oxide and nickel oxide.

symmetry	activity	oxide	Raman shift ω_e [cm^{-1}]				
			Literature	CuNi10 lines		CuNi30 lines	
				as- processed	etched	as- processed	etched
E_u	silent	Cu_2O	72–110 [53]	75	74	74	74
				106	103	104	105
				219	225	240	243
A_g	Raman	CuO	297 [48]	291	–	290	–
1P (TO)	Raman	NiO	400–440 [55], 548 [57]	554	551	539	523
1P (1LO)	Raman	NiO	498–570 [54–56],				
1P (1LO)	Raman	NiO	656 [57]	635	633	–	–
B_g	Raman	CuO	609–636 [48,58]				

prominent band appears at 554 cm^{-1}, accompanied by a low-intensity shoulder band at 635 cm^{-1}. Based on the literature [54–57], the prominent band can be attributed to the one-phonon (1P) modes of nickel oxide, specifically the transverse optical (TO) and longitudinal optical (1 LO) modes. Nickel oxide's Raman shift typically falls within the 400–600 cm^{-1} range, with the TO mode varying between 400–548 cm^{-1} and the 1 LO mode between 498–656 cm^{-1}. The precise position and intensity of these bands are influenced by several factors. For instance, doping can cause a shift toward higher Raman values. The greater the doping concentration, the more pronounced the shift [56]. One study on nanosized nickel oxide in powder form reported that structural defects significantly enhance the prominence of the 1P bands [54]. The shoulder band at 635 cm^{-1} can be assigned to the B_g mode of cupric oxide [48,58].

After etching the CuNi10 lines (pink spectrum in Fig. 5 a), the 219 cm^{-1} band shifts to a higher value without a significant change in intensity. Conversely, the band corresponding to the A_g mode (CuO) is no longer visible. Additionally, the 1P (NiO) and B_g (CuO) bands shift to lower values, accompanied by a significant reduction in intensity. These observations suggest that most of the nickel oxide and cupric oxide are removed after etching.

Next, the CuNi30 lines are examined. The Raman spectrum of the as-processed surface (black spectrum), shown in Fig. 5 b, the A_g (CuO) band is similar to the one observed in the CuNi10 lines in the as-processed state. Furthermore, a shoulder band is present at 539 cm^{-1}. However, the Raman shift value for the shoulder band is lower as compared to CuNi10 lines as-processed, indicating that it is not the B_g (CuO) band, but rather another 1P (NiO) band. This suggests that the cupric oxide content is lower on CuNi30 in comparison to CuNi10. This difference is likely due to variations in the alloy composition, which affects the oxide phases formed during laser processing.

After etching (blue spectrum in Fig. 5 b), the CuNi30 lines exhibit a Raman shift trend similar to that of CuNi10. However, the intensity of the 1P (NiO) band is only reduced by half, indicating that the amount of nickel oxide remaining after etching is higher for CuNi30 than for CuNi10. On the other hand, the cupric oxide band is no longer visible, indicating its complete removal through etching.

The findings from chemical analyses suggest the formation of oxide phases with defects, consistent with results observed in previous studies on USP laser-structured copper-based alloys [14,19]. The results suggest that USP-DLIP processing leads to the formation of higher amounts of copper oxide on CuNi10, whereas higher nickel oxide content on CuNi30. According to the results of Raman spectroscopy, the cupric oxide content is higher on CuNi10 in comparison to CuNi30. This can be attributed to the significantly higher copper content in the bulk composition of CuNi10, which likely causes a concurrence between the formation of copper and nickel oxides. Although nickel oxide formation is more likely, this concurrence is likely to result in a higher formation of copper oxide content on CuNi10. Furthermore, etching leads to the removal of nearly all oxide phases from CuNi10, whereas in CuNi30, the oxide phases are only partially removed, with comparatively higher nickel oxide content.

SEM images primarily show oxide-related flake-like structures on CuNi30, while EDX analysis indicates an increase in oxygen across all processed samples. XRD shows oxides only on CuNi10, contrasting with Raman spectroscopy, which detects oxides on both alloys. These differences highlight the complexities of oxide phase analysis at the nanoscale. After etching, the oxide on CuNi30 is only partially removed, likely due to surface modifications at the nanoscale. Previous studies suggest that the type of oxide formed depends on bulk composition, which can introduce analytical challenges, particularly in unstable, oxygen-rich regions [14,19].

Nevertheless, the combination of methods used in this study, supported by insights from prior research, provides a reliable and comprehensive understanding of oxide formation and surface modifications, despite the inherent challenges of nanoscale analysis.

For further experiments and characterization in this study, samples that are both laser-structured and etched will be used. Previous studies [14,19] have shown that etched samples are more effective at killing bacteria than as-processed samples, particularly in structured copper alloys like brass. This is primarily attributed to the removal of the oxide film during etching, which promotes increased copper corrosion on the surface, thereby improving antibacterial effectiveness. Importantly, this approach will further mitigate the influence of oxide formation due to laser treatment as far as possible, focusing instead on investigating the impact of surface topography on bacterial adhesion and killing.

3.3. *E. coli on DLIP-structures*

3.3.1. *Contact killing*

The antibacterial activity on structured surfaces was evaluated using the contact killing method. The results, presented in Fig. 6 as the number of surviving colony-forming units (CFU/mL) over a 90 min contact period, show the following trends: the reference steel (black graph) and pure copper (purple graph) samples exhibit the expected killing rates—no killing for steel and significant killing for copper [5,19,59].

Next, the polished alloy samples (■ solid line graph: pink for CuNi10 and blue for CuNi30) are compared with copper. It is observed that the killing behavior is similar to copper after 30 min of contact. As the contact time increases, the killing rates of copper (purple graph) and CuNi30 (■ blue graph) converge. In contrast, CuNi10 (■ pink graph) shows a significant increase in killing efficiency, nearly an order of magnitude higher, after 90 min. Previous literature [14,19] indicate a decrease in the killing rate due to reduced copper content in polished copper alloys. However, this trend does not apply to copper-nickel alloys in this study, likely due to the presence of nickel. Nickel is known for its higher corrosion resistance in humid and underwater conditions [17]. This would typically suggest that copper-nickel alloys should exhibit higher corrosion rates, but the results in this study show a different trend. Based on the results from both polished copper-nickel surfaces

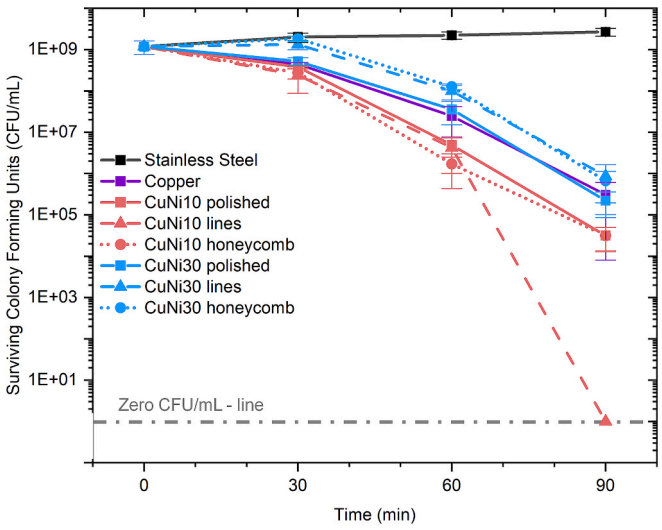

Fig. 6. Results of contact killing experiment, showing surviving CFU/mL over a 90 min period on laser-structured CuNi-alloys. Comparison of CuNi10 (pink graph) and CuNi30 (blue graph), showing polished samples (■ solid line graph), line-like structure (▲dash line graph), and honeycomb structures (● dot line graph). Also included are steel (black graph) and copper (purple graph) as references. (For interpretation of the references to colour in this figure legend, the reader is referred to the web version of this article.)

and the known properties of nickel, it is likely that copper experiences more corrosion in the presence of nickel when in contact with the bacterial solution, leading to a higher killing rate on these surfaces. This discrepancy may be related to the presence of bacteria, as one previous study [60] suggests that even pure copper experiences varied corrosion in the presence of *E. coli*. However, further investigation is needed to explore this phenomenon in future studies.

The antibacterial performance of the structured samples was assessed. Both the line-like (▲ blue graph) and honeycomb (● blue graph) CuNi30 structures show a further decrease in killing efficiency compared to the polished sample (■ blue graph). In comparison, the honeycomb-like structure of CuNi10 (● pink graph) demonstrates a killing rate similar to that of polished CuNi10 (■ pink graph). Similarly, the line-like structure of CuNi10 (▲ pink graph) exhibits comparable behavior during the first 60 min of contact. However, after 90 min, a significant increase in killing efficiency is observed in the line-like structure (▲ pink graph). Note that the error bar for the CuNi10 lines at 90 min is not visible due to its value of the error being zero.

Overall, the results suggest that enhanced bacteria-substrate contact is achieved through a combination of optimal composition, structure, and increased contact area. CuNi10 line-like structures exhibited the best killing rate which is most probably due to a higher copper content and likely due to better compatibility between the structure and the shape of the bacteria.

The long-rod-shaped *E. coli* bacteria are more likely to align and spread along the grooves of the linear structures, leading to a larger and more continuous contact area compared to the honeycomb pattern or the polished surface. This improved alignment may facilitate stronger mechanical interactions or membrane stress, contributing to enhanced antibacterial activity.

Although the honeycomb theoretically offers greater total surface area, its complex and curved geometry may limit effective contact with bacteria due to mismatches in scale and orientation. These findings underscore that total surface area alone is not the key determinant of antibacterial performance—rather, the spatial compatibility between surface features and bacterial dimensions is critical.

While precise quantification of the actual bacteria-surface contact area was beyond the scope of this work, the qualitative assessment based on structural parameters and bacterial size provides a solid basis for interpreting the observed trends. Future studies involving detailed contact area modeling and high-resolution morphological analyses will build on these findings by further explaining the underlying mechanisms.

Furthermore, the increased efficiency compared to pure copper is likely related to the larger contact area, and since the copper content in CuNi10 is relatively high, this effect may be further amplified in conjunction with the factors mentioned above.

Laser-structured CuNi30, regardless of the structure dimensions, showed reduced antibacterial activity, likely due to its copper content falling below 60 wt-%, as confirmed by EDX results. This aligns with prior studies on smooth copper-based surfaces, which suggest that copper content should not be lower than 60 wt-% in copper alloys to have significant antimicrobial properties [2,18]. The results of this study suggest that when working with laser-structuring, the copper content in the alloy should be higher, as it may decrease on the surface after the process, leading to a reduction in antibacterial efficacy. Specifically, for binary copper-nickel alloy system used in laser processing, the critical copper content threshold for the bulk composition appears to lie between 70 and 90 wt-%, with 70 wt-% already showing decreased antibacterial efficacy.

Nonetheless, the current results offer clear and compelling insights into how laser-induced microstructures and choice of material composition can be effectively enhance antibacterial properties, particularly in the case of copper-nickel alloys.

3.3.2. *Chemical analysis on structured surfaces with E. coli*

HIM-SIMS provides high-resolution chemical information of the surface through SIMS. Ni and Cu maps for etched laser-structured CuNi10 and CuNi30, with bacteria, are captured at different magnifications (field of view: FoV 10 (10 x 10 μm^2)/15(15 x 15 μm^2)/20 (20 x 20 μm^2)). However, this section only shows FoV 10. Additionally, SE images are captured alongside the SIMS images to correlate Ni and Cu distribution with topographical features. The results of CuNi10 and CuNi30 are displayed in Fig. 7. In all cases, the elemental Ni and Cu maps replicate the pattern showing a clear distinction between topographical peaks and valleys. Secondary ion signal intensity is multifactorial dependent (it is mainly a function of the chemical composition of the sample, ion species, energy, current, and angle of incidence of primary ion beam), hence SIMS is usually restricted to qualitative analysis. To mitigate the topographic effects of the elemental SI signal intensity, Ni and Cu maps were normalized with the total ion count (TIC).

The results in Fig. 7 indicate a distinctively higher intensity of Cu and Ni in the valley compared to the topographical peaks. This difference is likely visible due to higher amounts of oxide on the peaks than in the valleys, as observed in previous studies as well [14,19,22]. Another significant finding is that Cu is present on the bacterial surface, whereas Ni is not. This is indicative of the copper-ion release from metallic phases which is effectively incorporated into the bacteria wall. The chemical information is estimated to correspond to a depth of no more than 13 nm of the bacteria's surface. This estimation is calculated by measuring the dimensions change in length and width of individual bacteria from SE (He^+) images taken before and after the SIMS acquisitions.

The increased *E. coli* killing on CuNi10 lines, along with the higher copper content and copper oxide formation compared to CuNi30, suggests that copper is responsible for the enhanced antibacterial effect. Previous research indicates that copper ions kill bacteria by disrupting the cell membrane and degrading intracellular components [7,61,62]. In contrast, no studies indicate that nickel possesses antibacterial properties. Furthermore, the reduced *E. coli* killing effect observed in laser-structured CuNi30 samples with higher nickel content supports this. These findings are consistent with one another.

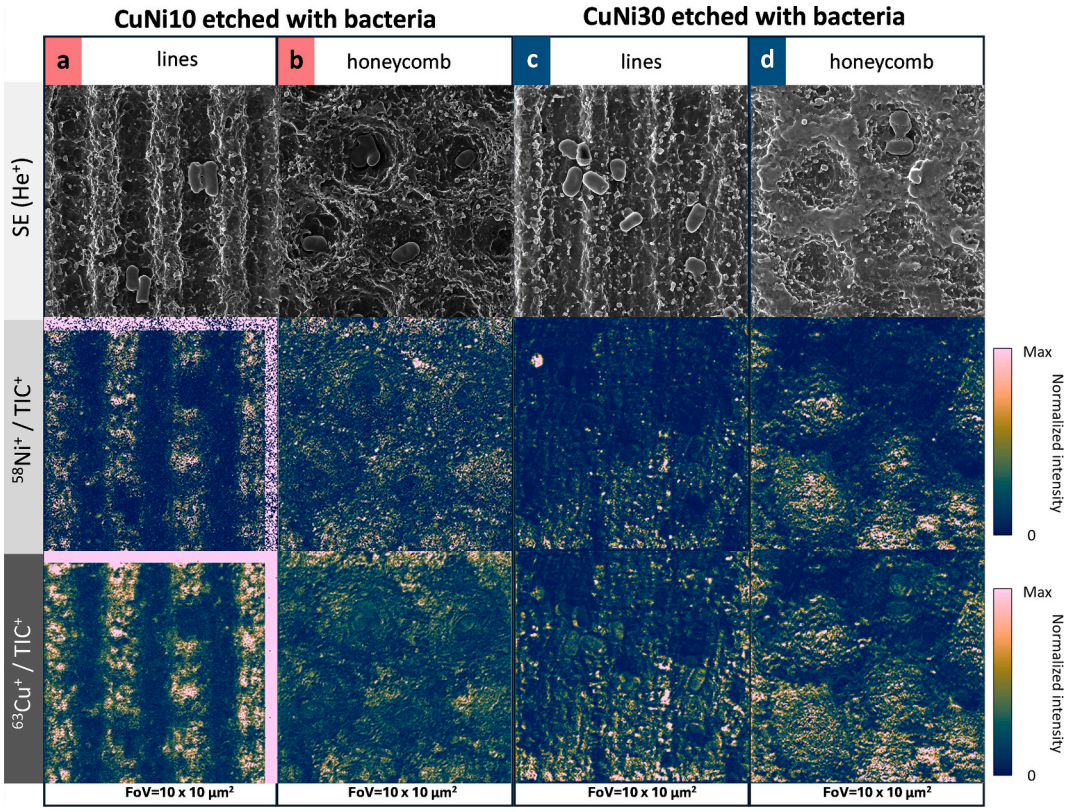

Fig. 7. High-Resolution Secondary Ion Mass Spectrometry (HR-SIMS) analysis of etched laser-structured samples with bacteria: CuNi10 a) lines, b) honeycomb, CuNi30 c) lines, and d) honeycomb. The images were recorded with a field of view (FoV) of 10 x 10 μm^2. The first row displays the respective SEM images. The second and third rows present SIM images of the elemental map of nickel (Ni) and copper (Cu), respectively. Warmer colours indicate higher concentrations, and cooler colours represent lower concentrations.

4. Conclusions

This study investigates the fabrication of two distinct periodic microscale structures, lines and honeycomb, on binary copper-nickel alloys with 10 wt-% and 30 wt-% nickel content. The focus is on the influence of bulk composition on laser structuring using ultrashort pulse durations, and its impact on the interaction between *Escherichia coli* (*E. coli*) and the structured surfaces.

The results show that topographical modifications are accompanied by the formation of copper- and nickel-rich oxide phases. Chemical analyses reveal that CuNi10 has a higher copper oxide content, whereas CuNi30 has a higher nickel oxide content. After chemical etching, most oxide is removed from the CuNi10 surface, while nearly half of the nickel oxide remains on CuNi30.

In the antibacterial tests, CuNi10 etched lines exhibited significantly faster bacterial killing compared to CuNi30, despite similar decreases in copper content. CuNi30′s copper content decreased near or below the 60 wt-% threshold, which is the lower limit for copper-based alloys to be considered antibacterial, explaining the decreased antibacterial efficiency. These results underscore the importance of copper content in laser-structured alloys for effective bacterial killing.

Furthermore, line-like structures outperformed the honeycomb structures in terms of antibacterial performance. While the honeycomb structure was designed to prevent bacterial agglomeration by trapping bacteria in the valleys, it was not effective in promoting bacterial killing. This highlights the importance of ensuring dimension compatibility between surface structures and bacterial size, while also increasing the contact area. Future studies involving spherical bacteria may help clarify the suitability of such designs for different bacterial types.

In conclusion, this study highlights the critical role of copper content and laser structuring in enhancing antibacterial performance. It suggests that the critical lower value of the copper content range for improved antibacterial activity in bulk composition through laser structuring lies between 70–90 wt-%. Future research should focus on determining the optimal copper content for bacterial killing in laser-structured copper-nickel alloys, exploring surface treatments like annealing to restore antibacterial effectiveness in CuNi30, and investigating the impact of bacterial presence on the corrosion behavior of these alloys.

CRediT authorship contribution statement

Aisha Saddiqa Ahmed: Conceptualization, Investigation, Validation, Visualization, Writing – original draft. **Sebastian Wältermann:** Investigation, Validation, Writing – review & editing. **Pablo María Delfino:** Investigation, Validation, Writing – review & editing. **Daniel Wyn Müller:** Writing – review & editing. **Jean–Nicolas Audinot:** Resources, Supervision, Writing – review & editing. **Jean-François Pierson:** Investigation, Supervision, Resources, Validation, Writing – review & editing. **Frank Mücklich:** Funding acquisition, Resources, Supervision, Writing – review & editing.

Declaration of competing interest

The authors declare that they have no known competing financial interests or personal relationships that could have appeared to influence the work reported in this paper.

Acknowledgement

The Author would like to thank to the group of Prof. Rolf Müller from the Helmholtz Centre of Infection Research in Saarbrücken for providing the *E. coli*. The authors acknowledge financial support in the project

"MatInnovat" supported by the Saarland State Ministry of Economics with resources from the European Fund for Regional Development (EFRE) and funding by the German Research Foundation for the Femtosecond Pulsed Laser System (DFG, INST 256/562 FUGG). This work made use of the resources of the Correlative Microscopy and Tomography (CoMiTo) core facility at Saarland University. The authors would like to thank the technical platforms "Optic and Lasers" at Institut Jean Lamour (IJL, Nancy, France) for access to Raman facility.

Funding

A.A. has been funded by the German Aerospace Center - Space Administration (DLR) within the project "Investigation of antimicrobial metal surfaces under space conditions - An effective strategy to prevent microbial biofilm formation" (project number 50WB1930). This work was funded by the German Research Foundation (DFG) within the project "Controlled bacterial interaction to increase the antimicrobial efficiency of copper surfaces" (project number 415956642). P.M.D thanks the funding to the Luxembourg National Research Fund (FNR) and the Agence Nationale de la Recherche (ANR) through the grants INTER/ANR/21/16227644 and ANR-21-CE05-0036-01.

Data availability

The datasets used and/or analyzed during the current study are available from the corresponding author on reasonable request.

References

[1] N. Bisht, N. Dwivedi, P. Kumar, M. Venkatesh, A.K. Yadav, D. Mishra, P. Solanki, N. K. Verma, R. Lakshminarayanan, S. Ramakrishna, D.P. Mondal, A.K. Srivastava, C. Dhand, Recent advances in copper and copper-derived materials for antimicrobial resistance and infection control, Curr. Opin. Biomed. Eng. 24 (2022), https://doi.org/10.1016/j.cobme.2022.100408.

[2] S. Mehtar, I. Wiid, S.D. Todorov, The antimicrobial activity of copper and copper alloys against nosocomial pathogens and Mycobacterium tuberculosis isolated from healthcare facilities in the Western Cape: an in-vitro study, J. Hosp. Infect. 68 (2008) 45–51, https://doi.org/10.1016/j.jhin.2007.10.009.

[3] J. Tanwar, S. Das, Z. Fatima, S. Hameed, Multidrug resistance: an emerging crisis, Interdiscip. Perspect. Infect Dis. 2014 (2014), https://doi.org/10.1155/2014/541340.

[4] R. Vivas, A.A.T. Barbosa, S.S. Dolabela, S. Jain, Multidrug-resistant bacteria and alternative methods to control them: an overview, Microb. Drug Resist. 25 (2019), https://doi.org/10.1089/mdr.2018.0319.

[5] D.W. Müller, S. Lößlein, E. Terriac, K. Brix, K. Siems, R. Moeller, R. Kautenburger, F. Mücklich, Increasing antibacterial efficiency of Cu surfaces by targeted surface functionalization via ultrashort pulsed direct laser interference patterning, Adv. Mater. Interfaces 8 (2021), https://doi.org/10.1002/admi.202001656.

[6] R. Borda D'Água, R. Branquinho, M.P. Duarte, E. Maurício, A.L. Fernando, R. Martins, E. Fortunato, Efficient coverage of ZnO nanoparticles on cotton fibres for antibacterial finishing using a rapid and low cost: In situ synthesis, New J. Chem. 42 (2018) 1052–1060, https://doi.org/10.1039/c7nj03418k.

[7] M. Raffi, S. Mehrwan, T.M. Bhatti, J.I. Akhter, A. Hameed, W. Yawar, M.M. Ul Hasan, Investigations into the antibacterial behavior of copper nanoparticles against Escherichia coli, Ann. Microbiol. 60 (2010) 75–80, https://doi.org/10.1007/s13213-010-0015-6.

[8] A.F. Lasagni, C. Gachot, K.E. Trinh, M. Hans, A. Rosenkranz, T. Roch, S. Eckhardt, T. Kunze, M. Bieda, D. Günther, V. Lang, F. Mücklich, Direct laser interference patterning, 20 years of development: from the basics to industrial applications, in: Laser-Based Micro- and Nanoprocessing XI, SPIE, 2017: p. 1009211. https://doi.org/10.1117/12.2252595.

[9] A. Rosenkranz, M. Hans, C. Gachot, A. Thome, S. Bonk, F. Mücklich, Direct laser interference patterning: tailoring of contact area for frictional and antibacterial properties, Lubricants 4 (2016), https://doi.org/10.3390/lubricants4010002.

[10] M. Hans, F. Müller, S. Grandthyll, S. Hüfner, F. Mücklich, Anisotropic wetting of copper alloys induced by one-step laser micro-patterning, Appl. Surf. Sci. 263 (2012) 416–422, https://doi.org/10.1016/j.apsusc.2012.09.071.

[11] M. Hans, J.C. Támara, S. Mathews, B. Bax, A. Hegetschweiler, R. Kautenburger, M. Solioz, F. Mücklich, Laser cladding of stainless steel with a copper-silver alloy to generate surfaces of high antimicrobial activity, Appl. Surf. Sci. 320 (2014) 195–199, https://doi.org/10.1016/j.apsusc.2014.09.069.

[12] T. Stark, S. Alamri, A.I. Aguilar-Morales, T. Kiedrowski, A.F. Lasagni, Positive effect of laser structured surfaces on tribological performance, J. Laser Micro Nanoeng. 14 (2019) 13–18, https://doi.org/10.2961/jlmn.2019.01.0003.

[13] Y. Fu, M. Soldera, W. Wang, S. Milles, K. Deng, B. Voisiat, K. Nielsch, A.F. Lasagni, Wettability control of polymeric microstructures replicated from laser-patterned stamps, Sci. Rep. 10 (2020), https://doi.org/10.1038/s41598-020-79936-1.

[14] A.S. Ahmed, D.W. Müller, S. Bruyère, A. Holtsch, F. Müller, K. Brix, S. Migot, R. Kautenburger, K. Jacobs, J.F. Pierson, F. Mücklich, Antibacterial property alterations induced by low zinc content in laser-structured brass, Appl. Surf. Sci. 665 (2024) 160338, https://doi.org/10.1016/J.APSUSC.2024.160338.

[15] J.R. Davis, ASM speciality handbook, Copper and Copper Alloys (2001).

[16] W.D. Jenkins, T.G. Digges, C.R. Johnson, Tensile properties of copper, nickel, and 70-percent-copper-30-percent-nickel and 30-percent-copper-70-percent-nickel alloys at high temperatures, J Res Natl Bur Stand (1934) 58 (1957). https://doi.org/10.6028/jres.058.027.

[17] Nickel and its alloys, J. Franklin Inst. 198 (1924), https://doi.org/10.1016/s0016-0032(24)90183-9.

[18] T.J. Karpanen, A.L. Casey, P.A. Lambert, B.D. Cookson, P. Nightingale, L. Miruszenko, T.S.J. Elliott, The antimicrobial efficacy of copper alloy furnishing in the clinical environment: a crossover study, Infect. Control Hosp. Epidemiol. 33 (2012), https://doi.org/10.1086/663644.

[19] A. Ahmed, D. Müller, S. Bruyère, A. Holtsch, F. Müller, J. Barrirero, K. Brix, S. Migot, R. Kautenburger, K. Jacobs, J.-F. Pierson, F. Mücklich, Surface modification of brass via ultrashort pulsed direct laser interference patterning and its effect on bacteria-substrate interaction, ACS Appl. Mater. Interfaces 15 (n.d.) 36908–36921. https://doi.org/10.1021/acsami.3c04801.

[20] K. Siems, D.W. Müller, L. Maertens, A. Ahmed, R. Van Houdt, R.L. Mancinelli, S. Baur, K. Brix, R. Kautenburger, N. Caplin, J. Krause, R. Demets, M. Vukich, A. Tortora, C. Roesch, G. Holland, M. Laue, F. Mücklich, R. Moeller, Testing laser-structured antimicrobial surfaces under space conditions: the design of the ISS experiment BIOFILMS, Front. Space Technol. 2 (2022), https://doi.org/10.3389/frspt.2021.773244.

[21] J.N. Audinot, P. Philipp, O. De Castro, A. Biesemeier, Q.H. Hoang, T. Wirtz, Highest resolution chemical imaging based on secondary ion mass spectrometry performed on the helium ion microscope, Rep. Prog. Phys. 84 (2021), https://doi.org/10.1088/1361-6633/ac1e32.

[22] D.W. Müller, A. Holtsch, S. Lößlein, C. Pauly, C. Spengler, S. Grandthyll, K. Jacobs, F. Mücklich, F. Müller, In-depth investigation of copper surface chemistry modification by ultrashort pulsed direct laser interference patterning, Langmuir 36 (2020) 13415–13425, https://doi.org/10.1021/acs.langmuir.0c01625.

[23] L. Mulko, M. Soldera, A.F. Lasagni, Structuring and functionalization of non-metallic materials using direct laser interference patterning: a review, Nanophotonics 11 (2022) 203–240, https://doi.org/10.1515/nanoph-2021-0591.

[24] A.F. Lasagni, Laser interference patterning methods: possibilities for high-throughput fabrication of periodic surface patterns, Adv. Opt. Technol. 6 (2017), https://doi.org/10.1515/aot-2017-0016.

[25] B.N. Chichkov, C. Momma, S. Nolte, F. Von Alvensleben, A. Tünnermann, Femtosecond, picosecond and nanosecond laser ablation of solids, Appl. Phys. A Mater. Sci. Process. 63 (1996) 109–115, https://doi.org/10.1007/BF01567637.

[26] K.M. Tanvir Ahmmed, C. Grambow, A.M. Kietzig, Fabrication of micro/nano structures on metals by femtosecond laser micromachining, Micromachines (Basel) 5 (2014) 1219–1253, https://doi.org/10.3390/mi5041219.

[27] A.A. Ionin, S.I. Kudryashov, A.A. Samokhin, Material surface ablation produced by ultrashort laser pulses, Uspekhi Fizicheskih Nauk 187 (2017) 159–172, https://doi.org/10.3367/ufnr.2016.09.037974.

[28] C. Momma, S. Nolte, B.N. Chichkov, F. V Alvensleben, A.T. Tunnermann, Precise laser ablation with ultrashort pulses, 1997.

[29] S. Nolte, C. Momma, H. Jacobs, A. Tünnermann, B.N. Chichkov, B. Wellegehausen, H. Welling, Ablation of metals by ultrashort laser pulses, J. Opt. Soc. Am. B 14 (1997) 2716, https://doi.org/10.1364/JOSAB.14.002716.

[30] J. Huang, Y. Zhang, J.K. Chen, M. Yang, Ultrafast solid-liquid-vapor phase change of a thin gold film irradiated by femtosecond laser pulses and pulse trains, Front. Energy 6 (2012) 1–11, https://doi.org/10.1007/s11708-012-0179-9.

[31] C. Wu, L.V. Zhigilei, Microscopic mechanisms of laser spallation and ablation of metal targets from large-scale molecular dynamics simulations, Appl. Phys. A Mater. Sci. Process. 114 (2014) 11–32, https://doi.org/10.1007/s00339-013-8086-4.

[32] C.A. Zuhlke, T.P. Anderson, D.R. Alexander, Formation of multiscale surface structures on nickel via above surface growth and below surface growth mechanisms using femtosecond laser pulses, Opt. Express 21 (2013) 8460, https://doi.org/10.1364/oe.21.008460.

[33] K.H. Leitz, B. Redlingshöer, Y. Reg, A. Otto, M. Schmidt, Metal ablation with short and ultrashort laser pulses, Phys. Procedia 12 (2011) 230–238, https://doi.org/10.1016/J.PHPRO.2011.03.128.

[34] A.I. Aguilar-Morales, S. Alamri, A.F. Lasagni, Micro-fabrication of high aspect ratio periodic structures on stainless steel by picosecond direct laser interference patterning, J. Mater. Process. Technol. 252 (2018) 313–321, https://doi.org/10.1016/j.jmatprotec.2017.09.039.

[35] M. Prudent, A. Borroto, F. Bourquard, S. Bruyère, S. Migot, F. Garrelie, J.F. Pierson, J.P. Colombier, Ultrafast laser-induced topochemistry on metallic glass surfaces, Mater. Des. 244 (2024) 113164, https://doi.org/10.1016/J.MATDES.2024.113164.

[36] M.P. Echlin, M. Straw, S. Randolph, J. Filevich, T.M. Pollock, The TriBeam system: femtosecond laser ablation in situ SEM, Mater. Charact. 100 (2015) 1–12, https://doi.org/10.1016/j.matchar.2014.10.023.

[37] M. Groenendijk, J. Meijer, Microstructuring using femtosecond pulsed laser ablation, in: 24th International Congress on Applications of Lasers and Electro-Optics, ICALEO 2005 - Congress Proceedings, Laser Institute of America, 2005: pp. 219–225. https://doi.org/10.2351/1.5060548.

[38] D.W. Müller, S. Lößlein, C. Pauly, M. Briesenick, G. Kickelbick, F. Mücklich, Multi-pulse agglomeration effects on ultrashort pulsed direct laser interference

patterning of Cu, Appl. Surf. Sci. 611 (2023) 155538, https://doi.org/10.1016/J.APSUSC.2022.155538.
[39] S. Barcikowski, A. Hahn, A.V. Kabashin, B.N. Chichkov, Properties of nanoparticles generated during femtosecond laser machining in air and water, Appl. Phys. A Mater. Sci. Process. 87 (2007) 47–55, https://doi.org/10.1007/s00339-006-3852-1.
[40] J.H.E. Jeffes, Ellingham diagrams, encyclopedia of materials, Sci. Technol. (2001), https://doi.org/10.1016/b0-08-043152-6/00490-3.
[41] H. Khalid, S. Shamaila, N. Zafar, R. Sharif, J. Nazir, M. Rafique, S. Ghani, H. Saba, Antibacterial behavior of laser-ablated copper nanoparticles, Acta Metallurgica Sinica (English Letters) 29 (2016), https://doi.org/10.1007/s40195-016-0450-x.
[42] I. Ban, J. Stergar, M. Drofenik, G. Ferk, D. Makovec, Synthesis of copper-nickel nanoparticles prepared by mechanical milling for use in magnetic hyperthermia, J. Magn. Magn. Mater. 323 (2011), https://doi.org/10.1016/j.jmmm.2011.04.004.
[43] C. Yang, W. Xue, H. Yin, Z. Lu, A. Wang, L. Shen, Y. Jiang, Hydrogenation of 3-nitro-4-methoxy-acetylaniline with H2 to 3-amino-4-methoxy-acetylaniline catalyzed by bimetallic copper/nickel nanoparticles, New J. Chem. 41 (2017), https://doi.org/10.1039/c7nj00066a.
[44] P. Rojas, R. Vera, C. Martínez, M. Villarroel, Effect of the powder metallurgy manufacture process on the electrochemical behaviour of copper, nickel and copper-nickel alloys in hydrochloric acid, Int. J. Electrochem. Sci. 11 (2016), https://doi.org/10.20964/2016.06.40.
[45] J. Duan, J. Liu, D. Mo, H. Yao, K. Maaz, Y. Chen, Y. Sun, M. Hou, X. Qu, L. Zhang, Y. Chen, Controlled crystallinity and crystallographic orientation of Cu nanowires fabricated in ion-track templates, Nanotechnology 21 (2010), https://doi.org/10.1088/0957-4484/21/36/365605.
[46] X.W. Wang, G.T. Fei, L. Chen, X.J. Xu, L. De Zhang, Orientation-controllable growth of Ni nanowire arrays with different diameters, Electrochem. Solid St. 10 (2007), https://doi.org/10.1149/1.2436642.
[47] H. Sun, Y. Yu, X. Li, W. Li, F. Li, B. Liu, X. Zhang, Controllable growth of electrodeposited single-crystal nanowire arrays: the examples of metal Ni and semiconductor ZnS, J. Cryst. Growth 307 (2007), https://doi.org/10.1016/j.jcrysgro.2007.07.007.
[48] J. Kaur, A. Khanna, R. Kumar, R. Chandra, Growth and characterization of Cu2O and CuO thin films, J. Mater. Sci. Mater. Electron. 33 (2022), https://doi.org/10.1007/s10854-022-08506-0.
[49] M.J. Nine, B. Munkhbayar, M.S. Rahman, H. Chung, H. Jeong, Highly productive synthesis process of well dispersed Cu2O and Cu/Cu2O nanoparticles and its thermal characterization, Mater. Chem. Phys. 141 (2013), https://doi.org/10.1016/j.matchemphys.2013.05.032.
[50] N. Dharmaraj, P. Prabu, S. Nagarajan, C.H. Kim, J.H. Park, H.Y. Kim, Synthesis of nickel oxide nanoparticles using nickel acetate and poly(vinyl acetate) precursor, Mater. Sci. Eng. B 128 (2006), https://doi.org/10.1016/j.mseb.2005.11.021.
[51] E.R. Beach, K. Shqau, S.E. Brown, S.J. Rozeveld, P.A. Morris, Solvothermal synthesis of crystalline nickel oxide nanoparticles, Mater. Chem. Phys. 115 (2009), https://doi.org/10.1016/j.matchemphys.2008.12.018.
[52] E.Y. Konysheva, X. Xu, J.T.S. Irvine, On the existence of A-site deficiency in perovskites and its relation to the electrochemical performance, Adv. Mater. 24 (2012), https://doi.org/10.1002/adma.201103352.
[53] M. Ivanda, D. Waasmaier, A. Endriss, J. Ihringer, A. Kirfel, W. Kiefer, Low-temperature anomalies of cuprite observed by Raman spectroscopy and x-ray powder diffraction, J. Raman Spectrosc. 28 (1997) 487–493, https://doi.org/10.1002/(sici)1097-4555(199707)28:7<487::aid-jrs115>3.0.co;2-v.
[54] N. Mironova-Ulmane, A. Kuzmin, I. Steins, J. Grabis, I. Sildos, M. Pärs, Raman scattering in nanosized nickel oxide NiO, J. Phys. Conf. Ser. 93 (2007), https://doi.org/10.1088/1742-6596/93/1/012039.
[55] N. Mironova-Ulmane, A. Kuzmin, I. Sildos, M. Pärs, Polarisation dependent Raman study of single-crystal nickel oxide, Cent. Eur. J. Phys. 9 (2011), https://doi.org/10.2478/s11534-010-0130-9.
[56] K.J. Shailja, R.C. Singh, Singh, Enhanced toluene sensing performance of nanostructured aluminium-doped nickel oxide gas sensor, Appl. Phys. A Mater. Sci. Process. 129 (2023), https://doi.org/10.1007/s00339-023-06473-9.
[57] H.G. Gebretinsae, M.G. Tsegay, Z.Y. Nuru, Biosynthesis of nickel oxide (NiO) nanoparticles from cactus plant extract, Mater. Today Proc. (2019), https://doi.org/10.1016/j.matpr.2020.05.331.
[58] L. Debbichi, M.C. Marco De Lucas, J.F. Pierson, P. Krüger, Vibrational properties of CuO and Cu 4O 3 from first-principles calculations, and raman and infrared spectroscopy, J. Phys. Chem. C 116 (2012) 10232–10237, https://doi.org/10.1021/jp303096m.
[59] O. Koseoglu Eser, A. Ergin, G. Hascelik, Antimicrobial activity of copper alloys against invasive multidrug-resistant nosocomial pathogens, Curr. Microbiol. 71 (2015), https://doi.org/10.1007/s00284-015-0840-8.
[60] J. Luo, C. Hein, J. Ghanbaja, J.F. Pierson, F. Mücklich, Bacteria accumulate copper ions and inhibit oxide formation on copper surface during antibacterial efficiency test, Micron 127 (2019), https://doi.org/10.1016/j.micron.2019.102759.
[61] G. Tong, M. Yulong, G. Peng, X. Zirong, Antibacterial effects of the Cu(II)-exchanged montmorillonite on Escherichia coli K88 and Salmonella choleraesuis, Vet. Microbiol. 105 (2005) 113–122, https://doi.org/10.1016/J.VETMIC.2004.11.003.
[62] F.A. Bezza, S.M. Tichapondwa, E.M.N. Chirwa, Fabrication of monodispersed copper oxide nanoparticles with potential application as antimicrobial agents, Sci. Rep. 10 (2020), https://doi.org/10.1038/s41598-020-73497-z.

6. Conclusion

This doctoral research sets out to develop reproducible antibacterial microscale structures on copper-based alloys using ultrashort pulsed direct laser interference patterning (USP-DLIP) and to systematically evaluate how alloy composition, surface chemistry, and structural design influence antibacterial performance. Across brass, bronze, and copper–nickel alloys, USP-DLIP enabled the **fabrication of periodic microscale structures** with feature sizes on the order of bacterial dimensions, thereby directly influencing bacterial adhesion and survival. Surfaces patterned with line-like geometries of approximately 3 μm periodicity proved particularly effective, consistently outperforming more complex designs such as point-honeycomb structures. **These findings confirm that structural compatibility between engineered features and bacterial size is a decisive factor for contact killing**.

Furthermore, **alloy composition** exhibited a central role in both the **laser–material interaction** and the **resulting antibacterial properties**. Brass, bronze, and copper–nickel alloys each exhibited distinct structuring behaviors and oxide chemistries, which in turn governed copper availability at the surface. Despite international standards requiring a minimum of 60 wt-% copper content for alloys to be designated antibacterial, the present work shows that the effective threshold depends not only on bulk composition but also on the type of alloying element and the processing conditions**. Maintaining sufficiently high surface copper concentration is therefore essential to ensure bactericidal performance, although the precise critical value varies between alloy systems**.

Oxidation was identified as a major factor modulating antibacterial activity. Laser structuring generally induced the formation of zinc-, tin-, or nickel-rich oxides, often accompanied by a reduction in surface copper. This effect was detrimental to antibacterial efficacy, as reduced copper ion release limited bacterial killing. **However, the study also showed that selective etching could restore copper-rich surfaces and**

significantly enhance antibacterial performance, as demonstrated in the brass and bronze systems. In contrast, annealing of copper-nickel alloys promoted the formation of stable cuprous oxide layers that improved the antibacterial activity. These findings highlight the complex interplay between surface chemistry, processing route, and functionality.

Beyond chemical composition, surface topography and wettability also influenced antibacterial behavior. The width of valleys within microscale-structured surfaces was found to govern bacterial interaction and thereby killing efficiency, whereas wettability plays a supporting role. Furthermore, the mechanistic insights were demonstrated by complementary analytical techniques: ICP-MS quantified **copper ion release**, HR-SIMS provided **evidence of copper ion incorporation into bacterial membranes**, and microscopic observations revealed **nano-agglomerates on cell surfaces**, **confirming direct copper–bacteria interactions**.

Collectively, this thesis establishes a systematic framework linking alloy composition, laser structuring parameters, surface chemistry, and antibacterial performance. The findings highlight that the design of effective antibacterial copper alloys requires a careful co-optimization of topographical and chemical modifications to ensure reproducibility and scalability. **By advancing the understanding of how USP-DLIP modulates both surface topography and chemistry, this work contributes to the rational design of durable, scalable antimicrobial materials with applications in healthcare, transportation, and public infrastructure.**

7. Outlook

While this thesis has established fundamental principles for designing antibacterial copper-based alloys via USP-DLIP, several aspects remain to be addressed in future research. A central challenge lies in precisely defining the critical copper content required for bactericidal activity across different alloy systems. Although international standards suggest a threshold of 60 wt-% copper, the results of this work demonstrate that nanoscale chemical modifications induced by femtosecond laser processing can significantly alter surface composition and antibacterial response. The exact threshold, therefore, depends not only on the alloying element but also on the processing parameters and resulting surface chemistry. Systematic studies on a wider range of alloy compositions, particularly at intermediate copper contents, are required to establish these critical values.

Another important avenue concerns the role of oxidation during laser processing. Oxygen diffusion into the surface region was shown to be unavoidable, leading to the formation of oxides that strongly influenced antibacterial performance. The results showed that selective post-treatment could partially restore copper-rich surfaces. However, a more robust strategy is needed that involves processing under controlled atmospheres, such as argon-filled chambers, to minimize unwanted oxidation and improve reproducibility. This would enable a clearer distinction between topographical and chemical effects, allowing their individual contributions to antibacterial activity to be more precisely determined.

The observed corrosion behavior of structured surfaces suggests a complex relationship between alloy chemistry, oxide distribution, and antibacterial function. Furthermore, the results showed variations between valleys and peaks, which indicative of a potential dual effect, i.e., enhanced bacterial killing in copper-rich valleys and increased corrosion resistance in oxidized peaks. Understanding this

interplay in greater detail could inform the design of surfaces that achieve both long-term durability and strong antibacterial efficacy in demanding environments.

Looking ahead, extending USP-DLIP beyond binary copper alloys to more complex systems may open new opportunities to combine antibacterial activity with mechanical strength, corrosion resistance, or optical functionality. The integration of laser processing with advanced alloy design thus represents a promising pathway toward multifunctional materials.

In addition, the insights gained here contribute to larger interdisciplinary efforts such as *BIOFILMS, Touching Surfaces*, and *ConTACTS Concordia*. These projects test polished, micro-, and nanoscale-structured materials, including copper, copper alloys, and stainless steel, under terrestrial and space conditions, ranging from classrooms and high-touch environments to isolated environments such as Concordia station. By exposing these materials to a broad spectrum of pathogenic microorganisms and varying environmental factors, including humidity and gravity, these studies provide comparative data that extend far beyond the single-species focus of most laboratory experiments. Integrating such diverse biological testing with the material-specific findings of this thesis will be critical for translating laser-structured copper alloys into robust, scalable, and application-ready antimicrobial surfaces for both Earth and space applications.

REFERENCES

1. Tanwar, J.; Das, S.; Fatima, Z.; Hameed, S. Multidrug Resistance: An Emerging Crisis. *Interdiscip Perspect Infect Dis* **2014**, *2014*, 541340, doi:10.1155/2014/541340.

2. Khan, A.U.M.; Torelli, A.; Wolf, I.; Gretz, N. AutoCellSeg: Robust Automatic Colony Forming Unit (CFU)/Cell Analysis Using Adaptive Image Segmentation and Easy-to-Use Post-Editing Techniques. *Sci Rep* **2018**, *8*, 486, doi:10.1038/s41598-018-24916-9.

3. Davis, K.A.; Stewart, J.J.; Crouch, H.K.; Florez, C.E.; Hospenthal, D.R. Methicillin-Resistant Staphylococcus Aureus (MRSA) Nares Colonization at Hospital Admission and Its Effect on Subsequent MRSA Infection. *Clinical Infectious Diseases* **2004**, *39*, 776–782, doi:10.1086/422997.

4. Donlan, R.M. Biofilm Formation: A Clinically Relevant Microbiological Process. *Clinical Infectious Diseases* **2001**, *33*, 1387–1392, doi:10.1086/322972.

5. Warnes, S.L.; Green, S.M.; Michels, H.T.; Keevil, C.W. Biocidal Efficacy of Copper Alloys against Pathogenic Enterococci Involves Degradation of Genomic and Plasmid DNAs. *Appl Environ Microbiol* **2010**, *76*, 5390–5401, doi:10.1128/AEM.03050-09.

6. Viegas, C.; Gomes, B.; Cervantes, R.; Moreira, S.; Dias, M.; Pena, P.; Carolino, E.; Twarużek, M.; Kosicki, R.; Soszczyńska, E.; et al. Microbial Contamination in Grocery Stores from Portugal and Spain — The Neglected Indoor Environment to Be Tackled in the Scope of the One Health Approach. *Science of the Total Environment* **2023**, *875*, doi:10.1016/j.scitotenv.2023.162602.

7. Sanborn, W.R. The Relation of Surface Contamination to the Transmission of Disease. *Am J Public Health Nations Health* **1963**, *53*, doi:10.2105/AJPH.53.8.1278.

8. Morawska, L.; Milton, D.K. It Is Time to Address Airborne Transmission of Coronavirus Disease 2019 (COVID-19). *Clinical Infectious Diseases* **2020**, *71*, 2311–2313, doi:10.1093/cid/ciaa939.

9. Cairncross, S.; Blumenthal, U.; Kolsky, P.; Moraes, L.; Tayeh, A. The Public and Domestic Domains in the Transmission of Disease. *Tropical Medicine and International Health* **1996**, *1*, 27–34, doi:10.1046/j.1365-3156.1996.d01-9.x.

10. Fairbrother, J.M.; Nadeau, É. Escherichia Coli: On-Farm Contamination of Animals. *OIE Revue Scientifique et Technique* **2006**, *25*, 555–569, doi:10.20506/rst.25.2.1682.

11. Santajit, S.; Indrawattana, N. Mechanisms of Antimicrobial Resistance in ESKAPE Pathogens. *Biomed Res Int* **2016**, *2016*, 2475067, doi:10.1155/2016/2475067.

12. Schmidt, F.R. The Challenge of Multidrug Resistance: Actual Strategies in the Development of Novel Antibacterials. *Appl Microbiol Biotechnol* **2004**, *63*, 335–343, doi:10.1007/s00253-003-1344-1.

13. Hasan, J.; Crawford, R.J.; Ivanova, E.P. Antibacterial Surfaces: The Quest for a New Generation of Biomaterials. *Trends Biotechnol* **2013**, *31*, 295–304, doi:10.1016/j.tibtech.2013.01.017.

14. Rößler, F.; Lang, V.; Günther, D.; Lasagni, A.F. Fabricating Three-Dimensional Periodic Micro Patterns on Photo-Resists Using Laser Interference Lithography. *Adv Eng Mater* **2017**, *19*, doi:10.1002/adem.201600855.

15. Nijhout, H.F. Elements of Butterfly Wing Patterns. *Journal of Experimental Zoology* **2001**, *291*, 213–225, doi:10.1002/jez.1099.

16. Wilson, S.J.; Hutley, M.C. The Optical Properties of 'Moth Eye' Antireflection Surfaces. *Opt Acta (Lond)* **1982**, *29*, 993–1009, doi:10.1080/713820946.

17. Kelleher, S.M.; Habimana, O.; Lawler, J.; O'reilly, B.; Daniels, S.; Casey, E.; Cowley, A. Cicada Wing Surface Topography: An Investigation into the Bactericidal Properties of Nanostructural Features. *ACS Appl Mater Interfaces* **2016**, *8*, 14966–14974, doi:10.1021/acsami.5b08309.

18. Ensikat, H.J.; Ditsche-Kuru, P.; Neinhuis, C.; Barthlott, W. Superhydrophobicity in Perfection: The Outstanding Properties of the Lotus Leaf. *Beilstein Journal of Nanotechnology* **2011**, *2*, 152–161, doi:10.3762/bjnano.2.19.

19. Gao, X.; Yan, X.; Yao, X.; Xu, L.; Zhang, K.; Zhang, J.; Yang, B.; Jiang, L. The Dry-Style Antifogging Properties of Mosquito Compound Eyes and Artificial Analogues Prepared by Soft Lithography. *Advanced Materials* **2007**, *19*, 2213–2217, doi:10.1002/adma.200601946.

20. Oeffner, J.; Lauder, G. V. The Hydrodynamic Function of Shark Skin and Two Biomimetic Applications. *Journal of Experimental Biology* **2012**, *215*, 785–795, doi:10.1242/jeb.063040.

21. Lasagni, A.F.; Gachot, C.; Trinh, K.E.; Hans, M.; Rosenkranz, A.; Roch, T.; Eckhardt, S.; Kunze, T.; Bieda, M.; Günther, D.; et al. Direct Laser Interference Patterning, 20 Years of Development: From the Basics to Industrial Applications. *Laser-based Micro- and Nanoprocessing XI, SPIE: Bellingham, WA, USA*, **2017**, *10092*, 1009211, doi:10.1117/12.2252595.

22. Aguilar-Morales, A.I.; Alamri, S.; Lasagni, A.F. Micro-Fabrication of High Aspect Ratio Periodic Structures on Stainless Steel by Picosecond Direct Laser Interference Patterning. *J Mater Process Technol* **2018**, *252*, 313–321, doi:10.1016/j.jmatprotec.2017.09.039.

23. Bieda, M.; Siebold, M.; Lasagni, A.F. Fabrication of Sub-Micron Surface Structures on Copper, Stainless Steel and Titanium Using Picosecond Laser Interference Patterning. *Appl Surf Sci* **2016**, *387*, 175–182, doi:10.1016/j.apsusc.2016.06.100.

24. Lang, V.; Voisiat, B.; Kunze, T.; Lasagni, A.F. Fabrication of High Aspect-Ratio Surface Micro Patterns on Stainless Steel Using High-Speed Direct Laser Interference Patterning. *Adv Eng Mater* **2019**, *21*, doi:10.1002/adem.201900151.

25. Müller, D.W.; Fox, T.; Grützmacher, P.G.; Suarez, S.; Mücklich, F. Applying Ultrashort Pulsed Direct Laser Interference Patterning for Functional Surfaces. *Sci Rep* **2020**, *10*, doi:10.1038/s41598-020-60592-4.

26. El-Khoury, M.; Voisiat, B.; Kunze, T.; Lasagni, A.F. Utilizing Fundamental Beam-Mode Shaping Technique for Top-Hat Laser Intensities in Direct Laser Interference Patterning. *Journal of Laser Micro/Nanoengineering* **2018**, *13*, 268–272, doi:10.2961/jlmn.2018.03.0021.

27. Chichkov, B.N.; Momma, C.; Nolte, S.; Von Alvensleben, F.; Tünnermann, A. Femtosecond, Picosecond and Nanosecond Laser Ablation of Solids. *Appl Phys A Mater Sci Process* **1996**, *63*, 109–115, doi:10.1007/BF01567637.

28. Zhang, Y.; Chen, J.K. Ultrafast Melting and Resolidification of Gold Particle Irradiated by Pico- to Femtosecond Lasers. *J Appl Phys* **2008**, *104*, 053507, doi:10.1063/1.2975972.

29. Vorobyev, A.Y.; Guo, C. Direct Femtosecond Laser Surface Nano/Microstructuring and Its Applications. *Laser Photon Rev* **2013**, *7*, 385–407, doi:10.1002/lpor.201200017.

30. Müller, D.W.; Lößlein, S.; Terriac, E.; Brix, K.; Siems, K.; Moeller, R.; Kautenburger, R.; Mücklich, F. Increasing Antibacterial Efficiency of Cu Surfaces by Targeted Surface Functionalization via Ultrashort Pulsed Direct Laser Interference Patterning. *Adv Mater Interfaces* **2021**, *8*, 2001656, doi:10.1002/admi.202001656.

31. Müller, D.W.; Holtsch, A.; Lößlein, S.; Pauly, C.; Spengler, C.; Grandthyll, S.; Jacobs, K.; Mücklich, F.; Müller, F. In-Depth Investigation of Copper Surface

Chemistry Modification by Ultrashort Pulsed Direct Laser Interference Patterning. *Langmuir* **2020**, *36*, 13415–13425, doi:10.1021/acs.langmuir.0c01625.

32. Hans, M.; Mathews, S.; Mücklich, F.; Solioz, M. Physicochemical Properties of Copper Important for Its Antibacterial Activity and Development of a Unified Model. *Biointerphases* **2016**, *11*, 018902, doi:10.1116/1.4935853.

33. Mathews, S.; Hans, M.; Mücklich, F.; Solioz, M. Contact Killing of Bacteria on Copper Is Suppressed If Bacterial-Metal Contact Is Prevented and Is Induced on Iron by Copper Ions. *Appl Environ Microbiol* **2013**, *79*, 2605–2611, doi:10.1128/AEM.03608-12.

34. Konieczny, J.; Rdzawski, Z. Antibacterial Properties of Copper and Its Alloys. *Archives of Materials Science and Engineering* **2012**, *56*, 53–60.

35. Grass, G.; Rensing, C.; Solioz, M. Metallic Copper as an Antimicrobial Surface. *Appl Environ Microbiol* **2011**, *77*, 1541–1547, doi:10.1128/AEM.02766-10.

36. Quaranta, D.; Krans, T.; Santo, C.E.; Elowsky, C.G.; Domaille, D.W.; Chang, C.J.; Grass, G. Mechanisms of Contact-Mediated Killing of Yeast Cells on Dry Metallic Copper Surfaces. *Appl Environ Microbiol* **2011**, *77*, doi:10.1128/AEM.01704-10.

37. Rosenkranz, A.; Hans, M.; Gachot, C.; Thome, A.; Bonk, S.; Mücklich, F. Direct Laser Interference Patterning: Tailoring of Contact Area for Frictional and Antibacterial Properties. *Lubricants* **2016**, *4*, doi:10.3390/lubricants4010002.

38. Davis, J.R. *ASM Specialty Handbook, Copper and Copper Alloys*; ASM International: Materials Park, OH, USA, 2001;

39. Rojas, P.; Vera, R.; Martínez, C.; Villarroel, M. Effect of the Powder Metallurgy Manufacture Process on the Electrochemical Behaviour of Copper, Nickel and Copper-Nickel Alloys in Hydrochloric Acid. *Int J Electrochem Sci* **2016**, *11*, doi:10.20964/2016.06.40.

40. Alfantazi, A.M.; Ahmed, T.M.; Tromans, D. Corrosion Behavior of Copper Alloys in Chloride Media. *Mater Des* **2009**, *30*, 2425–2430, doi:10.1016/j.matdes.2008.10.015.

41. Mehtar, S.; Wiid, I.; Todorov, S.D. The Antimicrobial Activity of Copper and Copper Alloys against Nosocomial Pathogens and Mycobacterium Tuberculosis Isolated from Healthcare Facilities in the Western Cape: An in-Vitro Study. *Journal of Hospital Infection* **2008**, *68*, 45–51, doi:10.1016/j.jhin.2007.10.009.

42. Siems, K.; Müller, D.W.; Maertens, L.; Ahmed, A.; Van Houdt, R.; Mancinelli, R.L.; Baur, S.; Brix, K.; Kautenburger, R.; Caplin, N.; et al. Testing Laser-Structured Antimicrobial Surfaces Under Space Conditions: The Design of the ISS Experiment BIOFILMS. *Frontiers in Space Technologies* **2022**, *2*, 773244, doi:10.3389/frspt.2021.773244.

43. Timofeev, S.M.; Siems, K.; Müller, D.W.; Ahmed, A.S.; Schiele, A.; Brix, K.; Krämer, C.L.; Arndt, F.; Kautenburger, R.; Mücklich, F.; et al. Stress Response of Aspergillus Niger Spores to Copper Surfaces and the Implications for Antifungal Surface Functionalization. *Adv Mater Interfaces* **2025**, *12*, doi:10.1002/admi.202400852.

44. Krämer, C.L.; Müller, D.W.; Arndt, F.; Rehm, A.; Walkenfort, B.; Ahmed, A.S.; Haben, A.; Schiele, A.; Auerhammer, A.; Hasenberg, M.; et al. Touching Surfaces – Presence of Microorganisms on Antimicrobial Metal Surfaces on the International Space Station and in German Schools. *BMC Microbiol* **2025**, *25*, 631, doi:10.1186/s12866-025-04316-6.

45. Lehtopolku, M.; Kotilainen, P.; Puukka, P.; Nakari, U.M.; Siitonen, A.; Eerola, E.; Huovinen, P.; Hakanen, A.J. Inaccuracy of the Disk Diffusion Method Compared with the Agar Dilution Method for Susceptibility Testing of Campylobacter Spp. *J Clin Microbiol* **2012**, *50*, 336–341, doi:10.1128/JCM.01090-11.

46. Lu, C.L.; Liu, C.Y.; Huang, Y.T.; Liao, C.H.; Teng, L.J.; Turnidge, J.D.; Hsueh, P.R. Antimicrobial Susceptibilities of Commonly Encountered Bacterial Isolates to Fosfomycin Determined by Agar Dilution and Disk Diffusion Methods. *Antimicrob Agents Chemother* **2011**, *55*, 4295–4301, doi:10.1128/AAC.00349-11.

47. Kamat, N.; Velho-Pereira, S. Screening of Actinobacteria for Antimicrobial Activities by a Modified "Cross-Streak" Method. *Nature Precedings* **2012**, doi:10.1038/npre.2012.6765.1.

48. Klepser, M.E.; Ernst, E.J.; Lewis, R.E.; Ernst, M.E.; Pfaller, M.A. Influence of Test Conditions on Antifungal Time-Kill Curve Results: Proposal for Standardized Methods. *Antimicrob Agents Chemother* **1998**, *42*, 1207–1212, doi:10.1128/aac.42.5.1207.

49. Tong, G.; Yulong, M.; Peng, G.; Zirong, X. Antibacterial Effects of the Cu(II)-Exchanged Montmorillonite on Escherichia Coli K88 and Salmonella Choleraesuis. *Vet Microbiol* **2005**, *105*, 113–122, doi:10.1016/J.VETMIC.2004.11.003.

50. Silvestry-Rodriguez, N.; Sicairos-Ruelas, E.E.; Gerba, C.P.; Bright, K.R. Silver as a Disinfectant. In *Reviews of Environmental Contamination and Toxicology*; 2007; Vol. 191.

51. Raffi, M.; Mehrwan, S.; Bhatti, T.M.; Akhter, J.I.; Hameed, A.; Yawar, W.; Ul Hasan, M.M. Investigations into the Antibacterial Behavior of Copper Nanoparticles against Escherichia Coli. *Ann Microbiol* **2010**, *60*, 75–80, doi:10.1007/s13213-010-0015-6.

52. Berney, M.; Hammes, F.; Bosshard, F.; Weilenmann, H.U.; Egli, T. Assessment and Interpretation of Bacterial Viability by Using the LIVE/DEAD BacLight Kit in Combination with Flow Cytometry. *Appl Environ Microbiol* **2007**, *73*, 3283–3290, doi:10.1128/AEM.02750-06.

53. Garrett, T.R.; Bhakoo, M.; Zhang, Z. Bacterial Adhesion and Biofilms on Surfaces. *Progress in Natural Science* **2008**, *18*, 1049–1056, doi:10.1016/j.pnsc.2008.04.001.

54. Wibisono, F.J.; Effendi, M.H.; Wibisono, F.M. Occurrence, Antimicrobial Resistance, and Potential Zoonosis Risk of Avian Pathogenic Escherichia Coli in Indonesia: A Review. *Int J One Health* **2022**, *8*, doi:10.14202/IJOH.2022.76-85.

55. Nataro, J.P.; Kaper, J.B. Diarrheagenic Escherichia Coli. *Clin Microbiol Rev* **1998**, *11*, 142–201, doi:10.1128/cmr.11.1.142.

56. Endesfelder, U. From Single Bacterial Cell Imaging towards in Vivo Single-Molecule Biochemistry Studies. *Essays Biochem* **2019**, *63*, 187–196, doi:10.1042/EBC20190002.

57. Erjavec, M.S. *Escherichia Coli - Old and New Insights*; IntechOpen, 2023;

58. Grenier, F.; Matteau, D.; Baby, V.; Rodrigue, S. Complete Genome Sequence of Escherichia Coli BW25113. *Genome Announc* **2014**, *2*, doi:10.1128/genomeA.01038-14.

59. Dollwet, H.H.A.; Sorenson, J.R.J. Historic Uses of Copper Compounds in Medicine. *Trace Elem Med* **1985**, *2*, 80–87.

60. Mijnendonckx, K.; Leys, N.; Mahillon, J.; Silver, S.; Van Houdt, R. Antimicrobial Silver: Uses, Toxicity and Potential for Resistance. *BioMetals* **2013**, *26*, doi:10.1007/s10534-013-9645-z.

61. Franci, G.; Falanga, A.; Galdiero, S.; Palomba, L.; Rai, M.; Morelli, G.; Galdiero, M. Silver Nanoparticles as Potential Antibacterial Agents. *Molecules* **2015**, *20*, 8856–8874, doi:10.3390/molecules20058856.

62. Tsvetkov, P.; Coy, S.; Petrova, B.; Dreishpoon, M.; Verma, A.; Abdusamad, M.; Rossen, J.; Joesch-Cohen, L.; Humeidi, R.; Spangler, R.D.; et al. Copper Induces

Cell Death by Targeting Lipoylated TCA Cycle Proteins. *Science 375* **2022**, *375*, 1254–1261, doi:10.1126/science.abf0529.

63. Zhang, L.; Wu, L.; Si, Y.; Shu, K. Size-Dependent Cytotoxicity of Silver Nanoparticles to Azotobacter Vinelandii: Growth Inhibition, Cell Injury, Oxidative Stress and Internalization. *PLoS One* **2018**, *13*, doi:10.1371/journal.pone.0209020.

64. Luo, J.; Hein, C.; Mücklich, F.; Solioz, M. Killing of Bacteria by Copper, Cadmium, and Silver Surfaces Reveals Relevant Physicochemical Parameters. *Biointerphases* **2017**, *12*, 020301, doi:10.1116/1.4980127.

65. Meister, T.L.; Fortmann, J.; Breisch, M.; Sengstock, C.; Steinmann, E.; Köller, M.; Pfaender, S.; Ludwig, A. Nanoscale Copper and Silver Thin Film Systems Display Differences in Antiviral and Antibacterial Properties. *Sci Rep* **2022**, *12*, 1–10, doi:10.1038/s41598-022-11212-w.

66. Sirelkhatim, A.; Mahmud, S.; Seeni, A.; Kaus, N.H.M.; Ann, L.C.; Bakhori, S.K.M.; Hasan, H.; Mohamad, D. Review on Zinc Oxide Nanoparticles: Antibacterial Activity and Toxicity Mechanism. *Nanomicro Lett* **2015**, *7*, 219–242, doi:10.1007/s40820-015-0040-x.

67. Visai, L.; de Nardo, L.; Punta, C.; Melone, L.; Cigada, A.; Imbriani, M.; Arciola, C.R. Titanium Oxide Antibacterial Surfaces in Biomedical Devices. *International Journal of Artificial Organs* **2011**, *34*, 929–946, doi:10.5301/ijao.5000050.

68. Gurunathan, S.; Han, J.W.; Abdal Dayem, A.; Eppakayala, V.; Kim, J.H. Oxidative Stress-Mediated Antibacterial Activity of Graphene Oxide and Reduced Graphene Oxide in Pseudomonas Aeruginosa. *Int J Nanomedicine* **2012**, *7*, doi:10.2147/IJN.S37397.

69. Liu, S.; Zeng, T.H.; Hofmann, M.; Burcombe, E.; Wei, J.; Jiang, R.; Kong, J.; Chen, Y. Antibacterial Activity of Graphite, Graphite Oxide, Graphene Oxide, and

Reduced Graphene Oxide: Membrane and Oxidative Stress. *ACS Nano* **2011**, *5*, doi:10.1021/nn202451x.

70. Borovanský, J.; Riley, P.A. Cytotoxicity of Zinc in Vitro. *Chem Biol Interact* **1989**, *69*, 279–291, doi:10.1016/0009-2797(89)90085-9.

71. Schlief, M.L.; West, T.; Craig, A.M.; Holtzman, D.M.; Gitlin, J.D. Role of the Menkes Copper-Transporting ATPase in NMDA Receptor-Mediated Neuronal Toxicity. *Proc Natl Acad Sci U S A* **2006**, *103*, 14919–14924, doi:10.1073/pnas.0605390103.

72. Lan, A.P.; Chen, J.; Chai, Z.F.; Hu, Y. The Neurotoxicity of Iron, Copper and Cobalt in Parkinson's Disease through ROS-Mediated Mechanisms. *BioMetals* **2016**, *29*, doi:10.1007/s10534-016-9942-4.

73. Tapiero, H.; Townsend, D.M.; Tew, K.D. Trace Elements in Human Physiology and Pathology. Copper. *Biomedicine & Pharmacotherapy* **2003**, *57*, 386–398, doi:10.1016/S0753-3322(03)00012-X.

74. Freudenberger, J.; Warlimont, H. Copper and Copper Alloys. In *Springer Handbook of Materials Data*; Springer, 2018; pp. 297–305.

75. Müller, A. V.; Böswirth, B.; Cerri, V.; Greuner, H.; Neu, R.; Siefken, U.; Visca, E.; You, J.H. Application of Tungsten-Copper Composite Heat Sink Materials to Plasma-Facing Component Mock-Ups. In Proceedings of the Physica Scripta; 2020; Vol. 2020.

76. Paul, H.; Lityńska-Dobrzyńska, L.; Prażmowski, M. Microstructure and Phase Constitution near the Interface of Explosively Welded Aluminum/Copper Plates. *Metall Mater Trans A Phys Metall Mater Sci* **2013**, *44*, doi:10.1007/s11661-013-1703-1.

77. Masoumi, M.; Rajasekhara, K.; Parati, D.; Bilgin, B. Manufacturing Techniques for Electric Motor Coils with Round Copper Wires. *IEEE Access* **2022**, *10*, doi:10.1109/ACCESS.2022.3229024.

78. Copper Wire and Electrical Conductors--the Shaping of a Technology. *Choice Reviews Online* **1993**, *30*, doi:10.5860/choice.30-3288.

79. *Copper Alloys - Early Applications and Current Performance - Enhancing Processes*; Collini, L., Ed.; 2012;

80. Vincent, M.; Hartemann, P.; Engels-Deutsch, M. Antimicrobial Applications of Copper. *Int J Hyg Environ Health* **2016**, *219*, 585–591, doi:10.1016/J.IJHEH.2016.06.003.

81. Dan, Z.G.; Ni, H.W.; Xu, B.F.; Xiong, J.; Xiong, P.Y. Microstructure and Antibacterial Properties of AISI 420 Stainless Steel Implanted by Copper Ions. *Thin Solid Films* **2005**, *492*, 93–100, doi:10.1016/j.tsf.2005.06.100.

82. Luo, J.; Hein, C.; Pierson, J.F.; Mücklich, F. Early-Stage Corrosion, Ion Release, and the Antibacterial Effect of Copper and Cuprous Oxide in Physiological Buffers: Phosphate-Buffered Saline vs Na-4-(2-Hydroxyethyl)-1-Piperazineethanesulfonic Acid. *Biointerphases* **2019**, *14*, doi:10.1063/1.5123039.

83. Luo, J.; Hein, C.; Ghanbaja, J.; Pierson, J.F.; Mücklich, F. Bacteria Accumulate Copper Ions and Inhibit Oxide Formation on Copper Surface during Antibacterial Efficiency Test. *Micron* **2019**, *127*, doi:10.1016/j.micron.2019.102759.

84. Bezza, F.A.; Tichapondwa, S.M.; Chirwa, E.M.N. Fabrication of Monodispersed Copper Oxide Nanoparticles with Potential Application as Antimicrobial Agents. *Sci Rep* **2020**, *10*, doi:10.1038/s41598-020-73497-z.

85. Noyce, J.O.; Michels, H.; Keevil, C.W. Use of Copper Cast Alloys to Control Escherichia Coli O157 Cross-Contamination during Food Processing. *Appl Environ Microbiol* **2006**, *72*, doi:10.1128/AEM.02532-05.

86. Karpanen, T.J.; Casey, A.L.; Lambert, P.A.; Cookson, B.D.; Nightingale, P.; Miruszenko, L.; Elliott, T.S.J. The Antimicrobial Efficacy of Copper Alloy Furnishing in the Clinical Environment: A Crossover Study. *Infect Control Hosp Epidemiol* **2012**, *33*, 3–9, doi:10.1086/663644.

87. Semih, Ö.; Recep, A. Investigation of Microstructure, Machinability, and Mechanical Properties of New-Generation Hybrid Lead-Free Brass Alloys. *High Temperature Materials and Processes* **2023**, *42*, 20220263, doi:10.1515/htmp-2022-0263.

88. Klosak, M.; Jankowiak, T.; Rusinek, A.; Bendarma, A.; Sielicki, P.W.; Lodygowski, T. Mechanical Properties of Brass under Impact and Perforation Tests for a Wide Range of Temperatures: Experimental and Numerical Approach. *Materials* **2020**, *13*, 5821, doi:10.3390/ma13245821.

89. Kejzlar, P.; Machuta, J.; Nová, I. Comparison of the Structure of CuZn40MnAl Alloy Casted into Sand and Metal Moulds. *Manufacturing Technology* **2017**, *17*, 44–48, doi:10.21062/ujep/x.2017/a/1213-2489/MT/17/1/44.

90. Leineweber, A. The Cu–Sn System: A Comprehensive Review of the Crystal Structures of Its Stable and Metastable Phases. *J Phase Equilibria Diffus* **2023**, *44*, 343–393, doi:10.1007/s11669-023-01041-3.

91. Tayyaba, Q.; Butt, A.Q.; Ali khan, T.; Nazar, Z.; Rehman, A.; Yusheng, W. Mechanical Alloying of Bronze with Aluminum and Nickel: Impact on Corrosion Resistance and Hardness. *Journal of Alloys and Metallurgical Systems* **2024**, *8*, 100136, doi:10.1016/J.JALMES.2024.100136.

92. Li, M.; Zinkle, S.J. Physical and Mechanical Properties of Copper and Copper Alloys. In *Comprehensive Nuclear Materials*; 2012; Vol. 4.

93. Ahmed Adnan, R.S.; Abbass, M.K.; Jomaa, D.M. Effect of Tin Addition on Corrosion Resistance and Microstructure of Cu-Based Shape Memory Alloy. *Mater Today Proc* **2021**, *42*, 2119–2124, doi:10.1016/J.MATPR.2020.12.295.

94. Fürtauer, S.; Li, D.; Cupid, D.; Flandorfer, H. The Cu-Sn Phase Diagram, Part I: New Experimental Results. *Intermetallics (Barking)* **2013**, *34*, doi:10.1016/j.intermet.2012.10.004.

95. Zhang, Y.; Zuo, T.T.; Tang, Z.; Gao, M.C.; Dahmen, K.A.; Liaw, P.K.; Lu, Z.P. Microstructures and Properties of High-Entropy Alloys. *Prog Mater Sci* 2014, *61*, 1–93.

96. Jenkins, W.D.; Digges, T.G.; Johnson, C.R. Tensile Properties of Copper, Nickel, and 70-Percent-Copper-30-Percent-Nickel and 30-Percent-Copper-70-Percent-Nickel Alloys at High Temperatures. *J Res Natl Bur Stand (1934)* **1957**, *58*, doi:10.6028/jres.058.027.

97. Nickel and Its Alloys. *J Franklin Inst* **1924**, *198*, doi:10.1016/s0016-0032(24)90183-9.

98. Taher, A.M.Y. Corrosion Behavior of Copper-Nickel Alloy in Marine Environment (Review Paper). *Applied Mechanics and Materials* **2015**, *799–800*, doi:10.4028/www.scientific.net/amm.799-800.222.

99. Powell, C. Corrosion and Biofouling Resistance Evaluation of 90-10 Copper-Nickel. *EUROCORR 2004 - European Corrosion Conference: Long Term Prediction and Modelling of Corrosion* 2004.

100. Chai, L.Q.; Zhou, L.; Zhang, K.Y.; Zhang, H.S. Structural Characterizations, Spectroscopic, Electrochemical Properties, and Antibacterial Activities of Copper (II) and Cobalt (II) Complexes Containing Imidazole Ring. *Appl Organomet Chem* **2018**, *32*, doi:10.1002/aoc.4576.

101. Iakovidis, I.; Delimaris, I.; Piperakis, S.M. Copper and Its Complexes in Medicine: A Biochemical Approach. *Mol Biol Int* **2011**, *2011*, doi:10.4061/2011/594529.

102. Bonham, M.; O'Connor, J.M.; Hannigan, B.M.; Strain, J.J. The Immune System as a Physiological Indicator of Marginal Copper Status? *British Journal of Nutrition* **2002**, *87*, doi:10.1079/bjn2002558.

103. Zeeshan, M.; Murugadas, A.; Ghaskadbi, S.; Rajendran, R.B.; Akbarsha, M.A. ROS Dependent Copper Toxicity in Hydra-Biochemical and Molecular Study.

Comparative Biochemistry and Physiology Part - C: Toxicology and Pharmacology **2016**, *185–186*, doi:10.1016/j.cbpc.2016.02.008.

104. Ameh, T.; Sayes, C.M. The Potential Exposure and Hazards of Copper Nanoparticles: A Review. *Environ Toxicol Pharmacol* **2019**, *71*, 103220, doi:10.1016/J.ETAP.2019.103220.

105. Crisan, M.C.; Teodora, M.; Lucian, M. Copper Nanoparticles: Synthesis and Characterization, Physiology, Toxicity and Antimicrobial Applications. *Applied Sciences* **2022**, *12*, 141, doi:10.3390/app12010141.

106. Wu, H.; Zhang, X.; He, X.; Li, M.; Huang, X.; Hang, R.; Tang, B. Wear and Corrosion Resistance of Anti-Bacterial Ti–Cu–N Coatings on Titanium Implants. *Appl Surf Sci* **2014**, *317*, 614–621, doi:10.1016/J.APSUSC.2014.08.163.

107. Zerbib, S.; Vallet, L.; Muggeo, A.; de Champs, C.; Lefebvre, A.; Jolly, D.; Kanagaratnam, L. Copper for the Prevention of Outbreaks of Health Care–Associated Infections in a Long-Term Care Facility for Older Adults. *J Am Med Dir Assoc* **2020**, *21*, 68-71.e1, doi:10.1016/J.JAMDA.2019.02.003.

108. Salgado, C.D.; Sepkowitz, K.A.; John, J.F.; Cantey, J.R.; Attaway, H.H.; Freeman, K.D.; Sharpe, P.A.; Michels, H.T.; Schmidt, M.G. Copper Surfaces Reduce the Rate of Healthcare-Acquired Infections in the Intensive Care Unit. *Infect Control Hosp Epidemiol* **2013**, *34*, doi:10.1086/670207.

109. Colin, M.; Klingelschmitt, F.; Charpentier, E.; Josse, J.; Kanagaratnam, L.; De Champs, C.; Gangloff, S.C. Copper Alloy Touch Surfaces in Healthcare Facilities: An Effective Solution to Prevent Bacterial Spreading. *Materials* **2018**, *11*, doi:10.3390/ma11122479.

110. Schaeffer, R.D. *Fundamentals of Laser Micromachining*; Taylor & Francis Group, LLC, 2016;

111. Hans, M.; Müller, F.; Grandthyll, S.; Hüfner, S.; Mücklich, F. Anisotropic Wetting of Copper Alloys Induced by One-Step Laser Micro-Patterning. *Appl Surf Sci* **2012**, *263*, 416–422, doi:10.1016/j.apsusc.2012.09.071.

112. Lasagni, A.F. Advanced Design of Periodical Structures by Laser Interference Metallurgy in the Micro/Nano Scale on Macroscopic Areas, Universität des Saarlandes, 2006.

113. Alamri, S.; Aguilar-Morales, A.I.; Lasagni, A.F. Controlling the Wettability of Polycarbonate Substrates by Producing Hierarchical Structures Using Direct Laser Interference Patterning. *Eur Polym J* **2018**, *99*, 27–37, doi:10.1016/j.eurpolymj.2017.12.001.

114. Lasagni, A.F.; Shao, P.; Hendricks, J.L.; Shaw, C.M.; Martin, D.C.; Das, S. Direct Fabrication of Periodic Patterns with Hierarchical Sub-Wavelength Structures on Poly(3,4-Ethylene Dioxythiophene)-Poly(Styrene Sulfonate) Thin Films Using Femtosecond Laser Interference Patterning. *Appl Surf Sci* **2010**, *256*, 1708–1713, doi:10.1016/j.apsusc.2009.09.099.

115. Aguilar-Morales, A.I.; Alamri, S.; Kunze, T.; Lasagni, A.F. Influence of Processing Parameters on Surface Texture Homogeneity Using Direct Laser Interference Patterning. *Opt Laser Technol* **2018**, *107*, 216–227, doi:10.1016/j.optlastec.2018.05.044.

116. Alamri, S.; Fraggelakis, F.; Kunze, T.; Krupop, B.; Mincuzzi, G.; Kling, R.; Lasagni, A.F. On the Interplay of DLIP and LIPSS upon Ultra-Short Laser Pulse Irradiation. *Materials* **2019**, *12*, doi:10.3390/ma12071018.

117. Lang, V.; Roch, T.; Lasagni, A.F. High-Speed Surface Structuring of Polycarbonate Using Direct Laser Interference Patterning: Toward 1 M2 Min−1 Fabrication Speed Barrier. *Adv Eng Mater* **2016**, *18*, 1342–1348, doi:10.1002/adem.201600173.

118. Alamri, S.; Lasagni, A.F. Development of a General Model for Direct Laser Interference Patterning of Polymers. *Opt Express* **2017**, *25*, 9603, doi:10.1364/oe.25.009603.

119. Fox, T.; Mücklich, F. Development and Validation of a Calculation Routine for the Precise Determination of Pulse Overlap and Accumulated Fluence in Pulsed Laser Surface Treatment. *Adv Eng Mater* **2022**, 2201021, doi:10.1002/adem.202201021.

120. Tanvir Ahmmed, K.M.; Grambow, C.; Kietzig, A.M. Fabrication of Micro/Nano Structures on Metals by Femtosecond Laser Micromachining. *Micromachines (Basel)* 2014, *5*, 1219–1253.

121. Shugaev, M. V.; Wu, C.; Armbruster, O.; Naghilou, A.; Brouwer, N.; Ivanov, D.S.; Derrien, T.J.Y.; Bulgakova, N.M.; Kautek, W.; Rethfeld, B.; et al. Fundamentals of Ultrafast Laser-Material Interaction. *MRS Bull* **2016**, *41*, 960–968, doi:10.1557/mrs.2016.274.

122. Jiang, L.; Tsai, H.L. Improved Two-Temperature Model and Its Application in Ultrashort Laser Heating of Metal Films. *J Heat Transfer* **2005**, *127*, doi:10.1115/1.2035113.

123. Weber, S.T.; Rethfeld, B. Laser-Excitation of Electrons and Nonequilibrium Energy Transfer to Phonons in Copper. *Appl Surf Sci* **2017**, *417*, 64–68, doi:10.1016/j.apsusc.2017.02.183.

124. Gamaly, E.G.; Rode, A. V; Tikhonchuk, V.T.; Luther-Davies, B. Ablation of Solids by Femtosecond Lasers: Ablation Mechanism and Ablation Thresholds for Metals and Dielectrics. *Physics of Plasma* **2002**, *9*, 949–957.

125. Anisimov, S.I.; Landau, L.D.; Rethfeld, B. Theory of Ultrashort Laser Pulse Interaction with a Metal. In Proceedings of the Nonresonant Laser-Matter Interaction; St. Petersburg, Russian Federation, 1997; Vol. 3093, p. 192.

126. Anisimov, S.I.; Kapeliovich, B.L.; Perel'man, T.L.; Landau, L.D. Electron Emission from Metal Surfaces Exposed to Ultrashort Laser Pulses. *Sov Phys JETP* **1975**, *39*, 375–377.

127. Hohlfeld, J.; Wellershoff, S.-S.; Gudde, J.; Conrad, U.; Jähnke, V.; Matthias, E. Electron and Lattice Dynamics Following Optical Excitation of Metals. *Chem Phys* **2000**, *251*, 237–258, doi:10.1016/S0301-0104(99)00330-4.

128. Ivanov, D.; Zhigilei, L. Combined Atomistic-Continuum Modeling of Short-Pulse Laser Melting and Disintegration of Metal Films. *Phys Rev B Condens Matter Mater Phys* **2003**, *68*, doi:10.1103/PhysRevB.68.064114.

129. Hopkins, P.E.; Norris, P.M. Substrate Influence in Electron-Phonon Coupling Measurements in Thin Au Films. *Appl Surf Sci* **2007**, *253*, 6289–6294, doi:10.1016/j.apsusc.2007.01.065.

130. Kirkwood, S.E.; Tsui, Y.Y.; Fedosejevs, R.; Brantov, A. V.; Bychenkov, V.Y. Experimental and Theoretical Study of Absorption of Femtosecond Laser Pulses in Interaction with Solid Copper Targets. *Phys Rev B Condens Matter Mater Phys* **2009**, *79*, doi:10.1103/PhysRevB.79.144120.

131. Nolte, S.; Momma, C.; Jacobs, H.; Tünnermann, A.; Chichkov, B.N.; Wellegehausen, B.; Welling, H. Ablation of Metals by Ultrashort Laser Pulses. *Journal of the Optical Society of America B* **1997**, *14*, 2716, doi:10.1364/JOSAB.14.002716.

132. Hirayama, Y.; Obara, M. Heat-Affected Zone and Ablation Rate of Copper Ablated with Femtosecond Laser. *J Appl Phys* **2005**, *97*, doi:10.1063/1.1852692.

133. Cheng, J.; Liu, C.S.; Shang, S.; Liu, D.; Perrie, W.; Dearden, G.; Watkins, K. A Review of Ultrafast Laser Materials Micromachining. *Opt Laser Technol* **2013**, *46*, 88–102, doi:10.1016/j.optlastec.2012.06.037.

134. Povarnitsyn, M.E.; Itina, T.E.; Sentis, M.; Khishchenko, K. V.; Levashov, P.R. Material Decomposition Mechanisms in Femtosecond Laser Interactions with

Metals. *Phys Rev B Condens Matter Mater Phys* **2007**, *75*, doi:10.1103/PhysRevB.75.235414.

135. Rethfeld, B.; Sokolowski-Tinten, K.; von der Linde, D.; Anisimov, S.I. Ultrafast Thermal Melting of Laser-Excited Solids by Homogeneous Nucleation. *Phys Rev B Condens Matter Mater Phys* **2002**, *65*, 1–4, doi:10.1103/PhysRevB.65.092103.

136. Margetic, V.; Pakulev, A.; Stockhaus, A.; Bolshov, M.; Niemax, K.; Hergenroder, R. A Comparison of Nanosecond and Femtosecond Laser-Induced Plasma Spectroscopy of Brass Samples. *Spectrochimica Acta Part B* **2000**, *55*, 1771–1785, doi:10.1016/S0584-8547(00)00275-5.

137. Shirk, M.D.; Molian, P.A. A Review of Ultrashort Pulsed Laser Ablation of Materials. *J Laser Appl* **1998**, *10*, doi:10.2351/1.521827.

138. Gamaly, E.G.; Rode, A. V. Physics of Ultra-Short Laser Interaction with Matter: From Phonon Excitation to Ultimate Transformations. *Prog Quantum Electron* 2013, *37*.

139. Martins, M.A.; Schäfer, C.; Mücklich, F.; Pauly, C. Influence of Oxide Formation Following Ultrashort Pulsed Laser Micromachining on Self-Propagating Reactions in Free-Standing Ni/Al Reactive Multilayer Foils. *Adv Eng Mater* **2025**, *27*, 1–10, doi:10.1002/adem.202400215.

140. Harilal, S.S.; Freeman, J.R.; Diwakar, P.K.; Hassanein, A. Femtosecond Laser Ablation: Fundamentals and Applications. In *Springer Series in Optical Sciences - Laser-Induced Breakdown Spectroscopy -Theory and Applications*; Springer, 2014; Vol. 182.

141. Hans, M.; Erbe, A.; Mathews, S.; Chen, Y.; Solioz, M.; Mücklich, F. Role of Copper Oxides in Contact Killing of Bacteria. *Langmuir* **2013**, *29*, 16160–16166, doi:10.1021/la404091z.

142. Luo, J.; Hein, C.; Pierson, J.F.; Mücklich, F. Sodium Chloride Assists Copper Release, Enhances Antibacterial Efficiency, and Introduces Atmospheric

Corrosion on Copper Surface. *Surfaces and Interfaces* **2020**, *20*, doi:10.1016/j.surfin.2020.100630.

143. Yousuf, B.; Ahire, J.J.; Dicks, L.M.T. Understanding the Antimicrobial Activity behind Thin- and Thick-Rolled Copper Plates. *Appl Microbiol Biotechnol* **2016**, *100*, 5569–5580, doi:10.1007/s00253-016-7361-7.

144. Hasegawa, M. Ellingham Diagram. In *Treatise on Process Metallurgy*; Elsevier, 2014; Vol. 1, pp. 507–516 ISBN 9780080969862.

145. Yohai, L.; Schreiner, W.H.; Vázquez, M.; Valcarce, M.B. Surface Characterization of Copper, Zinc and Brass in Contact with Tap Water Inhibited with Phosphate Ions. *Appl Surf Sci* **2011**, *257*, 10089–10095, doi:10.1016/j.apsusc.2011.07.002.

146. Choucri, J.; Balbo, A.; Zanotto, F.; Grassi, V.; Touhami, M.E.; Mansouri, I.; Monticelli, C. Corrosion Behavior and Susceptibility to Stress Corrosion Cracking of Leaded and Lead-Free Brasses in Simulated Drinking Water. *Materials* **2022**, *15*, doi:10.3390/ma15010144.

147. Song, Z.; Tegus, O. The Corrosion Properties of Bronze Alloys in NaCl Solutions. *Materials* **2023**, *16*, doi:10.3390/ma16145144.

148. Powell, C. Corrosion and Biofouling Resistance Evaluation of 90-10 Copper-Nickel. *Corrosion Management* **2005**.

149. Kasemets, K.; Ivask, A.; Dubourguier, H.C.; Kahru, A. Toxicity of Nanoparticles of ZnO, CuO and TiO2 to Yeast Saccharomyces Cerevisiae. *Toxicology in Vitro* **2009**, *23*, 1116–1122, doi:10.1016/J.TIV.2009.05.015.

150. Jin, S.E.; Jin, J.E.; Hwang, W.; Hong, S.W. Photocatalytic Antibacterial Application of Zinc Oxide Nanoparticles and Self-Assembled Networks under Dual UV Irradiation for Enhanced Disinfection. *Int J Nanomedicine* **2019**, *14*, doi:10.2147/IJN.S192277.

151. Xiao, Y.; Zheng, J.; He, Y.; Wang, L. Droplet and Bubble Wetting Behaviors: The Roles of Surface Wettability and Roughness. *Colloids Surf A Physicochem Eng Asp* **2022**, *653*, doi:10.1016/j.colsurfa.2022.130008.

152. Marmur, A.; Volpe, C. Della; Siboni, S.; Amirfazli, A.; Drelich, J.W. Contact Angles and Wettability: Towards Common and Accurate Terminology. *Surf Innov* **2017**, *5*, doi:10.1680/jsuin.17.00002.

153. Korczeniewski, E.; Bryk, P.; Koter, S.; Kowalczyk, P.; Kujawski, W.; Kujawa, J.; Terzyk, A.P. Revisiting Wetting, Freezing, and Evaporation Mechanisms of Water on Copper. *ACS Appl Mater Interfaces* **2021**, *13*, doi:10.1021/acsami.1c09733.

154. Cassie, A.B.D.; Baxter, S. Wettability of Porous Surfaces. *Transactions of the Faraday Society* **1944**, *40*, doi:10.1039/tf9444000546.

155. Wenzel, R.N. Resistance of Solid Surfaces to Wetting by Water. *Ind Eng Chem* **1936**, *28*, doi:10.1021/ie50320a024.

156. Cai, Y.; Lin, L.; Xue, Z.; Liu, M.; Wang, S.; Jiang, L. Filefish-Inspired Surface Design for Anisotropic Underwater Oleophobicity. *Adv Funct Mater* **2014**, *24*, doi:10.1002/adfm.201302034.

157. Wan, Y.; Cui, P.; Xu, J.; Yu, H. Directional Water-Collecting Behavior of Pine Needle Surface. *Mater Lett* **2019**, *255*, doi:10.1016/j.matlet.2019.126561.

158. Chen, H.; Zhang, P.; Zhang, L.; Liu, H.; Jiang, Y.; Zhang, D.; Han, Z.; Jiang, L. Continuous Directional Water Transport on the Peristome Surface of Nepenthes Alata. *Nature* **2016**, *532*, doi:10.1038/nature17189.

159. Zhang, J.; Wang, J.; Zhao, Y.; Xu, L.; Gao, X.; Zheng, Y.; Jiang, L. How Does the Leaf Margin Make the Lotus Surface Dry as the Lotus Leaf Floats on Water? *Soft Matter* **2008**, *4*, doi:10.1039/b807857b.

160. Lutey, A.H.A.; Gemini, L.; Romoli, L.; Lazzini, G.; Fuso, F.; Faucon, M.; Kling, R. Towards Laser-Textured Antibacterial Surfaces. *Sci Rep* **2018**, *8*, doi:10.1038/s41598-018-28454-2.

161. Song, Y.Y.; Zhang, L.H.; Dong, L.M.; Li, H.T.; Yu, Z.P.; Liu, Y.; Lv, G.J.; Ma, H. Le PH-Responsive Smart Wettability Surface with Dual Bactericidal and Releasing Properties. *ACS Appl Mater Interfaces* **2021**, *13*, doi:10.1021/acsami.1c08263.

162. Yong, J.; Chen, F.; Yang, Q.; Hou, X. Femtosecond Laser Controlled Wettability of Solid Surfaces. *Soft Matter* **2015**, *11*, doi:10.1039/c5sm02153g.

163. Marie Lößlein, S.; Merz, R.; Rodríguez-Martínez, Y.; Schäfer, F.; Grützmacher, P.G.; Horwat, D.; Kopnarski, M.; Mücklich, F. Influence of Chemistry and Topography on the Wettability of Copper. *J Colloid Interface Sci* **2024**, *670*, 658–675, doi:10.1016/J.JCIS.2024.04.212.

164. Aguilar-Morales, A.I.; Alamri, S.; Voisiat, B.; Kunze, T.; Lasagni, A.F. The Role of the Surface Nano-Roughness on the Wettability Performance of Microstructured Metallic Surface Using Direct Laser Interference Patterning. *Materials* **2019**, *12*, doi:10.3390/ma12172737.

165. Cloutier, M.; Mantovani, D.; Rosei, F. Antibacterial Coatings: Challenges, Perspectives, and Opportunities. *Trends Biotechnol* **2015**, *33*, 637–652, doi:10.1016/J.TIBTECH.2015.09.002.

166. Zhao, L.; Chu, P.K.; Zhang, Y.; Wu, Z. Antibacterial Coatings on Titanium Implants. *J Biomed Mater Res B Appl Biomater* **2009**, *91*, 470–480, doi:10.1002/jbm.b.31463.

167. Cheng, H.; Li, Y.; Huo, K.; Gao, B.; Xiong, W. Long-Lasting in Vivo and in Vitro Antibacterial Ability of Nanostructured Titania Coating Incorporated with Silver Nanoparticles. *J Biomed Mater Res A* **2014**, *102*, 3488–3499, doi:10.1002/jbm.a.35019.

168. da Silva, F.S.; Cinca, N.; Dosta, S.; Cano, I.G.; Guilemany, J.M.; Caires, C.S.A.; Lima, A.R.; Silva, C.M.; Oliveira, S.L.; Caires, A.R.L.; et al. Corrosion Resistance and Antibacterial Properties of Copper Coating Deposited by Cold Gas Spray. *Surf Coat Technol* **2019**, *361*, 292–301, doi:10.1016/J.SURFCOAT.2019.01.029.

169. Xu, J.; Li, Y.; Zhou, X.; Li, Y.; Gao, Z. Da; Song, Y.Y.; Schmuki, P. Graphitic C3N4-Sensitized TiO2 Nanotube Layers: A Visible-Light Activated Efficient Metal-Free Antimicrobial Platform. *Chemistry - A European Journal* **2016**, *22*, 3947–3951, doi:10.1002/chem.201505173.

170. Mahmoudi-Qashqay, S.; Zamani-Meymian, M.R.; Sadati, S.J. Improving Antibacterial Ability of Ti-Cu Thin Films with Co-Sputtering Method. *Sci Rep* **2023**, *13*, doi:10.1038/s41598-023-43875-4.

171. Osés, J.; Fuentes, G.G.; Palacio, J.F.; Esparza, J.; García, J.A.; Rodríguez, R. Antibacterial Functionalization of PVD Coatings on Ceramics. *Coatings* **2018**, *8*, doi:10.3390/coatings8050197.

172. Schwibbert, K.; Richter, A.M.; Krüger, J.; Bonse, J. Laser-Textured Surfaces: A Way to Control Biofilm Formation? *Laser Photon Rev* 2024, *18*.

173. Müller, D.W.; Pauly, C.; Brix, K.; Kautenburger, R.; Mücklich, F. Modifying the Antibacterial Performance of Cu Surfaces by Topographic Patterning in the Micro- and Nanometer Scale. *Biomaterials Advances* **2025**, *169*, 214184, doi:10.1016/J.BIOADV.2025.214184.

174. Caneve, L.; Colao, F.; Fantoni, R.; Spizzichino, V. Laser Ablation of Copper Based Alloys by Single and Double Pulse Laser Induced Breakdown Spectroscopy. *Appl Phys A Mater Sci Process* **2006**, *85*, 151–157, doi:10.1007/s00339-006-3661-6.

175. Helbig, R.; Günther, D.; Friedrichs, J.; Rößler, F.; Lasagni, A.; Werner, C. The Impact of Structure Dimensions on Initial Bacterial Adhesion. *Biomater Sci* **2016**, *4*, 1074–1078, doi:10.1039/c6bm00078a.

176. Müller, D.W.; Lößlein, S.; Terriac, E.; Brix, K.; Siems, K.; Moeller, R.; Kautenburger, R.; Mücklich, F. Increasing Antibacterial Efficiency of Cu Surfaces by Targeted Surface Functionalization via Ultrashort Pulsed Direct Laser Interference Patterning. *Adv Mater Interfaces* **2021**, *8*, doi:10.1002/admi.202001656.

177. Zhou, W.; Apkarian, R.; Wang, Z.L.; Joy, D. Fundamentals of Scanning Electron Microscopy (SEM). In *Scanning Microscopy for Nanotechnology: Techniques and Applications*; Springer, 2007; pp. 1–40.

178. Thompson, K.; Lawrence, D.; Larson, D.J.; Olson, J.D.; Kelly, T.F.; Gorman, B. In Situ Site-Specific Specimen Preparation for Atom Probe Tomography. *Ultramicroscopy* **2007**, *107*, 131–139, doi:10.1016/j.ultramic.2006.06.008.

179. Simeone, D.; Baldinozzi, G.; Gosset, D.; Le Caer, S.; Bérar, J.F. Grazing Incidence X-Ray Diffraction for the Study of Polycrystalline Layers. *Thin Solid Films* **2013**, *530*, 9–13, doi:10.1016/j.tsf.2012.07.068.

180. Degen, T.; Sadki, M.; Bron, E.; König, U.; Nénert, G. The High Score Suite. *Powder Diffr* **2014**, *29*, S13–S18, doi:10.1017/S0885715614000840.

181. Stevie, F.A.; Donley, C.L. Introduction to X-Ray Photoelectron Spectroscopy. *Journal of Vacuum Science & Technology A: Vacuum, Surfaces, and Films* **2020**, *38*, doi:10.1116/6.0000412.

182. Ferraro, J.R.; Nakamoto, K.; Brown, C.W. *Introductory Raman Spectroscopy: Second Edition*; Academic Press: San Diego, CA, 2003;

183. Ahmed, A.S.; Müller, D.W.; Bruyère, S.; Holtsch, A.; Müller, F.; Barrirero, J.; Brix, K.; Migot, S.; Kautenburger, R.; Jacobs, K.; et al. Surface Modification of Brass via Ultrashort Pulsed Direct Laser Interference Patterning and Its Effect on Bacteria-Substrate Interaction. *ACS Appl Mater Interfaces* **2023**, *15*, 36908–36921, doi:10.1021/acsami.3c04801.

184. Ahmed, A.S.; Müller, D.W.; Bruyère, S.; Holtsch, A.; Müller, F.; Brix, K.; Migot, S.; Kautenburger, R.; Jacobs, K.; Pierson, J.F.; et al. Antibacterial Property Alterations Induced by Low Zinc Content in Laser-Structured Brass. *Appl Surf Sci* **2024**, *665*, 160338, doi:10.1016/J.APSUSC.2024.160338.

185. Ahmed, A.S.; Sancio, D.; Müller, D.W.; Pierson, J.F.; Mücklich, F. Femtosecond-DLIP on Tin-Alloyed Bronze: Effect of Pulse Fluence on Surface Topography for Antibacterial Application. *Mater Today Adv* **2025**, *27*, doi:10.1016/j.mtadv.2025.100596.

186. Ahmed, A.S.; Wältermann, S.; Delfino, P.M.; Müller, D.W.; Audinot, J.; Pierson, J.-F.; Mücklich, F. 3D Periodic Microscale Structures on Binary Copper-Nickel Alloys via Fs-DLIP: Impact on E. Coli-Substrate Interaction. *Mater Des* **2025**, *258*, 114545, doi:10.1016/J.MATDES.2025.114545.

187. Luo, J.; Ahmed, A.; Pierson, J.F.; Mücklich, F. Tailor the Antibacterial Efficiency of Copper Alloys by Oxidation: When to and When Not To. *J Mater Sci* **2022**, *57*, 3807–3821, doi:10.1007/s10853-022-06879-5.

FIGURES AND TABLES

The End… for now….

because research never really ends — it just changes form.